UNIVERSITY OF CALIFORNIA

Los Angeles

Modeling and Control of Thin Film Surface Morphology: Application to Thin Film Solar Cells

A dissertation submitted in partial satisfaction of the

requirements for the degree Doctor of Philosophy

in Chemical Engineering

by

Jianqiao Huang

2012

ABSTRACT OF THE DISSERTATION

Modeling and Control of Thin Film Surface Morphology:

Application to Thin Film Solar Cells

by

Jianqiao Huang

Doctor of Philosophy in Chemical Engineering

University of California, Los Angeles, 2012

Professor Panagiotis D. Christofides, Co-Chair

Professor Gerassimos Orkoulas, Co-Chair

Thin film solar cells, which consist of multiple layers such as the PIN layers and the Transparent Conducting Oxide (TCO) layers, are playing a more and more important role in the overall solar cell market owing to the potential of improving light conversion efficiencies (currently on the order of 10% for production modules). Over the last decade, it has been widely recognized that the surface morphology at each interface, which is characterized by surface root-mean-square roughness and slope, has crucial influence on the light conversion efficiency of thin film solar cells. Therefore, precisely shaping the surface morphologies of different layers in thin film solar cells during the thin film deposition process is a promising way to improve solar cell efficiency. Despite its importance, the computa-

tional modeling and control of the surface morphology, especially of the root-mean-square surface mean slope, during the thin film deposition process and its application to improve solar cell performance have not received enough attention.

This dissertation presents a systematic framework for modeling and control of thin film surface morphology in both PIN layers and TCO layers. Specifically, we will present novel definitions for describing surface morphology by introducing both the surface root mean square roughness and slope to describe the surface morphology, study its physical properties and dependence on model parameters such like lattice size, activation energies and temperature, introduce and identify stochastic closed-form equations describing surface morphology, and finally design model predictive controllers to control the surface morphology to desired levels. Extensive simulation results are presented to demonstrate the effectiveness of the proposed modeling and control framework.

The dissertation of Jianqiao Huang is approved.

Alan J. Laub

James F. Davis

Gerassimos Orkoulas, Committee Co-Chair

Panagiotis D. Christofides, Committee Co-Chair

University of California, Los Angeles

2012

Contents

List of Figures

ACKNOWLEDGEMENTS

I would like to express my most gratitude to my co-advisor, Professor Panagiotis D. Christofides, for his patience, encouragement, and support throughout my doctoral work. Being his student has been a great fortune for me in my doctoral research study and in my life as well. The PhD offer I got from UCLA was the last one among all my offers. I think my experience has proved that God always saves the best thing for last.

I would like to equally thank my co-advisor, Professor Gerassimos Orkoulas, for his instruction and attention. His knowledge and achievements in the research area of molecular simulation and statistical mechanics are admirable and helpful in my research study.

I would like to thank Professor James F. Davis and Professor Alan J. Laub for agreeing to serve on my doctoral committee.

I would like to thank my parents for their support and encouragement throughout all my life and my wife, in particular, for everything that we have been experiencing together in a different country.

Financial support from NSF, CBET-0652131, and from the UCLA Graduate Division through a 2011–2012 Doctoral Dissertation Year Fellowship, is gratefully acknowledged.

Chapter 2 is a version of: Huang, J., G. Hu, G. Orkoulas, and P. D. Christofides. Dependence of Film Surface Roughness and Slope on Surface Migration and Lattice Size in Thin Film Deposition Processes. *Chemical Engineering Science*, 65:6101–6111, 2010.

Chapter 3 is a version of: Huang, J.,G. Hu, G. Orkoulas, and P. D. Christofides. Dynamics and Lattice-Size Dependence of Surface Mean Slope in thin-film Deposition. *Industrial*

& Engineering Chemistry Research, 50:1219–1230, 2011.

Chapter 4 is a version of: Huang, J., X. Zhang, G. Orkoulas, and P. D. Christofides. Dynamics and Control of Aggregate Thin Film Surface Morphology for Improved Light Trapping: Implementation on a Large-Lattice Kinetic Monte-Carlo Model. *Chemical Engineering Science*, 66:5955–5967, 2011.

Chapter 5 is a version of: Huang, J., G. Orkoulas, and P. D. Christofides. Simulation and Control of Aggregate Surface Morphology in a Two-Stage Thin Film Deposition Process for Improved Light Trapping. *Chemical Engineering Science*, 71:520–530, 2012.

Chapter 6 is a version of: Huang, J., G. Orkoulas, and P. D. Christofides. Modeling and Control of Transparent Conducting Oxide Layer Surface Morphology for Improved Light Trapping. *Chemical Engineering Science*, 74:135–147, 2012.

Chapter 7 is a version of: Huang, J., G. Orkoulas, and P. D. Christofides. Surface Morphology Control of Transparent Conducting Oxide Layers for Improved Light Trapping Using Wafer Grating and Feedback Control. *Chemical Engineering Science*, submitted.

VITA

2003–2008 Bachelor of Science, Chemical Engineering

Dalian University of Technology

Dalian, China

2008–2009 Master of Science, Chemical Engineering

Department of Chemical and Biomolecular Engineering

University of California, Los Angeles

2008–2012 Graduate Student Researcher/Teaching Assistant/Fellow

Department of Chemical and Biomolecular Engineering

University of California, Los Angeles

2011–2012 Dissertation Year Fellowship

University of California, Los Angeles

PUBLICATIONS

1. J. Huang, G. Orkoulas and P. D. Christofides. Surface Morphology Control of Transparent Conducting Oxide Layers for Improved Light Trapping Using Wafer Grating and Feedback Control. *Chemical Engineering Science*, submitted.

2. J. Huang, G. Orkoulas and P. D. Christofides. Modeling and Control of Transparent Conducting Oxide Layer Surface Morphology for Improved Light Trapping. *Chemical Engineering Science*, 74, 135-147, 2012.

3. J. Huang, X. Zhang, G. Orkoulas and P. D. Christofides. Dynamics and Control

of Aggregate Thin Film Surface Morphology for Improved Light Trapping: Implementation on a Large-Lattice Kinetic Monte-Carlo Model. *Chemical Engineering Science*, 66, 5955-5967, 2011.

4. J. Huang, G. Orkoulas and P. D. Christofides. Simulation and Control of Aggregate Surface Morphology in a Two-Stage Thin Film Deposition Process for Improved Light Trapping. *Chemical Engineering Science*, 71, 520-530, 2012.

5. J. Huang, G. Hu, G. Orkoulas and P. D. Christofides. Dynamics and Lattice-Size Dependence of Surface Mean Slope in thin-film Deposition. *Industrial & Engineering Chemistry Research*, 50, 1219-1230, 2011.

6. J. Huang, G. Hu, G. Orkoulas and P. D. Christofides. Dependence of film surface roughness and slope on surface migration and lattice size in thin film deposition processes. *Chemical Engineering Science*, 65: 6101C6111, 2010.

7. X. Zhang, J. Huang, G. Hu, G. Orkoulas and P. D. Christofides. Controlling Aggregate Thin Film Surface Morphology for Improved Light Trapping Using a Patterned Deposition Rate Profile. *Chemical Engineering Science*, 67,101-110,2012.

8. G. Hu, J. Huang, G. Orkoulas and P. D. Christofides. Investigation of film surface roughness and porosity dependence on lattice size in a porous thin film deposition process. *Physical Review E*, 80: 041122, 2009.

Chapter 1

Introduction

1.1 Background on modeling and control of thin film microstructure

Thin film solar cells constitute an important and growing component of the overall solar cell market (see, for example, [14, 46]) owing to their reduced cost relative to silicon-based solar cell modules as well as to the potential of using various thin film materials which may lead to improved light conversion efficiencies (currently on the order of 10% for production modules.) In addition to investigating the performance with respect to light conversion efficiency and long-term stability of an array of materials, thin film solar cell technology stands to benefit from optimal thin film manufacturing (deposition) control strategies that produce thin films with desired light reflectance and transmittance properties. Extensive research

on optical properties of thin-film, primarily silicon, solar cells has demonstrated that the scattering properties of the thin film interfaces directly influence the light trapping ability and the efficiency of thin-film silicon solar cells and the scattering properties are strongly affected by the surface/interface morphologies at each surface/interface in thin film solar cell systems (see, for example, [54, 42, 40, 43]). Shaping the morphology of the various surfaces/interfaces at the thin film deposition stage is therefore critical in order to maximize the amount of light trapped within the solar cell and converted to electrical energy. With respect to visible light trapping by thin film solar cells, the light scattering properties of the various surfaces/interfaces have a complex dependence on the surface morphology interface. In the context of solar cell performance, it is noticed that the wavelength of the visible light is much larger than the size of the silicon atom and the atomic level surface morphology will not be accurately sensed by the visible light. Thus, the aggregate surface roughness and slope are defined at a length scale that is comparable to the wavelength of visible light. While developing accurate models for predicting optical properties of thin films is an on-going research topic, it is well-established that the root-mean-square surface roughness and slope at characteristic length scales that are comparable to the wavelength of the visible light are key factors that influence thin film reflectance and transmittance (e.g., [9, 50]). Specifically, significant increase of conversion efficiency with appropriately roughened interfaces has been reported in several works [45, 33, 44, 30, 28].

To provide a concrete example of this issue, we focus on a typical p-i-n thin-film solar cell (Fig. 1.1). In this thin-film solar cell, light comes into the hydrogenated amorphous

silicon (a-Si:H) semiconductor layers (p, i, n layers) through a front transparent conducting oxide (TCO) layer (made, for example, of ZnO:Al), and part of this light is absorbed by the semiconductor layers before it reaches the back TCO layer. At the back TCO layer, the remaining light is either reflected back to the semiconductor layers to potentially be absorbed again or leaves the system by transmitting through the back TCO layer. The reflected light that is not absorbed reaches the front TCO layer again and this process of reflection and transmission is repeated until all the light leaves the cell or is absorbed by the cell. We focus on a thin film a-Si:H p-i-n solar cell with glass/ZnO:Al as the front TCO layer and ZnO:Al as the back TCO layer to demonstrate quantitatively the influence of sufrace/interface roughness, r, and slope, m, on thin film light reflectance and transmittance.

Light scattering (Rayleigh scattering) occurs when the incident light goes through a rough interface, where it is divided into four components: specular reflection, specular transmission, diffused reflection and diffused transmission; see Fig. 1.2 [45, 33]. If a rough thin film surface is illuminated with a beam of monochromatic light at normal incidence, the total reflectance, R, can be approximately calculated as follows [9]:

$$\begin{aligned} R = \quad & R_0 \exp(-4\pi r_\Delta^2/\lambda^2) + R_0 \int_0^{\pi/20} 2\pi^4 \left(\frac{a}{\lambda}\right)^2 \\ & \times \left(\frac{r_\Delta}{\lambda}\right)^2 (\cos\theta + 1)^4 \sin\theta \exp[-(\pi a \sin\theta)^2/\lambda^2] d\theta \end{aligned} \tag{1.1}$$

where R_0 is the reflectance of a perfectly smooth surface of the same material, r_Δ is the aggregate rms roughness, Δ is the aggregation size and in this work Δ = 400, θ is the incident angle, λ is the light wavelength and a is the auto-correlation length of the interface.

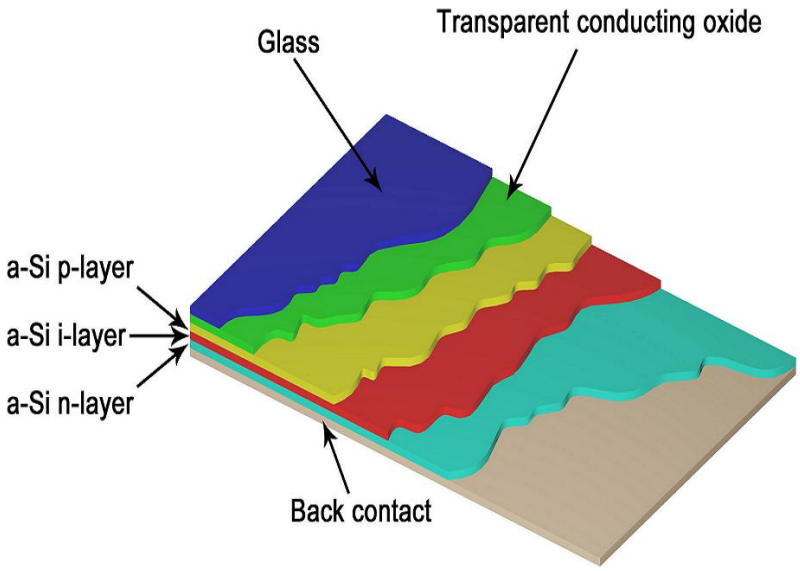

Figure 1.1: Typical structure of a p-i-n thin-film solar cell with front transparent conducting oxide (TCO) layer and back contact.

It can be proved that $a = \sqrt{2} r_\Delta / m_\Delta$, where m_Δ is the aggregate rms slope of the profile of the interface [2]. The numerical integration result of Eq. 1.1 is shown in Fig. 1.3. It is necessary to note that Eq. 1.1 is only valid when θ is small, so in the integration $\theta \in [0, \pi/20]$. From Fig. 1.3, it can be inferred that both r_Δ and m_Δ strongly influence the intensity of light reflection (and light transmission) at the surface/interface. Specifically, for a thin-film solar cell, the objective is to maximize the light trapping efficiency by controlling the intensities and directions of light reflection and transmission at surfaces and interfaces in the thin film solar cell. This control objective can be achieved by attaining proper values of r_Δ and m_Δ during the thin-film manufacturing process. Therefore, it is important during the manufacturing of thin-film solar cells to regulate process input variables such that the surfaces/interfaces of the produced thin-film solar cells have appropriate values (set-points) of r_Δ and m_Δ that optimize light reflectance and transmittance.

In the context of modeling of thin film growth and surface morphology, two mathematical approaches have been developed and widely used: kinetic Monte Carlo (kMC) methods and stochastic differential equation (SDE) models. KMC methods provide unbiased realizations of thin film growth processes based on pre-defined microscopic rules. The corresponding thermodynamic and kinetic parameters that differentiate the microscopic growth models are obtained from experiments and/or molecular dynamics simulations [35, 55, 34, 7]. However, kMC models are not available in closed form, and thus, they cannot be readily used for feedback control design and system-level analysis. On the other hand, SDE models can be derived from the corresponding master equation of the

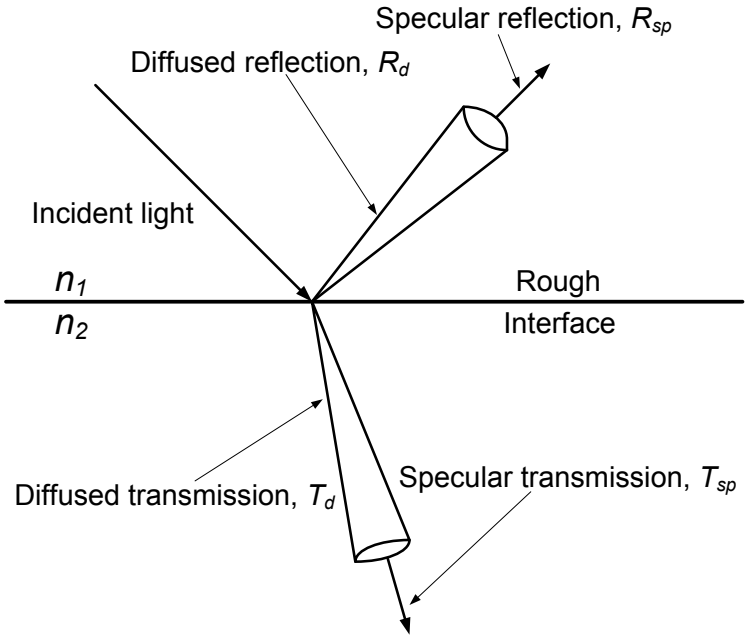

Figure 1.2: Light scattering at a rough interface: specular reflection, R_{sp}, diffused reflection, R_d, specular transmission, T_{sp}, and diffused transmission, T_d. n_1 and n_2 are the refractive indices of the two substances above and below the rough interface, respectively.

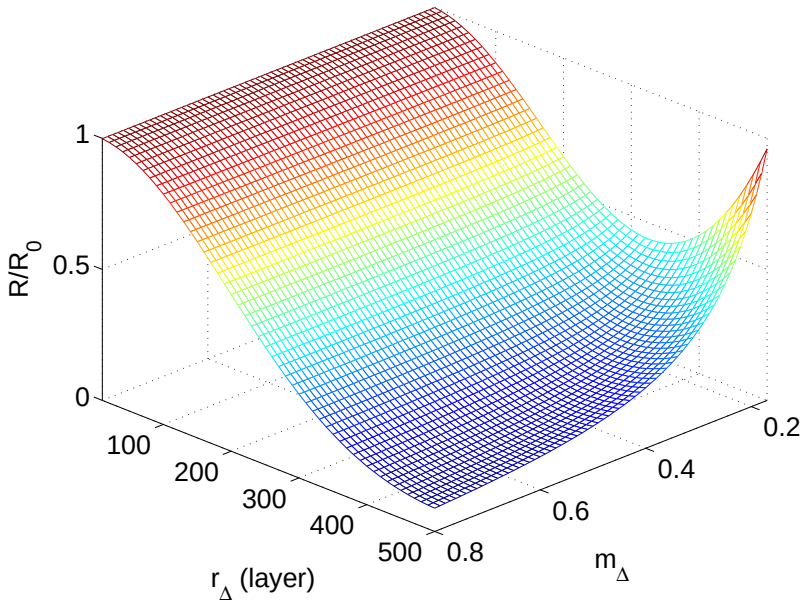

Figure 1.3: Reflectance as a function of r_Δ and m_Δ of thin film surface.

microscopic process and/or identified from process data. Specifically, methodologies have been developed to construct SDE models and estimate their parameters from first principles (e.g., [15, 16, 17]) and numerical simulations (e.g., [7, 19]). The closed form of the SDE models enables their use as the basis for the design of feedback controllers which can regulate thin film surface roughness [7, 19], film porosity [22], and film thickness [21].

In kMC models, different lattices are utilized for different applications. Specifically, a triangular lattice is utilized when the film porosity is studied. This model allows for overhangs and vacancies inside the film and it is perfect to simulate the properties of film porosity. However,0 for solar cell applications, the research focus is to study the surface properties' influence on solar cell performance and it is not necessary to keep the information inside the film. Therefore, a solid-on-solid square lattice is introduced to simulate the

thin film solar cell growth process. In this model, every particle is placed right over another particle and no vacancies are allowed inside the film, which is sufficient to study the surface morphology's influence on solar cell performance. Beyond the choice of lattice, different growth mechanisms have been developed to describe thin film growth processes. Specifically, a random deposition with surface relaxation (RDSR) model was introduced in [11]. The dependence of surface irregularity on the lattice size of the RDSR model, i.e., scaling properties, was investigated via both numerical simulations and theoretical derivations [11, 1]. A competitive growth model that considers separate deposition and migration processes (deposition/migration model) was further developed to capture the balance of these two processes at different substrate temperatures [41]. In addition, the dynamics and the scaling properties of surface roughness in the deposition/migration model were also investigated both numerically and analytically and revealed a temperature dependence.

In SDE models, an Edwards–Wilkinson (EW) type equation is introduced to describe the thin film dynamics. Both the numerical and analytical solutions of the EW equation are derived at the length scale that is comparable to the wavelength of visible light. The parameters of the EW equation are identified by fitting the analytical solutions of EW equations to open-loop kMC simulation data. Since the solution of EW equation is available in closed form, it can be readily used for feedback controller design.

Over the last twenty years within the control engineering literature, extensive efforts have been made on the modeling and model-based feedback control of thin film deposition processes with emphasis on the problems of film thickness, roughness and porosity

regulation. With respect to model-based feedback control of thin film deposition, early efforts focused on deposition spatial uniformity control on the basis of continuum-type distributed parameter models (e.g., [6]), while within the last ten years, most attention has focused on control of thin film surface morphology and microstructure. Since kMC models are not available in closed form and cannot be readily used for feedback control design and system-level analysis, stochastic differential equation (SDE) models (whose parameters are computed from kMC model data) have been used as the basis for the design of feedback controllers to regulate thin film surface roughness (e.g., [7, 41, 47, 48, 18]), film porosity [20, 18], and film thickness [21].

After the successful regulation of silicon thin film deposition process, we extend our method to simulate and control the manufacturing process of Transparent Conducting Oxide (TCO) layers. Transparent Conducting Oxide (TCO) layer, which consists of zinc oxide (ZnO) and aluminum (Al), is an important component of thin film solar cells and has a crucial influence on the performance of thin film solar cell systems (see, for example, [31, 13]). Extensive research on optical properties of thin-film TCO layers has demonstrated that the surface morphology at the interface, which is characterized by surface roughness and slope, directly influences the efficiency of thin-film silicon solar cells (see, for example, [13, 31, 54, 42, 40, 43]). To simulate this process, a two-species kinetic Monte Carlo model is utilized and different growth mechanisms are defined for each species. After that, model predictive controller is designed to shape the surface properly for improved solar cell performance, and a patterned deposition rate profile is used to shape

the surface. To make the process more practical, the wafer grating method, which means using suitably patterned wafers for solar panel manufacturing, is used in combination with patterned deposition rate profiles to precisely control the surface morphology [36, 12, 5, 4].

1.2 Dissertation objectives and structure

Motivated by the above considerations, this dissertation focuses on the modeling and the control of film surface morphology in thin film solar cell growth processes. Kinetic Monte Carlo models are developed to simulate the thin film growth processes on the basis of different lattice structures and growth mechanisms. Surface height profile, surface roughness and slope are defined and computed from the kMC simulation data and are used to characterize the surface morphology and microstructure of the thin films. Stochastic differential equation models are introduced to describe the evolution of the thin film surface morphology and used as the basis for the feedback control design. The model parameters of the dynamic equation models can be estimated on the basis of the kMC simulation data using least-square methods. MPC algorithms are developed to regulate and stabilize the thin film surface roughness and slope at desired levels. The dissertation has the following structure:

Chapter 2 focuses on the simulation of silicon thin film growth process. Both RDSR and deposition/migration models are considered on a square lattice in both one-dimension and two-dimensions using the solid-on-solid assumption. Kinetic Monte Carlo methods are used to simulate both models. The surface roughness and surface slope are defined

to characterize the surface morphology and their dependence on lattice size are carefully studied. Furthermore, activation energy barrier is changed to study its influence on surface morphology. The results suggest that preferential migration (i.e., surface particles with zero or one nearest neighbor dominate the migration events) results in a stronger dependence of surface roughness and slope on the lattice size in thin film deposition processes. Finally, the different dynamics of surface roughness and slope evaluated under different characteristic length scales is investigated, and the need for spatially distributed control actuation to induce desired roughness and slope levels at large characteristic length scales is demonstrated.

Chapter 3 focuses on the study of the dynamic behavior and lattice size dependence of the surface root-mean-square slope of thin-film deposition processes. Two different lattices, solid-on-solid square lattice and triangular lattice, are used. Two different deposition processes are investigated: a random deposition with surface relaxation process and a porous thin-film deposition process. Both deposition processes involve a deposition (adsorption) process and a relaxation (migration) process, which strongly influence the resulting thin-film surface morphology. KMC methods are used to simulate the deposition processes and generate film surface height profiles and compute rms slope and roughness. A theoretical analysis is provided using an Edwards–Wilkinson (EW)-type partial differential equation (PDE) that can describe the dynamics of the surface height profile in the deposition processes under consideration. The kMC simulation findings are corroborated by the analytical results of appropriate finite-difference discretizations of the solutions of the EW equation

model.

Chapter 4 presents an integrated control actuator and control algorithm design for the regulation of deposition of thin films such that the final thin film surface morphology is characterized by a desired visible light reflectance/transmittance level. To demonstrate the approach, a thin film growth process is simulated via kMC method and thin film surface morphology characteristics like roughness and slope are computed for different characteristic length scales and it is found that a patterned actuator design is needed to induce thin film surface roughness and slope at visible light wavelength spatial scales, that lead to desired thin film reflectance and transmittance values. An Edwards-Wilkinson-type equation is used to model the surface evolution at the visible light wavelength spatial scale and to form the basis for feedback controller design within a model predictive control framework. Extensive simulation studies demonstrate that the proposed controller and patterned actuator design successfully regulate surface roughness and slope at visible light wavelength spatial scales to set-point values at the end of the deposition that yield desired levels of thin film reflectance and transmittance.

In Chapters 5 focuses on the development of a model predictive control (MPC) algorithm to simultaneously regulate the aggregate surface slope and roughness of a two-stage thin film growth process to optimize thin film light reflectance and transmittance. In the first stage of the process, a uniform deposition rate profile is utilized and in the second stage of the deposition process, a spatially distributed deposition profile is used to carry out the simulation. This process is modeled on a one-dimensional solid-on-solid square lattice

using kMC methods. An Edwards–Wilkinson (EW)-type equation is used to describe the dynamics of the aggregate surface height profile obtained form the kMC model and predict the evolution of the aggregate rms roughness and aggregate rms slope. A model predictive control algorithm is then developed on the basis of the dynamic equation model to regulate the aggregate rms slope and the aggregate rms roughness at desired levels. Closed-loop simulation results demonstrate the effectiveness of the proposed model predictive control algorithm in successfully regulating the aggregate rms slope and the aggregate rms roughness at desired levels that optimize thin film light reflectance and transmittance.

Chapter 6 focuses on the application of microscopic modeling and control to the process of TCO thin film deposition, which consists of ZnO and Al. Specifically, this work introduces a two species simulation for TCO layer deposition process and presents an integrated control actuator and control algorithm design framework for the regulation of deposition of TCO thin films such that the final thin film surface morphology is controlled to a desired level. An Edwards-Wilkinson-type equation is used to model the surface evolution at the visible light wavelength spatial scale and to form the basis for feedback controller design within a model predictive control framework. The cost function of the predicted controller involves penalties on both surface roughness and slope from set-point values as well as constraints on the magnitude and rate of change of the control action. Extensive simulation studies demonstrate that the proposed controller and patterned actuator design successfully regulate surface roughness and slope at visible light wavelength spatial scales to set-point values at the end of the deposition.

Chapter 7 focuses on the application of microscopic modeling and analysis of a TCO thin film deposition process on a sinusoidal grated wafer, and model predictive control is utilized to control the surface morphology to desired values. To demonstrate the approach, we focus on a two species thin film deposition process using a grated initial lattice, which is modeled via kinetic Monte-Carlo simulation. The initial lattice is defined based on a sinusoidal function with proper magnitude ($M = 100$ layers) and 5 sine waves are placed across the lattice. An Edwards–Wilkinson-type equation is used to model the surface evolution and to form the basis for feedback controller design within a model predictive control framework. The cost function of the predicted controller involves penalties on both surface roughness and slope, following [26]. Extensive simulation studies demonstrate that the proposed controller and patterned actuator design successfully regulate surface roughness and slope at visible light wavelength spatial scales to desired set-point values at the end of the deposition.

Finally, Chapter 8 summarizes the contributions of this dissertation.

Chapter 2

Dependence of Film Surface Roughness and Slope on Surface Migration and Lattice Size in Thin Film Deposition Processes

2.1 Introduction

This chapter focuses on the study of the dependence of film surface roughness and slope on the lattice size in thin film deposition processes. Both random deposition with surface relaxation (RDSR) model and deposition/migration models are considered on a square lattice in both one-dimension and two-dimensions using the solid-on-solid assumption. Kinetic

Monte Carlo methods are used to simulate both models. The surface roughness and surface slope are defined as the root-mean-squares of the surface height profile and of the surface slope profile, respectively. We find that both surface roughness and slope evolve to steady-state values at large times but are subject to different dynamics and scaling properties. A linear dependence and a logarithmic dependence of surface roughness square on the lattice size are observed in the one-dimensional and two-dimensional models, respectively, of the random deposition with surface relaxation model and the deposition/migration model with zero activation energy contribution from each neighboring particle. Furthermore, a stronger lattice-size dependence is found in the deposition/migration model with a significant migration activation energy contribution from each neighboring particle. This finding suggests that preferential migration (i.e., surface particles with zero or one nearest neighbor dominate the migration events) results in a stronger dependence of surface roughness on the lattice size in thin film deposition processes. In contrast, a weak lattice-size dependence is found for the surface mean slope in all growth models considered, especially at large lattice sizes. Finally, the different dynamics of surface roughness and slope evaluated under different characteristic length scales is investigated, and the need for spatially distributed control actuation to induce desired roughness and slope levels at large characteristic length scales is demonstrated.

2.2 Description of thin film deposition processes

In this section, two different thin film deposition process models are introduced: a random deposition with surface relaxation (RDSR) model and a process model involving deposition and surface migration (deposition/migration model). Both deposition models are constructed on a square lattice in both one-dimension (1D) and two-dimensions (2D) using the solid-on-solid (SOS) assumption, where particles land on top of the existing surface particles. Periodic boundary conditions are applied to these lattice models in the directions that are perpendicular to the growth direction. Lattice size is defined as the number of sites in the lateral direction bounded by the periodic boundaries. In the two-dimensional lattice, the lattice sizes in the two lateral directions are the same, i.e., the deposition process models take place on a square lattice in the two-dimensional case.

Fig. 2.1 shows the lattice models of the thin film deposition processes in both 1D and 2D cases. In Fig. 2.1, the incident particles are deposited vertically onto the thin film. The surface particles, i.e., the highest particles of the lattice sites, are subject to an instantaneous surface relaxation event (the RDSR model) or a migration event (the deposition/migration model). The details of the microscopic events in these two models will be discussed in the following subsections. Kinetic Monte Carlo methods are used to simulate both deposition process models. Specifically, we use the continuous-time Monte Carlo (CTMC) algorithm [49] to simulate the thin deposition process models.

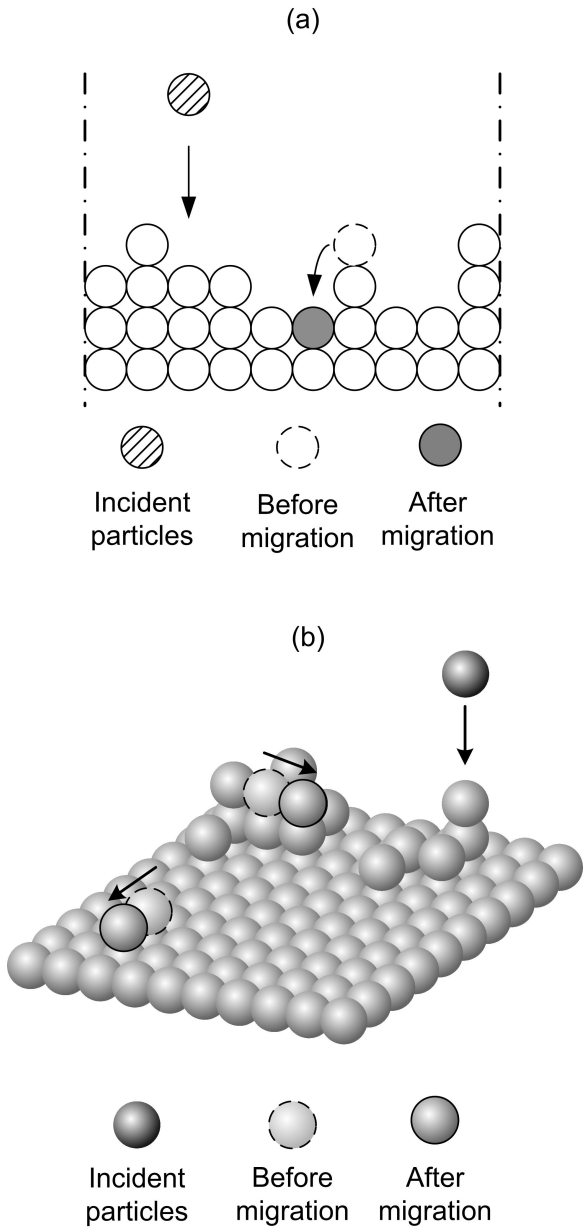

Figure 2.1: Thin film deposition processes on (a) a one-dimensional square lattice and (b) a two dimensional square lattice.

2.2.1 Random deposition with surface relaxation model

The RDSR model is a convenient basic model of the thin film deposition process since its microscopic rules are simple and its dynamic behavior is known [24, 1, 29]. In the RDSR model, there is only one type of microscopic event: the random deposition with surface relaxation event. When a particle is deposited, a site is first randomly chosen among all lattice sites. After the site is determined, an incident particle deposits on the top of the surface particle on that site. Upon deposition, the deposited particle is subject to a surface relaxation event if any of the nearest neighbors of the site is lower than the initial deposition site. When the surface relaxation event is conducted, the deposited particle moves to the neighboring site with the lowest height among its nearest neighboring sites. For the case for which two or more neighboring sites have the same lowest heights, the deposited particle randomly chooses (with equal probability) a neighboring site as its final deposition site. When the lowest height of the nearest neighbors is only one layer lower than the center site after deposition, the deposited particle may stay in the original deposited site subject to the same probability to the one that this particle moves to the lowest nearest neighboring site. We note that the number of nearest neighboring sites varies with respect to the dimension of the lattice model. Specifically, there are two nearest neighboring sites in the one-dimensional square lattice and the number of nearest neighboring sites is four in the two-dimensional case.

In the RDSR model, there is only one macroscopic process parameter that characterizes the deposition process: the deposition rate, W, in units of deposited layers per second.

Since random deposition is always followed by surface relaxation of the same deposited particle, the deposition rate, W, does not influence the balance between the deposition and relaxation events. A different W only scales the dynamics of the thin film evolution. Thus, the deposition rate is fixed at $W = 1$ layer/s for the RDSR model in all simulations presented in this work.

2.2.2 Deposition/migration model

In the deposition/migration model [41], the deposition and migration events are separate and independent microscopic events. The deposition event is a random process, i.e., the same random deposition (without surface relaxation) as in the RDSR model in Section 2.2.1. However, the migration event does not follow immediately the deposition of the particle. Instead, each surface particle, i.e., the top particle of a lattice site, is subject to its own migration event with a probability that depends on its local environment and the substrate temperature. The migration rate (probability) follows an Arrhenius-type law as follows:

$$r_{m,i} = \nu_0 \exp\left(-\frac{E_s + n_i E_n}{k_B T}\right), \tag{2.1}$$

where $r_{m,i}$ denotes the migration rate of the i-th surface particle, $\nu_0 = 2k_B T/h$ is a pre-exponential factor, $n_i = 0,\ 1,\ 2,\ \ldots$, is the number of the nearest neighbors in the same layer of the surface particle on the ith lattice site, E_s and E_n are the contribution to the activation energy barrier from the surface site and from each nearest neighbor, respectively, k_B is Boltzmann's constant, h is Planck's constant, and T is the substrate temperature.

When a surface particle is subject to migration, the particle moves onto a neighboring site with a lower surface height. If two or more neighboring sites have lower height than the height of the initial particle site, the migrating particle randomly moves to one of these neighboring sites with equal probability. We note that when n_i equals the number of nearest neighboring sites (i.e., two for the 1D lattice and four for the 2D lattice), the particle is fully surrounded and cannot move. Multi-step moves are not included in this deposition/migration model but can be realized via several successive but separate migration events of the same particle.

In the deposition/migration model, the macroscopic process parameters include the deposition rate, W, and the substrate temperature, T. These two process parameters together determine the growth conditions of the thin film as well as its surface morphology. As in the RDSR model in Section 2.2.1, the deposition rate is fixed as $W = 1$ layer/s for the deposition/migration model. The substrate temperature may be varied at different values.

2.3 Surface roughness

Surface roughness is commonly used to describe the irregularity of surface morphology and measures the vertical deviation of the surface from an ideal, flat surface. In this work, surface roughness is defined as the root-mean-square (rms) of the surface height profile, which is the connection of the centers of the surface particles on all lattice sites. The

definition of surface roughness is given as follows:

$$r = \left[\frac{1}{L}\sum_{i=1}^{L}(h_i - \bar{h})^2\right]^{1/2}, \qquad \text{one-dimension},$$
$$r = \left[\frac{1}{L^2}\sum_{i=1}^{L}\sum_{j=1}^{L}(h_{i,j} - \bar{h})^2\right]^{1/2}, \quad \text{two-dimensions}, \tag{2.2}$$

where r denotes surface roughness, h_i ($h_{i,j}$), $i = 1, 2, \ldots, L$, is the surface height at the i-th (i, j-th) position in the unit of layer, L denotes the lattice size, and $\bar{h} = \frac{1}{L}\sum_{i=1}^{L} h_i$ is the average surface height defined as follows:

$$\bar{h} = \frac{1}{L}\sum_{i=1}^{L} h_i, \qquad \text{one-dimension},$$
$$\bar{h} = \frac{1}{L^2}\sum_{i=1}^{L}\sum_{j=1}^{L} h_{i,j}, \quad \text{two-dimensions}. \tag{2.3}$$

To investigate the scaling properties of surface roughness, we perform a series of kMC simulations for the two deposition models for different lattice sizes. Both one-dimensional and two-dimensional lattices are investigated. The surface roughness is computed on the basis of the surface height profile that is obtained from the kMC simulation at each sampling time. For the convenience of observing the lattice size dependence, the roughness square, r^2, is used to express the results. Since the deposition process is a stochastic process in nature, multiple independent kMC simulations ($1,000$–$30,000$, depending on the level of fluctuations) under the same operating conditions are repeated to generate the expected value of the roughness square. The range of lattice size is chosen as large as possible under the limitation of currently available computing power and the requirement to compute

accurate values of expected film surface properties. In this work, all deposition processes start with flat initial surface height profiles.

Remark 2.1 *For each specific point we include in the results, we run a sufficiently large number of simulations so that the computed expected value does not change with the addition of more simulations for that specific condition. For example, for an expected value that is computed using 10,000 runs, the addition of more runs will not change the location of the point at all; this has been checked for all points. For this reason, we use different number of runs for different conditions because some temperature/deposition rate conditions or variables (roughness/slope) require more runs to get an accurate (one that does not change with the addition of more simulations) expected value. With respect to the computation of the errors of the computed mean values, we follow the following procedure: we group the simulations for a specific condition into ten different groups (for example, in the case of running 10,000 simulations, we form 10 groups of 1,000 simulations each) and compute the mean of each group first and then the standard deviation of these ten means which is equal to the size of the error bar. This exact procedure is repeated for all points included in the results.*

2.3.1 Random deposition with surface relaxation model

In the RDSR model of the deposition process, the deposition rate is fixed at $W = 1$ layer/s for all simulations. The lattice size ranges from 20 to 200 sites. Fig. 2.2 shows the evolution profiles of the expected surface roughness square. All profiles in Fig. 2.2 start from

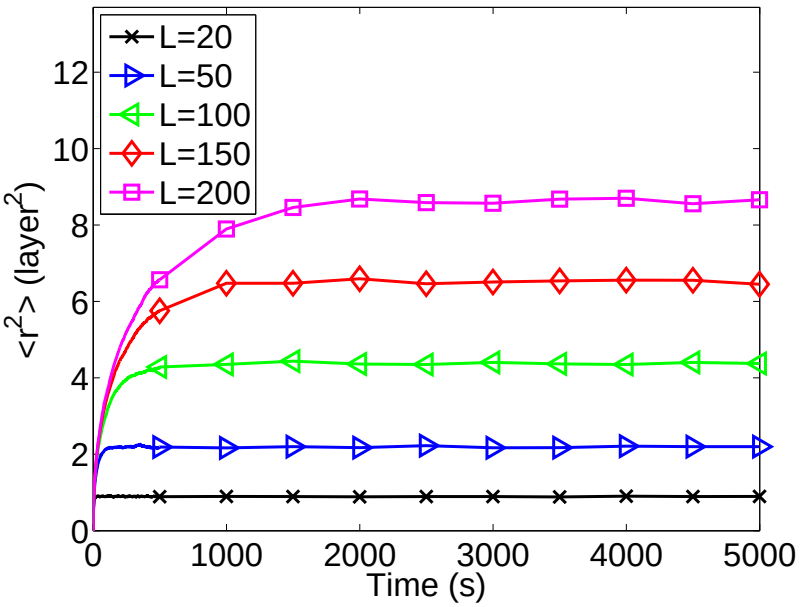

Figure 2.2: Profiles of the expected surface roughness square at different lattice sizes, $L =$ 20, 50, 100, 150, and 200; 1D RDSR model with $W = 1$ layer/s.

zero, since the surface is assumed to be flat at the beginning of the deposition process. At the initial stages of deposition (the time is sufficiently small), all roughness profiles evolve similarly. As time increases, the roughness profiles in Fig. 2.2 increase and approach their respective steady-state values. It is evident from Fig. 2.2 that the lattice size strongly influences the dynamic behavior of surface roughness. The roughness square of the RDSR model with a larger lattice size takes longer time to reach a higher steady-state value. Thus, the roughness profiles for $L = 150$ and $L = 200$ require a longer time frame ($\sim$ 2000 s) to reach their respective steady-states.

To further investigate the scaling properties of surface roughness of the deposition process, we examine the behavior of surface roughness square v.s. lattice size. Fig. 2.3 shows

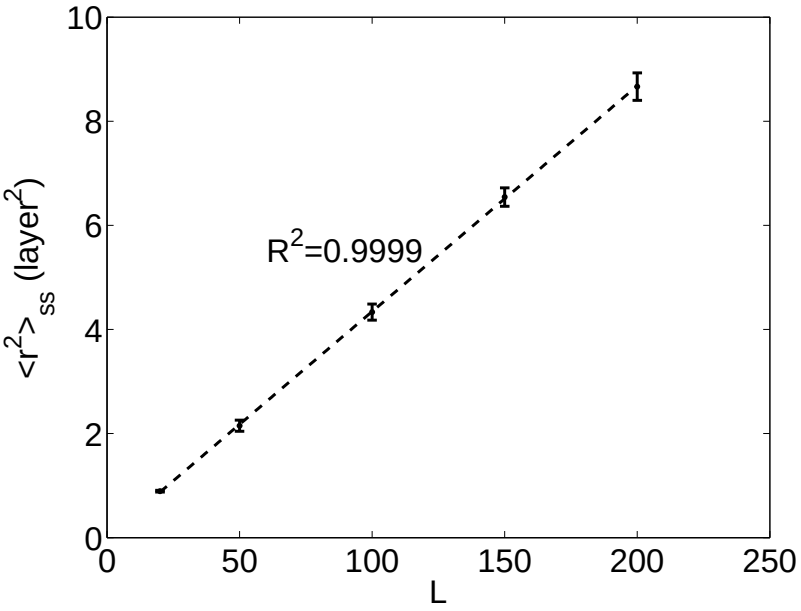

Figure 2.3: Dependence of the expected steady-state value of surface roughness square on the lattice size; 1D RDSR model with $W = 1$ layer/s.

the L-dependent expected steady-state values of surface roughness square, $\langle r^2 \rangle_{ss}$, with respect to the lattice size. A clear linear dependence on the lattice size is observed in Fig. 2.3. This linear lattice-size dependence is consistent with the dynamic equation, the Edwards-Wilkinson (EW) equation, of the RDSR model [29, 18].

Subsequently, we study the scaling properties of the 2D RDSR model. Figs. 2.4 and 2.5 show the profiles of the expected roughness square and the lattice-size dependence of the expected steady-state values of the roughness square of the 2D RDSR model. The evolution profiles in Fig. 2.4 have similar dynamics as the ones in the 1D system shown in Fig. 2.2. This similarity is because the surface height dynamic behavior of the RDSR model belongs to the EW universality class, irrespective of the dimension of the model.

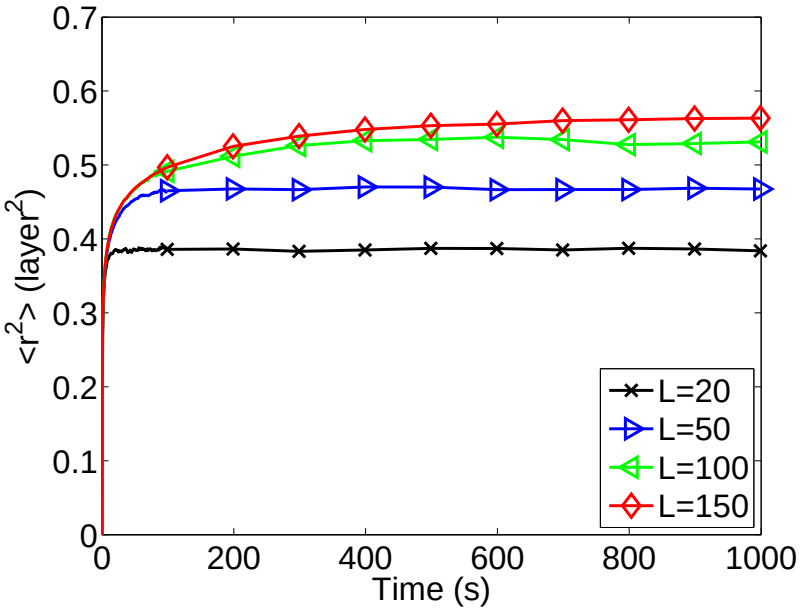

Figure 2.4: Profiles of the expected surface roughness square at different lattice sizes; 2D RDSR model with $W = 1$ layer/s.

A logarithmic dependence on the lattice size can be seen in Fig. 2.5. A semi-log plot is used in Fig. 2.5 with a least-square-fitted line to show clearly the logarithmic dependence. The logarithmic lattice-size dependence of roughness square is consistent with the EW dynamics, from which a dependence of zeroth order on lattice size can be derived (which is consistent with logarithmic dependence) [29].

However, by comparing Figs. 2.2 and 2.4, it can be seen that there is a difference in the dynamics between the 1D and 2D RDSR models. The roughness square in the 2D RDSR model reaches a lower steady-state value at a shorter time, given the same lattice size. The different dynamic behavior of the 2D RDSR model is due to the extra dimension for the surface relaxation, i.e., the deposited particles have more freedom of migrating in

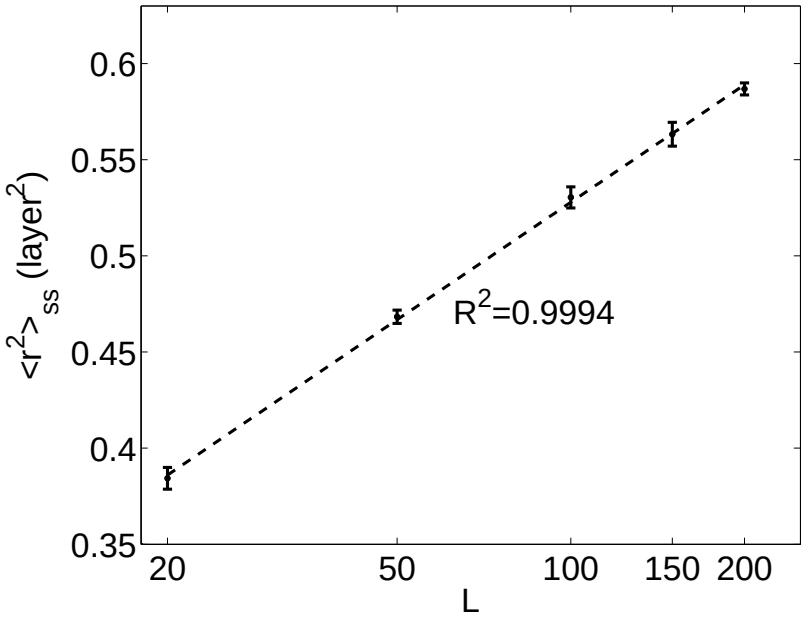

Figure 2.5: Dependence of the expected steady-state value of surface roughness square on the lattice size; 2D RDSR model with $W = 1$ layer/s.

the 2D model than in the 1D model. Thus, it takes less time for the surface roughness in the 2D model to reach a steady-state, which can be thought of as an equilibrium state between the deposition and migration events. Furthermore, the extra dimension for the surface relaxation also leads to different lattice-size dependence of surface roughness; a linear dependence in the 1D RDSR model and a logarithmic dependence in the 2D case, as shown in Figs. 2.3 and 2.5.

2.3.2 Deposition/migration model

In the RDSR model, the ratio between the particle deposition and relaxation rates is fixed and the particles after the deposition/relaxation process cannot move. However, in the deposition/migration model, the deposition and migration events are independent and the particles on the surface are subject to migration unless fully surrounded by nearest neighbors. The thin film surface morphology is the result of a complex interplay between adsorption and migration events. Thus, the surface roughness of the deposition/migration model may have different dynamic behavior, i.e., time of approaching the steady-state value, from the one of the surface roughness in the RDSR model. To carry out the kMC simulations of the deposition/migration model, the values of the activation energy barriers are chosen to be consistent with silicon thin films [18] in the two-dimensional lattice model and are taken as follows: $E_s = 1.2$ eV and $E_n = 0.6$ eV. The operating conditions for the deposition/migration model are chosen so that the resulting surface roughness under these operating conditions is close to the one in the RDSR model; $T = 680$ K and $W = 1$ layer/s

for the 1D model and $T = 650$ K and $W = 1$ layer/s for the 2D model.

In the deposition/migration model, the dynamic behavior of surface roughness square is similar to the one in the RDSR model; the profile of roughness square increases from zero and approaches a steady-state value at large times. However, the scaling properties of roughness are different in the two deposition process models. Figs. 2.6 and 2.7 show the lattice-size dependence of $\langle r^2 \rangle_{ss}$ in the 1D and 2D deposition/migration process models with $E_n = 0.6$ eV, respectively. By comparing to the dependence of $\langle r^2 \rangle_{ss}$ in the RDSR models in Figs. 2.3 and 2.5, both 1D and 2D deposition/migration models have a stronger roughness dependence on the lattice size. The 1D lattice-size dependence is quasi-exponential, $\langle r^2 \rangle_{ss} \sim \exp(L)$ (Fig. 2.6); while the 2D dependence is quasi-linear, $\langle r^2 \rangle_{ss} \sim O(L)$ (Fig. 2.7).

This stronger dependence of surface roughness on the lattice size has a correlation with a larger difference of the rates of the various migration possibilities of the surface particles. Here the migration possibilities refer to the dimension of the lattice and the classifications of surface particles with respect to the number of neighboring particles (particles belonging in different classes are associated with different migration rates when $E_n \neq 0$). In the 1D lattice, the migration of surface particles is limited to one direction; while in the 2D lattice, the surface particles have an extra dimension to migrate. Thus, the roughness dependence on the lattice size in the 1D model is stronger (linear) than in the 2D model (logarithmic). Similarly, in the deposition/migration model with a non-zero E_n, the surface particles are classified according to the number of nearest neighbors, n_i, in Eq. 2.1. The particles in

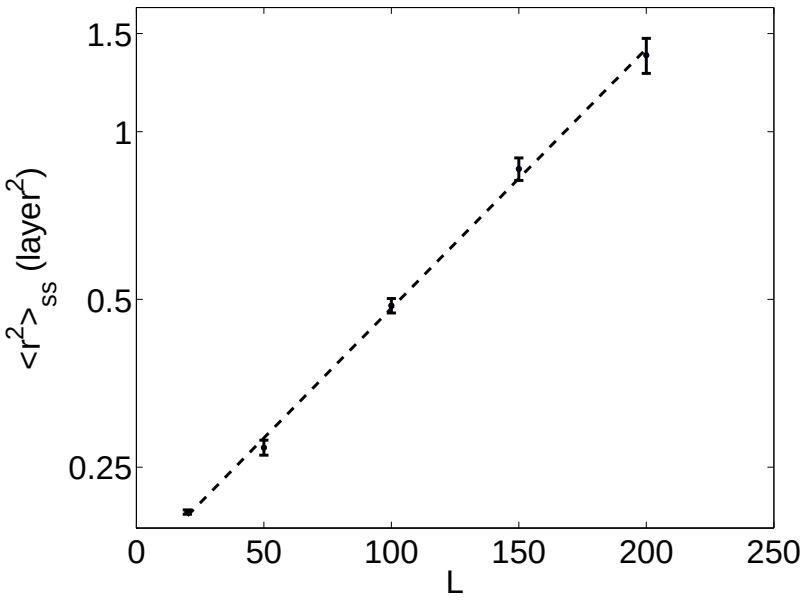

Figure 2.6: Dependence of the expected steady-state value of surface roughness square on the lattice size; 1D deposition/migration model with $E_n = 0.6$ eV, $T = 680$ K, $W = 1$ layer/s.

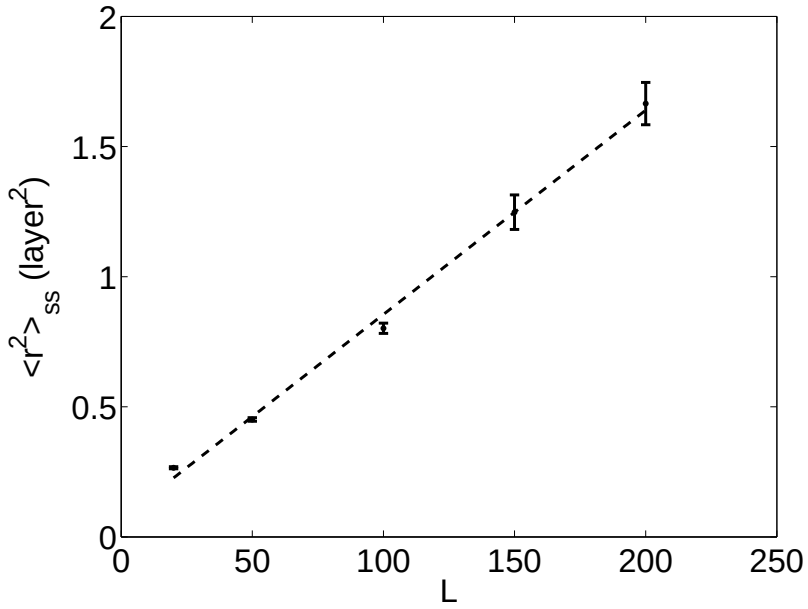

Figure 2.7: Dependence of the expected steady-state value of surface roughness square on the lattice size; 2D deposition/migration model with $E_n = 0.6$ eV, $T = 650$ K, $W = 1$ layer/s.

different classes have different migration rates; a larger migration rate for the class with a smaller n_i. Thus, the surface particles with less nearest neighbors are more likely to migrate than the particles with more nearest neighbors. However, in the RDSR model, all surface particles have the same migration probabilities, since the relaxation event is executed instantaneously following a random deposition. This difference of the migration possibilities (classification of migration particles) in the deposition/migration model results in a stronger lattice-size dependence than in the RDSR model.

To further support the correlation between the scaling properties and the difference of the migration possibilities, kMC simulations are carried out for the deposition/migration model with $E_n = 0$ eV. In the deposition/migration model, a zero E_n indicates no additional energy barrier from each nearest neighbor, and thus, all particles have the same migration rates. From a physical significance point of view, $E_n = 0$ implies that the rate of migration of each surface particle is only dependent on temperature and the activation energy E_s of the surface site and it is independent of the number of nearest neighbors of the particle; this scenario is appropriate in the case where the nearest neighbor interactions of the surface particle are very weak relative to the bonding of the particle with its site. Lower substrate temperatures ($T = 480$ K for the 1D model and $T = 460$ K for the 2D model) are selected for the operating conditions due to the lower total activation energy barriers compared to the deposition/migration model with $E_n = 0.6$ eV. Figs. 2.8 and 2.9 show the lattice-size dependence of $\langle r^2 \rangle_{ss}$ in the 1D and 2D deposition/migration models with $E_n = 0$ eV, respectively. The dependence of $\langle r^2 \rangle_{ss} \sim \exp(L)$ in the deposition/migration model with zero

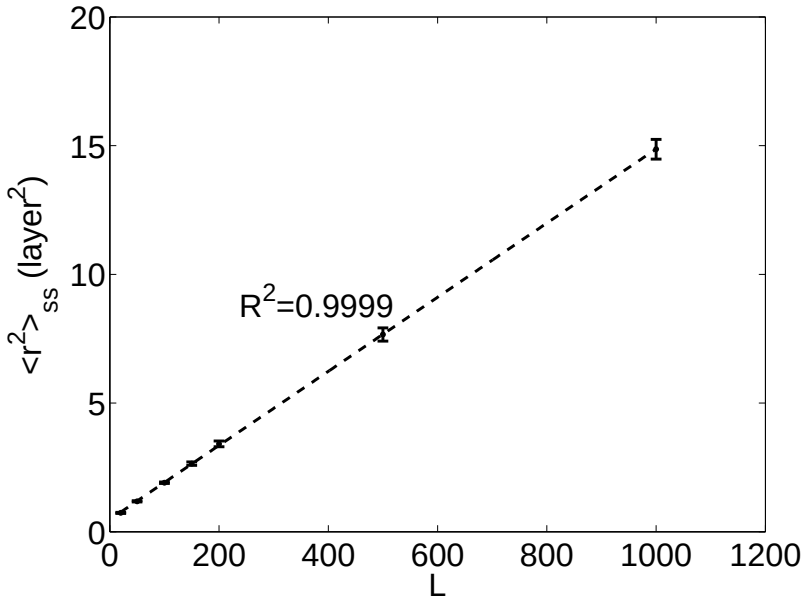

Figure 2.8: Dependence of the expected steady-state value of surface roughness square on the lattice size; 1D deposition/migration model with $E_n = 0$ eV, $T = 480$ K, $W = 1$ layer/s.

E_n on the lattice size, shown in Figs. 2.8 and 2.9, is consistent with the dependence found in the RDSR model; both models have linear lattice-size dependence in the 1D lattice and logarithmic lattice-size dependence in the 2D lattice. The close relationship of the surface roughness dependence on the lattice size for the RDSR model and the deposition/migration model with $E_n = 0$ is expected, since the surface relaxation model has a migration step that is always performed if the neighboring sites have lower height, and this is also achieved in the deposition/migration model with E_n being 0. Furthermore, the roughness is higher in the deposition/migration model versus the RDSR model because the relaxation step takes place in every deposition event in the RDSR model.

Remark 2.2 *Regression coefficients R^2 were only added to the plots where linear depen-*

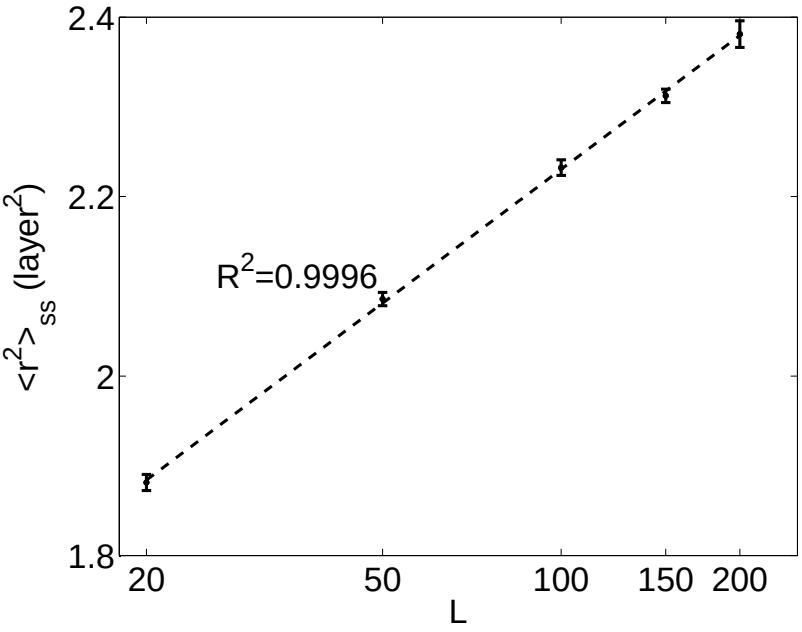

Figure 2.9: Dependence of the expected steady-state value of surface roughness square on the lattice size; 2D deposition/migration model with $E_n = 0$ eV, $T = 460$ K, $W = 1$ layer/s.

dence can be proved analytically (using closed-form equations (stochastic PDEs) of the surface evolution profile) to hold for any lattice size range (Figs. 2.3, 2.5, 2.8 and 2.9). Specifically, in previous works (e.g., [1, 18]), the linear dependence of $\langle r^2 \rangle_{ss}$ *on lattice size L for RDSR models has been proved analytically for any lattice size range, so in the present paper regression coefficients were added in all related plots (Figs. 2.3 and 2.5) to support this conclusion. In addition, regression coefficients were also added to Figs. 2.8 and 2.9 to show that the scaling properties of the deposition/migration model with* $E_n = 0$ *are similar to the ones of the RDSR model. For all the other plots, although quasi-linear or quasi-exponential dependences were observed locally (for the range of lattice size used in the simulations) from the results, there is no proof that these types of dependences hold globally (for any range of lattice size), so regression coefficients were not added.*

2.4 Surface slope

Although rms roughness can be used to capture the height deviations of a thin film surface profile, neither surfaces slope nor surface height correlation between different surface locations can be captured by the rms roughness. Under certain assumptions for surface height distribution functions, these additional surface characteristics can be simplified to the quantities of surface mean slope and auto-correlation length. In this work, the surface

mean slope is defined in a fashion similar to surface roughness as follows:

$$m = \left[\frac{1}{L}\sum_{i=1}^{L} h_{s,i}^2\right]^{1/2}, \qquad \text{one-dimension},$$
$$m = \left[\frac{1}{L^2}\sum_{i=1}^{L}\sum_{j=1}^{L} h_{s,i,j}^2\right]^{1/2}, \quad \text{two-dimensions}, \tag{2.4}$$

where m denotes the rms slope and $h_{s,i}$ ($h_{s,i,j}$), is the surface slope at the i-th (i, j-th) lattice site, which is a dimensionless variable. The surface slope, $h_{s,i}$ ($h_{s,i,j}$), is computed as follows:

$$h_{s,i} = h_{i+1} - h_i, \qquad \text{one-dimension},$$
$$h_{s,i,j} = h_{i+1,j} - h_{i,j}, \quad \text{two-dimensions}. \tag{2.5}$$

Due to the use of PBCs, the slope at the boundary lattice site ($i = L$) is computed as the slope between the last lattice site (h_L) and the first lattice site (h_1). It is necessary to point out that the surface slope in the 2D lattice is calculated as the slope in one dimension. Due to the isotropy of the lattice model, the surface slope can be obtained in either dimension of the lattice, i.e., $(h_{i+1,j} - h_{i,j})$ or $(h_{i,j+1} - h_{i,j})$. To be consistent with the roughness plots, the mean slope square, m^2, is used to present the results.

2.4.1 Random deposition with surface relaxation model

The evolution profiles of the expected mean slope square in the RDSR model, both 1D and 2D, are obtained from the same kMC simulation data for the roughness profiles in Section 2.3. Fig. 2.10 shows the profiles of the expected mean slope square at different

lattice sizes in the 1D and 2D RDSR models. From Fig. 2.10, it can be seen that the mean slope square of the RDSR model has a smaller value and faster dynamics than the roughness square. The different dynamic behavior of the slope is because the correlation between the heights of two adjacent lattice sites in the slope definition in Eq. 2.4 is higher than the correlation between the heights of a lattice site and the average height in the roughness definition in Eq. 2.2 [24].

The dependence of the mean slope square on the lattice size is also different from the dependence of the roughness square; see Fig. 2.11 for the lattice-size dependence of the mean slope square. The expected steady-state value of the mean slope square, $\langle m^2 \rangle_{ss}$, has a very weak dependence on the lattice size in both 1D and 2D RDSR models; $\langle m^2 \rangle_{ss}$ converges to a fixed value. To show the weak dependence, Fig. 2.11 is generated in a semi-log plot, which indicates that the dependence is weaker than logarithmic dependence.

2.4.2 Deposition/migration model

In the deposition/migration model, the weak lattice-size dependence of the mean slope square can be also observed. As is shown in Section 2.3.2, the deposition/migration model with $E_n = 0$ eV exhibits a consistent dynamic behavior and scaling property of surface roughness with the RDSR model. A similar weak dependence of the mean slope square on the lattice size is found in the deposition/migration model with $E_n = 0$ eV; see Fig. 2.12.

However, in the deposition/migration model with non-zero E_n, the lattice-size dependence of the mean slope square is slightly stronger. Fig. 2.13 shows the dependence of

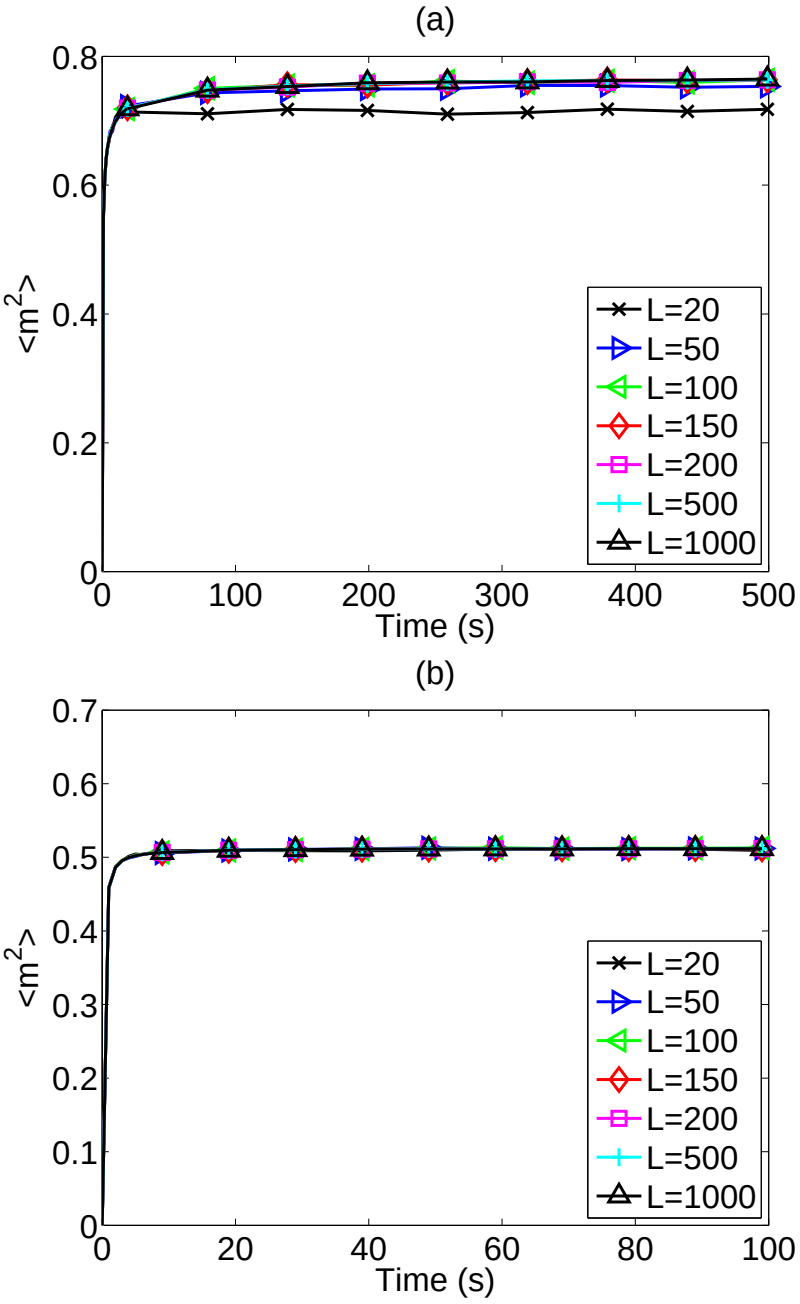

Figure 2.10: Profiles of the expected mean slope square at different lattice sizes; (a) 1D RDSR model and (b) 2D RDSR model with $W = 1$ layer/s.

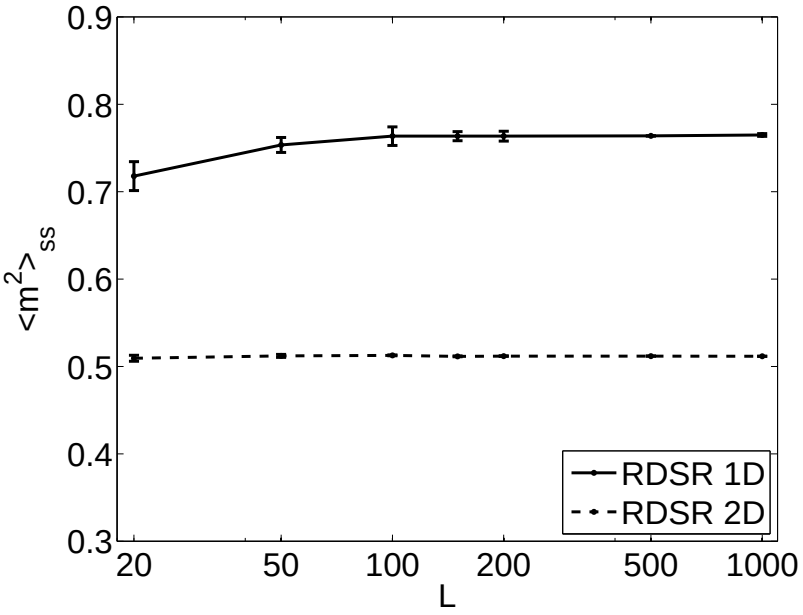

Figure 2.11: Dependence of the expected steady-state value of mean slope square on the lattice size; 1D and 2D RDSR models with $W = 1$ layer/s.

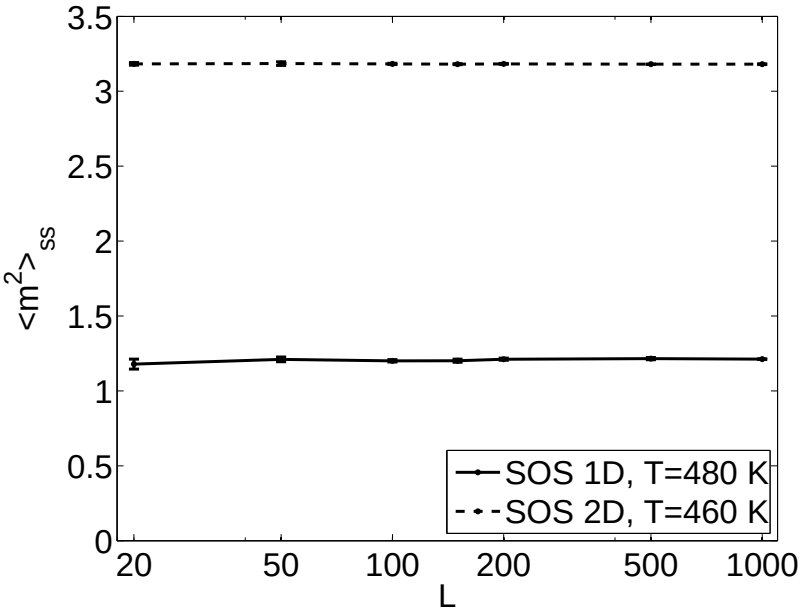

Figure 2.12: Dependence of the expected steady-state value of mean slope square on the lattice size; 1D and 2D deposition/migration models with $E_n = 0$ eV, $T = 480$ K for the 1D model and $T = 460$ K for the 2D model, and $W = 1$ layer/s for both models.

$\langle m^2 \rangle_{ss}$ on the lattice size in the deposition/migration model with $E_n = 0.6$ eV for both 1D and 2D lattices. In the 1D deposition/migration model with non-zero E_n, the lattice-size dependence is quasi-linear; in the 2D model, the dependence is quasi-logarithmic. Overall, the mean slope square has a weaker dependence on the lattice size than the roughness square, especially at large lattice sizes.

2.5 Applications to light trapping efficiency

In this section, the influence of the surface morphology characteristics, i.e., the surface roughness and slope, on the light reflectance/transmittance is investigated in a light scattering (Rayleigh scattering) process. When the incident light goes through a rough interface, the light is divided into four components: specular reflection, specular transmission, diffused reflection and diffused transmission; see Fig. 2.14 [45, 33]. Under the assumptions of normal surface height distribution and correlation, the total reflectance of a beam of monochromatic light at normal incidence to a rough surface, which is denoted by R, can be approximately calculated as follows [9]:

$$\begin{aligned} R &= R_0 \exp\left(-\frac{4\pi r^2}{\lambda^2}\right) \\ &\quad + R_0 \int_0^{\pi/2} 2\pi^4 \left(\frac{a}{\lambda}\right)^2 \left(\frac{r}{\lambda}\right)^2 (\cos\theta + 1)^4 \sin\theta \exp\left[-\frac{(\pi a \sin\theta)^2}{\lambda^2}\right] d\theta \end{aligned} \tag{2.6}$$

where R_0 is the reflectance of a perfectly smooth surface of the same material, θ is the incident angle, λ is the light wavelength, and a is the auto-covariance length of the

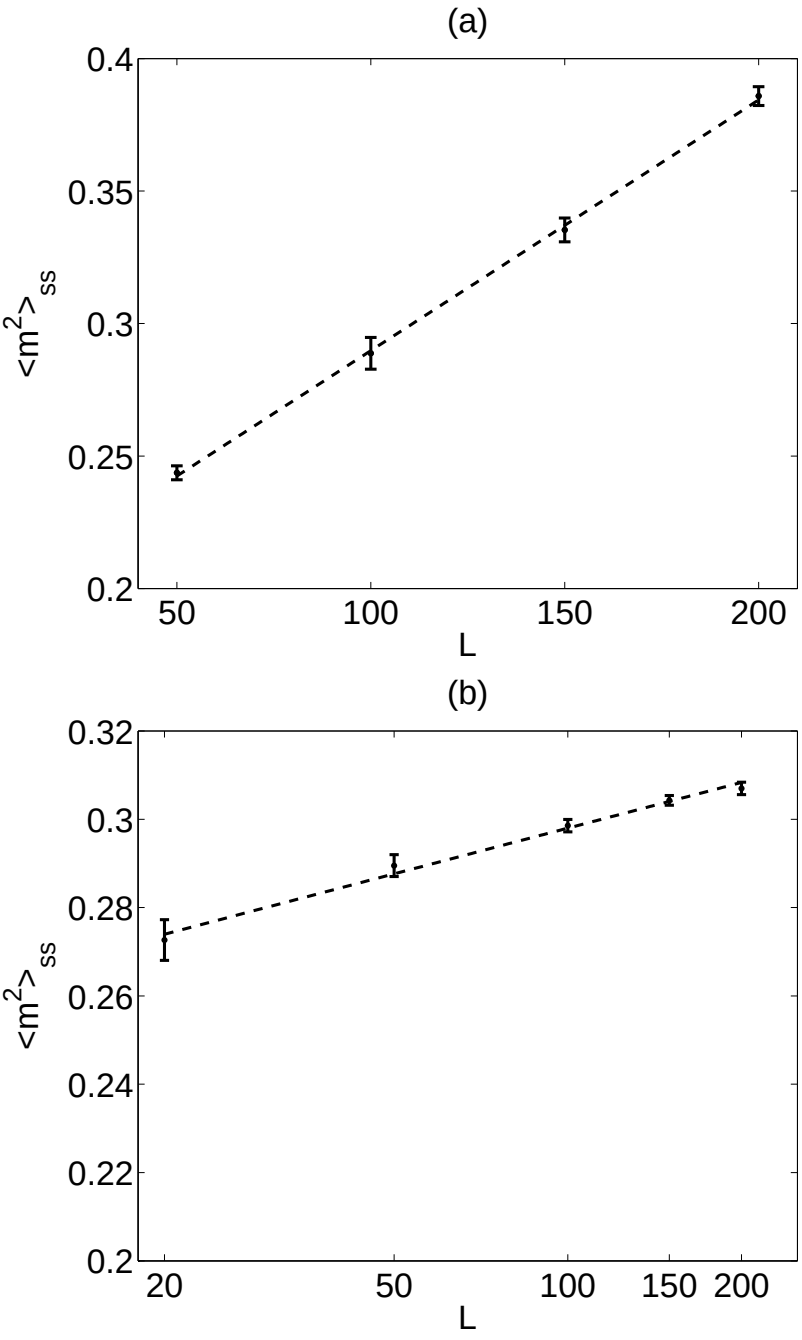

Figure 2.13: Dependence of the expected steady-state value of mean slope square on the lattice size; (a) 1D deposition/migration model with $E_n = 0.6$ eV, $T = 610$ K, and $W = 1$ layer/s and (b) 2D deposition/migration model with $E_n = 0.6$ eV, $T = 650$ K, and $W = 1$ layer/s.

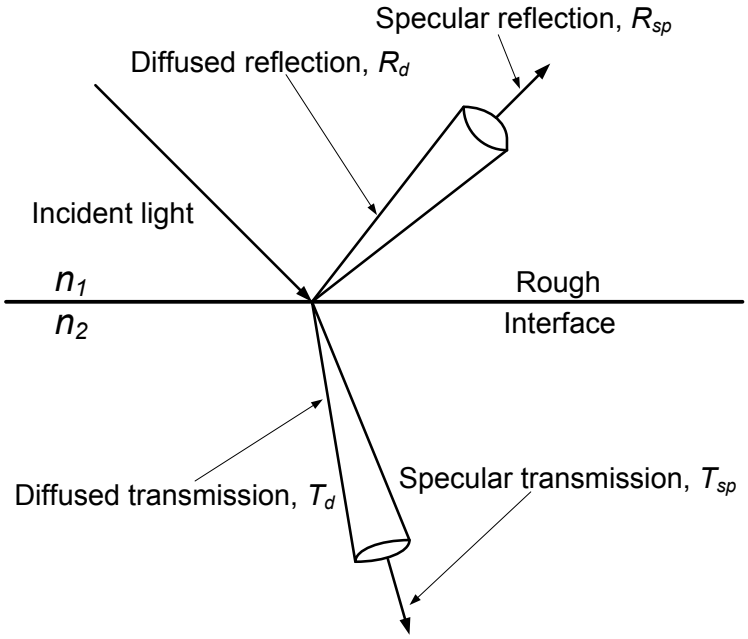

Figure 2.14: Light scattering at a rough interface: specular reflection, R_{sp}, diffused reflection, R_d, specular transmission, T_{sp}, and diffused transmission, T_d. n_1 and n_2 are the refractive indices of the two substances above and below the rough interface, respectively.

interface, which can rewritten as a ratio between the rms roughness and the rms slope, $a = \sqrt{2}r/m$ [2]. Eq. 2.6 shows that both r and m have a strong influence on the intensity of light reflection (and light transmission) at the surface/interface. The distributions of the four components of light reflectance and transmittance are also affected by r and m [30, 32] even though this dependence cannot be expressed by an approximate equation like the one of Eq. 2.6. For thin-film solar cells, specifically, a maximum or minimum of the light reflectance is desired for a certain surface/interface. For example, the top surface of the solar cell favors a minimum reflectance so as to absorb the incident light as much as possible. The objective of an optimal light trapping efficiency can be achieved by attaining certain values of r and m during the manufacturing of thin-film solar cells.

The mean surface slope investigated in this work is defined on the basis of the slope profile computed from the surface heights of the adjacent lattice sites; see Eq. 2.4. Thus, the characteristic length scale of the mean surface slope computed using Eq. 2.4 is the atomic/molecular diameter (~ 0.25 nm). However, the wavelength of visible light (400 nm – 700 nm) is much larger than the diameters of atoms/molecules; it may result in different surface slope under the larger length scale. Thus, it is necessary to compute the mean surface slope over the length scale of the light wavelength.

The new surface slope, m_Δ, is computed similarly to the original mean surface slope of Eq. 2.4, but on the basis of the averaged surface height profile, $h_{\Delta,i}$, which is defined on the basis of the aggregation of Δ surface sites as follows in one-dimension:

$$h_{\Delta,i} = (h_{i\Delta+1} + h_{i\Delta+2} + \cdots + h_{(i+1)\Delta})/\Delta, \quad i = 0, 1, \ldots, L_\Delta - 1 \tag{2.7}$$

where $h_{\Delta,i}$ denotes the averaged surface height, Δ denotes the aggregation size, i.e., the number of lattice sites used to calculate the averaged surface height, and L_Δ denotes the number of aggregated surface heights. For the wavelength of visible light and silicon thin-film solar cells, the corresponding aggregation size, Δ, is around 2000. The computation of aggregated surface mean slope, m_Δ, is given as follows in one-dimension:

$$m_\Delta = \left[\frac{1}{L} \sum_{i=1}^{L_\Delta} \left(\frac{h_{\Delta,i} - h_{\Delta,i+1}}{\Delta} \right)^2 \right]^{1/2}. \tag{2.8}$$

The dynamics of the new surface slope is dependent on the characteristic length scale, Δ. To show this dependence, kMC simulations of the 1D deposition/migration model with $E_n = 0$ eV and $L = 10000$ are carried out at $T = 430$ K and $W = 1$ layer/s. The mean slope square, m_Δ^2, is calculated from the surface height profile from the kMC simulations at different length scales. Fig. 2.15 shows the profiles of the expected mean slope square, $\langle m_\Delta^2 \rangle$, under different characteristic length scales, Δ. It is evident from Fig. 2.15 that the larger the characteristic length scale, the smaller the mean slope square and the slower the dynamics of evolution (i.e., the longer the time to reach the steady-state value).

Furthermore, Fig. 2.16 shows the dependence of the steady-state value of the expected mean slope square, $\langle m_\Delta^2 \rangle_{ss}$, on the characteristic length scale, Δ. This dependence is quasi-quadratic on $1/\Delta$, i.e., $\langle m_\Delta^2 \rangle_{ss} \sim 1/\Delta^2$. Following this dependence, the corresponding mean slope square for Δ around 2000 is very small ($\langle m_\Delta^2 \rangle_{ss} \sim 10^{-5}$). This close-to-zero value of the mean slope square reveals a smoothly changing surface profile with respect to a relatively large characteristic length scale. The smoothness of the surface profile persists at larger lattice sizes as well, due to the very weak lattice-size dependence of the mean slope

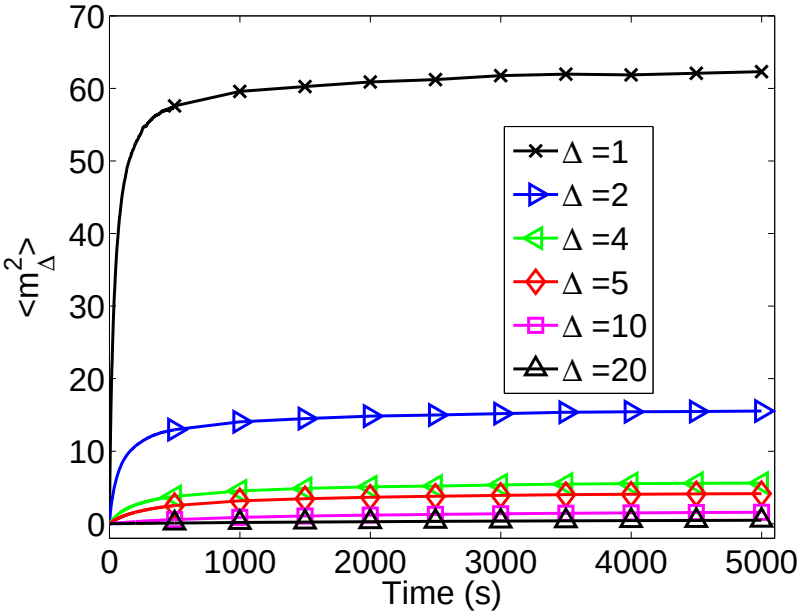

Figure 2.15: Profiles of the expected mean slope square under different characteristic length scales; 1D deposition/migration model with $E_n = 0$ eV, $T = 430$ K, and $W = 1$ layer/s.

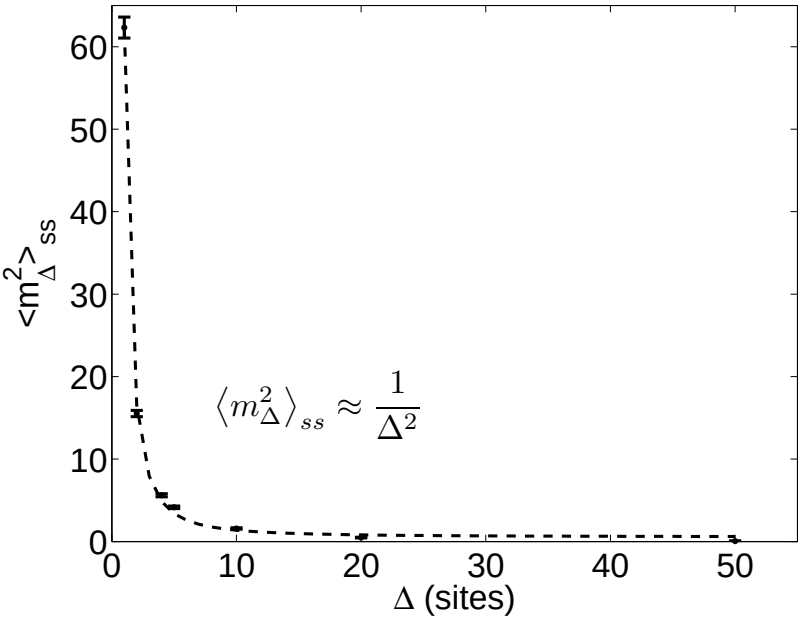

Figure 2.16: Dependence of the steady-state value of the expected mean slope square on the characteristic length scale (symbols) and the fitted quadratic dependence on the characteristic length scale (dashed line); 1D deposition/migration model with $E_n = 0$ eV, $T = 430$ K, and $W = 1$ layer/s.

square. This small mean slope square under larger length scales is partly because the operating conditions are spatially uniform during the entire deposition process, i.e., the same deposition rate or substrate temperature are applied throughout the spatial domain. Thus, spatially distributed operating conditions (implemented via spatially-distributed control actuators) are necessary for the purpose of optimizing thin film light reflectance/transmittance by manipulation of film surface roughness and slope at length scales relevant to visible light wavelength.

On the other hand, the surface roughness behaves differently from the surface slope at

large length scales. Specifically, the new surface roughness, r_Δ, is computed as the surface roughness in Eq. 2.2 but on the basis of the average surface height profile computed from Eq. 2.7. The surface roughness has a weaker dependence on the characteristic length scale, Δ, than the surface slope. To show this weak dependence, kMC simulations of the 1D deposition/migration model with $E_n = 0$ eV are carried out at $T = 500$ K and $W = 1$ layer/s. A smaller lattice size, $L = 500$, is used in the kMC simulations because it takes much longer time for the surface roughness square than the mean slope square to reach the steady-state value at larger lattice sizes. Fig. 2.17 shows the profiles of the expected surface roughness square, $\left\langle r_\Delta^2 \right\rangle$, under different characteristic length scales, Δ. It can be seen that the surface roughness square attains smaller steady-state values for larger length scales. However, the surface roughness square does not drop as prominently as the mean slope square when the characteristic length scale increases. This weak dependence of the steady-state value of the expected surface roughness square, $\left\langle r_\Delta^2 \right\rangle_{ss}$, on the characteristic length scale, Δ, is also shown in Fig. 2.18. The weak dependence on the length scale indicates a different behavior of surface roughness: the high frequency components in the surface height profile (i.e., local ripples below the characteristic length scale) contribute less significantly to the surface roughness than to the surface slope. Therefore, smooth surface height profiles with respect to large length scales have a very small mean slope square but considerable surface roughness square. Due to the insensitivity of the surface roughness to the high frequency components, spatially distributed control actuators may have less influence on the surface roughness while achieving the desired surface slope under certain characteristic

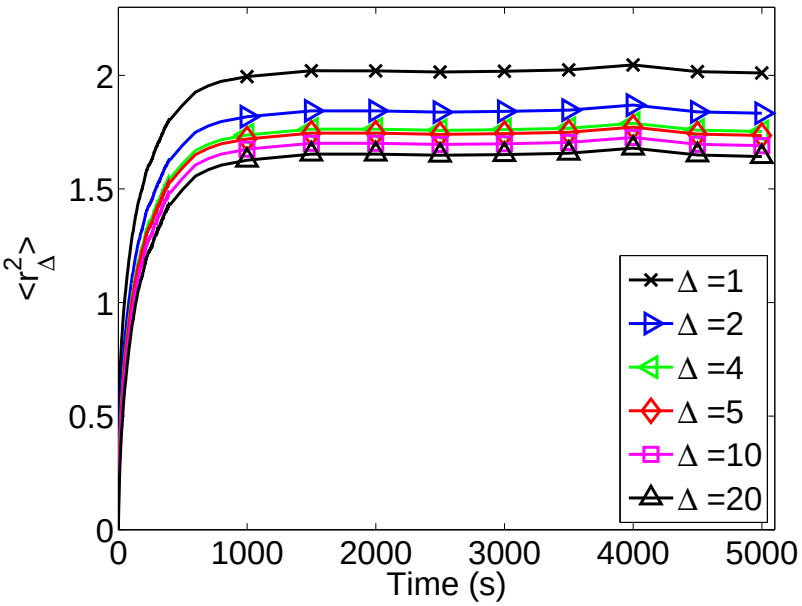

Figure 2.17: Profiles of the expected surface roughness square under different characteristic length scales; 1D deposition/migration model with $E_n = 0$ eV, $T = 500$ K, and $W = 1$ layer/s.

length scales. This decoupled relationship between the surface roughness and slope can be utilized in the controller design for improving the light trapping efficiency of thin-film solar cells. This problem will be studied in future research work.

The results of this section also suggest that given a monochromatic light of wavelength λ, the light trapping efficiency of a thin film should be computed using surface roughness and slope values corresponding to an aggregate length scale which is on the order of λ; this implies that the lattice size to be used to carry out this simulation should be at least two orders of magnitude larger than the one corresponding to a length λ to minimize boundary effects (i.e, the use of periodic boundary conditions) on the computed properties.

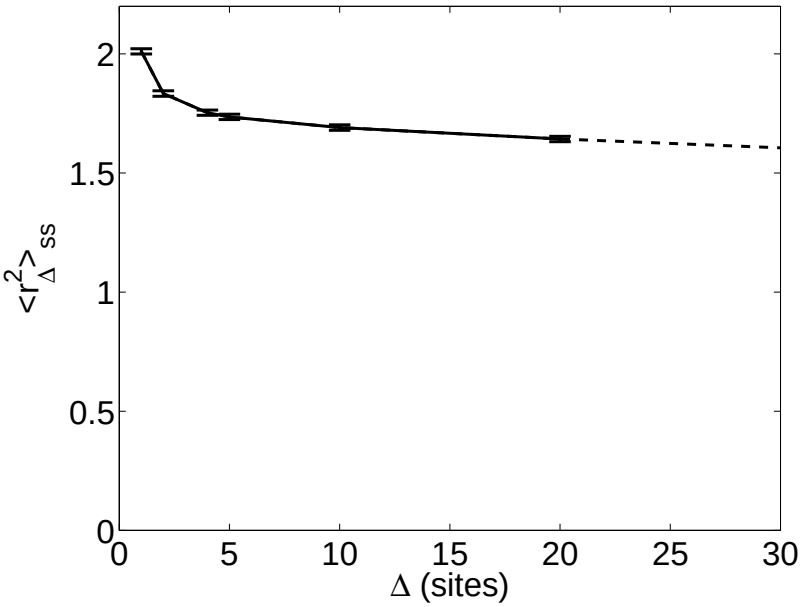

Figure 2.18: Dependence of the steady-state value of the expected surface roughness square on the characteristic length scale (symbols); 1D deposition/migration model with $E_n = 0$ eV, $T = 500$ K, and $W = 1$ layer/s.

Finally, we note that while the results for aggregate roughness and slope in Figs. 2.16 and 2.18 have been computed for $E_n = 0$ (which corresponds to the case where the migration rates of all surface particles are the same), the reduction of the aggregate roughness and slope with increasing aggregation length will continue to hold for non-zero E_n value; however, the exact shape of the curves will depend on the specific E_n values.

Chapter 3

Dynamics and Lattice-Size Dependence of Surface Mean Slope in thin-film Deposition

3.1 Introduction

This chapter focuses on the study of the dynamic behavior and lattice size dependence of the surface root-mean-square slope of thin-film deposition processes. Two different deposition processes are investigated: a random deposition with surface relaxation process and a porous thin-film deposition process. Both deposition processes involve a deposition (adsorption) process and a relaxation (migration) process, which strongly influence the resulting thin-film surface morphology. KMC methods are used to simulate the de-

position processes and generate film surface height profiles and compute rms slope and roughness. The simulation results indicate that the expected mean slope square reaches quickly a steady-state value and exhibits a very weak dependence with respect to lattice size variation. A theoretical analysis is provided using an Edwards–Wilkinson (EW)-type partial differential equation (PDE) that can describe the dynamics of the surface height profile in the deposition processes under consideration. The kMC simulation findings are corroborated by the analytical results of appropriate finite-difference discretizations of the solutions of the EW equation model.

3.2 Thin-Film Deposition Processes

In this section, two thin-film deposition processes are considered and modeled by using on-lattice kMC models. The first process is a random deposition process with surface relaxation taking place on a square lattice where solid-on-solid (SOS) assumption is made [37]. The second process is a porous thin-film deposition process taking place on a triangular lattice where vacancies and overhangs are allowed to develop [22, 18]. Periodic boundary conditions (PBCs) are applied to both lattice models. In both deposition processes, there are two competing effects which influence the evolution of the surface height profiles: a growth effect and a relaxation effect. The definitions of surface height profile and root-mean-square slope are also introduced.

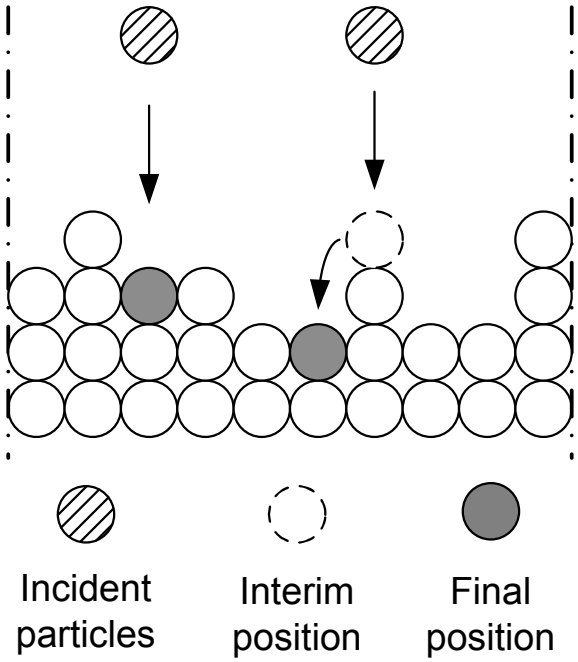

Figure 3.1: Random deposition process with surface relaxation and examples of deposition and surface relaxation processes. A square lattice is used.

3.2.1 Random Deposition with Surface Relaxation Process Model

The random deposition process with surface relaxation is modeled on a one-dimensional in the lateral direction square lattice with SOS assumption, where particles land on top of the existing surface particles. The lattice size in this model denotes the number of sites. The deposition rate is denoted by W and has the unit of deposited layers per second. Fig. 3.1 shows the lattice model of the random deposition process with surface relaxation and examples of the deposition processes.

When a particle is deposited, a site is first randomly chosen among all lattice sites. After the site is determined, an incident particle deposits on the top of the highest particle

on that site. Upon deposition, a surface relaxation process takes places if the height of the deposited site (before the deposition process) is higher in the growth direction than the height of any of the two adjacent sites. When the surface relaxation process is conducted, the incident particle relaxes to the lowest site among its two nearest neighboring sites. If both neighboring sites have lower heights, the incident particle randomly chooses (with equal probability) a neighboring site as its final deposition site.

3.2.2 Porous Thin-Film Deposition Process Model

Fig. 3.2 shows the porous thin-film growth process taking place on a one-dimensional in the lateral direction triangular lattice. In this lattice model, the lattice size denotes the number of sites in the lateral direction per layer, i.e., the maximum number of particles that can be packed within one horizontal layer. The coordination number of the triangular lattice is six, so a particle on the lattice can have at most six nearest neighbors. In the bottom of the lattice, a fully packed and fixed substrate layer is initially placed and is used to initiate the thin-film deposition process.

We consider two different types of microprocesses taking place in this deposition process: an adsorption process and a migration process. In the adsorption process, incident particles are deposited from the gas phase and are incorporated into the thin-film. In this work, only vertical incidence is considered in the adsorption process. When an incident particle is incorporated into the film, it moves to the nearest vacant site of the contacting particle. If the incident particle moves to a site that has only one nearest neighbor, it is con-

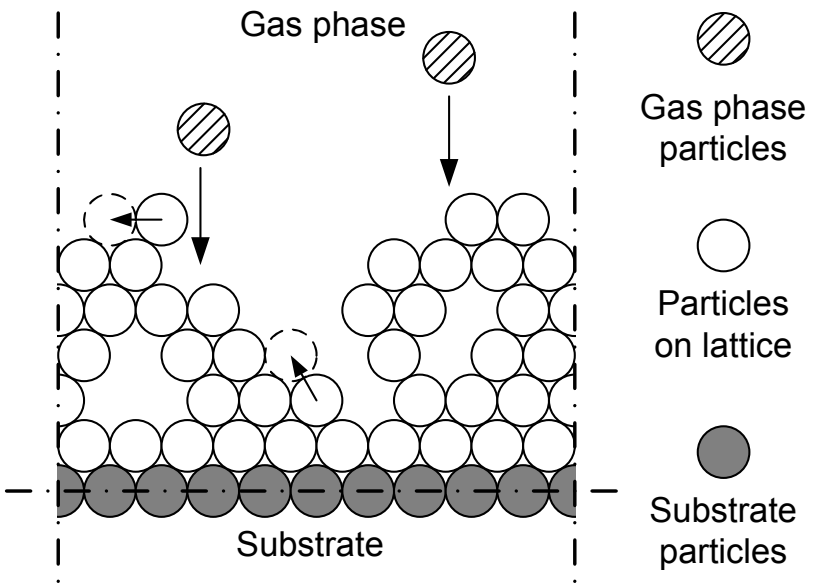

Figure 3.2: Thin-film growth process on a triangular lattice. The arrows denote adsorption and migration processes.

sidered to be an unstable particle in the lattice and relaxes instantaneously to the most stable vacant site neighboring the unstable site, i.e., the site that has the most nearest neighbors.

In a migration process, particles on the thin-film overcome the energy barrier of their sites and move to their adjacent vacant sites [52, 53]. Substrate particles cannot move. The migration rate follows an Arrhenius-type law, where the pre-exponential factor and the activation energy are taken from a silicon film [see ref [18] for details].

The microstructure of the porous thin-film is the result of a complex interplay between adsorption and migration processes. The macroscopic operating variables of the deposition process influence the resulting film microstructure. The two variables that are considered in this process are the adsorption rate and the substrate temperature. The adsorption rate,

which is denoted by W, is defined as the number of deposited layers per second. The substrate temperature, which is denoted by T, has a strong influence on the migration rate via the Arrhenius rate law.

In this work, the microscopic rules are used in kMC methods to simulate both the random deposition with surface relaxation process and the porous thin-film deposition process. Specifically, a continuous-time Monte Carlo (CTMC)-type method (e.g., [49]) is used to carry out the kMC simulations.

3.2.3 Definition of Variables

In this section, the variables that characterize the film surface morphology are defined. Surface height profile represents the film surface morphology and is defined as the connection of the centers of the surface particles. For the porous thin-film deposition process, surface particles are determined as the particles that can be reached from above in the vertical direction without being fully blocked by other particles on the film [22, 18]. Fig. 3.3 shows an example of the surface height profile of the porous thin-film deposition process. For the random deposition process with surface relaxation, the surface particles can be easily identified as the top particles on all lattice sites due to the SOS assumption.

Surface roughness is a commonly used measure of thin-film surface morphology and is defined as the root-mean-square (rms) of surface height profile as follows:

$$r = \left[\frac{1}{n_L} \sum_{i=1}^{n_L} (h_i - \bar{h})^2 \right]^{1/2}, \tag{3.1}$$

where r denotes surface roughness, h_i, $i = 1, 2, \ldots, n_L$, is the surface height at the i-th position in the unit of layer, and $\bar{h} = \frac{1}{n_L}\sum_{i=1}^{n_L} h_i$ is the average surface height. We note that the number of height positions in Eq. 3.1, n_L, does not always equal the lattice size, L. In the porous thin-film deposition process, the number of height positions equals $2L$ due to the nature of the triangular lattice in the porous thin-film deposition process; see Fig. 3.3 for example. For the random deposition process with surface relaxation, n_L is simply L due to the use of a square lattice.

In addition to surface roughness, the gradient (slope) of surface height profile is another important variable that determines the surface morphology. In this work, the root-mean-square (rms) slope represents the extent of surface slope and is defined in a similar fashion to surface roughness as follows:

$$m = \left[\frac{k_m^2}{n_L}\sum_{i=1}^{n_L}(h_{i+1} - h_i)^2\right]^{1/2}, \tag{3.2}$$

where m denotes the rms slope, which is a dimensionless variable, and k_m denotes the geometric ratio between the single-layer height and the interval between adjacent height positions. Due to the use of PBCs, the slope at the last position ($i = n_L$) is computed as the surface height difference between the last lattice site and the first lattice site. The value of the geometric ratio in Eq. 3.2, k_m, is 1 for the random deposition process with surface relaxation and $\sqrt{3}$ for the porous thin-film deposition process. Fig. 3.3 shows an example of the surface slope obtained from the surface height profile in the porous thin-film deposition process.

The two variables that are related to the surface morphology, surface roughness and rms

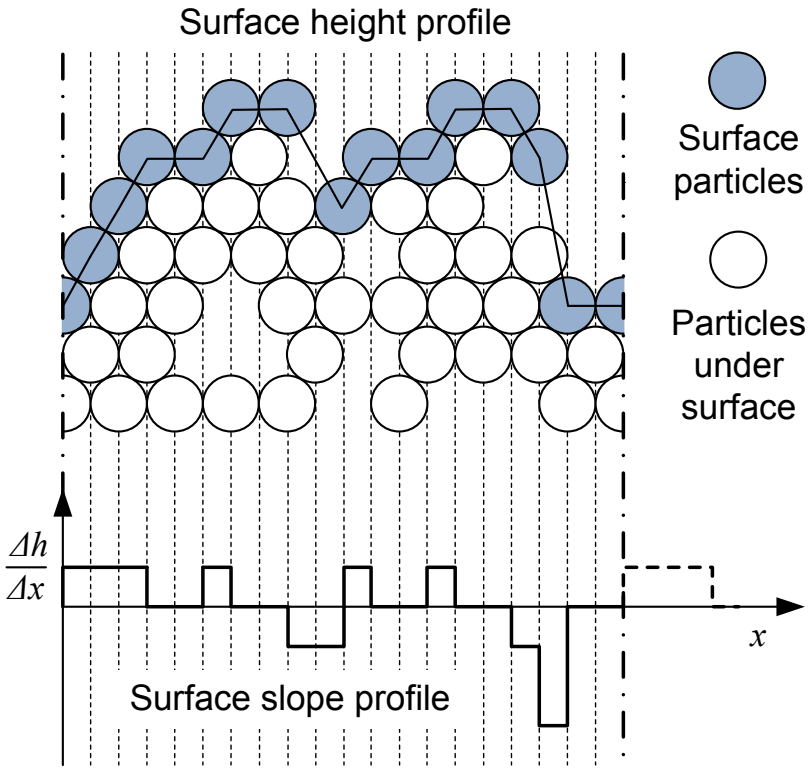

Figure 3.3: Example showing the definition of the surface height profile and the calculation of the corresponding surface slope profile.

slope, are defined in a similar fashion, i.e., root mean squares of a spatial profile. However, surface roughness is calculated on the basis of surface height profile, while rms slope is based on the surface slope profile. Thus, the two variables describe different properties of the surface height profile. Surface roughness measures the correlation of surface height at all sites with the average height, and thus, the sequence of the surface sites does not affect the calculation of surface roughness. On the contrary, surface slope is the height difference between two adjacent surface sites. As a result, rms slope measures the height correlation of adjacent surface sites and is sensitive to the sequence of surface sites. Therefore, two surface profiles with the same roughness may have very different rms slope profiles. We also note that surface roughness and rms slope are not fully independent. In the extreme case of a flat surface, surface roughness and rms slope both have zero values.

3.3 Rms Slope Behavior

In this section, the rms slope is calculated from the surface height profiles of the two deposition processes. The behavior of rms slope, i.e., its dynamics and dependence on lattice size, is then investigated. For the convenience of theoretical analysis and comparison with the simulations, the square of rms slope (mean slope square), i.e., m^2, is used to present the results.

3.3.1 Dynamics of Rms Slope

To investigate the dynamics of rms slope, kMC simulations of the two deposition processes are carried out with fixed operating conditions throughout the entire simulation. The lattice size is fixed to 100 sites for both processes for the results to be presented in this section. The simulation duration is large enough to allow the rms slope to reach its steady-state value. Due to the stochastic nature of kMC methods, different simulation runs may result in different lattice configurations and different surface morphology. Multiple independent simulations runs (10000–25000 runs) are carried out to generate smooth profiles of statistical moments, i.e., expected values and variances.

Fig. 3.4 and Fig. 3.5 show the profiles of the expected mean slope square. The operating conditions are fixed at a substrate temperature of 300 K (in the porous thin-film deposition process) and an adsorption rate of 1 layer/s (in both deposition processes). Fig. 3.4 and Fig. 3.5 also include the profiles of the corresponding expected roughness square. In both figures, the mean slope square profiles evolve similarly to the roughness square profiles: mean slope square increases from zero and approaches a finite steady-state value at large times.

However, it can be seen from Fig. 3.4 and Fig. 3.5 that the dynamics of roughness square and mean slope square are different in many aspects. First, the mean slope square has faster dynamics than roughness square. Here, the dynamics of a profile refer to the steady-state time, t_{ss}, that is needed for the profile to reach the steady-state value (practically, we take 99% of the steady-state value as the threshold to calculate t_{ss}). In general, a smaller

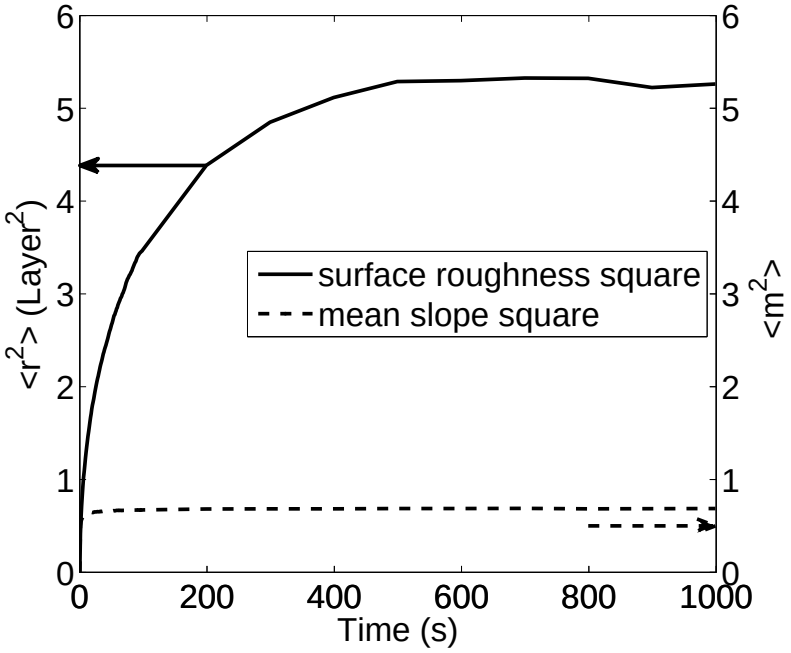

Figure 3.4: Profiles of the expected mean slope square (dashed line) and surface roughness square (solid line) from kMC simulations with lattice size $L = 100$; random deposition process with surface relaxation with $W = 1$ layer/s.

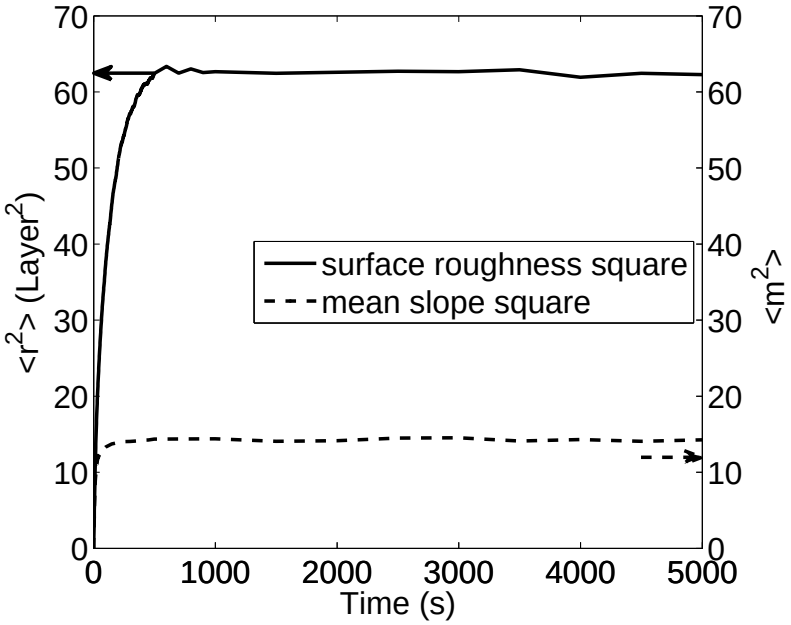

Figure 3.5: Profiles of the expected mean slope square (dashed line) and surface roughness square (solid line) from kMC simulations with lattice size $L = 100$; porous thin-film deposition process with $W = 1$ layer/s and $T = 300$ K.

steady-state time indicates faster dynamics. Specifically, in the random deposition with surface relaxation process of Fig. 3.4, $t_{ss} \simeq 125$ s for slope and $t_{ss} \simeq 469$ s for roughness; in the porous thin-film deposition process of Fig. 3.5, for $T = 300$ K, $t_{ss} \simeq 190$ s for slope and $t_{ss} \simeq 467$ s for roughness. Second, the steady-state values of mean slope square are smaller than the steady-state values of roughness square (even taking into consideration the geometric ratios). These differences can be explained as follows: the height correlation of adjacent surface sites, which mean slope square measures, is higher than the surface height correlation with the average height which is measured by the surface roughness. The higher correlation results in a smaller difference, i.e., a smaller steady-state value, and faster dynamics of mean slope square than surface roughness.

3.3.2 Dependence of Rms Slope on Operating Conditions

The dynamics of rms slope depend on operating conditions and lattice size. KMC simulations are also carried out to find out the dependence of rms slope with respect to different operating conditions. For the random deposition with surface relaxation process, the dynamics of the entire process scales proportionally with the adsorption rate, i.e., the higher the adsorption rate, the faster the rms slope and rms roughness approach their steady state values. However, the dynamics of the porous thin-film deposition process have a complex dependence on the operating conditions, i.e., substrate temperature or adsorption rate below.

Fig. 3.6 shows the profile of the expected mean slope square and roughness square

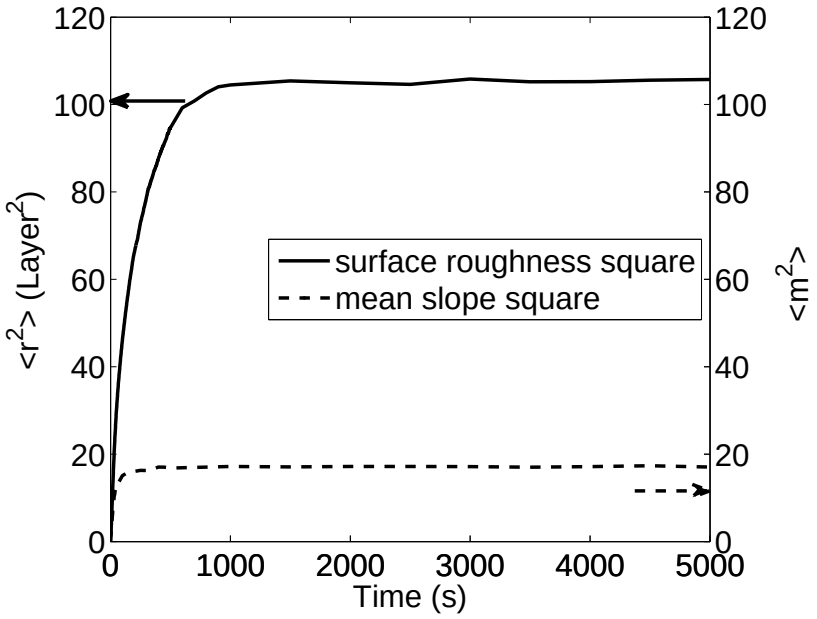

Figure 3.6: Profiles of the expected mean slope square (dashed line) and surface roughness square (solid line) from kMC simulations with lattice size $L = 100$; porous thin-film deposition process with $W = 1$ layer/s and $T = 500$ K.

of the porous thin-film deposition process at a substrate temperature of $T = 500$ K; the adsorption rate is kept at $W = 1$ layer/s. From the comparison between Fig. 3.5 and Fig. 3.6, it is evident that both the rms slope and the surface roughness increase as the substrate temperature increases from 300 K to 500 K. These consistent results indicate that the rms slope and surface roughness can be captured by the same analytical dynamic equation, as we will discuss in Section 3.4.

Fig. 3.7 shows the profiles of the expected mean slope square at different substrate temperatures. The adsorption rate is kept at $W = 1$ layer/s. A lattice size of 100 sites is used in

all simulations for a meaningful comparison. It can be clearly seen from Fig. 3.7 that the substrate temperature has a strong influence on the evolution of the rms slope. At low temperatures ($T \leq 400$ K), the particles have limited mobility, and thus, the evolution profiles of the mean slope square are nearly insensitive to temperature variation. As temperature increases, however, the mean slope square profiles have higher values. At high temperatures ($T \geq 700$ K), the intensive mobility of particles results in an almost flat surface and the mean slope square is close to zero.

A similar dependence of the expected mean slope square on adsorption rate can be found in Fig. 3.8, which shows the profiles of the expected mean slope square at different adsorption rates with a fixed substrate temperature of $T = 500$ K. The thin-film morphology is determined by the thermal balance between the adsorption process and the migration process. Thus, the expected mean slope square under a high adsorption rate behaves similarly to the one under a low substrate temperature (equivalently a low migration rate) and vise versa. This strong dependence on operating conditions can be used to design feedback controllers that regulate the rms slope of the thin-film surface at desired values that optimize thin-film reflectance and transmittance.

3.3.3 Lattice-Size Dependence of Rms Slope

In this subsection, the lattice-size dependence of rms slope is studied for both deposition processes. To investigate the dependence of rms slope on lattice size, kMC simulations of the deposition processes are carried out for different lattice sizes (from 20 to 500). The

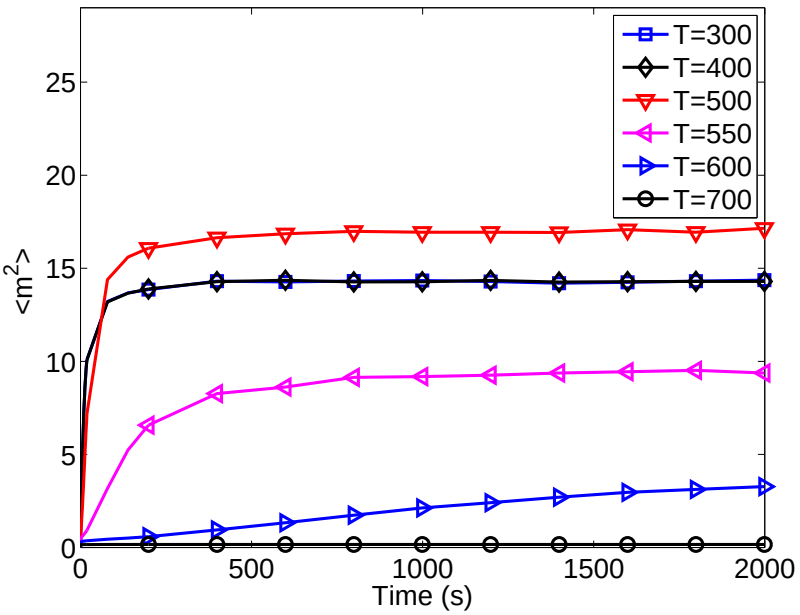

Figure 3.7: Profiles of the expected mean slope square from kMC simulations at different substrate temperatures; porous thin-film deposition process with $W = 1$ layer/s and $L = 100$.

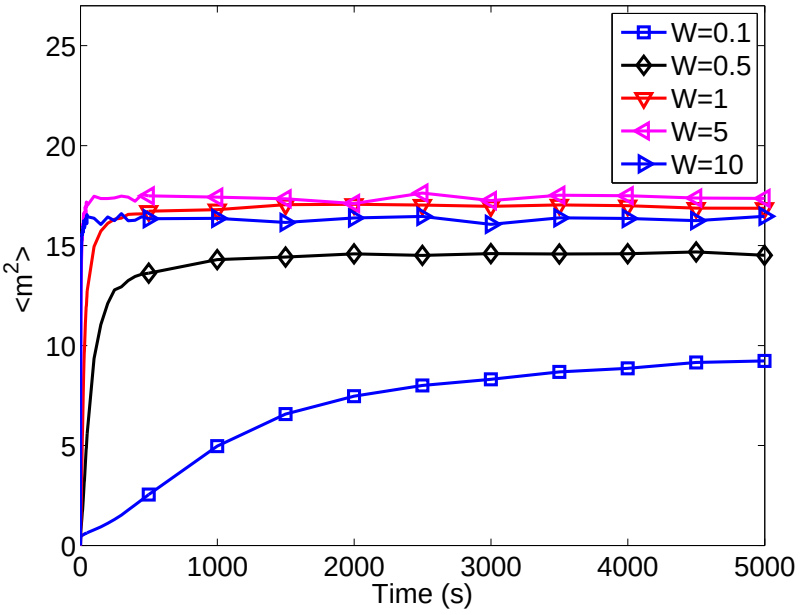

Figure 3.8: Profiles of the expected mean slope square from kMC simulations at different adsorption rates; porous thin-film deposition process with $T = 500$ K and $L = 100$.

operating conditions are fixed at $T = 300$ K and $W = 1$ layer/s for all simulations where applicable. Both evolution profiles and steady-state dependence of the expected mean slope square are presented. In the figures of steady-state dependence, the error bars are calculated from 20 averages of evenly divided groups of all simulation runs.

Fig. 3.9 shows the profiles of the expected mean slope square of the random deposition with surface relaxation process for different lattice sizes. From Fig. 3.9, it can be seen that the dynamics of mean slope square have a weak relationship with the lattice size at large lattice sizes, i.e., the profiles of mean slope square evolve and reach their steady states at similar time instants regardless of the lattice size. Similar to the dynamics, the steady-state values of mean slope square also have a weak dependence on lattice size, especially at large lattice sizes. This dependence of steady-state values on lattice size is different from the scaling properties of the surface roughness [1], i.e., the lattice-size dependence of mean slope square does not follow a power law. The weak dependence can be observed more clearly in Fig. 3.10, which shows the steady-state values of the expected mean slope square for different lattice sizes in a log–log plot. Similar evolution profiles and lattice-size dependence can be seen for the porous thin-film deposition process at different operating conditions; see Fig. 3.11 and Fig. 3.12 for $T = 300$ K and Fig. 3.13 and Fig. 3.14 for $T = 500$ K (the deposition rate is 1 layer/s for both cases).

In previous work, a linear lattice-size dependence of the steady-state value of expected surface roughness square was found [18]. In the next section, analytical and numerical results will be obtained and discussed from a stochastic PDE model of the thin-film de-

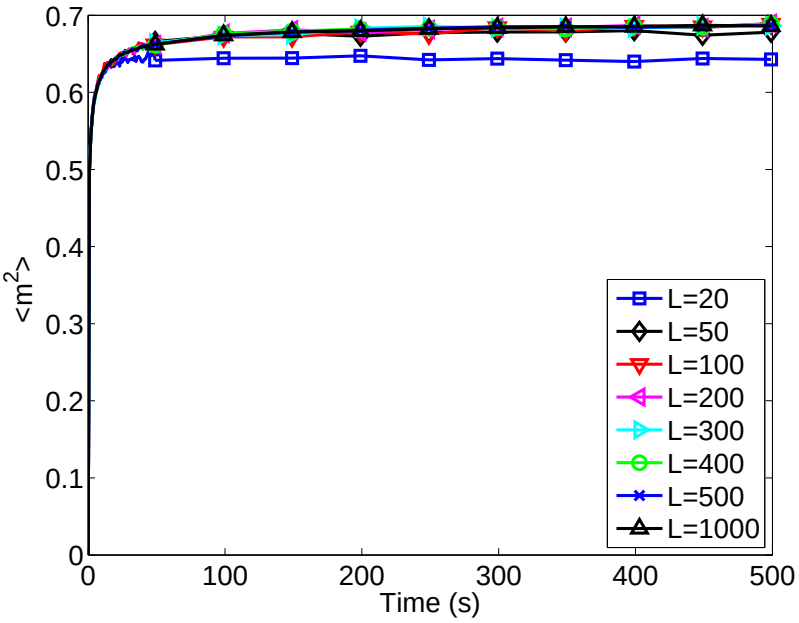

Figure 3.9: Profiles of the expected mean slope square from kMC simulations with different lattice sizes; random deposition process with surface relaxation with $W = 1$ layer/s.

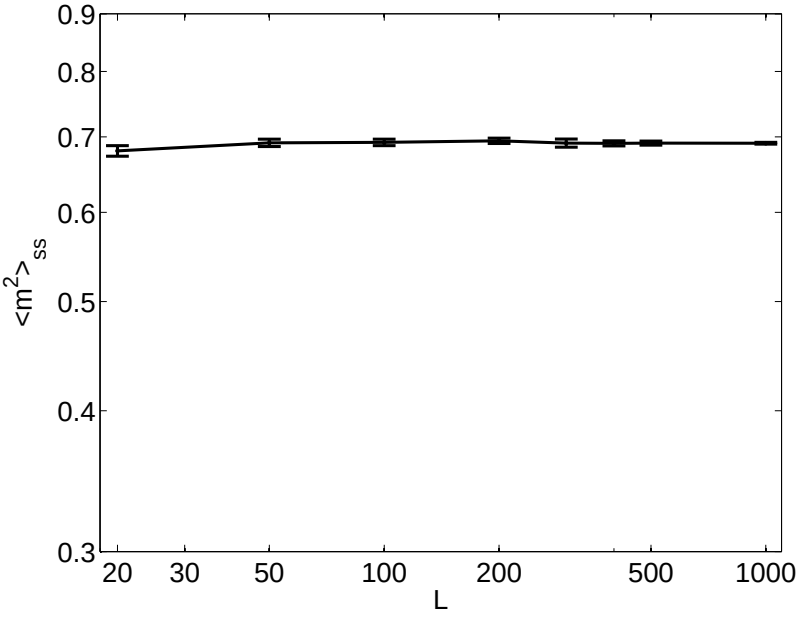

Figure 3.10: Dependence of the steady-state values of the expected mean slope square with error bars from kMC simulations, on the lattice size, L; random deposition process with surface relaxation with $W = 1$ layer/s.

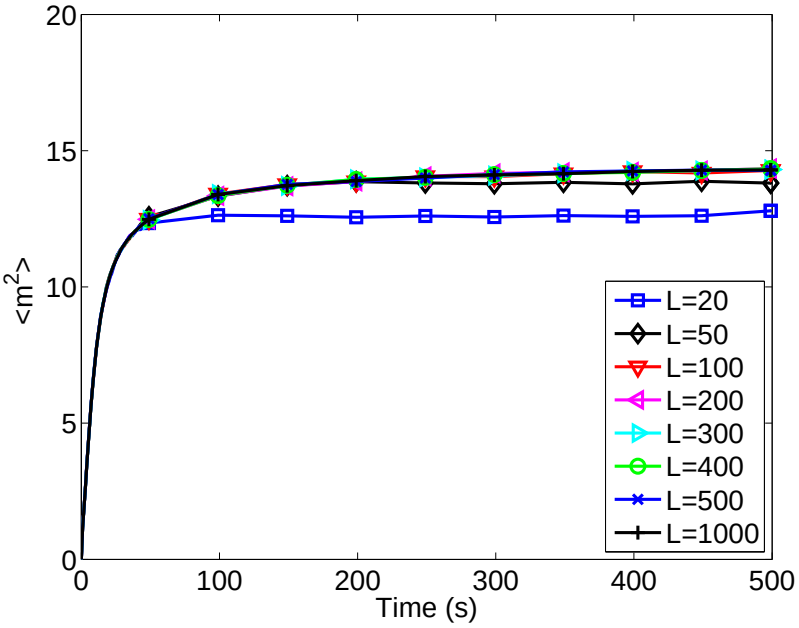

Figure 3.11: Profiles of the expected mean slope square from kMC simulations for different lattice sizes; porous thin-film deposition process with $W = 1$ layer/s and $T = 300$ K.

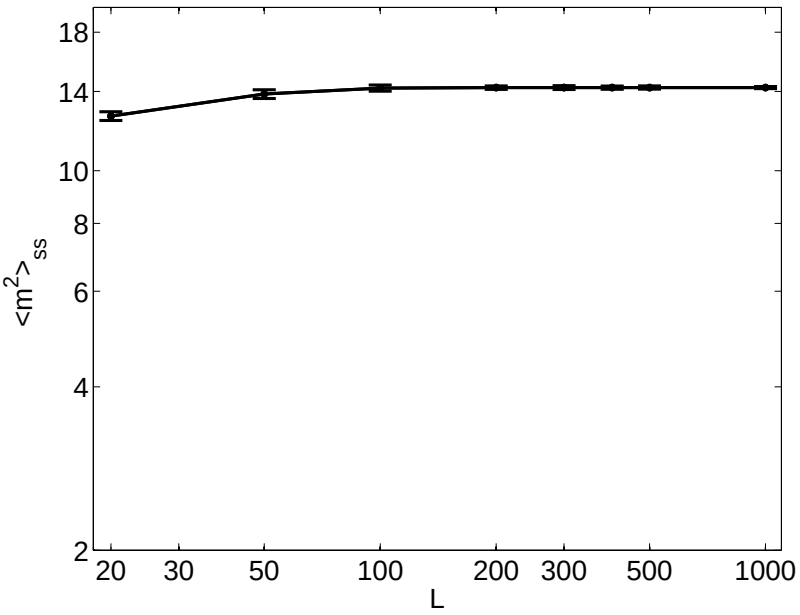

Figure 3.12: Dependence of the steady-state values of the expected mean slope square with error bars from kMC simulations, on the lattice size, L; porous thin-film deposition process with $W = 1$ layer/s and $T = 300$ K.

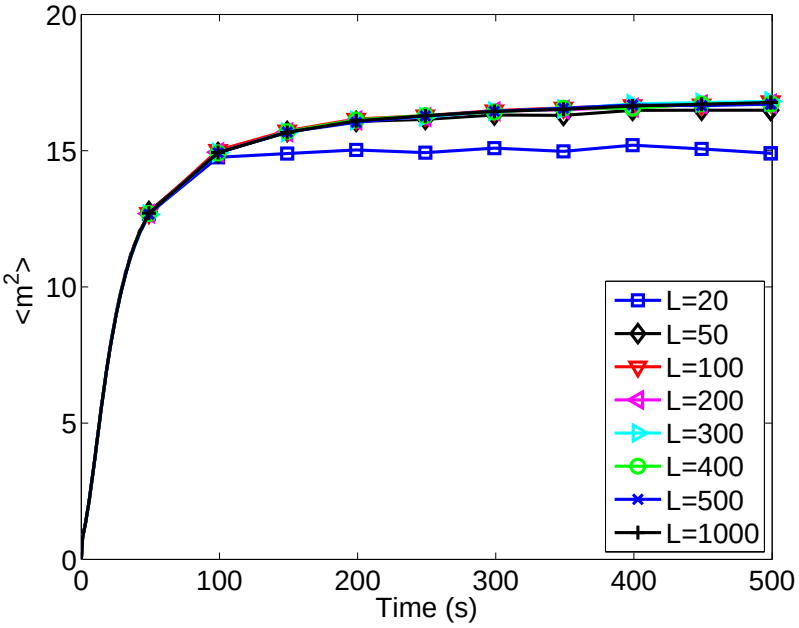

Figure 3.13: Profiles of the expected mean slope square from kMC simulations for different lattice sizes; porous thin-film deposition process with $W = 1$ layer/s and $T = 500$ K.

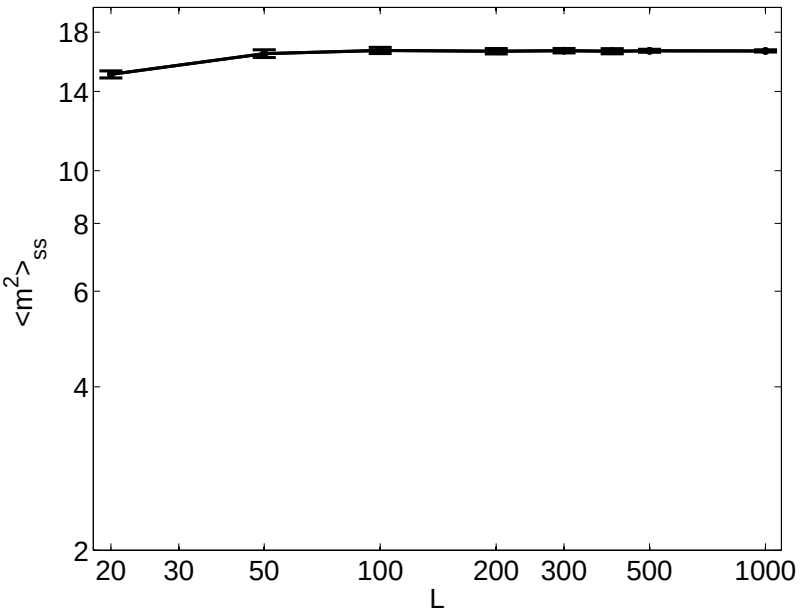

Figure 3.14: Dependence of the steady-state values of the expected mean slope square with error bars from kMC simulations, on the lattice size, L; porous thin-film deposition process with $W = 1$ layer/s and $T = 500$ K.

position processes under consideration to explain the behavior of the expected mean slope square.

Remark 3.1 *For atomic depositions, the length scale of the crystalline lattice (*0.5 *nm) is smaller than the scale of the wavelength of the visible light (*400–700 *nm). Thus, the surface irregularity at the atom/molecular level cannot be related to the optical property of thin-films. To be able to simulate a realistic domain size, we would need to have a lattice size of the order of* 10^6 *(with each site corresponding to atomic dimension) or higher, which is beyond the currently available computing power. If this simulation were possible, we would look at subdomains of the lattice of dimension of the order* 400–700 *nm and estimate an overall subdomain slope that the light "sees". In this setup, the overall slope of a given subdomain could be computed in an approximate way by computing average heights of groups of sites embedded in the subdomain and then connecting these average heights to compute the overall slope of the subdomain. We have applied this approach to the maximum order of domain size that we can simulate with our current computing power,* $L = 1000$*, and have computed average heights of groups of* 10 *sites and the corresponding m profile. Fig. 3.15 shows the resulting m profile; we can see that the fast dynamics and approach of m to a finite steady-state value that we observe for the small lattice-size problem (*$L = 100$ *and m defined between adjacent heights as done in our work) from Fig. 3.5 and Fig. 3.6 are also observed in this larger scale problem. Therefore, the metric m we have used for* $L = 100$ *gives us some insight into the behavior of a more complex problem that cannot be currently simulated.*

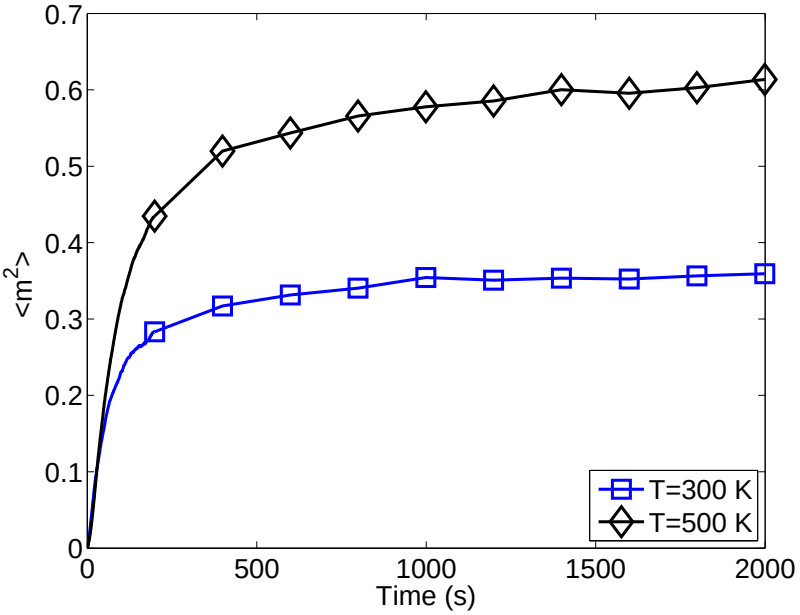

Figure 3.15: Profiles of the expected mean slope square computed on the basis of the average heights of groups of 10 surface particles from kMC simulations with $L = 1000$ at $T = 300$ K and 500 K; porous thin-film deposition process with $W = 1$ layer/s.

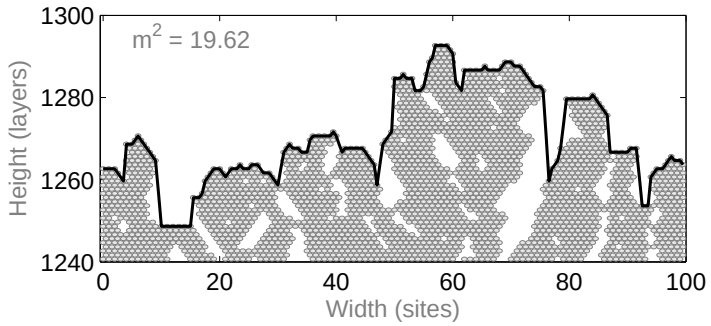

Figure 3.16: Snapshot of the film surface morphology at steady state ($t = 1000$s); porous thin-film deposition process with $T = 500$ K and $W = 1.0$ layer/s.

Remark 3.2 *We note that, in the triangular lattice in the porous thin-film growth process, particles are only stable with two or more nearest neighbors, and thus, the typical height difference between adjacent lattice sites is zero or one layer. However, it can be inferred on the basis of the steady-state values in Fig. 3.12 and Fig. 3.14 that an average vertical height difference between adjacent lattice sites is between* 2 *and* 3 *layers. This difference is significantly higher than the typical value, which is less than one layer. Such a large height difference between adjacent lattice size is the result of the columnar growth film structure in the low temperature region (*$T = 300$–500 *K); as can be seen in Fig. 3.16, which shows that the surface height profile of the thin-film with a columnar structure formed at* $T = 500$ *K contains steep "cliffs" (large differences between few adjacent surface height positions). These large height differences, although very few, contribute significantly to the root-mean-square value of the vertical height difference, i.e.,* 2 *or* 3 *in the porous thin-film growth process at* $T = 300$ *and* 500 *K.*

3.4 Analytical and Numerical Results from the Stochastic PDE Model

The thin-film deposition is a stochastic process, where fluctuations are intrinsic and should be considered in the dynamic equation that describes the dynamics of the process. However, the surface irregularities of the thin-film are not purely random; otherwise, the surface roughness square and the mean slope square cannot reach their respective steady states but rather increase (linearly) to infinity as time increases. To this end, an Edwards–Wilkinson (EW)-type equation with appropriately fitted parameters, which is a second-order stochastic PDE, is used to describe the dynamics and evolution of the surface height profile of the random deposition with surface relaxation process and the porous thin-film growth process [10, 11, 41, 18].

Furthermore, due to the fact that stochastic PDEs are defined on a continuous spatial domain, the dynamics of the rms slope obtained from the EW equation are different from the kMC simulations on the discrete lattice, i.e., an infinite value of mean slope square and a reciprocal dependence on the domain size are obtained from the continuum EW equation (see also Remark 3 for more discussion on this issue). This inconsistency of the dynamics of the rms slope originates from the discretization of a continuous domain. Consistent numerical results to the ones of the kMC simulation are obtained from the discretization of the solution of the EW equation. This corroboration further supports the use of the EW equation as a continuum model to describe the evolution of surface height profile and the

dynamics of the rms slope in the deposition processes considered in this work.

In the EW formalism, $h(x,t)$ represents the surface height profile in the continuum spatial domain case and the equation takes the following form [10, 18]:

$$\frac{\partial h}{\partial t} = r_h + \nu \frac{\partial^2 h}{\partial x^2} + \xi(x,t), \tag{3.3}$$

subject to the following PBCs

$$h(-L_0,t) = h(L_0,t), \quad \frac{\partial h}{\partial x}(-L_0,t) = \frac{\partial h}{\partial x}(L_0,t) \tag{3.4}$$

and the initial condition:

$$h(x,0) = h_0(x), \tag{3.5}$$

where $x \in [-L_0, L_0]$ is the spatial coordinate, t is the time, and $\xi(x,t)$ is a Gaussian white noise with the following expressions for its mean and covariance:

$$\begin{aligned} \langle \xi(x,t) \rangle &= 0, \\ \langle \xi(x,t)\xi(x',t') \rangle &= \sigma^2 \delta(x-x')\delta(t-t'), \end{aligned} \tag{3.6}$$

where $\langle \cdot \rangle$ denotes the mean value, σ^2 is a parameter which measures the intensity of the Gaussian white noise and $\delta(\cdot)$ denotes the standard Dirac delta function.

In the EW equation of Eq. 3.3, r_h, ν, and σ^2 are model parameters. Specifically, r_h is related to the growth of average surface height, ν is related to the effect of surface particle relaxation and migration, and σ^2 is related to the noise intensity. Since r_h is only related to the averaged surface height, this term can be ignored for the purpose of studying the dynamics and scaling behavior of surface roughness and rms slope, i.e., $r_h = 0$ [18].

3.4.1 Analytical Derivation

The behavior of surface roughness can be derived from the EW equation of Eq. 3.3. Specifically, the steady-state value of the expected surface roughness square scales linearly with the domain size. This lattice-size dependence of surface roughness is consistent with the kMC simulation results of the porous thin-film deposition process as well as of other processes [18].

The dynamics of rms slope can be derived from the EW equation using modal decomposition. A direct computation of the following eigenvalue problem of the linear operator of Eq. 3.3 subject to the PBCs of Eq. 3.4,

$$\begin{gathered} \nu \frac{d^2 \bar{\phi}_n(x)}{dx^2} = \lambda_n \bar{\phi}_n(x), \\ \bar{\phi}_n(-L_0) = \bar{\phi}_n(L_0), \quad \frac{d\bar{\phi}_n}{dx}(-L_0) = \frac{d\bar{\phi}_n}{dx}(L_0), \end{gathered} \tag{3.7}$$

yields the following solution for the eigenvalues, λ_n, and the eigenfunctions, $\bar{\phi}_n(x)$:

$$\begin{aligned} \lambda_n &= -\nu k^2 n^2, \qquad n = 0, 1, \ldots, \\ \phi_n(x) &= c_n \sin(knx), \quad n = 1, 2, \ldots, \\ \psi_n(x) &= c_n \cos(knx), \quad n = 0, 1, \ldots, \end{aligned} \tag{3.8}$$

where $\phi_n(x)$ and $\psi_n(x)$ are the two eigenfunctions corresponding to the same nonzero eigenvalue λ_n, $n \geq 1$, with a multiplicity of 2, $k = \pi/L_0$ is used to satisfy the PBCs, and c_n is introduced for the purpose of normalization with the values of $c_0 = 1/(2L_0)^{1/2}$ and $c_n = 1/(L_0)^{1/2}$, $n = 1, 2, 3, \ldots$. The solution of Eq. 3.3 is expanded into an infinite series

in terms of the eigenfunctions of the operator of Eq. 3.7 as follows:

$$h(x,t) = \sum_{n=1}^{\infty} \alpha_n(t)\phi_n(x) + \sum_{n=0}^{\infty} \beta_n(t)\psi_n(x). \tag{3.9}$$

Substituting the above expansion for the solution, $h(x,t)$, into Eq. 3.3 and taking the inner product with the adjoint eigenfunctions, the following system of infinite stochastic ordinary differential equations (ODEs) is obtained:

$$\begin{aligned} \frac{d\alpha_n}{dt} &= \lambda_n \alpha_n + \xi_\alpha^n(t), \quad n = 1,2,\ldots,\infty, \\ \frac{d\beta_n}{dt} &= \lambda_n \beta_n + \xi_\beta^n(t), \quad n = 0,1,\ldots,\infty, \end{aligned} \tag{3.10}$$

where $\xi_\alpha^n = \int_{-L_0}^{L_0} \xi(x,t)\phi_n(x)dx$ and $\xi_\beta^n = \int_{-L_0}^{L_0} \xi(x,t)\psi_n(x)dx$ is the projection of the noise $\xi(x,t)$ in the n-th ODE. We note that ξ_α^n and ξ_β^n, $n = 0$, 1, …, are independent Gaussian white noise terms. Due to the linearity of the stochastic ODE system of Eq. 3.10, the system state, α_n or β_n, is independent from any other state. Therefore, the analytical solution of the state variance can be directly obtained from a direct computation as follows:

$$\begin{aligned} \left\langle \alpha_n^2(t) \right\rangle &= -\frac{\sigma^2}{2\lambda_n} + \left(\left\langle \alpha_n^2(t_0) \right\rangle + \frac{\sigma^2}{2\lambda_n} \right) e^{2\lambda_n(t-t_0)}, \quad n = 1,2,\ldots,\infty, \\ \left\langle \beta_n^2(t) \right\rangle &= -\frac{\sigma^2}{2\lambda_n} + \left(\left\langle \beta_n^2(t_0) \right\rangle + \frac{\sigma^2}{2\lambda_n} \right) e^{2\lambda_n(t-t_0)}, \quad n = 1,2,\ldots,\infty, \end{aligned} \tag{3.11}$$

where only expressions of the non-zeroth state variance are provided, since the zeroth state does not contribute to the mean slope square due to the spatially invariant zeroth eigenfunction.

Specifically, the expression of the steady-state value of the state variance can be ob-

tained at the infinite-time limit as follows:

$$\left\langle \alpha_n^2 \right\rangle_{ss} = \left\langle \beta_n^2 \right\rangle_{ss} = -\frac{\sigma^2}{2\lambda_n} = \frac{\sigma^2}{2\nu k^2 n^2} = \frac{\sigma^2 L_0^2}{2\nu\pi^2 n^2}, \quad n = 1,2,\ldots,\infty. \tag{3.12}$$

Similar to the discrete lattice definition of Eq. 3.2, the continuum form of the rms slope is defined as follows:

$$m(t) = \left\{ \frac{1}{2L_0} \int_{-L_0}^{L_0} \left[\frac{\partial h}{\partial x}(x,t) \right]^2 dx \right\}^{1/2}. \tag{3.13}$$

Substituting the infinite-series expansion of $h(x,t)$ of Eq. 3.9 into Eq. 3.13, the expected mean slope square, $\left\langle m^2(t) \right\rangle$, can be rewritten as follows:

$$\begin{aligned}
\left\langle m^2(t) \right\rangle &= \left\langle \frac{1}{2L_0} \int_{-L_0}^{L_0} \left[\frac{\partial h}{\partial x}(x,t) \right]^2 dx \right\rangle \\
&= \frac{1}{2L_0} \left\langle \int_{-L_0}^{L_0} \left[\sum_{n=1}^{\infty} \alpha_n(t) \frac{\partial \phi_n}{\partial x}(x) + \sum_{n=0}^{\infty} \beta_n(t) \frac{\partial \psi_n}{\partial x}(x) \right]^2 dx \right\rangle \\
&= \frac{1}{2L_0} \left\langle \int_{-L_0}^{L_0} \left[\sum_{n=1}^{\infty} \alpha_n(t) kn \psi_n(x) - \sum_{n=1}^{\infty} \beta_n(t) kn \phi_n(x) \right]^2 dx \right\rangle \\
&= \frac{1}{2L_0} \left\langle \sum_{n=1}^{\infty} k^2 n^2 \alpha_n^2(t) + \sum_{n=1}^{\infty} k^2 n^2 \beta_n^2(t) \right\rangle \\
&= \frac{1}{2L_0} \sum_{n=1}^{\infty} k^2 n^2 \left\langle \alpha_n^2(t) \right\rangle + \frac{1}{2L_0} \sum_{n=1}^{\infty} k^2 n^2 \left\langle \beta_n^2(t) \right\rangle.
\end{aligned} \tag{3.14}$$

Eq. 3.14 provides a direct link between the state variance of the infinite stochastic ODEs of Eq. 3.10 and the expected mean slope square of the surface height profile. The steady-state value of the expected mean slope square, $\left\langle m^2 \right\rangle_{ss}$, can be obtained as $t \to \infty$. By

substituting the steady-state variances of Eq. 3.12 and the expressions of the eigenvalues of Eq. 3.8, the analytical form of $\langle m^2 \rangle_{ss}$ is as follows:

$$\begin{aligned} \langle m^2 \rangle_{ss} &= \frac{1}{2L_0} \sum_{n=1}^{\infty} k^2 n^2 \langle \alpha_n^2 \rangle_{ss} + \frac{1}{2L_0} \sum_{n=1}^{\infty} k^2 n^2 \langle \beta_n^2 \rangle_{ss} \\ &= -2 \frac{1}{2L_0} \sum_{n=1}^{\infty} k^2 n^2 \frac{\sigma^2}{2\lambda_n} = \frac{1}{2L_0} \sum_{n=1}^{\infty} k^2 n^2 \frac{\sigma^2}{2\nu k^2 n^2} \\ &= \frac{1}{L_0} \sum_{n=1}^{\infty} \frac{\sigma^2}{2\nu} = \frac{\sigma^2}{2\nu L_0} + \frac{\sigma^2}{2\nu L_0} + \frac{\sigma^2}{2\nu L_0} + \ldots . \end{aligned} \tag{3.15}$$

From Eq. 3.15, it can be seen that each state contributes an equal finite part, $\sigma^2/(2\nu L_0)$, to the steady-state value of the expected mean slope square, $\langle m^2 \rangle_{ss}$. Since the stochastic ODE system of Eq. 3.10 has infinite number of states, the steady-state value of the expected mean slope square has an infinite value. It can be also seen that $\langle m^2 \rangle_{ss}$ has a reciprocal dependence on the domain size, L_0.

3.4.2 Discretization Analysis

In the previous section, the analytical derivation from the EW equation in a continuum domain results in an infinite steady-state value and a reciprocal domain-size dependence of the expected mean slope square. This behavior is different from the one obtained from the kMC simulations of the lattice model, which leads to a finite steady-state value and a weak lattice-size dependence of the expected mean slope square. This difference does not mean that the EW equation cannot be used to describe the evolution of the surface height

profile and of the rms slope. The infinite value of the expected mean slope square from the EW equation is due to the infinitesimal discretization intervals in the continuum domain. The same behavior of rms slope can be obtained from the EW equation under a suitable finite-difference discretization of the continuum surface height profile.

Specifically, a spatial discretization is introduced to the continuum domain, $[-L_0, L_0]$. This spatial discretization contains L evenly distributed nodes, where L corresponds to the lattice size of the kMC models and is also referred to here as lattice size. The spatial coordinates of the discretization nodes can be obtained as follows:

$$x_i = x_1 + (i-1)\Delta x, \quad i = 2, 3, \ldots, L, \tag{3.16}$$

where $x_1 \in [-L_0, -L_0 + \Delta x)$ denotes the coordinate of the first node and $\Delta x = 2L_0/L$ is the interval between two adjacent nodes. The range of x_1 indicates a freedom of choosing the discretization, as long as the continuum domain is evenly discretized. The choice of the specific discretization does not affect the analysis and the numerical results.

With the finite-dimensional discretization, the mean slope square of a discrete surface height profile can be computed in a similar fashion as in the kMC simulations:

$$m^2 = \frac{1}{L} \sum_{i=1}^{L} \left(\frac{h_{i+1} - h_i}{\Delta x} \right)^2, \tag{3.17}$$

where h_i denotes the surface height at the i-th node and $h_i(t) = h(x_i, t)$.

By substituting the definition of mean slope square of Eq. 3.17 and the expansion of the surface height profile of Eq. 3.9, the expected mean slope square can be manipulated as follows (the zeroth state does not contribute to the expected mean slope square because

$\phi_0(x)$ is a constant function):

$$\begin{aligned}
\left\langle m^2(t)\right\rangle &= \left\langle \frac{1}{L\Delta^2 x}\sum_{i=1}^{L}\left[\sum_{n=1}^{\infty}\alpha_n(t)\Delta\phi_n(x_i)+\sum_{n=1}^{\infty}\beta_n(t)\Delta\psi_n(x_i)\right]^2\right\rangle \\
&= \frac{1}{L\Delta^2 x}\sum_{i=1}^{L}\left[\sum_{n=1}^{\infty}\left\langle\alpha_n^2(t)\right\rangle\Delta^2\phi_n(x_i)+\sum_{n=1}^{\infty}\left\langle\beta_n^2(t)\right\rangle\Delta^2\psi_n(x_i)\right] \\
&= \sum_{n=1}^{\infty}\left[\frac{1}{L\Delta^2 x}\sum_{i=1}^{L}\Delta^2\phi_n(x_i)\right]\left\langle\alpha_n^2(t)\right\rangle+\sum_{n=1}^{\infty}\left[\frac{1}{L\Delta^2 x}\sum_{i=1}^{L}\Delta^2\psi_n(x_i)\right]\left\langle\beta_n^2(t)\right\rangle,
\end{aligned} \tag{3.18}$$

where $\Delta f(x_i) = f(x_{i+1}) - f(x_i)$ and $\Delta^2 f(x_i) = [\Delta f(x_i)]^2$. We note that, due to the independence of the system states, $\langle\alpha_{n_1}(t)\alpha_{n_2}(t)\rangle = \langle\beta_{n_1}(t)\beta_{n_2}(t)\rangle = 0$, for $n_1 \neq n_2$, and $\langle\alpha_{n_1}(t)\beta_{n_2}(t)\rangle = 0$, for any n_1 and n_2, $n_1 = 1, 2, \ldots$, and $n_2 = 1, 2, \ldots$.

The expression of the expected mean slope square of Eq. 3.18 can be further simplified into the following form:

$$\left\langle m^2(t)\right\rangle = \sum_{n=1}^{\infty}K_n^{\alpha}\left\langle\alpha_n^2(t)\right\rangle+\sum_{n=1}^{\infty}K_n^{\beta}\left\langle\beta_n^2(t)\right\rangle, \tag{3.19}$$

where K_n^{α} and K_n^{β} denote the coefficients of the state variance and have the following analytical form:

$$K_n^{\alpha} = K_n^{\beta} = \frac{4}{L\Delta^3 x}\sin^2\left(\frac{n\pi}{L}\right). \tag{3.20}$$

With the solution expression of the expected mean slope square of Eq. 3.19, it can be proved that the expected mean slope square from finite discretization has a finite steady-state value, which is consistent with the kMC simulation results of the lattice models. Derivation of the analytical form of K_n of Eq. 3.20 and proof of the finite steady-state

value of the expected mean slope square can be found in the Appendix at the end of this chapter.

Remark 3.3 *We note that there is no connection, established from a physical (first principles) point of view, between the metric m computed on the basis of the surface profile of the kMC simulations and the derivative of the surface height of the EW equation. The reason we consider the EW equation and present profiles of the metric m on the basis of the surface height profile of the EW equation is because the EW equation with appropriately fitted parameters to kMC data can be used to approximately predict the evolution of m of the kMC simulation with finite lattice size, and thus, it can be incorporated in model-based feedback control schemes to make predictions of the evolution of the mean slope m. In previous work, we have demonstrated that this approach leads to a controller design that works well for simultaneous regulation of surface slope and roughness [56]. We also note that the EW equation is a reasonable model for the thin-film growth process because it captures the balance between random adsorption and thermal migration (diffusion) and predicts certain scaling properties (lattice-size dependence of roughness) obtained from kMC simulation of the deposition processes under consideration. Furthermore, EW equation-based control can be applied to an actual thin-film manufacturing process when the EW equation parameters are computed on the basis of experimental data.*

3.4.3 Numerical Results of Discretized Solution

In this subsection, the numerical simulations of the EW equation are used to verify the solution of the expected mean slope square derived in the previous subsection under the finite discretization. The numerical results are also compared to demonstrate their consistency with the kMC simulation results of the lattice models.

To carry out the numerical calculations of the mean slope square under the finite difference discretization, numerical simulations are first carried out to compute solutions of the EW equation, i.e., the solutions of surface height profile. The numerical solutions of the EW equation can be obtained from a high-order approximation of the infinite ODE system of Eq. 3.10. Due to the decoupled nature of the linear ODE system, the solution of each state is a stochastic process, which is independent from the other states. Since the ODE system contains an infinite number of states and results in an infinite computational time for the solution, a reduced-order system with a sufficiently large number of modes (the number of modes is 100 times the number of discretization nodes) is used as an approximation of the infinite-order system. The solution of the surface height profile is then sampled at discrete positions to obtain a discrete surface height profile. The sampled positions are the coordinates of the discretization nodes defined in Eq. 3.16, which are evenly distributed in the spatial domain. Finally, the expected rms slope and the expected mean slope square can be computed from the discrete surface height profile. Since the numerical solutions are stochastic realizations of the analytical solution, multiple independent numerical solutions are obtained to calculate the expected mean slope square.

Fig. 3.17 shows the profile of the expected mean slope square of the discretized solution of the EW equation. In Fig. 3.17, the profile from numerical solutions is compared with the profile from the analytical solution that is derived previously in Section 3.4.2. The analytical solution is obtained from the same high-order approximation as the numerical solutions. The values of parameters of the EW equation are $\nu = 1$ and $\sigma^2 = 1$ for all simulations in this subsection. The domain size is $L_0 = 50$ and the discretization interval is $\Delta x = 1$. Thus, the lattice size is $L = 100$. From Fig. 3.17, it can be seen that the derived analytical solution of the expected mean slope square fits very well with numerical solutions of the EW equation. Therefore, the analytical solution can be used to predict the mean slope square evolution.

Fig. 3.18 shows the profiles of the expected mean slope square obtained from the EW equation for different domain sizes ranging from $L_0 = 5$ to $L_0 = 250$. We note that the lattice size changes simultaneously and proportionally with the domain size. As a result, the same discretization interval, Δx, is preserved, which corresponds to the size of particles in the lattice model. Therefore, the number of discretization nodes, which is also denoted by L, ranges from $L = 10$ to 500. In Fig. 3.18, the expected mean slope square profiles evolve similarly to the profiles from the discrete lattice kMC model shown in Fig. 3.5.

The lattice-size dependence of the expected mean slope square can be obtained from the analytical solution for different domain sizes and correspondingly different lattice sizes. Fig. 3.19 shows the lattice-size dependence of the steady-state value of the expected mean slope square. From Fig. 3.19, it can be seen that the steady-state value of the expected

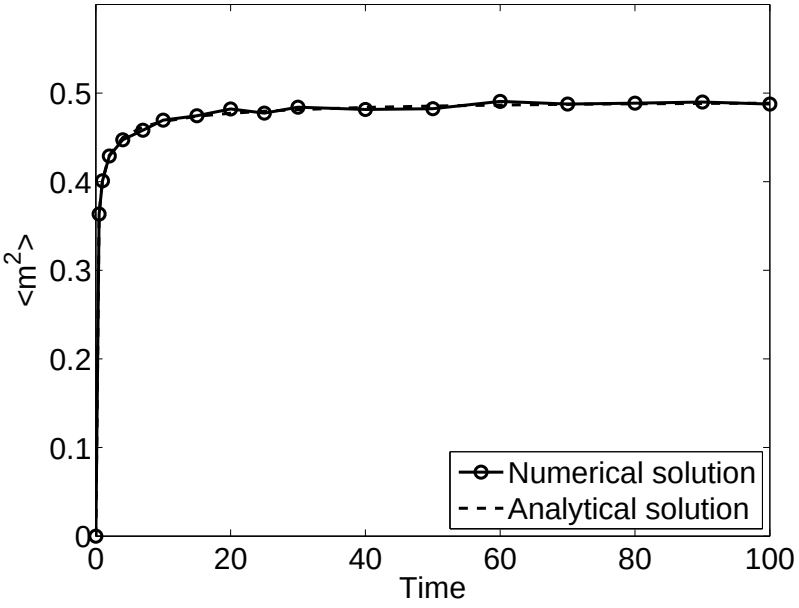

Figure 3.17: Profile of the expected mean slope square from the discretized solution of the EW equation from numerical simulations (solid line) and from analytical solutions (dashed line); $\Delta x = 1$, $L = 100$.

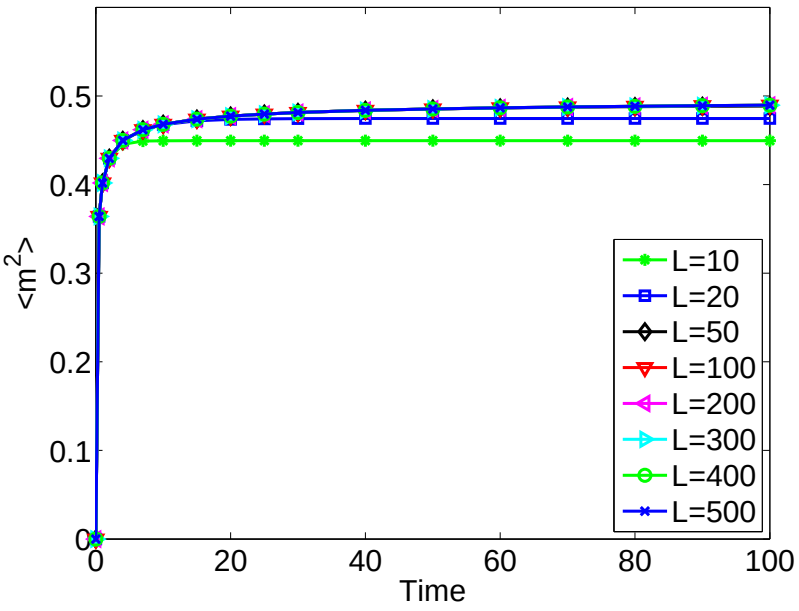

Figure 3.18: Profile of the expected mean slope square from the discretized solution of the EW equation with different domain sizes; $\Delta x = 1$.

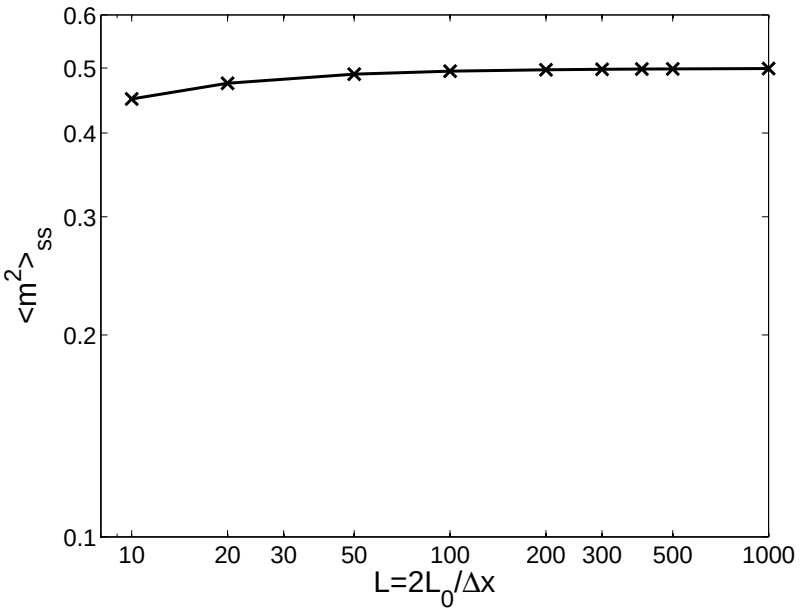

Figure 3.19: Dependence of the steady-state value of the expected mean slope square obtained from the discretized solution of the EW equation, on the lattice size, L; $\Delta x = 1$.

mean slope square has a weak dependence on lattice size, especially at large lattice sizes. We note that this lattice-size dependence is obtained on the basis of the fixed discretization interval, Δx.

From Fig. 3.18 and Fig. 3.19, the same behavior is observed from the discretized solution of the EW equation as the ones from the kMC simulations of the lattice model, i.e., a finite steady-state value and a weak lattice-size dependence of the steady-state value of the expected mean slope square. The consistency between the discretized solution of the EW equation and of the kMC simulations supports the choice of the EW equation as the dynamic model for the surface height profile evolution in the deposition processes under consideration.

The discretization can also explain the infinite steady-state value of the mean slope square of the EW equation in the continuum domain of Eq. 3.15. The infinite value originates from the infinitesimal discretization intervals in the continuum case, which can be observed from the analytical results of the discretized solutions of the EW equation with decreasing discretization intervals. The domain size is kept constant, and thus, the lattice size is proportional to $1/\Delta x$. Fig. 3.20 shows the dependence of the steady-state value of the expected mean slope square from the discretized solution of the EW equation for different discretization intervals. It can be clearly seen that as the discretization interval decreases to zero, the steady-state means slope square increases and the dependence of $\langle m^2 \rangle_{ss}$ on $1/\Delta x$ is linear. The same behavior of the steady-state value of $\langle m^2 \rangle_{ss}$ can be obtained from the kMC simulations of both deposition processes; see Fig. 3.21 for the random deposition with surface relaxation process and Fig. 3.22 for the porous thin-film deposition process. We note that the counterpart of the discretization interval in the kMC models of the deposition processes is the sampling interval, i.e., the distance between the points of the surface height profile that are used to calculate the surface slope and is denoted as Δx as well. Thus, the sampling intervals of the deposition process have a minimum value of one; smaller sampling intervals are not possible due to the lattice size limitation, which is different from the EW equation in the continuum domain where Δx can be chosen at will.

Remark 3.4 *The dependence of the steady-state value of the expected mean slope square on the sampling interval, Δx, in the porous thin-film deposition process is linear for large Δx, as shown in Fig. 3.22, which is similar to the linear dependence observed in the random*

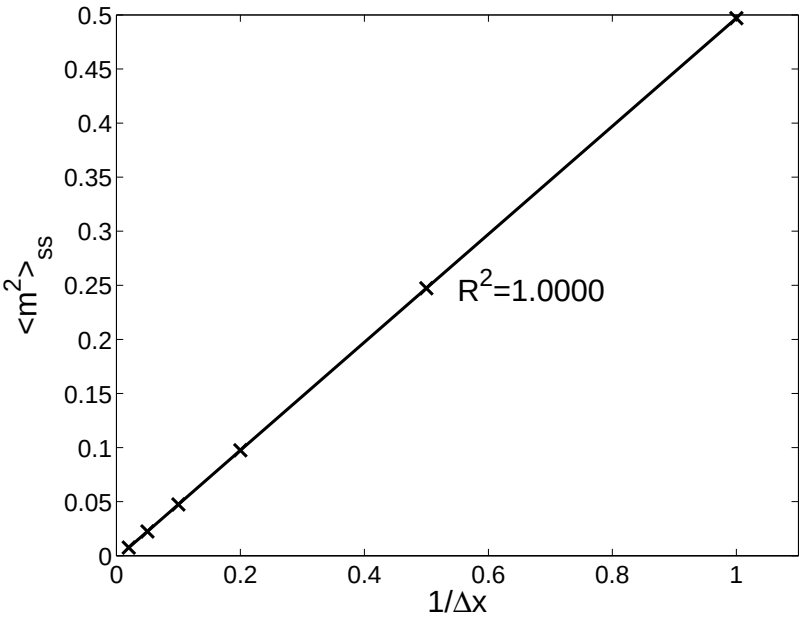

Figure 3.20: Dependence of the steady-state value of the expected mean slope square obtained from the discretized solution of the EW equation on the discretization interval; $L_0 = 100$.

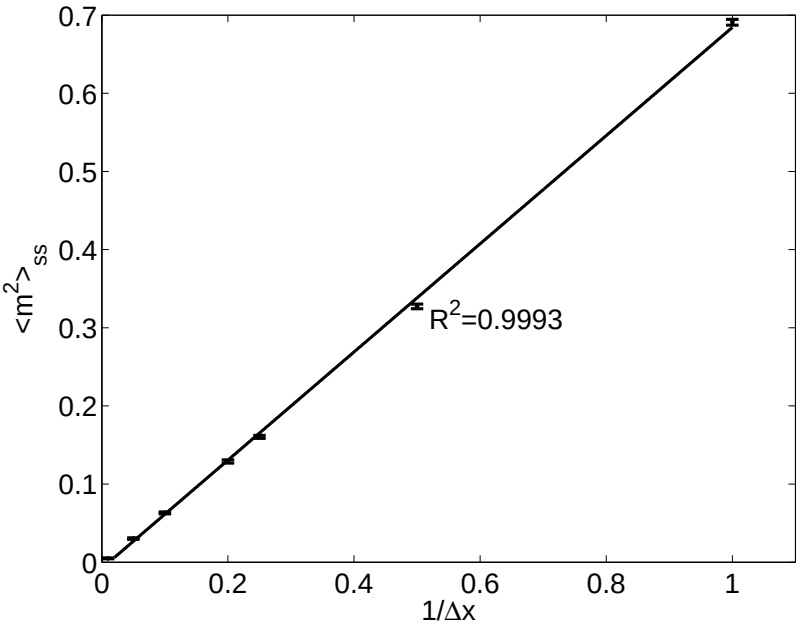

Figure 3.21: Dependence of the steady-state value of the expected mean slope square with error bars on the sampling interval; random deposition with surface relaxation process with $W = 1$ layer/s and $L = 200$.

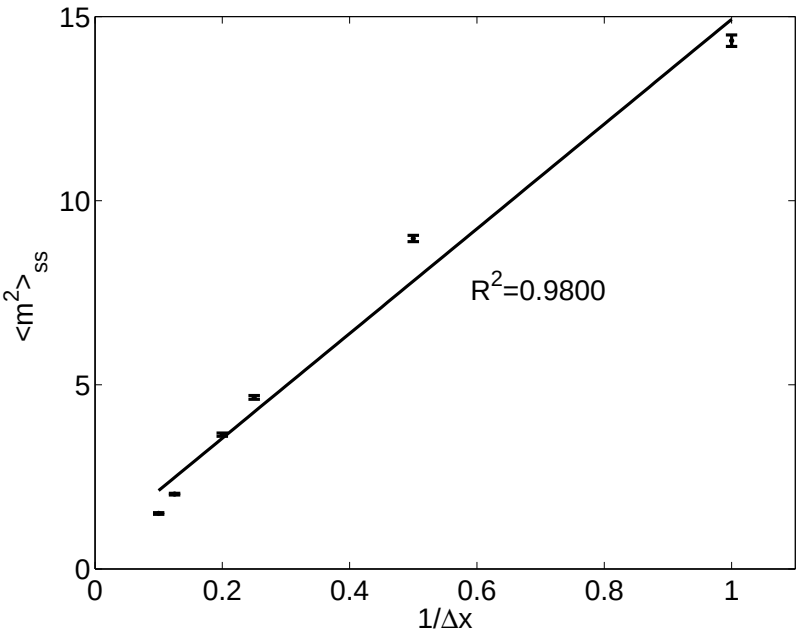

Figure 3.22: Dependence of the steady-state value of the expected mean slope square with error bars on the sampling interval; porous thin-film deposition process with $W = 1$ layer/s, $T = 300$ K, and $L = 200$.

deposition with surface relaxation process and in the EW equation shown in Fig. 3.20 and Fig. 3.21, respectively. However, at the discrete limit, $\Delta x = 1$*, the dependence on* Δx *in the porous film process has a notable deviation from the linear dependence. This deviation is due to the triangular lattice structure and the porosity allowed in the thin-film deposition process. To calculate the surface height profile of the deposition process taking place on a triangular lattice,* $2L$ *points are needed for the surface height positions, i.e.,* h_1*,* h_2*, ...,* h_{2L}*. However, since there are only* L *lattice sites in a row (in the lateral direction), the* $2L$ *surface heights are not fully independent. Instead, these heights are correlated to their neighboring heights via the structure of the triangular lattice. This correlation reduces the irregularity of the surface and results in close steady-state values of expected mean slope square for* $\Delta x = 1$ *and* $\Delta x = 2$ *in the porous thin-film deposition process.*

Remark 3.5 *This chapter mainly focuses on the dynamic behavior of the surface slope of thin-film growth processes that can be described by the EW equation. A potential application of this work is to improve light trapping efficiency of thin-film solar cells by simultaneously regulating surface roughness and slope of the thin-films during the manufacturing process. To achieve the control objectives, macroscopic variables including the substrate temperature and the deposition rate or the inlet concentration of the deposition reactor may be chosen as the manipulated variable(s). Model predictive control can be designed based on state feedback or measurements by formulating an optimization problem that minimizes the deviations of the surface roughness square and of the mean slope square from desired set-point values that optimize light trapping. With respect to measurement of surface mean*

slope, atomic force microscopy measurements of the film surface can be used to obtain surface height profiles up to atomic dimensions and from this compute the local surface mean slope variable. Aggregate surface height can also be computed from the atomic force microscopy measurements of the film surface to compute surface slope of aggregate surface height that is relevant to visible light trapping of thin-film solar cells. The detailed development of this controller design approach has been the subject of another work.

Appendix

Derivation of the state coefficients, K_n^α and K_n^β, of Eq. 3.20, can be found in the following steps. Since K_n^α and K_n^β have the same value and the derivation steps are similar, we only show the derivation of K_n^α from $\phi_n(x)$. The same value of K_n^β can be obtained from $\psi_n(x)$ via a similar derivation procedure.

From Eq. 3.18, the state coefficient, K_n^α has the following form:

$$K_n^\alpha = \frac{1}{L\Delta^2 x}\sum_{i=1}^{L}\Delta^2\bar{\phi}_n(x_i). \tag{3.21}$$

By substituting the expression of the eigenfunction ϕ_n of Eq. 3.8 into Eq. 3.21, the

expression of K_n^α can be rewritten as follows:

$$\begin{aligned}
K_n^\alpha &= \frac{1}{L\Delta^2 x}\sum_{i=1}^{L}[\phi_n(x_{i+1})-\phi_n(x_i)]^2 \\
&= \frac{1}{L\Delta^2 x}\sum_{i=1}^{L}[c_n\sin(knx_{i+1})-c_n\sin(knx_i)]^2 \\
&= \frac{1}{L\Delta^2 x}\sum_{i=1}^{L}\left\{2c_n\cos\left[\frac{kn}{2}[x_{i+1}+x_i)\right]\sin\left[\frac{kn}{2}[x_{i+1}-x_i)\right]\right\}^2 \qquad (3.22)\\
&= \frac{4}{L\Delta^2 x}\sum_{i=1}^{L}c_n^2\cos^2\left[\frac{kn}{2}(x_{i+1}+x_i)\right]\sin^2\left(\frac{kn\Delta x}{2}\right) \\
&= \frac{4}{L\Delta^2 x}\sum_{i=1}^{L}c_n^2\cos^2\left[\frac{kn}{2}(x_{i+1}+x_i)\right]\sin^2\left(\frac{kn\Delta x}{2}\right).
\end{aligned}$$

Eq. 3.22 can be further simplified into the following form by substituting the expressions of $\Delta x = 2L_0/L$, $k=\pi/L_0$, $c_n = 1/\sqrt{L_0}$ (for $n\geq 1$), and the expression of x_i of Eq. 3.16:

$$\begin{aligned}
K_n^\alpha &= \frac{4}{L\Delta^2 x}\sum_{i=1}^{L}\frac{1}{L_0}\cos^2\left[knx_1-\frac{n\pi}{L}+i\frac{2n\pi}{L}\right]\sin^2\left(\frac{n\pi}{L}\right) \qquad (3.23)\\
&= \frac{8}{L^2\Delta x^3}\sum_{i=1}^{L}\cos^2\left[knx_1-\frac{n\pi}{L}+i\frac{2n\pi}{L}\right]\sin^2\left(\frac{n\pi}{L}\right).
\end{aligned}$$

The following result is used to simplify the expression of K_n^α further:

Result 1 *If (1) $\theta_0 \in R$, (2) $n_1 \geq 1$ and $n_2 \geq 2$ are integers, and (3) $\theta = 2n_1\pi/n_2$, then it*

can be derived that:

$$\sum_{i=1}^{n_2}\cos^2(\theta_0+i\theta)=\begin{cases} n_2 cos^2\theta_0, & n_2=2,4,6,\ldots, \text{ and } n_1=\dfrac{1}{2}n_2, n_2, \dfrac{3}{2}n_2,\ldots, \\ \\ \dfrac{n_2}{2}, & \textit{otherwise.} \end{cases} . \quad (3.24)$$

Proof of Result 1:

If n_2 is a even integer and $n_1 = n_2/2$, n_2, $3n_2/2$, ..., i.e., $\theta = 2n_1\pi/n_2 = \pi$, 2π, ..., the sum of the series of cosine square can be directly obtained as follows:

$$\sum_{i=1}^{n_2}\cos^2(\theta_0+i\theta)=\sum_{i=1}^{n_2}\cos^2\theta_0 = n_2\cos^2\theta_0. \quad (3.25)$$

Otherwise, the sum of the series of cosine square can be rewritten in the following form:

$$\begin{aligned}\sum_{i=1}^{n_2}\cos^2(\theta_0+i\theta)&=\sum_{i=1}^{n_2}\left[\frac{1}{2}+\frac{1}{2}\cos(2\theta_0+2i\theta)\right] \\ &=\frac{n_2}{2}+\frac{1}{2}\sum_{i=1}^{n_2}Re\left(e^{j(2\theta_0+2i\theta)}\right)=\frac{n_2}{2}+\frac{1}{2}Re\left(e^{j2\theta_0}\sum_{i=1}^{n_2}e^{j2i\theta}\right),\end{aligned} \quad (3.26)$$

where j denotes the imaginary unit, and $Re(\cdot)$ denote the real part of a complex number. The sum of the geometric series can be further simplified as follows:

$$\begin{aligned}\sum_{i=1}^{n_2}\cos^2(\theta_0+i\theta)&=\frac{n_2}{2}+\frac{1}{2}Re\left(e^{j2\theta_0}e^{j2\theta}\frac{1-e^{j2n_2\theta}}{1-e^{j2\theta}}\right) \\ &=\frac{n_2}{2}+\frac{1}{2}Re\left(e^{j2\theta_0}e^{j2\theta}\frac{1-e^{j4n_1\pi}}{1-e^{j2\theta}}\right)=\frac{n_2}{2}+\frac{1}{2}Re(0)=\frac{n_2}{2},\end{aligned} \quad (3.27)$$

since the denominator $1-\exp(j2\theta) = 1-\exp(j2\pi\frac{2n_1}{n_2}) \neq 0$. □

By using Result 1, the expression of K_n can be obtained as follows:

$$K_n^\alpha = \begin{cases} \dfrac{8}{L\Delta x^3}\sin^2\left(\dfrac{n\pi}{L}\right) cos^2\left(knx_1 - \dfrac{n\pi}{L}\right), & n = \dfrac{1}{2}L, L, \dfrac{3}{2}L, \ldots, \\ \\ \dfrac{4}{L\Delta x^3}\sin^2\left(\dfrac{n\pi}{L}\right), & \text{otherwise.} \end{cases} \tag{3.28}$$

Eq. 3.28 indicates that for certain values of n ($n = \frac{1}{2}L$, L, $\frac{3}{2}L$, $\ldots$), the value of K_n depends on the choice of the spatial coordinate of the first discretization node, x_1, which can be any value from $-L_0$ to $-L_0 + \Delta x$. Thus, a general expression of K_n^α is desired and can be obtained by averaging over all possible $x_1 \in [-L_0, -L_0 + \Delta x)$ as follows:

$$K_n^\alpha = \frac{1}{\Delta x}\int_{-L_0}^{-L_0+\Delta x} K_n(x_1)dx_1 = \frac{4}{L\Delta x^3}\sin^2\frac{n\pi}{L}, \quad n \geq 1. \tag{3.29}$$

Similarly, K_n^β can be obtained with the same value as K_n^α.

After the expressions of K_n^α and K_n^β are obtained, the steady-state value of the expected mean slope square can be computed by taking the infinite-time limit of Eq. 3.19 and substituting the steady-state variance of Eq. 3.12 as follows:

$$\begin{aligned} \left\langle m^2 \right\rangle_{ss} &= \sum_{n=1}^{\infty} K_n^\alpha \left\langle \alpha_n^2 \right\rangle_{ss} + \sum_{n=1}^{\infty} K_n^\beta \left\langle \beta_n^2 \right\rangle_{ss} \\ &= \sum_{n=1}^{\infty} 2\frac{4}{L\Delta x^3}\frac{\sigma^2 L^2}{2\nu\pi^2 n^2}\sin^2\left(\frac{n\pi}{L}\right) \\ &= \frac{4L\sigma^2}{\nu\pi^2\Delta x^3}\sum_{n=1}^{\infty}\frac{1}{n^2}\sin^2\left(\frac{n\pi}{L}\right). \end{aligned} \tag{3.30}$$

Since $0 \leq \sin^2(n\pi/L) \leq 1$, it can be shown that the steady-state expected mean slope

square has an finite upper bound as follows:

$$\left\langle m^2 \right\rangle_{ss} \leq \frac{4L\sigma^2}{\nu\pi^2\Delta x^3} \sum_{n=1}^{\infty} \frac{1}{n^2} = \frac{4L\sigma^2}{\nu\pi^2\Delta x^3} \frac{\pi^2}{6} = \frac{2L\sigma^2}{\nu\Delta x^3}. \tag{3.31}$$

Therefore, the expected mean slope square has a finite value at the steady state. ■

Chapter 4

Dynamics and Control of Aggregate Thin Film Surface Morphology for Improved Light Trapping: Implementation on a Large-Lattice Kinetic Monte-Carlo Model

4.1 Introduction

This chapter presents an integrated control actuator and control algorithm design for the regulation of deposition of thin films such that the final thin film surface morphology is

characterized by a desired visible light reflectance/transmittance level. To demonstrate the approach, we focus on a thin film deposition process involving atom adsorption and surface migration and use a large-lattice (lattice size=40,000) kinetic Monte-Carlo simulation to describe its spatiotemporal behavior; this allows computing surface roughness and slope at different length-scales ranging from atomic scale to visible light wavelength scale. Subsequently, thin film surface morphology characteristics like roughness and slope are computed for different characteristic length scales and it is found that a patterned actuator design is needed to induce thin film surface roughness and slope at visible light wavelength spatial scales, that lead to desired thin film reflectance and transmittance values. Since a large-lattice kinetic Monte-Carlo model cannot be used as the basis for controller design and real-time controller calculations, an Edwards-Wilkinson-type equation is used to model the surface evolution at the visible light wavelength spatial scale and to form the basis for feedback controller design within a model predictive control framework. The cost function of the predicted controller involves penalties on both surface roughness and slope from set-point values as well as constraints on the magnitude and rate of change of the control action. The Edwards-Wilkinson equation model parameters are estimated from kinetic Monte-Carlo simulations and their dependence on the manipulated input (deposition rate) is used to predict the influence of the control action on the surface roughness and slope during the growth process. The controller formulation takes advantage of analytical solutions of the expected surface roughness and surface slope at the visible light wavelength spatial scale and the controller is applied to the large-lattice kinetic Monte-Carlo simulation. Ex-

tensive simulation studies demonstrate that the proposed controller and patterned actuator design successfully regulate surface roughness and slope at visible light wavelength spatial scales to set-point values at the end of the deposition that yield desired levels of thin film reflectance and transmittance.

4.2 Thin film deposition process description and modeling

In this section, a one-dimensional solid-on-solid (SOS) on-lattice kinetic Monte Carlo (kMC) model is used to simulate the thin film deposition process, which includes two microscopic processes: an adsorption process, in which particles are incorporated onto the film from the gas phase, and a migration process, in which surface particles move to adjacent sites [35, 34, 52, 53]. The model is valid for temperatures $T < 0.5T_m$, where T_m is the melting point of the deposited material [35]. At high temperatures ($T \lesssim T_m$), the particles cannot be assumed to be constrained on the lattice sites and the on-lattice model may not be valid. In this work, a square lattice is selected to represent the structure of the film, as shown in Fig.4.1. All particles are modeled as identical hard spheres and the centers of the particles deposited on the film are located on the lattice sites. The diameter of the particles equals the distance between two neighboring sites. The width of the lattice is fixed so that the lattice contains a fixed number of sites in the lateral direction. The new particles are always deposited from the top side of the lattice with vertical incidence; see Fig.4.1. Particle deposition results in film growth in the direction normal to the lateral direction. The direction normal to the lateral direction is thus designated as the growth direction. The number

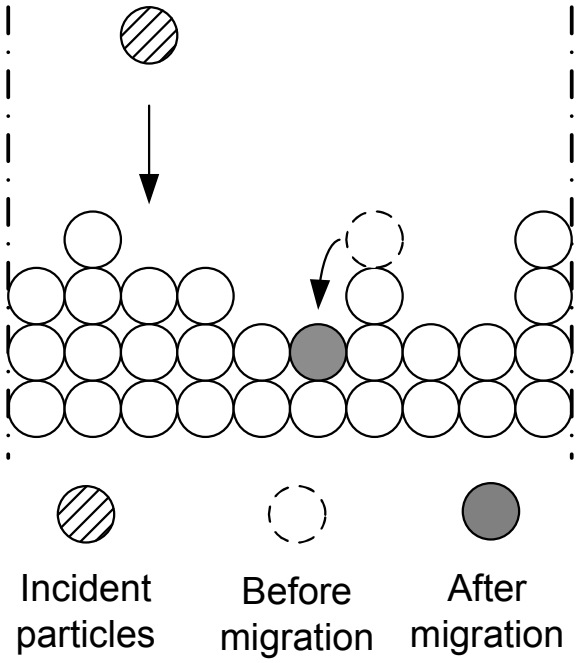

Figure 4.1: Thin film growth process on a solid-on-solid one-dimensional square lattice.

of sites in the lateral direction is defined as the lattice size and is denoted by L. Periodic boundary conditions (PBCs) are applied at the edges of the lattice in the lateral direction.

The top particles of each column are defined as the surface particles and the positions of the centers of all surface particles form the surface height profile. The number of nearest neighbors of a surface particle ranges from zero to two. A surface particle with zero nearest neighbors is possible to migrate to one of its adjacent columns with equal probability. A surface particle with one nearest neighbor is possible to migrate to its adjacent column with lower height with appropriate probability based on the migration rate (please see Eq. 4.1 below). A surface particle with two nearest neighbors can not migrate. Particles that are not on the film surface can not migrate.

In the adsorption process, a site is randomly selected with uniform probability among all lattice sites and a particle is deposited on top of this site. The overall adsorption rate, w, is expressed in the unit of layer per second. In the migration process, a surface particle overcomes the energy barrier of the site and jumps to a vacant neighboring site. The migration rate (probability) of a particle follows an Arrhenius-type law with a pre-calculated activation energy barrier that depends on the local environment of the particle, i.e., the number of the nearest neighbors of the particle chosen for a migration event. The migration rate of the ith surface particle is calculated as follows:

$$r_m = \nu_0 \exp\left(-\frac{E_s + n_i E_n}{k_B T}\right) \tag{4.1}$$

where ν_0 denotes the pre-exponential factor, n_i is the number of the nearest neighbors of the ith particle and can take the values of 0 and 1, (r_m is zero when $n_i = 2$ since in the one-dimensional lattice this surface particle is fully surrounded by other particles and cannot migrate), E_s is the contribution to the activation energy barrier from the site itself, E_n is the contribution to the activation energy barrier from each nearest neighbor, k_B is the Boltzmann's constant and T is the substrate temperature of the thin film. Since the film is thin, the temperature is assumed to be uniform throughout the film.

4.2.1 Surface morphology at atomic level

Thin film surface morphology, which can be expressed in terms of surface roughness and slope, is a very important surface property influencing the light trapping properties of thin films. Surface roughness is defined as the root-mean-square (rms) of the surface height

profile. Specifically, the definition of surface roughness is given as follows:

$$r = \left[\frac{1}{L} \sum_{i=1}^{L} (h_i - \bar{h})^2 \right]^{1/2} \tag{4.2}$$

where r denotes surface roughness, h_i, $i = 1, 2, \ldots, L$, is the surface height at the i-th position in the unit of layer, L denotes the lattice size, and the surface mean height is given by $\bar{h} = \frac{1}{L} \sum_{i=1}^{L} h_i$.

In addition to surface roughness, another quantity that also determines the surface morphology is the surface mean slope. In this work, the surface mean slope is defined as the rms of the surface gradient profile as follows:

$$m = \left[\frac{1}{L} \sum_{i=1}^{L} h_{s,i}^2 \right]^{1/2} \tag{4.3}$$

where m denotes the rms slope and $h_{s,i}$ is the surface slope at the i-th lattice site, which is a dimensionless variable. The surface slope, $h_{s,i}$ is computed as follows:

$$h_{s,i} = \frac{h_{i+1} - h_i}{1} \tag{4.4}$$

Since the unit of height is layer and the distance between two adjacent particles (the diameter of particles) always equal to one layer, the denominator of $h_{s,i}$ is always one. Due to the use of PBCs, the slope at the boundary lattice site ($i = L$) is computed as the slope between the last lattice site (h_L) and the first lattice site (h_1).

To investigate the open-loop properties of surface morphology, a set of kMC simulations is carried out at different w with $T = 480$ K and $L = 40000$. In particular, the continuous-time Monte Carlo (CTMC) method is used in the kMC simulations. In this

method, a list of events is constructed and an event is selected randomly with its respective probability. After the execution of the selected event, the list is updated based on the new lattice configuration. The following values are used for the parameters of the migration rate of Eq. 4.1, $\nu_0 = 10^{13}\text{s}^{-1}$, $E_s = 1.2$ eV and $E_n = 0$ eV. Fig. 4.2 and Fig. 4.3 show that both atomic roughness and slope increase with time and approach steady-state values at different time scales. Furthermore, both surface roughness and slope increase with deposition rate w. It is important to note that surface roughness and slope are correlated to some extent in the deposition process, but they are separate variables that describe different aspects of the film surface. Films with the same surface roughness may have different mean slope values.

4.2.2 Aggregate surface morphology and spatial deposition rate profile

One of the most important application of our work is to simulate and control the deposition process of thin film solar cells in order to improve solar cell efficiency via enhanced light trapping. However, the wavelength of visible light ($400\text{nm} - 700\text{nm}$) is much larger than the diameter of silicon atoms (~ 0.25 nm) and thus, it is necessary to define an aggregate surface morphology at length scales comparable to visible light wavelength.

Specifically, the aggregate surface morphology is computed similarly to the atomic surface morphology, but on the basis of the aggregate surface height profile, $h_{\Delta,i}$, which is

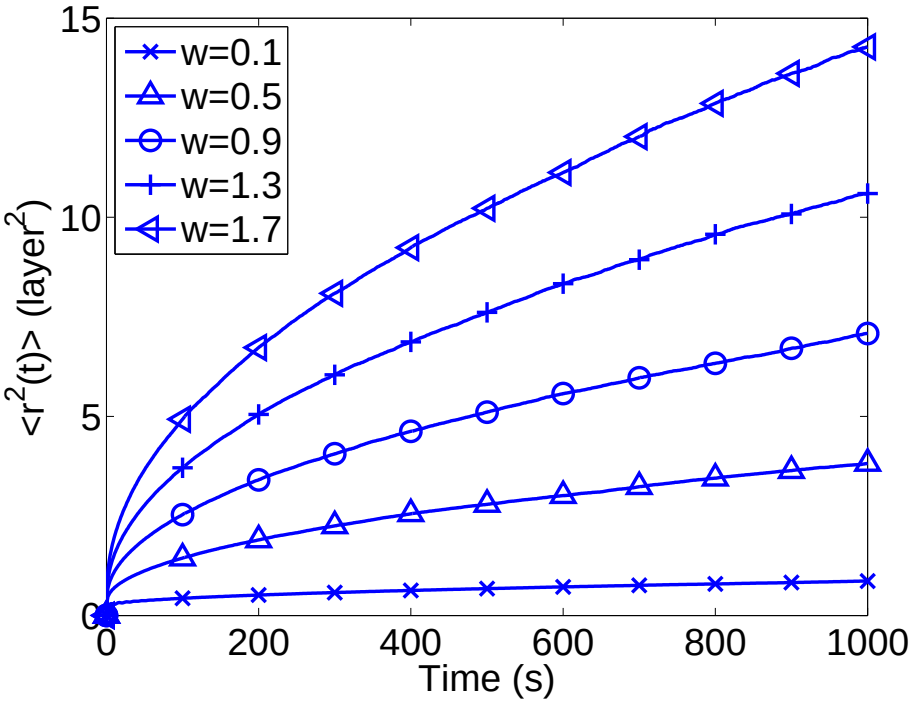

Figure 4.2: Evolution of expected atomic surface roughness with respect to time for different deposition rates (unit of w is layer/s) obtained from kMC simulations.

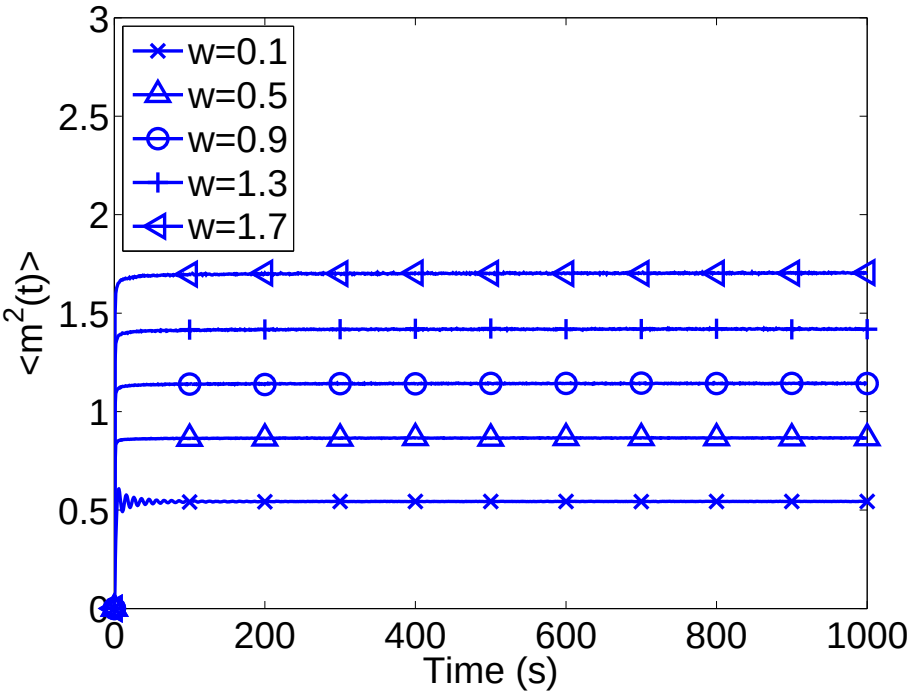

Figure 4.3: Evolution of expected atomic surface slope with respect to time for different deposition rates (unit of w is layer/s) obtained from kMC simulations.

defined as follows:

$$h_{\Delta,i} = (h_{i\Delta+1} + h_{i\Delta+2} + \cdots + h_{(i+1)\Delta})/\Delta, \quad i = 0, 1, \ldots, L/\Delta - 1 \tag{4.5}$$

where $h_{\Delta,i}$ denotes the averaged surface height over the length scale of Δ sites, Δ denotes the aggregation size, i.e., the number of lattice sites used to calculate the aggregate surface height, and L/Δ denotes the number of aggregate sites of size Δ included in the spatial domain of the process. For the wavelength of visible light and silicon thin-film solar cells, the corresponding Δ is around 400; this follows from the fact that $0.25nm \cdot 400 = 100nm$, which is a length scale comparable to visible light wavelength. The definition of aggregate surface roughness and slope is given as follows:

$$\begin{aligned} r_\Delta &= \left[\frac{1}{L} \sum_{i=1}^{L/\Delta} \left(h_{\Delta,i} - \bar{h}_\Delta \right)^2 \right]^{1/2}, \\ m_\Delta &= \left[\frac{1}{L} \sum_{i=1}^{L/\Delta} \left(\frac{h_{\Delta,i} - h_{\Delta,i+1}}{\Delta} \right)^2 \right]^{1/2}. \end{aligned} \tag{4.6}$$

The dynamics of the aggregate surface roughness and slope are dependent on the characteristic length scale, Δ. To investigate this dependence, kMC simulations with $E_n = 0$ eV and $L = 40000$ were carried out. The expected aggregate surface roughness square, $\left\langle r_\Delta^2(t) \right\rangle$, and the expected aggregate surface slope square, $\left\langle m_\Delta^2(t) \right\rangle$, are calculated from the aggregate surface height profile from kMC simulations for different aggregation lengths. The simulation duration is $t_f = 1000$ s and 100 independent simulations were carried out to calculate the expected values of aggregate surface roughness and slope. Fig. 4.4 and Fig. 4.5 show the profiles of aggregate surface roughness square and slope square for different characteristic length scales, Δ. It is clear that the larger the characteristic length

scale, the smaller the aggregate roughness and slope square. Furthermore, Fig. 4.5 shows that as the aggregation size increases, the aggregate slope square decreases very fast; a much weaker dependence is observed for aggregate roughness in Fig. 4.4. From these results, we see that the corresponding aggregate slope square for $\Delta = 400$ is very small ($\left\langle m_{\Delta}^{2} \right\rangle_{ss} \sim 10^{-5}$). This close-to-zero value of aggregate slope square reveals a smoothly changing surface profile with respect to characteristic length scales that are comparable to visible light wavelength. The smoothness of the surface profile persists at larger lattice sizes as well, due to the very weak lattice-size dependence of the mean slope square. This small aggregate slope square at large characteristic length scales is partly because the operating conditions are spatially uniform throughout the entire deposition process, i.e., the same deposition rate and substrate temperature are applied throughout the spatial domain. Thus, a spatially non-uniform deposition rate profile is necessary for the purpose of optimizing thin film light reflectance/transmittance by manipulation of film aggregate surface roughness and slope at length scales comparable to visible light wavelength; this conclusion is also consistent with recent experimental data [28]. To this end, we introduce a patterned in space deposition rate profile, which is defined as follows:

$$w(x) = w_0 + A \sin\left(\frac{2k\pi}{L}x\right), \quad A \leq w_0 \tag{4.7}$$

where x is a position along the lattice, w_0 is the mean deposition rate, A is the magnitude of the patterned deposition profile, k is the number of sine waves along the entire lattice, and L is the lattice size. Referring to the difference between w and w_0, it is necessary to point out that w_0 is the mean deposition rate of the patterned deposition rate profile, $w(x)$, while

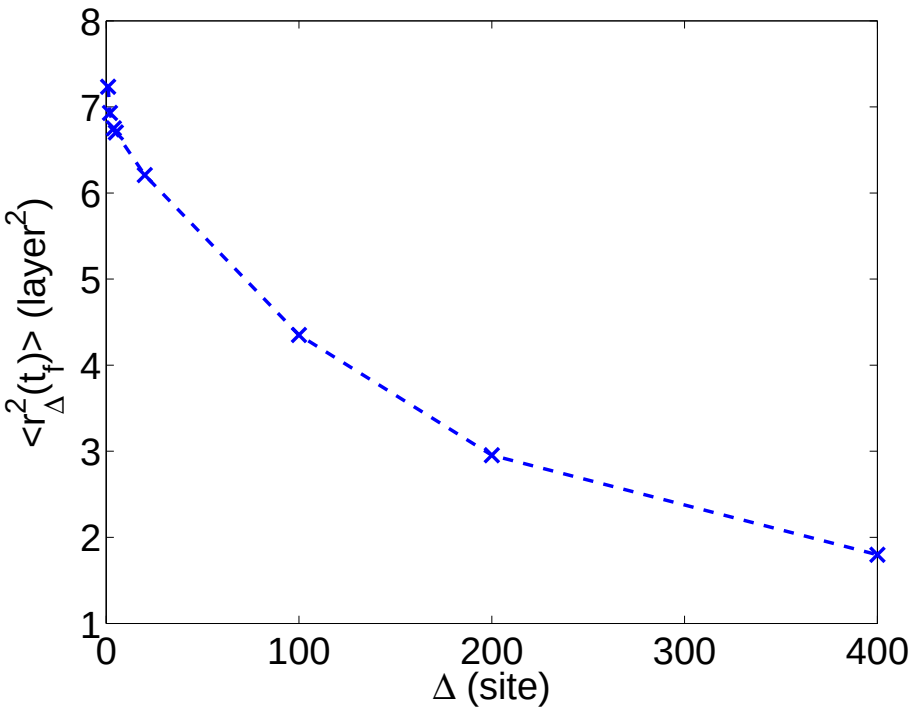

Figure 4.4: Dependence of expected aggregate surface roughness on aggregation size obtained from kMC simulations; $t_f = 1000$ s.

the w used in subsection 4.2.1 is a spatially-uniform deposition rate.

The dynamics of aggregate surface morphology with patterned deposition rate profile is studied by carrying out a series of simulations at different mean deposition rates w_0 with $L = 40000$, $\Delta = 400$, $T = 480K$, $k = 5$ and $A = 0.1w_0$. The evolution profiles are shown in Fig. 4.6 and Fig. 4.7. The introduction of patterned deposition rate profiles significantly changes the dynamic profiles of aggregate surface morphology. However, some properties of uniform deposition rate evolution profiles remain valid, for example, the expected values of aggregate surface roughness and slope still increase with mean deposition rate w_0. Fur-

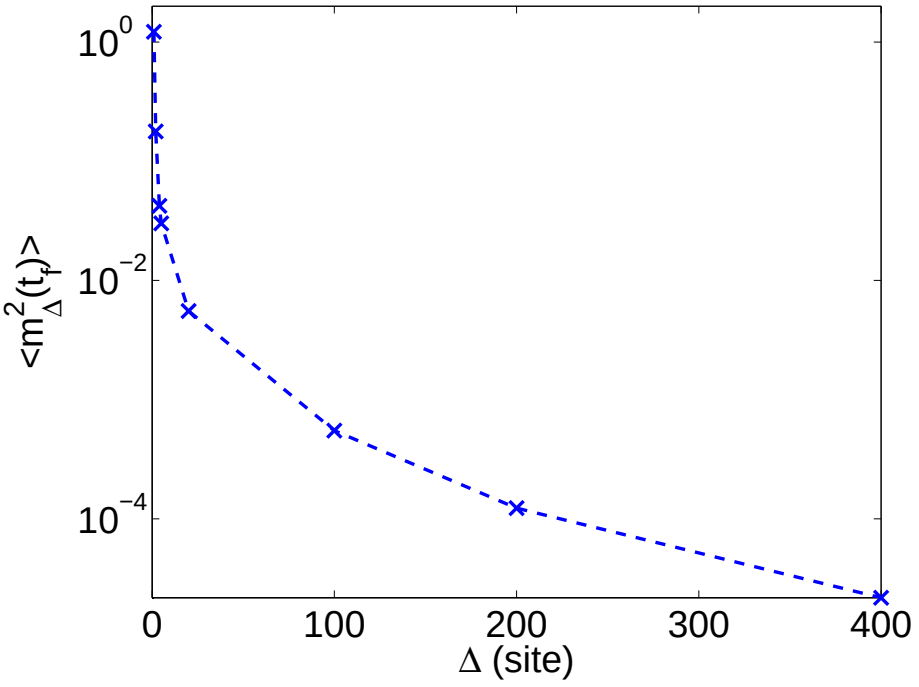

Figure 4.5: Dependence of expected aggregate surface slope on aggregation size obtained from kMC simulations; $t_f = 1000$ s.

thermore, simulations are carried out at $w_0 = 1$ layer/s with different magnitude, A, values to investigate the influence of the strength of patterned deposition on the evolution profiles of aggregate surface morphology. As shown in Fig. 4.8 and Fig. 4.9, the magnitude, A, has substantial influence on the dynamics of aggregate surface morphology. Both aggregate roughness and aggregate slope can be increased by 10000 times by manipulating A compared to the aggregate surface morphology achieved with a uniform deposition rate profile. Thus, the introduction of a patterned deposition rate profile substantially expands the range of surface morphology values that can be obtained and makes light trapping optimization at length scales comparable to visible light wavelength possible. Finally, referring to the influence of the migration activation energy values on the aggregate surface roughness and slope steady state values, we note that such an influence exists but it is small at aggregation levels corresponding to visible light wavelength.

4.3 Closed-form modeling and parameter estimation

4.3.1 Edward-Wilkinson-type equation of aggregate surface height

Given the complexity of the deposition process and the need to control surface roughness and slope at spatial scales comparable to the wavelength of visible light, the direct computation of a closed-form model, describing the surface height evolution and is suitable for controller design, from the microscopic deposition mechanisms is a very difficult (if not impossible) task. Therefore, a hybrid modeling approach should be used in which a basic

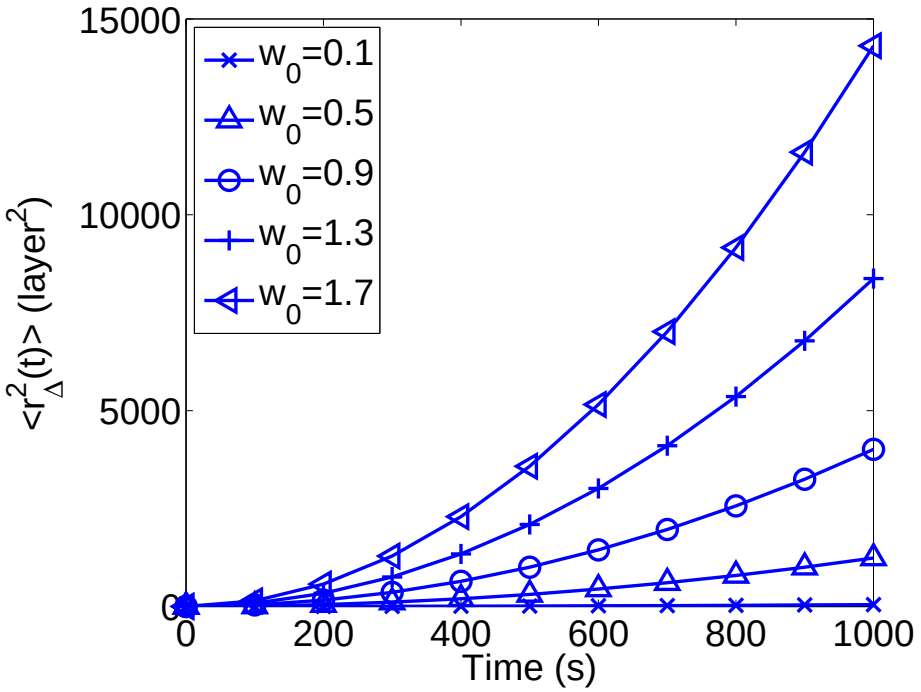

Figure 4.6: Evolution of expected aggregate surface roughness with respect to time for different mean deposition rates (unit of w_0 is layer/s) obtained from kMC simulations. Patterned deposition with $k = 5$ and $A = 0.1w_0$.

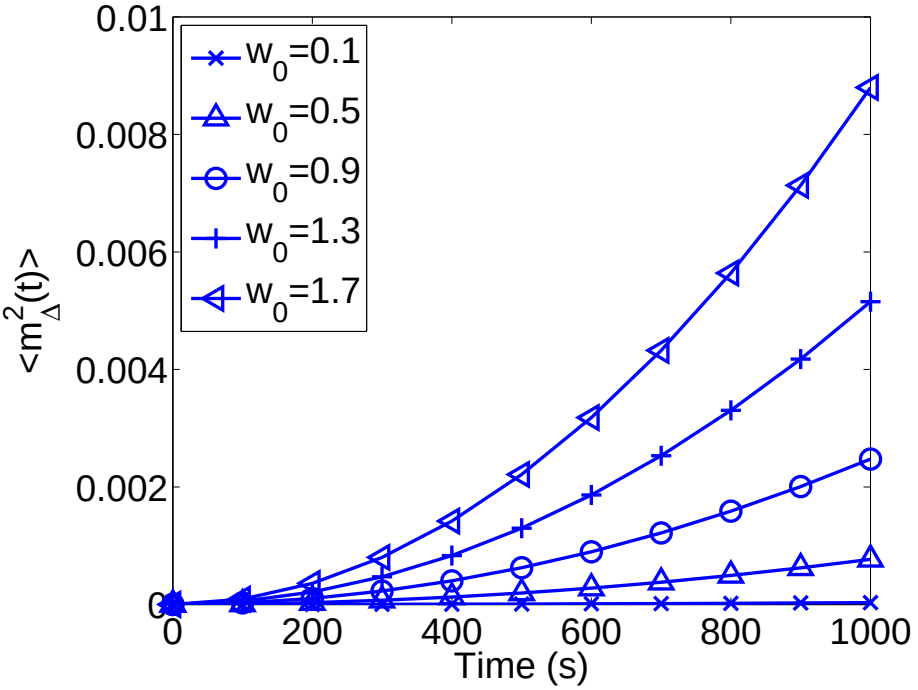

Figure 4.7: Evolution of expected aggregate surface slope with respect to time for different mean deposition rates (unit of w_0 is layer/s) obtained from kMC simulations. Patterned deposition with $k = 5$ and $A = 0.1w_0$.

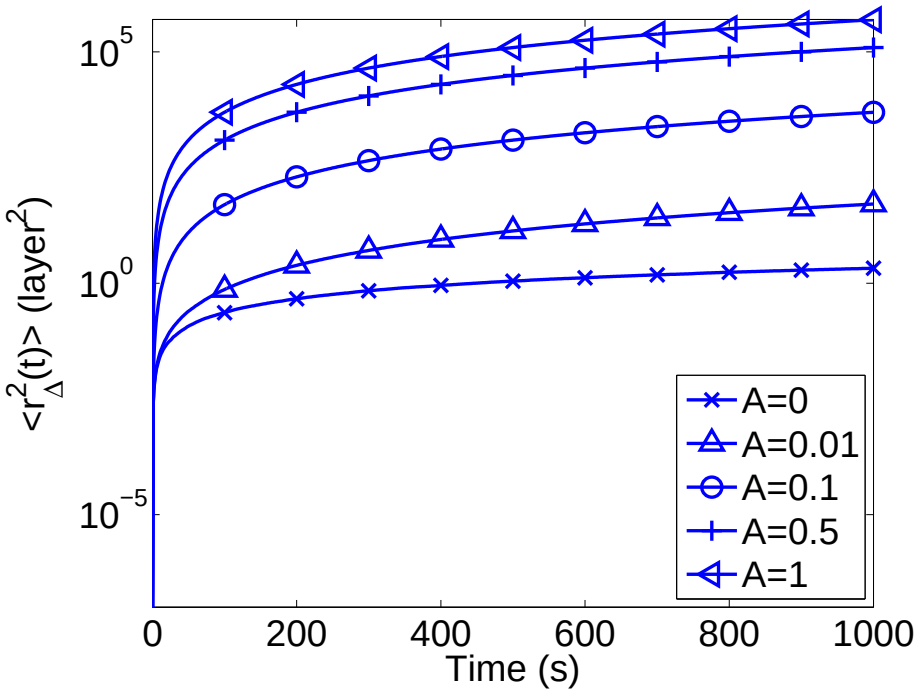

Figure 4.8: Evolution of expected aggregate surface roughness with respect to time for different patterned deposition rate magnitudes obtained from kMC simulations. Patterned deposition with $k = 5$ and $w_0 = 1$ layer/s.

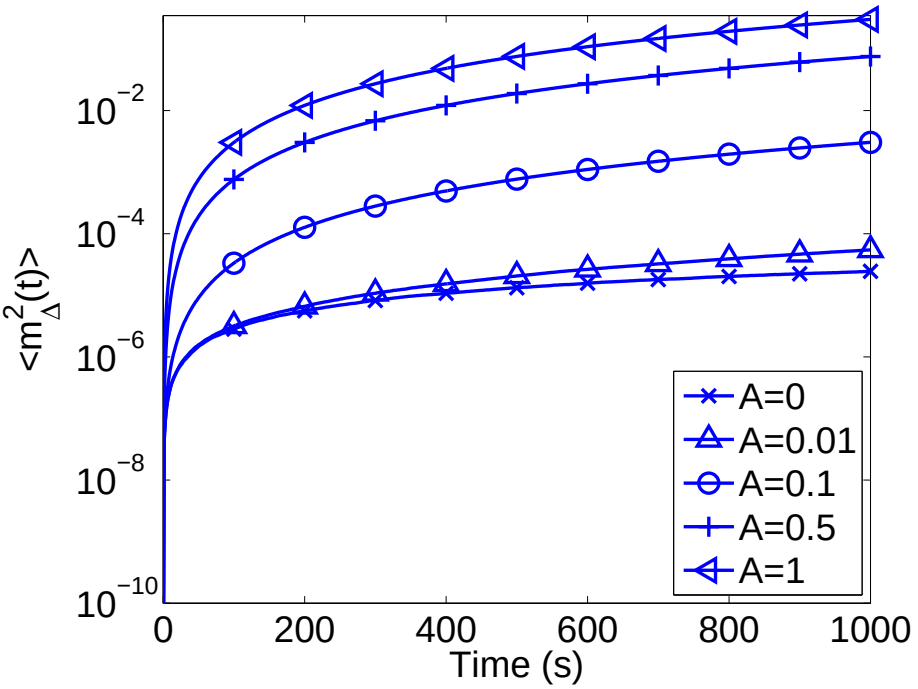

Figure 4.9: Evolution of expected aggregate surface slope with respect to time for different patterned deposition rate magnitudes obtained from kMC simulations. Patterned deposition with $k = 5$ and $w_0 = 1$ layer/s.

closed-form modeling structure is used and the model parameters are computed such that the predictions of key variables from the closed-form model are close to the one of the kinetic Monte-Carlo model for a broad set of operating conditions. To this end, we use an Edward-Wilkinson(EW)-type equation, which is a second-order stochastic PDE to describe the aggregate surface height evolution and compute its parameters from kMC data. The choice of the EW-equation is motivated by the fact that it has been used in many deposition processes that involve a thermal balance between adsorption (deposition) and migration (diffusion) [3]. Specifically, a one-dimensional EW-type equation is used to describe the evolution of aggregate surface height profile:

$$\frac{\partial h_\Delta}{\partial t} = w(x,t) + c_2 \frac{\partial^2 h_\Delta}{\partial x^2} + \xi(x,t) \tag{4.8}$$

subject to the following periodic boundary conditions

$$h_\Delta(0,t) = h_\Delta(L,t) \tag{4.9}$$

$$\frac{\partial h_\Delta}{\partial x}(0,t) = \frac{\partial h_\Delta}{\partial x}(L,t) \tag{4.10}$$

and the initial condition

$$h_\Delta(x,0) = h_\Delta^0(x) \tag{4.11}$$

where $x \in [0,L]$ is the spatial coordinate, t is the time, $h_\Delta(x,t)$ is the aggregate surface height and $\xi(x,t)$ is a Gaussian white noise with zero mean and the following covariance:

$$\left\langle \xi(x,t)\xi(x',t') \right\rangle = \sigma^2 \delta(x-x')\delta(t-t') \tag{4.12}$$

where $\delta(\cdot)$ denotes the Dirac delta function. In Eq. 4.8, the parameters c_2 and σ^2, corresponding to diffusion effects and stochastic noise respectively, depend on the deposition

rate $w(x,t)$. In the case of a patterned deposition rate profile (control actuation), the term $w(x,t)$ is of the form:

$$w(x,t) = w_0(t) + A(t)\sin\left(\frac{2k\pi}{L}x\right) \tag{4.13}$$

where $w_0(t)$ is the mean deposition rate, $A(t)$ is the magnitude of patterned deposition rate, and k is the number of sine waves between 0 and L.

To analyze the dynamics and obtain a solution of the EW equation suitable for real-time controller calculations, we first consider the eigenvalue problem of the linear operator of Eq. 4.8 subject to the periodic boundary conditions of Eqs. 4.9-4.10:

$$\mathscr{A}\bar{\phi}_n(x) = c_2\frac{d^2\bar{\phi}_n(x)}{dx^2} = \lambda_n\bar{\phi}_n(x), \tag{4.14}$$

$$\nabla^j\bar{\phi}_n(0) = \nabla^j\bar{\phi}_n(L), \quad j = 0,1 \tag{4.15}$$

where λ_n denotes an eigenvalue, $\bar{\phi}_n$ denotes an eigenfunction, and ∇^j, $j = 0$, 1, denotes the gradient of a given function. The solution of the eigenvalue problem of Eqs. 4.14–4.15 is as follows:

$$\lambda_n = -\frac{4c_2\pi^2n^2}{L^2} \tag{4.16}$$

$$\phi_{1,n}(x) = \phi_n = \sqrt{\frac{2}{L}}\sin(\frac{2n\pi}{L}x) \tag{4.17}$$

$$\phi_{2,n}(x) = \psi_n = \begin{cases} \sqrt{\frac{1}{L}} & n = 0 \\ \\ \sqrt{\frac{2}{L}}\cos(\frac{2n\pi}{L}x) & n \neq 0 \end{cases} \tag{4.18}$$

The solution of the EW equation of Eq. 4.8 can be expanded in an infinite series in terms

of the eigenfunctions of the operator of Eq. 4.14 as follows:

$$h_\Delta(x,t) = \sum_{n=0}^{L/(2\Delta)} \left(\phi_{1,n}(x) z_{1,n}(t) + \phi_{2,n}(x) z_{2,n}(t)\right), \tag{4.19}$$

where $z_{1,n}(t)$, $z_{2,n}(t)$ are time-varying coefficients.

Substituting the above expansion for the solution, $h_\Delta(x,t)$, into Eq. 4.8 and taking the inner product with the adjoint eigenfunctions, the following system of infinite stochastic linear ordinary differential equations (ODEs) for the temporal evolution of the time-varying coefficients in Eq. 4.19 is obtained:

$$\frac{dz_{2,0}(t)}{dt} = w_{2,0} + \xi_{2,0}(t), \tag{4.20}$$

$$\frac{dz_{p,n}(t)}{dt} = w_{p,n} + \lambda_n z_{p,n} + \xi_{p,n}(t) \tag{4.21}$$

$$p = 1,2, \quad n = 1, \cdots, \frac{L}{2\Delta},$$

where $\xi_{p,n}(t) = \int_0^L \xi(x,t)\phi_{p,n}(x)dx$ is the projection of the noise $\xi(x,t)$ on the ODE for $z_{p,n}$. The noise term, $\xi_{p,n}$, has zero mean and covariance

$$\left\langle \xi_{p,n}(t)\xi_{p,n}(t')\right\rangle = \sigma^2\delta(t-t'). \tag{4.22}$$

Similarly, $w_{p,n}$ is the projection of w on the ODE for $z_{p,n}(t)$, $w_{p,n} = \int_0^L \phi_{p,n}(x)w(x)dx$

- If $p = 1$,

$$w_{1,n} = \begin{cases} 0, & n \neq k \\ \\ A\sqrt{\dfrac{L}{2}}, & n = k \end{cases} \tag{4.23}$$

- If $p = 2$,

$$w_{2,n} = \begin{cases} 0, & n \neq 0 \\ \\ A\sqrt{L}, & n = 0 \end{cases} \tag{4.24}$$

The temporal evolution of the variance of mode $z_{p,n}$ can be obtained from the solution of the linear ODEs of Eqs. 4.20 and 4.21 as follows:

$$\left\langle z_{2,0}(t) \right\rangle = w_{2,0}(t - t_0) \tag{4.25}$$

$$\text{var}(z_{2,0}(t)) = \sigma^2 (t - t_0) \tag{4.26}$$

$$\langle z(t) \rangle = e^{\lambda (t - t_0)} \langle z(t_0) \rangle + \frac{w_p}{\lambda} (e^{\lambda (t - t_0)} - 1) \tag{4.27}$$

$$\text{var}(z(t)) = e^{2\lambda (t - t_0)} \text{var}(z(t_0)) + \sigma^2 \frac{e^{2\lambda (t - t_0)} - 1}{2\lambda} \tag{4.28}$$

where $z(t) = z_{p,n}(t)$, $\lambda = \lambda_n$ and $w_p = w_{p,n}$ for $n \neq 0$.

Finally, it is necessary to point out that, when aggregate (discrete) surface height profile is used, the highest number of modes that can be accurately estimated from $h_\Delta(x,t)$ is limited by the spatial sampling points, $n \leq \frac{L}{2\Delta}$; the reader may refer to [57] for a detailed discussion of the issue.

4.3.2 Aggregate surface root–mean–square roughness

Aggregate surface roughness of the thin film is defined as the standard deviation of the aggregate surface height profile from its average height

$$r_\Delta(t) = \sqrt{\frac{1}{L} \int_0^L \left[h_\Delta(x,t) - \bar{h}_\Delta(t) \right]^2 dx} \tag{4.29}$$

where $\bar{h}_\Delta(t) = \dfrac{1}{L}\displaystyle\int_0^L h_\Delta(x,t)dx$ is the average aggregate surface height. According to Eq. 4.19, we have

$$\bar{h}_\Delta(t) = \frac{1}{L}\int_0^L \phi_{2,0} z_{2,0} dx = \sqrt{\frac{1}{L}} z_{2,0} \tag{4.30}$$

Using that

$$h_\Delta(x,t) - \bar{h}_\Delta(t) = \sum_{n=1}^{L/(2\Delta)} \sum_{p=1}^{2} \phi_{p,n}(x) z_{p,n}(t) \tag{4.31}$$

the expected aggregate surface roughness, $\left\langle r_\Delta^2(t) \right\rangle$, of Eq. 4.29 can be re-written as

$$\begin{aligned} \left\langle r_\Delta^2(t) \right\rangle &= \left\langle \frac{1}{L}\int_0^L \left[\sum_{p=1}^{2} \sum_{n=1}^{L/(2\Delta)} z_{p,n}(t)\phi_{p,n}(x) \right]^2 dx \right\rangle \\ &= \left\langle \frac{1}{L}\int_0^L \sum_{n=1}^{L/(2\Delta)} \left(\phi_{1,n}^2(x) z_{1,n}^2(t) + \phi_{2,n}^2(x) z_{2,n}^2(t) \right) dx \right\rangle \\ &= \frac{1}{L} \sum_{n=1}^{L/(2\Delta)} \left(\left\langle z_{1,n}^2 \right\rangle + \left\langle z_{2,n}^2 \right\rangle \right) \end{aligned} \tag{4.32}$$

where

$$\left\langle z_{p,n}^2 \right\rangle = \mathrm{var}(z_{p,n}) + \left\langle z_{p,n} \right\rangle^2 . \tag{4.33}$$

The expression of Eqs. 4.32- 4.33 will be used in the MPC formulation; please see Eq. 4.42 below.

4.3.3 Aggregate surface root–mean–square slope

The aggregate rms slope is defined as the root–mean–square of the aggregate surface slope in the x–direction as follows:

$$\begin{aligned} m_{\Delta}(t) &= \sqrt{\frac{1}{L}\int_0^L \left(\frac{\partial h_{\Delta}}{\partial x}\right)^2 dx} \\ &= \sqrt{\frac{1}{L}\sum_{i=0}^{L/\Delta}\left(\frac{h_{\Delta}(i+1,t)-h_{\Delta}(i,t)}{\Delta}\right)^2 \Delta} \end{aligned} \tag{4.34}$$

Using the expansion of Eq. 4.19, Eq. 4.34 can be written as:

$$\begin{aligned} \left\langle m_{\Delta}^2(t)\right\rangle &= \left\langle \frac{1}{L}\sum_{i=0}^{L/\Delta}\left(\frac{h_{\Delta}(i+1,t)-h_{\Delta}(i,t)}{\Delta}\right)^2 \Delta \right\rangle \\ &= \left\langle \frac{1}{L\Delta}\sum_{i=0}^{L/\Delta}\left\{\sum_{p=1}^{2}\sum_{n=0}^{L/(2\Delta)} z_{p,n}\left[\phi_{p,n}(i+1)-\phi_{p,n}(i)\right]\right\}^2 \right\rangle \\ &= \left\langle \frac{1}{L\Delta}\sum_{i=0}^{L/\Delta}\sum_{p_1=1}^{2}\sum_{n_1=0}^{L/(2\Delta)}\sum_{p_2=1}^{2}\sum_{n_2=0}^{L/(2\Delta)} z_{p_1,n_1}z_{p_2,n_2}d\phi_{p_1,n_1}(i)d\phi_{p_2,n_2}(i) \right\rangle \\ &= \frac{1}{L\Delta}\sum_{p_1=1}^{2}\sum_{n_1=0}^{L/(2\Delta)}\sum_{p_2=1}^{2}\sum_{n_2=0}^{L/(2\Delta)} \left\langle z_{p_1,n_1}z_{p_2,n_2}\right\rangle \left(\sum_{i=0}^{L/\Delta} d\phi_{p_1,n_1}(i)d\phi_{p_2,n_2}(i)\right) \end{aligned} \tag{4.35}$$

where

$$\begin{aligned} &\sum_{i=0}^{L/\Delta} d\phi_{p_1,n_1}(i)d\phi_{p_2,n_2}(i) \\ =&\sum_{i=0}^{L/\Delta}\left(\phi_{p_1,n_1}(i+1)-\phi_{p_1,n_1}(i)\right)\left(\phi_{p_2,n_2}(i+1)-\phi_{p_2,n_2}(i)\right) \\ =&\frac{2}{L}\left(\sum_{i=0}^{L/\Delta}\left(\sin(\frac{2n_1\pi}{L/\Delta}(i+1))-\sin(\frac{2n_1\pi}{L/\Delta}i)\right)\left(\sin(\frac{2n_2\pi}{L/\Delta}(i+1))-\sin(\frac{2n_2\pi}{L/\Delta}i)\right)\right) \\ =&\frac{8}{L}\sin(\frac{n_1\pi}{L/\Delta})\sin(\frac{n_2\pi}{L/\Delta})\sum_{i=0}^{L/\Delta}\left(\cos(\frac{n_1\pi}{L/\Delta}(2i+1))\cos(\frac{n_2\pi}{L/\Delta}(2i+1))\right) \end{aligned} \tag{4.36}$$

or more compactly:

$$\begin{aligned}\left\langle m_{\Delta}^{2}(t)\right\rangle &= \frac{1}{L\Delta}\sum_{p_1=1}^{2}\sum_{n_1=0}^{L/(2\Delta)}\sum_{p_2=1}^{2}\sum_{n_2=0}^{L/(2\Delta)}\left\langle z_{p_1,n_1}z_{p_2,n_2}\right\rangle\left(\sum_{i=0}^{L/\Delta}d\phi_{p_1,n_1}(i)d\phi_{p_2,n_2}(i)\right)\\ &= \frac{1}{L\Delta}\sum_{p=1}^{2}\sum_{n=0}^{L/(2\Delta)}\left\langle z_{p,n}\right\rangle^{2}\left(\frac{8}{L}\sin^{2}(\frac{n\pi}{L/\Delta})\sum_{i=0}^{L/\Delta}\left(\cos^{2}(\frac{n\pi}{L/\Delta}(2i+1))\right)\right)\\ &= \sum_{p=1}^{2}\sum_{n=0}^{L/(2\Delta)}K_{p,n}\left\langle z_{p,n}^{2}\right\rangle\end{aligned} \tag{4.37}$$

where

$$\begin{aligned}K_{p,n} &= \frac{8}{L\Delta}\sin^{2}\left(\frac{\pi n}{L/\Delta}\right)\sum_{i=0}^{L/(2\Delta)}\left(\cos^{2}\left(\frac{n\pi}{L/\Delta}(2i+1)\right)\right)\\ &= \begin{cases}\dfrac{8}{L\Delta}\sin^{2}\left(\dfrac{\pi n}{L/\Delta}\right) & n=0\\ \dfrac{4}{L\Delta}\sin^{2}\left(\dfrac{\pi n}{L/\Delta}\right) & n\neq 0\end{cases}\end{aligned} \tag{4.38}$$

Finally, using that

$$\begin{aligned}&\sum_{i=0}^{L/(2\Delta)}\left(\cos^{2}\left(\frac{n\pi}{L/\Delta}(2i+1)\right)\right)\\ &\quad= \sum_{i=0}^{L/(2\Delta)}\left(\frac{\cos\left(2n\pi(2i+1)/(L/\Delta)\right)+1}{2}\right)\\ &\quad= \begin{cases}\dfrac{L}{\Delta} & \text{if } n=0\\ \\ \dfrac{L}{2\Delta} & \text{if } n\neq 0\end{cases}\end{aligned} \tag{4.39}$$

$\left\langle m_{\Delta}^{2}(t)\right\rangle$ can be expressed as:

$$\left\langle m^{2}(t)\right\rangle = \sum_{m=1}^{L/(2\Delta)}\left(K_{1,m}\left\langle z_{1,m}^{2}\right\rangle + K_{2,m}\left\langle z_{2,m}^{2}\right\rangle\right) \tag{4.40}$$

The expression of Eq. 4.40 will be used in the MPC formulation; please see Eq. 4.42 below.

4.3.4 Parameter estimation

Referring to the EW equation of Eq. 4.8, there are two model parameters, c_2 and σ^2 that must be determined as functions of the mean deposition rate w_0 and of the patterned deposition rate magnitude A. These parameters affect the dynamics of aggregate surface roughness and slope and can be estimated by fitting the predicted evolution profiles for aggregate surface roughness and slope from the EW equation to profiles of aggregate surface roughness and slope from kMC simulations. Least-square methods are used to estimate the model parameters so that the EW-model predictions are close in a least-square sense to the kMC simulation data. Comparison of the predictions of both models are shown in Fig. 4.10. It is necessary to point out that 20 groups of EW-equation-simulations are carried out with mean deposition rate w_0 ranging from $w_0 = 0.1$ layer/s to $w_0 = 2$ layer/s, but in Fig. 4.10 only five groups of simulation results are shown. Based on c_2 and σ^2 values obtained from these fitting results, polynomial functions are chosen to estimate c_2 and σ^2 values at different w_0 with the least-square method. Specifically, a fourth order polynomial function with respect to w_0 is chosen to estimate c_2 and a linear function is chosen to estimate σ^2, and the expressions are given as follows:

$$c_2(w) = a_{c_2} w^4 + b_{c_2} w^3 + c_{c_2} w^2 + d_{c_2} w + e_{c_2}, \tag{4.41}$$

$$\sigma^2 = a_{\sigma^2} w + b_{\sigma^2}$$

where a_{c_2}, b_{c_2}, c_{c_2}, d_{c_2}, e_{c_2}, a_{σ^2} and b_{σ^2} are time-invariant fitting model parameters. The fitting results are shown in Fig. 4.11 and Fig. 4.12, where $a_{c_2} = -0.0003$, $b_{c_2} = -0.0002$,

$c_{c_2} = 0.001$, $d_{c_2} = 0.0018$, $e_{c_2} = 0.001$, $a_{\sigma^2} = 0.8739$ and $b_{\sigma^2} = -0.0043$. These fitting results are based on kMC simulations with uniform deposition rate profiles ($A = 0$). For simulations with patterned deposition rate profiles ($A \neq 0$), it is assumed that c_2 and σ^2 models obtained from uniform deposition rate simulations ($A = 0$) can be used to estimate c_2 and σ^2 values. To verify this assumption, the solutions of EW equations for aggregate surface evolution with patterned deposition rate profile are obtained based on c_2 and σ^2 models from open-loop kMC data with uniform deposition rate, and these dynamic evolution profiles are compared with open-loop kMC dynamic evolution profiles with patterned deposition rate profiles. As shown in Fig. 4.13 and Fig. 4.14, c_2 and σ^2 models from open-loop kMC data with uniform deposition rate can be used in the EW equation to predict aggregate surface roughness and slope of the kMC model with patterned deposition rate. It is important to emphasize that the y–axes in Fig. 4.13 and Fig. 4.14 are logarithmic in order to make this comparison clear. We note that the approach presented for the computation of the parameters of the closed-form PDE model of Eq. 4.8 is not limited to the specific PDE system and can be used in the context of other dissipative PDE systems that model the evolution of surface height of deposition processes. Finally, referring to the dependence of surface roughness and slope on lattice size, we note that both atomic and aggregate surface roughness and slope increase with increasing lattice size (this issue has been extensively studied other works [24, 23]); however, the proposed approach to closed-form modeling and MPC design is scalable and can be used in the context of different lattice size as long as the parameters of the stochastic PDE model of Eq. 4.8 and their dependence on deposition

rate are computed on the basis of data obtained from the lattice size considered.

4.4 Model predictive control

In this section, we design a model predictive controller based on the dynamic models of aggregate surface roughness and slope to simultaneously control the expected values of aggregate surface roughness and slope square to desired levels. The dynamics of aggregate surface roughness and slope of the thin film are described by the EW equation of aggregate surface height of Eq. 4.8 with the computed parameters of subsection 4.3.4. State feedback control is considered in this work, i.e., $h_\Delta(x,t)$ is assumed to be available for feedback. In practice, real-time surface height measurements can be obtained via atomic force microscopy (AFM) systems.

4.4.1 MPC formulation for regulation of aggregate roughness and slope

We consider the problem of regulation of aggregate surface roughness and slope to desired levels within a model predictive control framework. Due to the stochastic nature of the variables, the expected values of aggregate surface roughness and slope, $\left\langle r_\Delta^2(t)\right\rangle$ and $\left\langle m_\Delta^2(t)\right\rangle$, are chosen as the control objectives. The mean deposition rate, w_0, and magnitude of patterned deposition rate, A, are chosen as the manipulated inputs; the substrate temperature is fixed at $T = 480K$ during all closed-loop simulations. To account for a number of practical considerations, several constraints are added to the control problem.

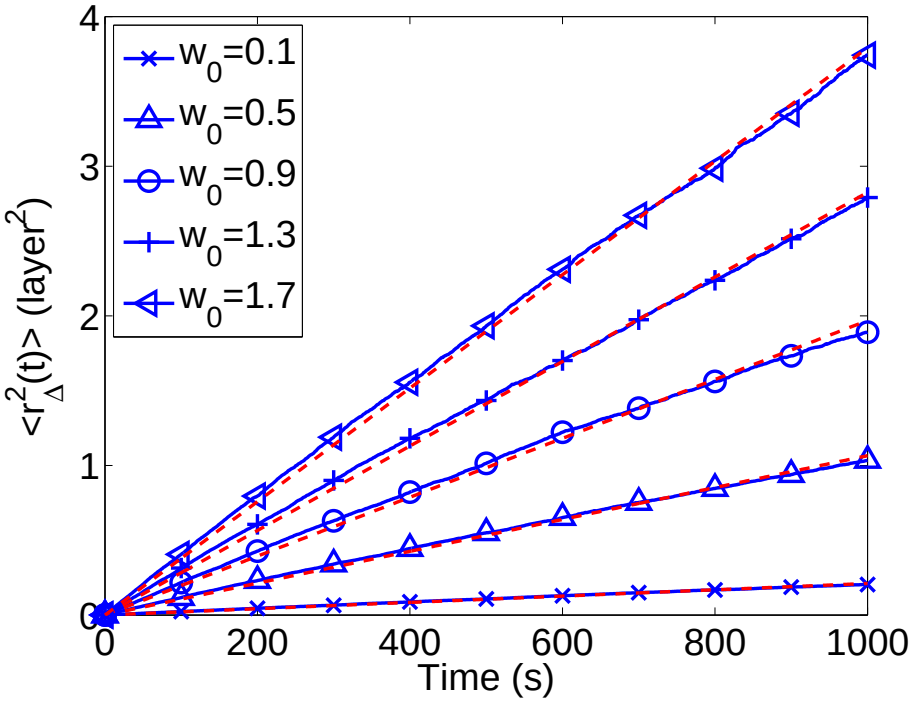

Figure 4.10: Evolution of expected aggregate surface roughness with respect to time for different spatially-uniform deposition rates obtained from kMC simulations (solid lines with symbols).The analytical solutions for the aggregate surface roughness obtained from the corresponding EW equations with the fitted values for c_2 and σ^2 are also shown (dashed lines).

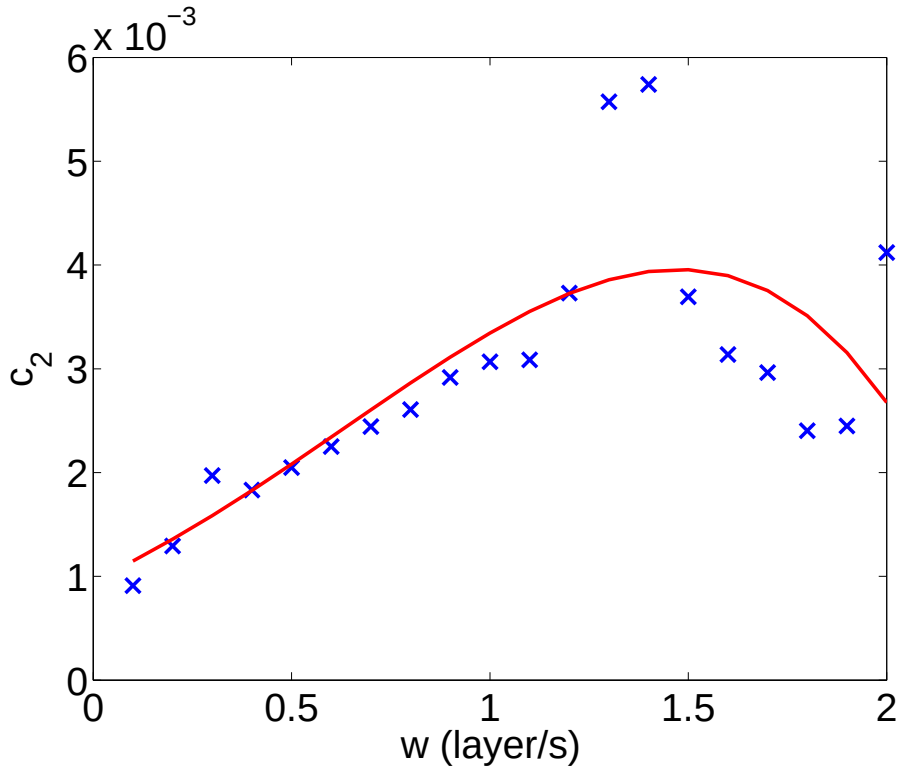

Figure 4.11: c_2 values for different spatially-uniform deposition rates w. The solid line is the result of a fourth-order polynomial fitting function and it is the c_2 versus w relationship used by the predictive controller.

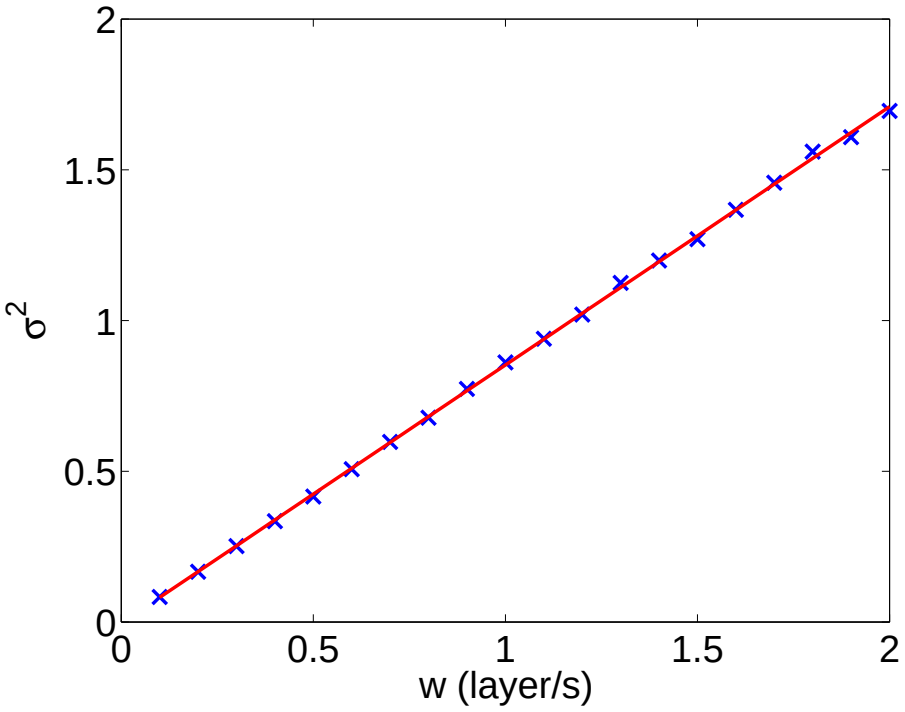

Figure 4.12: σ^2 values for different spatially-uniform deposition rates w. The solid line is the result of a linear fitting function.

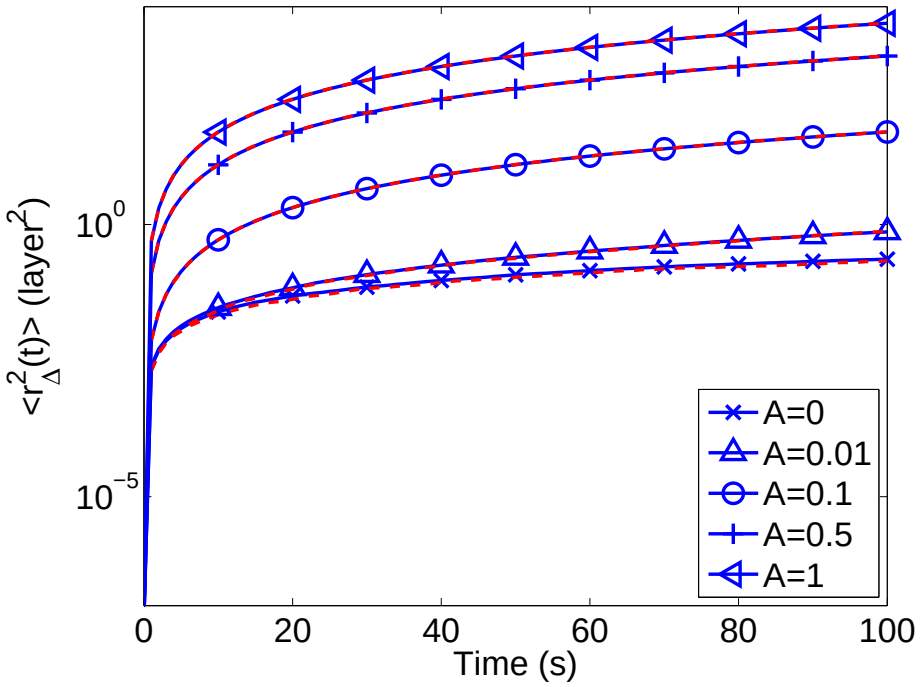

Figure 4.13: Evolution of expected aggregate surface roughness for different patterned deposition magnitudes from the kMC model (solid lines with symbols) and expected aggregate roughness solutions from the corresponding EW equations (dashed lines). The c_2 and σ^2 values of the EW equations were estimated from open-loop aggregate surface roughness kMC model data with spatially-uniform deposition rates.

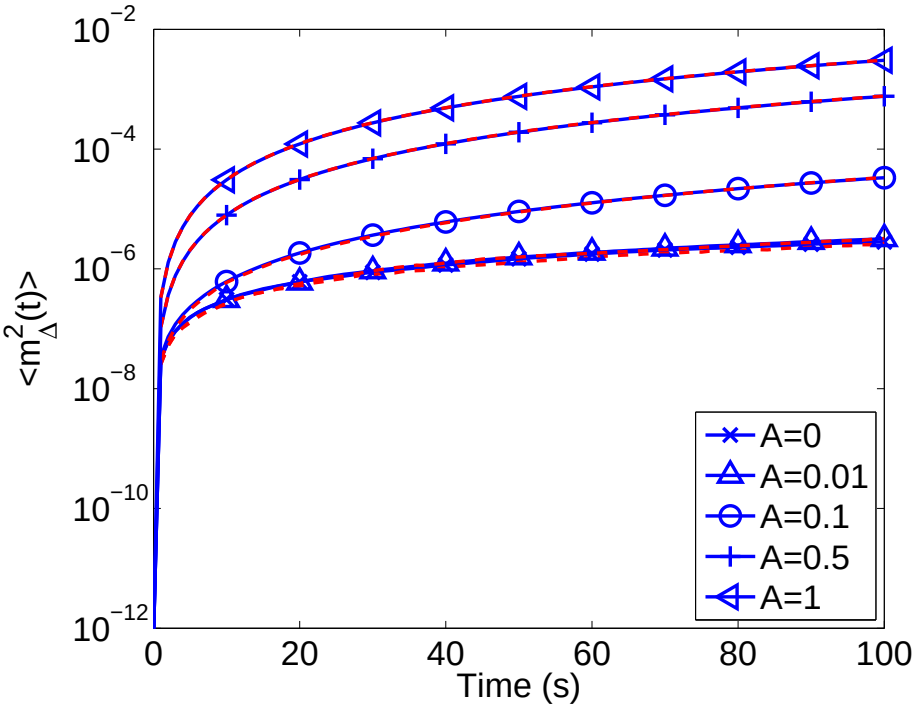

Figure 4.14: Evolution of expected aggregate surface slope for different patterned deposition magnitudes from the kMC model (solid lines with symbols) and expected aggregate slope solutions from the corresponding EW equations (dashed lines). The c_2 and σ^2 values of the EW equations were estimated from open-loop aggregate surface roughness kMC model data with spatially-uniform deposition rates.

In particular, since $w(x) \geq 0$, the constraint $0 \leq A \leq w_0$ is imposed to ensure $w(x,t) > 0$, $\forall(x,t)$. To ensure the validity of the closed-form process model, there is a constraint on the range of variation of the mean deposition rate. Another constraint is imposed on the rate of change of the mean deposition rate to account for actuator limitations. The control action at time t is obtained by solving a finite-horizon optimal control problem. The cost function in the optimal control problem includes penalty on the deviation of $\left\langle r_\Delta^2 \right\rangle$ and $\left\langle m_\Delta^2 \right\rangle$ from their respective set-point values. Different weighting factors are assigned to the aggregate surface roughness and slope. Aggregate surface roughness and slope have very different magnitudes, ($\left\langle r_\Delta^2 \right\rangle$ ranges from 10^2 to 10^4 and $\left\langle m_\Delta^2 \right\rangle$ ranges from 10^{-5} to 10^{-2}). Therefore, relative deviations are used in the formulation of the cost function to make the magnitude of the two terms comparable in the cost function. The optimization problem is subject to the dynamics of the aggregate surface height of Eq. 4.8. The optimal w_0 and A values are calculated at each sampling time by solving a finite-dimensional optimization problem in a receding horizon fashion. Specifically, the MPC problem at time t is formulated as follows:

$$\min_{w_0,A} f(w_0,A) = q_{r^2}\left[\frac{r_{set}^2 - \left\langle r_\Delta^2(t_f)\right\rangle}{r_{set}^2}\right]^2 + q_{m^2}\left[\frac{m_{set}^2 - \left\langle m_\Delta^2(t_f)\right\rangle}{m_{set}^2}\right]^2 \tag{4.42}$$

where

$$\left\langle r_\Delta^2(t_f)\right\rangle = \frac{1}{L}\sum_{n=1}^{L/(2\Delta)}\sum_{p=1}^{2}\left\langle z_{p,n}^2(t_f)\right\rangle, \quad \left\langle m_\Delta^2(t_f)\right\rangle = \sum_{n=1}^{L/(2\Delta)}\sum_{p=1}^{2}\left(K_{p,n}\left\langle z_{p,n}^2(t_f)\right\rangle\right) \tag{4.43}$$

$$\left\langle z_{p,n}^2(t_f)\right\rangle = \mathrm{var}(z_{p,n}(t_f)) + \left\langle z_{p,n}(t_f)\right\rangle^2 \tag{4.44}$$

$$\left\langle z_{p,n}(t_f)\right\rangle = e^{\lambda_n(t_f-t)}\left\langle z_{p,n}(t)\right\rangle + \frac{w_p}{\lambda_n}(e^{\lambda_n(t_f-t)}-1) \tag{4.45}$$

$$\mathrm{var}(z_{p,n}(t_f)) = e^{2\lambda_n(t_f-t)}\,\mathrm{var}(z_{p,n}(t)) + \sigma^2(w)\frac{e^{2\lambda_n(t_f-t)}-1}{2\lambda_n} \tag{4.46}$$

$$\lambda_n = -\frac{4c_2(w)\pi^2}{L^2}n^2 \tag{4.47}$$

and

$$c_2(w) = a_{c_2}w^4 + b_{c_2}w^3 + c_{c_2}w^2 + d_{c_2}w + e_{c_2} \tag{4.48}$$

$$\sigma^2(w) = a_{\sigma^2}w + b_{\sigma^2} \tag{4.49}$$

subject to:

$$w_{min} \le w_0 \le w_{max}, \quad |w_0(t) - w_0(t-dt)| \le \delta w_{max}, \tag{4.50}$$

$$w = w_0 + A\sin\left(\frac{k\pi x}{L}\right), \quad 0 \le A \le w_0 \tag{4.51}$$

where t is the current time, dt is the sampling time, q_{r^2} and q_{m^2} are the weighting penalty factors for the deviations of $\left\langle r_\Delta^2\right\rangle$ and $\left\langle m_\Delta^2\right\rangle$ from their respective set-points at the ith prediction step, w_{min} and w_{max} are the lower and upper bounds on the mean deposition rate, respectively, and δw_{max} is the limit on the rate of change of the mean deposition rate. Given the batch nature of the deposition process, the MPC of Eq. 4.42 includes penalty on the discrepancy of the expected surface roughness and slope at the end of the deposition from the set-points values of surface roughness and slope that lead to desired film reflectance levels.

The optimal control actions are obtained from the solution of the multivariable optimization problem of Eq. 4.42, and are applied to the deposition process model over dt (i.e.,

either the EW equation model or the kMC model) during the time interval $(t, t+dt)$. At time $t+dt$, a new measurement of aggregate surface roughness and slope is received by the controller and the MPC problem of Eq. 4.42 is solved for the next set of control actions. An interior point method optimizer, IPOPT [51], is used to solve the optimization problem in the MPC formulation. With respect to the stability of the closed-loop system, we note the following: the deposition process considered including atom adsorption and atom migration is an inherently stable process; this is evident by the negative values of all the eigenvalues of the spatial differential operator of the Edwards-Wilkinson-type equation (Eq. 4.8) used to model the evolution of surface height for all values of the deposition rare. Given this stability property of the open-loop process and the specific MPC design, the stability of the closed-loop system is ensured.

4.5 Simulation results

In this section, the model predictive controller of Eq. 4.42 is applied to both the one-dimensional EW equation type model of Eq. 4.8 and the one-dimensional kMC model of the thin film growth process. The mean deposition rate ranges from 0.1 to 2 layer/s, the substrate temperature is fixed at 480K, the lattice size of the kMC model is fixed at 40,000 sites, the aggregation size is fixed at 400 to make the results relevant to thin film solar cell applications and five sine waves are used in the patterned deposition rate profile. The sampling time is 5 s; this sampling time is enough for the MPC to carry out the calculations needed to compute the control action. In addition to the deposition rate, the temperature

may be used as a manipulated input but it should vary in space to induce substantial aggregate surface roughness and slope values at spatial scales corresponding to the visible light wavelength. Each closed-loop simulation lasts for 100 s. Expected values are calculated from 100 independent closed-loop system simulation runs. In all the simulations, the aggregate surface roughness and slope set-points remain the same, specifically, $r^2_{set} = 10000$ and $m^2_{set} = 0.002$.

4.5.1 MPC application to EW equation model

In this subsection, the EW equation model is utilized in the closed-loop control problem as the plant model. First, the problem of regulating aggregate surface roughness is considered. In this problem, the cost function has only penalty on the deviation of the expected aggregate surface roughness square from its set-point, *i.e.*, $q_{r^2} = 1$ and $q_{m^2} = 0$. Fig. 4.15 shows the evolution profile of $\left\langle r^2_\Delta(t) \right\rangle$ under the model predictive controller of Eq. 4.42. It is clear that the controller drives the expected aggregate surface roughness to its set-point at the end of the simulation. Fig. 4.16 shows the input profiles of w_0 and A for these simulations. It is necessary to point out that during the first half of the simulation time, the optimal solutions of w_0 are constrained by the rate of change constraint and the optimal solutions of A are bounded by the values of w_0.

Next, the aggregate surface slope is regulated. The cost function includes only penalty on the deviation of the expected value of aggregate surface slope square from its set-point ($q_{m^2} = 1$, $q_{r^2} = 0$). Fig. 4.17 shows the evolution profile of the expected aggregate slope

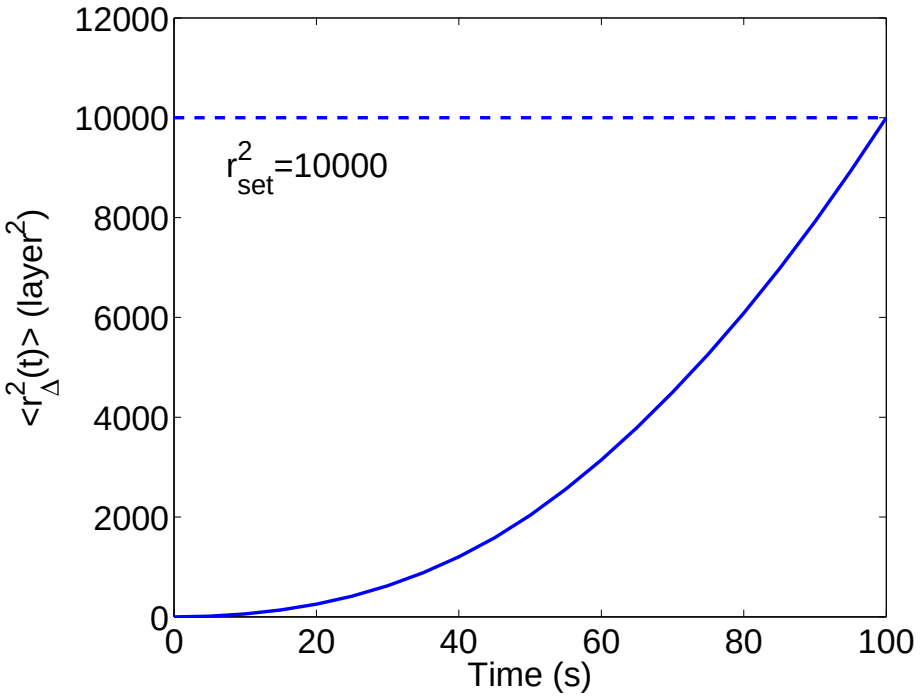

Figure 4.15: Profile of expected aggregate surface roughness square with EW equation as the plant model. $q_{r^2} = 1$, $q_{m^2} = 0$ and $r^2_{set} = 10000$.

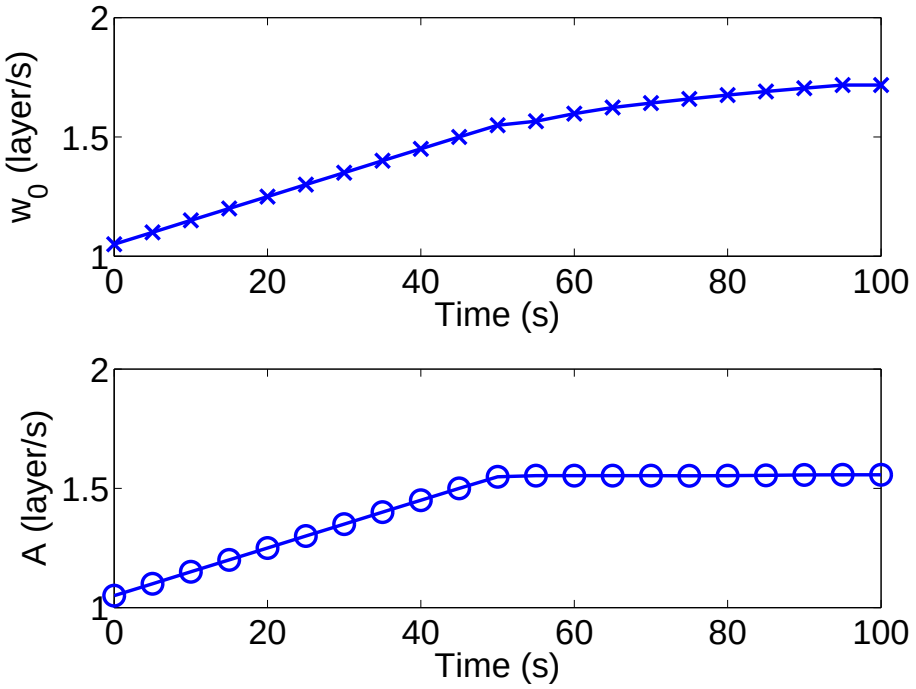

Figure 4.16: Input profiles for aggregate roughness-only control problem with EW equation as the plant model. $q_{r^2} = 1$, $q_{m^2} = 0$ and $r_{set}^2 = 10000$.

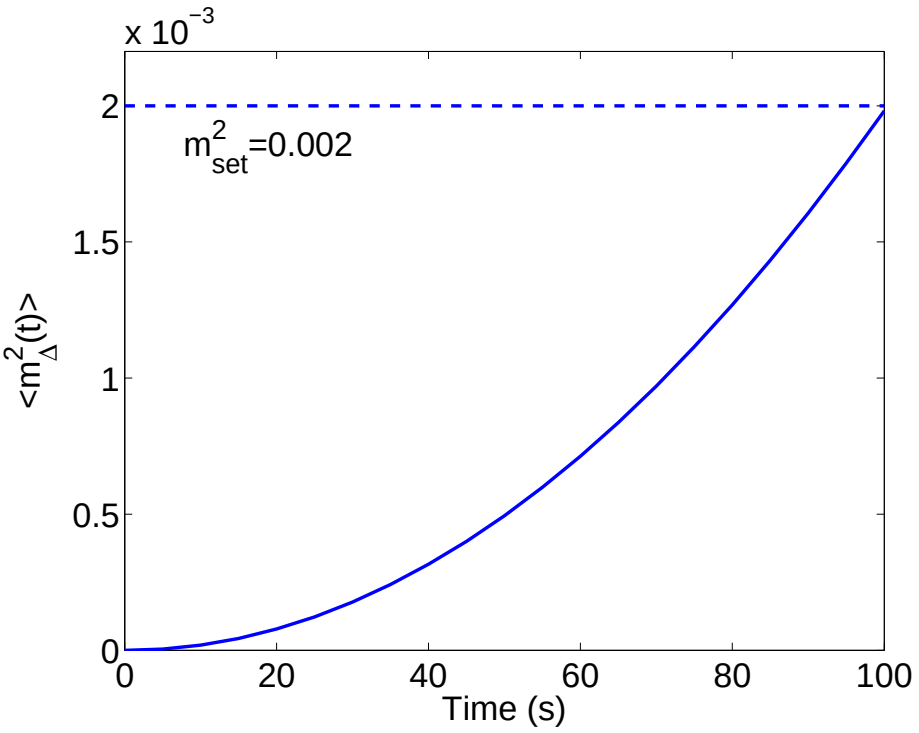

Figure 4.17: Profile of expected aggregate surface slope square with EW equation as the plant model. $q_{r^2} = 0$, $q_{m^2} = 1$ and $m^2_{set} = 0.002$.

square. The aggregate slope reaches its set-point at $t = 100s$. Fig. 4.18 displays the input profile in this scenario. Compared with Fig. 4.16, the controller requires less time to find the input values needed to reach the desired slope value.

The next step is the simultaneous regulation of aggregate surface roughness and slope. The weighting factor of aggregate slope square, q_{m^2}, is kept at 1, while the weighting factor of aggregate roughness square, q_{r^2}, increases from 10^{-2} to 10^3. Fig. 4.19 shows the values of expected aggregate surface roughness and slope at the end of closed-loop simulations ($t_f = 100$s) as a function of q_{r^2}/q_{m^2}. It can be seen that as the weighting on aggregate

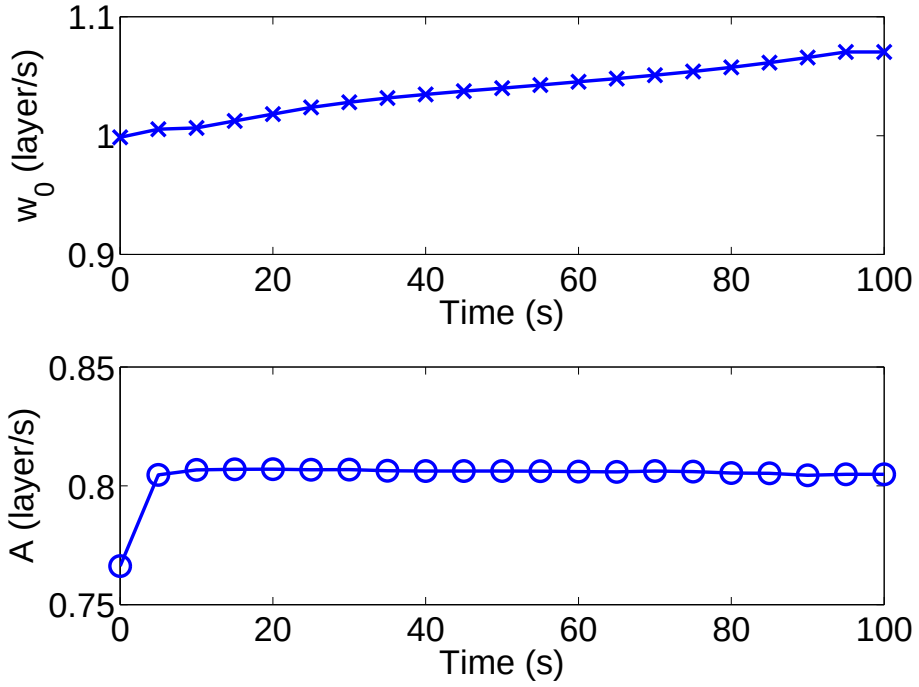

Figure 4.18: Input profiles for aggregate slope-only control problem with EW equation as the plant model. $q_{r^2} = 0$, $q_{m^2} = 1$ and $m^2_{set} = 0.002$.

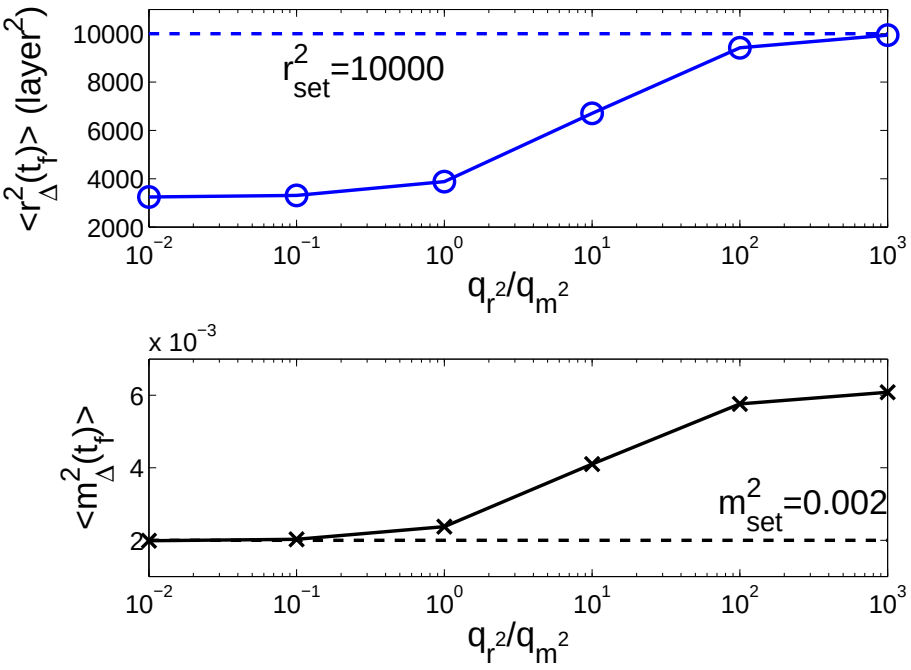

Figure 4.19: $\left\langle r^2_\Delta(t_f)\right\rangle$ and $\left\langle m^2_\Delta(t_f)\right\rangle$ at the end of closed-loop simulations ($t = 100s$) for different penalty weighting factors in the predictive controller with EW equation as the plant model. $10^{-2} \leq q_{r^2} \leq 10^3$, $q_{m^2} = 1$, $r^2_{set} = 10000$ and $m^2_{set} = 0.002$.

roughness increases, the expected value of aggregate roughness approaches its set-point at the cost of larger deviation of the aggregate slope from its set-point.

4.5.2 MPC application to kMC model

In this subsection, the kMC model is used in the closed-loop control problem as the plant model, while all the other settings remain the same. Fig. 4.20 shows the aggregate surface roughness in the case of roughness-only control while Fig. 4.21 shows the aggregate surface slope in the case of slope-only control. From both plots, we see that both aggre-

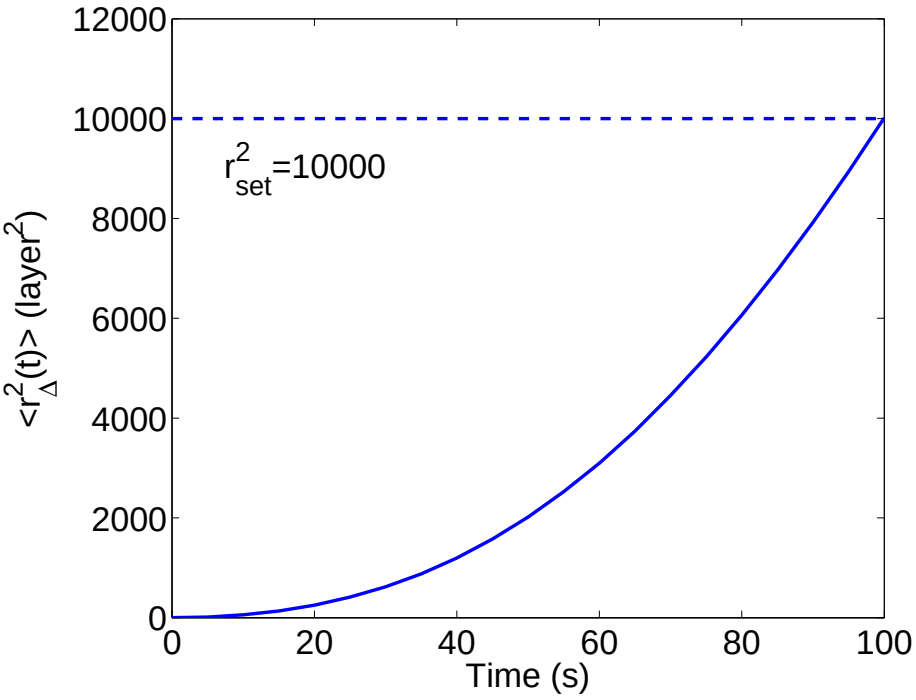

Figure 4.20: Profile of expected aggregate surface roughness square with kMC model as the plant model. $q_{r^2} = 1$, $q_{m^2} = 0$ and $r^2_{set} = 10000$.

gate roughness and slope successfully reach their set-points at the end of the simulations. Furthermore, the closed-loop evolution profiles with kMC as the plant model are very similar to the closed-loop profiles that use the EW equation as the plant model, which implies that the EW equation model used in this work can accurately predict the kMC simulation results.

Simultaneous regulation of aggregate surface roughness and slope has also been investigated. Similar to the case where the EW equation is used as the plant model, the weighting factor of aggregate slope square, q_{m^2}, is kept at 1, and the weighting factor of

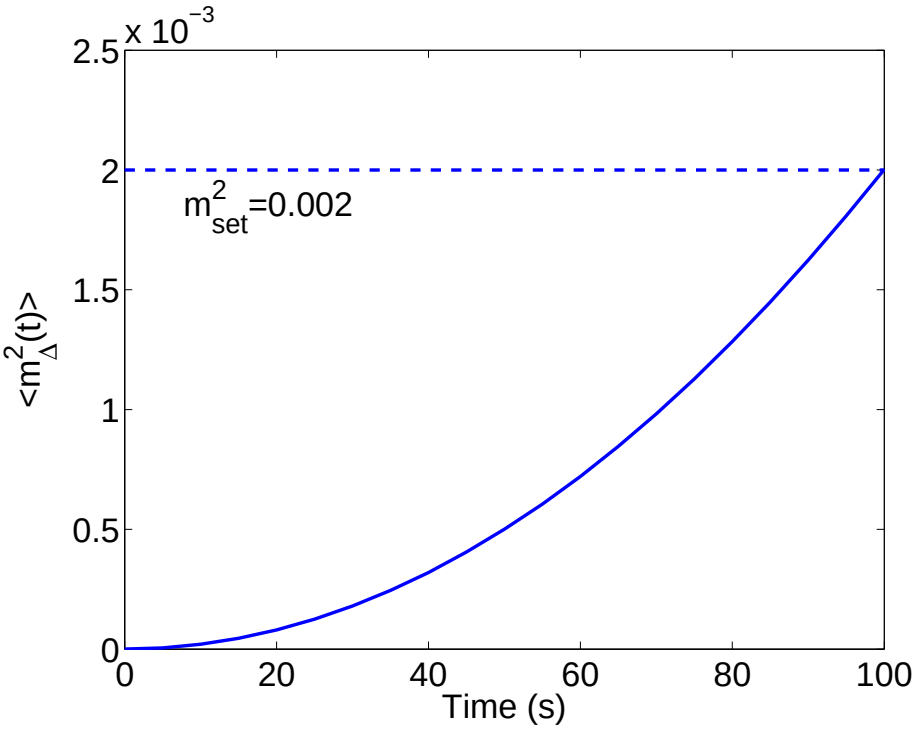

Figure 4.21: Profile of expected aggregate surface slope square with kMC model as the plant model. $q_{r^2} = 0$, $q_{m^2} = 1$ and $m^2_{set} = 0.002$.

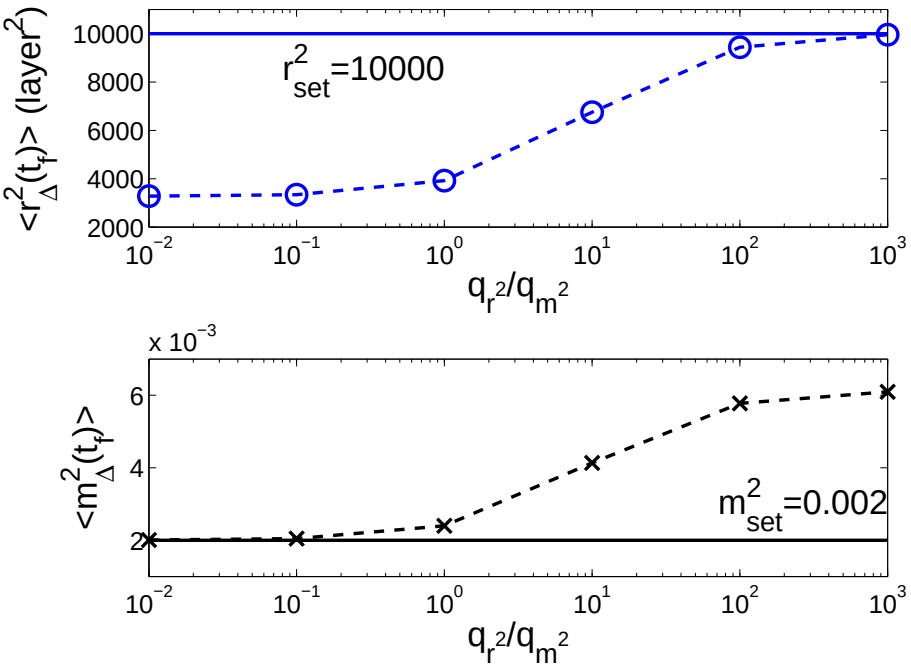

Figure 4.22: $\left\langle r^2_\Delta(t_f)\right\rangle$ and $\left\langle m^2_\Delta(t_f)\right\rangle$ at the end of closed-loop simulations ($t = 100s$) for different penalty weighting factors in the predictive controller with kMC model as the plant model. $10^{-2} \leq q_{r^2} \leq 10^3$, $q_{m^2} = 1$, $r^2_{set} = 10000$ and $m^2_{set} = 0.002$.

aggregate roughness square, q_{r^2}, ranges from 10^{-2} to 10^3. Fig. 4.22 shows the values of expected aggregate roughness and slope at the end of simulations as a function of q_{r^2}/q_{m^2}. It can be seen that the expected value of aggregate roughness approaches its set-point as q_{r^2} increases at the cost of larger deviation of the aggregate slope from its set-point.

4.5.3 Application to light trapping efficiency

In this subsection, we demonstrate an application of the proposed modeling and control framework to improve thin film solar cell performance. When the incident light goes

through a rough interface, the light is divided into four components: specular reflection, specular transmission, diffused reflection, and diffused transmission [45, 33]. The total reflectance of a beam of monochromatic light at normal incidence to a rough surface, which is denoted by R, can be approximately calculated as follows [9]:

$$\begin{aligned} R = \quad & R_0 \exp\left(-\frac{4\pi r_\Delta^2}{\lambda^2}\right) + \\ & R_0 \int_0^{\pi/20} 2\pi^4 \left(\frac{a_\Delta}{\lambda}\right)^2 \left(\frac{r_\Delta}{\lambda}\right)^2 (\cos\theta + 1)^4 \sin\theta \exp\left[-\frac{(\pi a \sin\theta)^2}{\lambda^2}\right] d\theta \end{aligned} \tag{4.52}$$

where R_0 is the reflectance of a perfectly smooth surface of the same material, λ is the light wavelength, a_Δ is the auto-covariance length of the interface, which can be rewritten as a ratio between the aggregate roughness and aggregate slope as $a_\Delta = \sqrt{2} r_\Delta / m_\Delta$ [2], and θ is the incident angle. Eq. 4.52 is only valid when θ is small [9], so the integration upper limit of θ is assumed to be $\pi/20$. Furthermore, aggregate roughness and slope at aggregation length $\Delta = 400$ are used in Eq. 4.52.

Fig. 4.23 shows how films with different reflectance values can be produced by simultaneous regulation of film surface aggregate roughness and aggregate slope. Specifically, the weighting factor of aggregate slope square, q_{m^2}, is kept at 1, and the weighting factor of aggregate roughness square, q_{r^2}, ranges from 10^{-2} to 10^3, and the resulting aggregate roughness and slope are used to compute the light reflectance of the thin film according to Eq. 4.52. It is clear that films with different reflectance values can be generated by regulating aggregate surface roughness and slope; please see the small circles in Fig. 4.23.

Remark 4.1 *Referring to the model predictive controller of Eq. 4.42, we note that in the absence of measurement feedback it can still be used to compute in an open-loop fashion an*

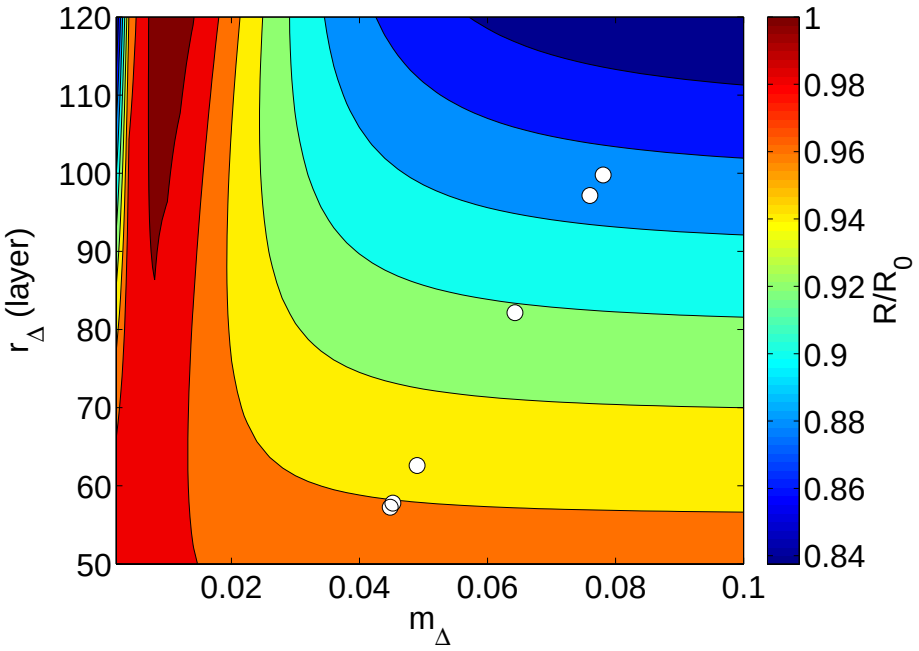

Figure 4.23: Light reflectance of thin films deposited under closed-loop operations with different weighting factor ratios. $q_{r^2} = 10^{-2}$, 10^{-1}, 10^{0}, 10^{1}, 10^{2} and 10^{3} (corresponding to small circles inside the figure from left to right), $q_{m^2} = 1$, $r^2_{set} = 10000$ and $m^2_{set} = 0.002$.

input trajectory for manipulating the deposition rate profile to drive the surface roughness and slope to desired levels at the end of the deposition; however, such an approach is inherently non-robust to process disturbances and model uncertainty owing to the lack of feedback. Furthermore, when measurements of the film surface height are available at specific locations across the film surface, a state estimator based on the stochastic PDE model can be used to provide estimates of the entire film thickness; these estimated can be subsequently used in the model predictive controller of Eq. 4.42. Finally, we note that even though the controller of Eq. 4.42 focuses on the regulation of surface roughness and slope at desired levels, it is possible to incorporate in the controller additional objectives like, for example, achieving a desired film thickness; this can be done by the incorporation of additional thickness requirement constraints in the controller to ensure that the deposition rate is above a certain value that ensures that final film thickness is achieved at the end of the deposition that meets the specifications.

Chapter 5

Simulation and Control of Aggregate Surface Morphology in a Two-Stage Thin Film Deposition Process for Improved Light Trapping

5.1 Introduction

This chapter focuses on the development of a model predictive control (MPC) algorithm to simultaneously regulate the aggregate surface slope and roughness of a two-stage thin film growth process to optimize thin film light reflectance and transmittance. In the first stage of the process, a uniform deposition rate profile is utilized and in the second stage of the

deposition process, a spatially distributed deposition profile is used to carry out the simulation. Initially, a two-stage thin film deposition process is modeled on a one-dimensional solid-on-solid square lattice that involves an adsorption process and a migration process in the microscopic scale using kMC methods. An Edwards-Wilkinson (EW)-type equation (second-order stochastic partial differential equation) is used to describe the dynamics of the aggregate surface height profile obtained form the kMC model and predict the evolution of the aggregate rms roughness and aggregate rms slope. A model predictive control algorithm is then developed on the basis of the dynamic equation model to regulate the aggregate rms slope and the aggregate rms roughness at desired levels. Closed-loop simulation results demonstrate the effectiveness of the proposed model predictive control algorithm in successfully regulating the aggregate rms slope and the aggregate rms roughness at desired levels that optimize thin film light reflectance and transmittance.

5.2 Two-stage thin film deposition process modeling

In this section, an on-lattice kMC model is introduced to simulate the two-stage thin film growth process. Aggregate surface height profile, aggregate rms roughness, and aggregate rms slope are defined on the basis of the surface micro-configuration of the thin film. An EW-type equation model is then constructed to describe the dynamics of the surface height profile.

5.2.1 Two-stage thin film deposition: on-lattice kinetic Monte Carlo model and variable definitions

The two-stage thin film deposition process considered in this work takes place on a one-dimensional solid-on-solid square lattice with periodic boundary conditions (PBCs), as shown in Fig. 5.1. In this thin film deposition process, two different micro-processes significantly influence the thin film surface morphology [52, 53]: an adsorption process and a migration process. In an adsorption process, vertically incident particles are deposited from the gas phase into the thin film. In a migration process, particles on the thin film overcome the energy barriers of the sites and move to neighboring vacant sites with probabilities that obey an Arrhenius-type rate law. In the first state of this deposition process, uniform adsorption rate (in the unit of laryer/s) is used to carry out the simulation, i.e.,

$$w(x) = w_{fix} \tag{5.1}$$

where $x \in [0, L]$ is the position along the lattice, L is the lattice size and in this work $L = 40000$, and w_{fix} is the uniform adsorption rate in this stage. The simulation time for the first stage of the deposition process is denoted as t_{fix}. In the second stage of this deposition process, a spatially distributed deposition rate profile is utilized, i.e.,

$$w(x) = w_0 + \sum_{i=1}^{m} A_i \sin\left(\frac{2\pi k_i x}{L}\right) \tag{5.2}$$

where w_0 is the average adsorption rate (in the unit of layer/s), A_i is the amplitude of sine waves and it is requested that $0 \leq \sum_{i=1}^{m} A_i \leq w_0$ to ensure that $w(x) \geq 0$, $\forall x \in [0, L]$, k_i is the

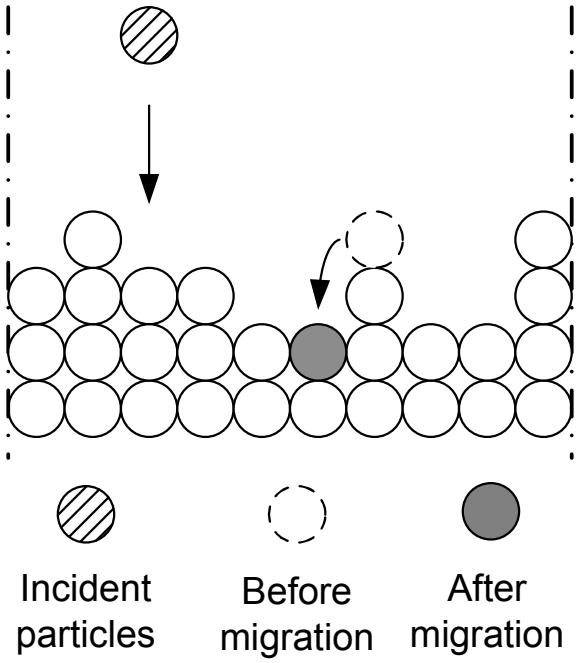

Figure 5.1: Thin film growth process on a solid-on-solid one-dimensional square lattice.

frequency of a sine wave and L is the lattice size. The innovation of introducing the spatially distributed deposition rate profile was introduced in [27]. The average adsorption rate and the amplitude value are the macroscopic variables that can be used as the manipulated variables for control purposes. By introducing the two-stage deposition model, the thickness of the thin film can be manipulated during the first stage and the surface morphology of the thin film can be shaped during the second stage. Throughout this work, Eq. 5.2 will be used with $m = 2$.

After the introduction of the two-stage thin film deposition process, two variables, aggregate rms surface roughness and slope, are precisely defined to characterize the film aggregate surface morphology which is represented by the aggregate surface height profile. The aggregate rms surface roughness and aggregate rms surface slope can be then defined

as the root-mean-square of the aggregate surface height profile and the aggregate height slope profile, respectively, as follows:

$$r_\Delta = \left[\frac{1}{L/\Delta} \sum_{i=1}^{L/\Delta} (h_{\Delta,i} - \bar{h}_\Delta)^2 \right]^{1/2}, \tag{5.3}$$

$$m_\Delta = \left[\frac{1}{L/\Delta} \sum_{i=1}^{L/\Delta} \left(\frac{h_{\Delta,i} - h_{\Delta,i+1}}{\Delta} \right)^2 \right]^{1/2} \tag{5.4}$$

where r_Δ denotes the aggregate rms surface roughness, m_Δ denotes the aggregate rms slope, $h_{\Delta,i}, i = 1,2,\ldots,L/\Delta$, are the aggregate surface height (with a unit of layer) and $\bar{h}_\Delta = \frac{1}{L} \sum_{j=1}^{L} h_j, j = 1,1,\ldots,L$, is the average surface height and L is the lattice size on the lateral direction. Due to the use of PBCs, we have that, $h_{\Delta,L+1} = h_{\Delta,1}$.

5.2.2 Spatially distributed deposition rate profile

To improve the performance of the two-stage deposition process, a spatially distributed deposition rate profile is introduced in the second stage of the deposition process [28]. Specifically, in the second stage of the deposition process, a spatially distributed deposition rate profile with two sine waves is introduced to carry out the deposition,

$$w(x) = w_0 + A_1 \sin\left(\frac{2\pi k_1 x}{L}\right) + A_2 \sin\left(\frac{2\pi k_2 x}{L}\right) \tag{5.5}$$

where k_1 and k_2 are the frequencies of the two sine wave functions. It is necessary to note that the amplitude values for both sine wave functions should satisfy $0 \leq A_1 + A_2 \leq w_0$.

To explore the properties of this spatially distributed deposition rate profile with multiple sine waves, a series of simulations are carried out at different amplitude values with

$k_1 = 5$, $k_2 = 10$, $w_0 = 20$ layer/s, $L = 40000$ and $A_1 = A_2 = A$ where $A \in [0, 10]$ layer/s. In this series of simulations, the simulation time for the first stage (the stage with uniform deposition rate profile) is zero ($t_{fix} = 0$ s). Fig. 5.2 shows a snapshot of one of these simulations with $A_1 = A_2 = A = 5$ layer/s. It is clear that the introduction of multiple sine waves changes the shape of the thin film surface and provides more potential to design and control the surface morphology of silicon thin film and improve the performance of thin film solar cells. To further explore its application in improving thin film solar cells, reflectance values are calculated with aggregate roughness and slope values obtained from these simulations; the results are mapped in Fig. 5.3. R_0 in the plot is the light reflectance of a perfectly smooth surface. Light reflectance of thin films deposited with different A values ($A \in [0, 10]$ layer/s) and spatially distributed deposition rate profiles with ($k_1 = 5$, $k_2 = 0$) and ($k_1 = 0$, $k_2 = 10$) are also mapped in the plot. It is clear that different reflectance values can be generated by utilizing spatially distributed deposition rate profile with multiple sine waves.

5.2.3 Closed-form dynamic model construction

The dynamics and evolution of the aggregate surface height profile, as well as of the aggregate rms roughness and slope, of the thin film of Fig. 5.1 can be described by an Edwards-Wilkinson (EW)-type equation of the form [10, 11, 24]:

$$\frac{\partial h_\Delta}{\partial t} = w(x,t) + c_2 \frac{\partial^2 h_\Delta}{\partial x^2} + \xi(x,t), \tag{5.6}$$

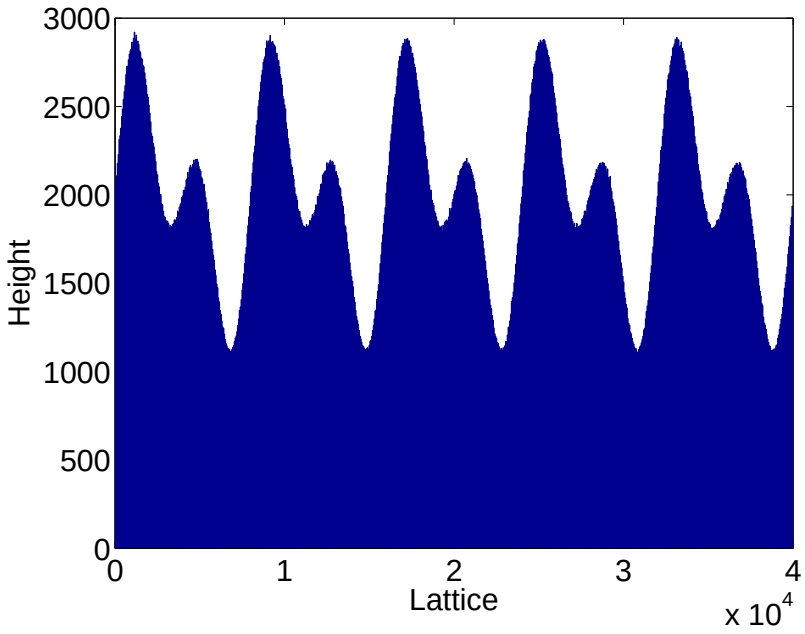

Figure 5.2: Snapshot of thin-film with $A_1 = A_2 = A = 5$ layer/s, $k_1 = 5$, $k_2 = 10$, $w_0 = 20$ layer/s and $L = 40000$.

subject to the initial condition and the following PBCs:

$$h_\Delta(0,t) = h_\Delta(L,t), \quad \frac{\partial h_\Delta}{\partial x}(0,t) = \frac{\partial h_\Delta}{\partial x}(L,t), \tag{5.7}$$

where $w(x,t)$ is the deposition rate profile. Specifically, in the first stage of the deposition process, $w(x,t) = w_{fix}(t)$ and in the second stage,

$$w(x,t) = w_0(t) + A_1(t)\sin\left(\frac{2\pi k_1 x}{L}\right) + A_2(t)\sin\left(\frac{2\pi k_2 x}{L}\right)$$

where $x \in [0,L]$ is the aggregate spatial coordinate, t is the time, c_2 is the model parameter related to the effect of surface particle migration, and $\xi(x,t)$ is a Gaussian white noise term with a zero mean and a covariance as $\langle \xi(x,t)\xi(x',t')\rangle = \sigma^2\delta(x-x')\delta(t-t')$, where σ^2 is a parameter that measures the noise intensity and $\sigma(\cdot)$ denotes the standard Dirac delta

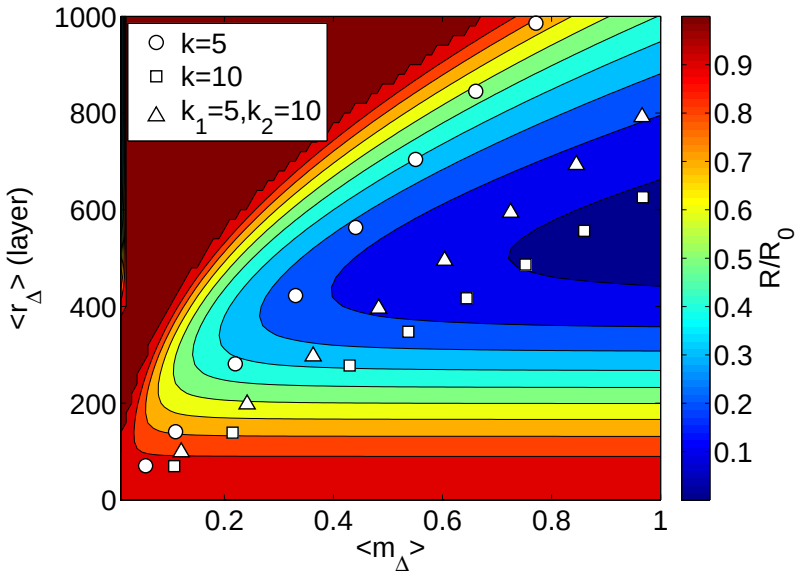

Figure 5.3: Light reflectance of thin film deposited with spatially distributed deposition rate profiles of varying complexity with ($k_1 = 5$, $k_2 = 0$), ($k_1 = 0$, $k_2 = 10$) and ($k_1 = 5$, $k_2 = 10$). Circles are reults with $k_1 = 5$ and $k_2 = 0$; Squares are results with $k_1 = 0$ and $k_2 = 10$; Triangles are results with $k_1 = 5$, $k_2 = 10$. $A_1 = A_2 = A$ and $A \in [0, 10]$ layer/s.

function. These model parameters, c_2 and σ^2, can be estimated on the basis of the kMC simulation data of the thin film deposition process in a least-square sense. It is necessary to note that the initial condition for the first stage of simulation is $h_{\Delta,1}(x,0) = 0$ and the initial condition for the second stage of simulation is the final condition of the first stage, $h_{\Delta,2}(x,0) = h_{\Delta,1}(x,t_{fix})$.

To obtain the dynamics of the aggregate rms roughness and of the aggregate rms slope, the EW equation is first decomposed into a stochastic system of infinite ODEs as follows [27]:

$$\frac{dz_{2,0}}{dt} = w_{2,0} + \xi_{2,0}(t), \tag{5.8}$$

$$\frac{dz_{p,n}}{dt} = w_{p,n} + \lambda_n z_{p,n} + \xi_{p,n}(t), \tag{5.9}$$

$$p = 1,2, \quad n = 1,\ldots,\frac{L}{2\Delta},$$

where λ_n denotes the $n-th$ eigenvalue of the linear second-order operator of Eq. 5.6, $z_{p,n}(t)$ is the state projection of $h_\Delta(x,t)$ in the $n-th$ ODE, and similarly the $\xi_{p,n}$ and $w_{p,n}$ are the projection of noise and $w(x,t)$ on the $n-th$ ODE [27], the value of $w_{p,n}$ is shown as follows:

- If $p = 1$,

$$w_{1,n} = \begin{cases} A\sqrt{\frac{L}{2}}, & n = k_1 \\ A\sqrt{\frac{L}{2}}, & n = k_2 \\ 0, & \text{else} \end{cases} \tag{5.10}$$

- If $p = 2$

$$w_{2,n} = \begin{cases} 0, & n \neq 0 \\ A\sqrt{L}, & n = 0 \end{cases} \tag{5.11}$$

Since the infinite stochastic ODEs of Eqs. 5.8 and 5.9 are linear and uncoupled, the state variance can be directly obtained from the analytical solution of Eqs. 5.8 and 5.9 as follows:

$$\left\langle z_{2,0}(t) \right\rangle = w_{2,0}(t - t_0) \tag{5.12}$$

$$var(z_{2,0}(t) = \sigma^2(t - t_0) \tag{5.13}$$

$$\langle z(t) \rangle = e^{\lambda(t-t_0)} \langle z(t_0) \rangle + \frac{w_p}{\lambda}(e^{\lambda(t-t_0)} - 1) \tag{5.14}$$

$$var(z(t)) = e^{2\lambda(t-t_0)} var(z(t_0)) + \sigma^2 \frac{e^{2\lambda(t-t_0)} - 1}{2\lambda} \tag{5.15}$$

where $z(t) = z_{p,n}(t)$ and $w_p = w_{p,n}$ for $n \neq 0$.

For the purpose of theoretical analysis and control design, the expected value of aggregate rms roughness square, $\left\langle r_\Delta^2 \right\rangle$, and expected value of aggregate rms slope square, $\left\langle m_\Delta^2 \right\rangle$, are used in the analysis and controller design later in this work. Both expected aggregate

roughness square and expected aggregate slope square can be expressed in terms of state variance, $\left\langle z_{p,n}^2 \right\rangle$. The derivation processes can be found in [27], and the results are shown as follows:

$$\left\langle r_\Delta^2(t) \right\rangle = \frac{1}{L} \sum_{n=1}^{L/(2\Delta)} \left(\left\langle z_{1,n}^2 \right\rangle + \left\langle z_{1,n}^2 \right\rangle \right), \tag{5.16}$$

$$\left\langle m_\Delta^2(t) \right\rangle = \sum_{p=1}^{2} \sum_{n=0}^{L/(2\Delta)} K_{p,n} \left\langle z_{p,n}^2 \right\rangle \tag{5.17}$$

where

$$\left\langle z_{p,n}^2 \right\rangle = var(z_{p,n}) + \left\langle z_{p,n} \right\rangle^2 \tag{5.18}$$

$$\begin{aligned} K_{p,n} &= \frac{8}{L\Delta} \sin^2\left(\frac{\pi n}{L/\Delta}\right) \sum_{i=0}^{L/(2\Delta)} \left(\cos^2\left(\frac{n\pi}{L/\Delta}(2i+1) \right) \right) \\ &= \begin{cases} \dfrac{8}{L\Delta} \sin^2\left(\dfrac{\pi n}{L/\Delta}\right) & n = 0 \\ \dfrac{4}{L\Delta} \sin^2\left(\dfrac{\pi n}{L/\Delta}\right) & n \neq 0 \end{cases} \end{aligned} \tag{5.19}$$

It is necessary to point out that, when aggregate (discrete) surface height profile is used, the highest number of modes that can be accurately estimated from $h_\Delta(x,t)$ is limited by the spatial sampling points, $n \leq \frac{L}{2\Delta}$; the reader may refer to [57] for a detailed discussion of the issue.

5.2.4 Parameter identification and model verification

The model parameters, c_2 and σ^2, of the EW equation of Eq. 5.6 can be estimated based on the kinetic Monte Carlo simulations results as functions of the mean deposition rate w_0

and/or of the patterned deposition rate magnitudes, A_1 and A_2. These parameters affect the dynamics of aggregate surface roughness and slope and can be estimated by fitting the predicted evolution profiles for aggregate surface roughness and slope from the EW equation to profiles of aggregate surface roughness and slope from kMC simulations. Least-square methods are used to estimate the model parameters so that the EW-model predictions are close in a least-square sense to the kMC simulation data. It is assumed that EW parameters fitted to the kMC results with non-pattern deposition rate profiles can be used to predict the dynamics of kMC simulations with spatially distributed deposition rate profiles; this assumption will be proved to be a valid one in the simulations below. In this work, 40 groups of kMC simulations are carried out from $w_0 = 0.1$ layer/s to $w_0 = 20$ layer/s to compute the dependence of c_2 and σ^2 on w_0. Based on the fitted c_2 and σ^2 values obtained from these fitting results in Fig. 5.4 and Fig. 5.5, polynomial functions are chosen to estimate c_2 and σ^2 values at different w_0 with the least-square method. Specifically, a second-order polynomial function with respect to w_0 is chosen to estimate c_2 and a linear function is chosen to estimate σ^2, and the expressions are given as follows:

$$c_2(w_0) = a_{c_2} w_0^2 + b_{c_2} w_0 + c_{c_2}, \tag{5.20}$$

$$\sigma^2(w_0) = a_{\sigma^2} w_0 + b_{\sigma^2} \tag{5.21}$$

where a_{c_2} , b_{c_2} , c_{c_2}, a_{σ^2} and b_{σ^2} are time-invariant fitting model parameters with the following values, $a_{c_2} = -0.0002$, $b_{c_2} = 0.0018$, $c_{c_2} = 0.0007$, $a_{\sigma^2} = 0.9261$ and $b_{\sigma^2} = -0.1168$. These fitting results are based on kMC simulations with uniform deposition rate

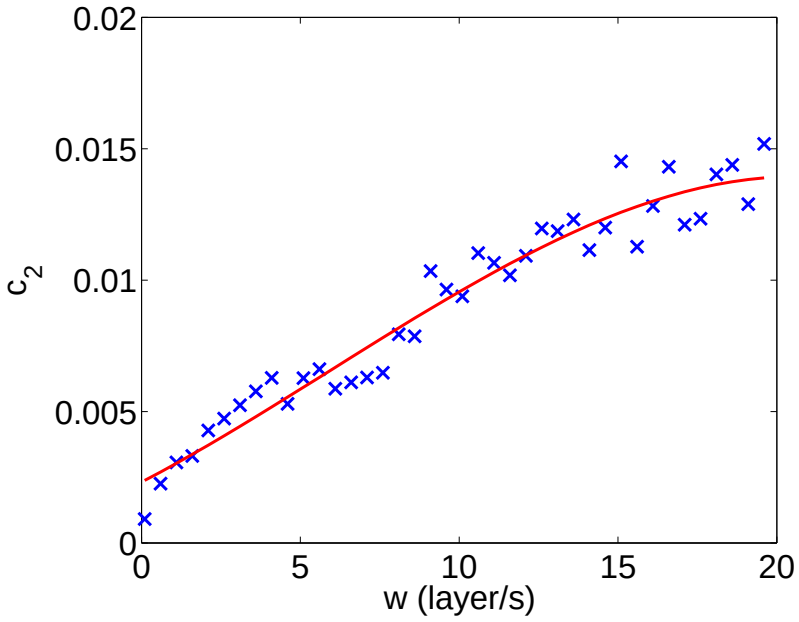

Figure 5.4: c_2 values for different spatially-uniform deposition rates w_0, ($A_1 = A_2 = 0$). The solid line is the result of a second-order polynomial fitting function and it is the c_2 versus w_0 relationship used by the predictive controller.

profiles ($A_i = 0$). To verify that these fittings can be used in the EW equation to predict the open-loop kMC results with spatially distributed deposition rate profiles, the solutions of EW equations for aggregate surface evolution with patterned deposition rate profile are obtained based on c_2 and σ^2 models from open-loop kMC data with uniform deposition rate, and these dynamic evolution profiles are compared with open-loop kMC dynamic evolution profiles with patterned deposition rate profiles. As shown in Fig. 5.6 and Fig. 5.7, c_2 and σ^2 models from open-loop kMC data with uniform deposition rate can be used in the EW equation to very accurately predict aggregate surface roughness and slope of the kMC model with patterned deposition rate; this conclusion is consistent with [27].

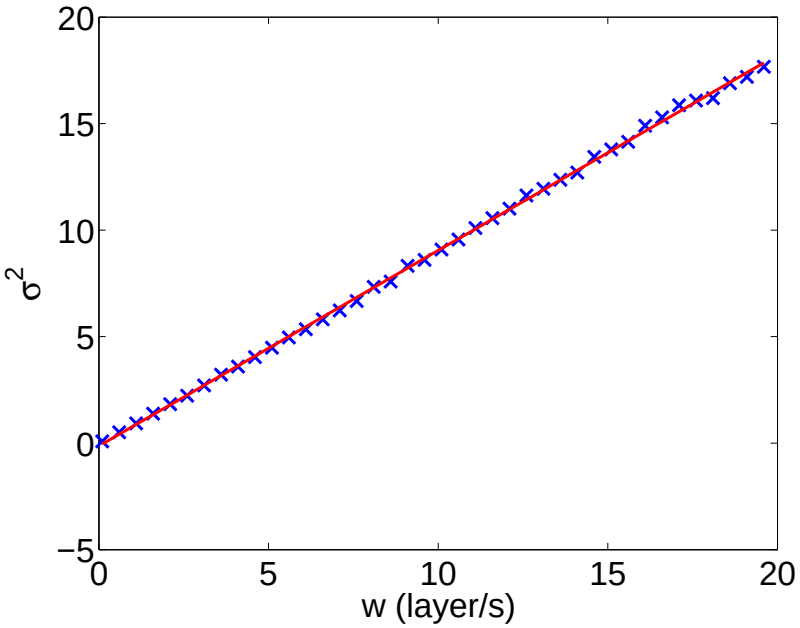

Figure 5.5: σ^2 values for different spatially-uniform deposition rates w_0, ($A_1 = A_2 = 0$). The solid line is the result of a first-order polynomial fitting function and it is the σ^2 versus w_0 relationship used by the predictive controller.

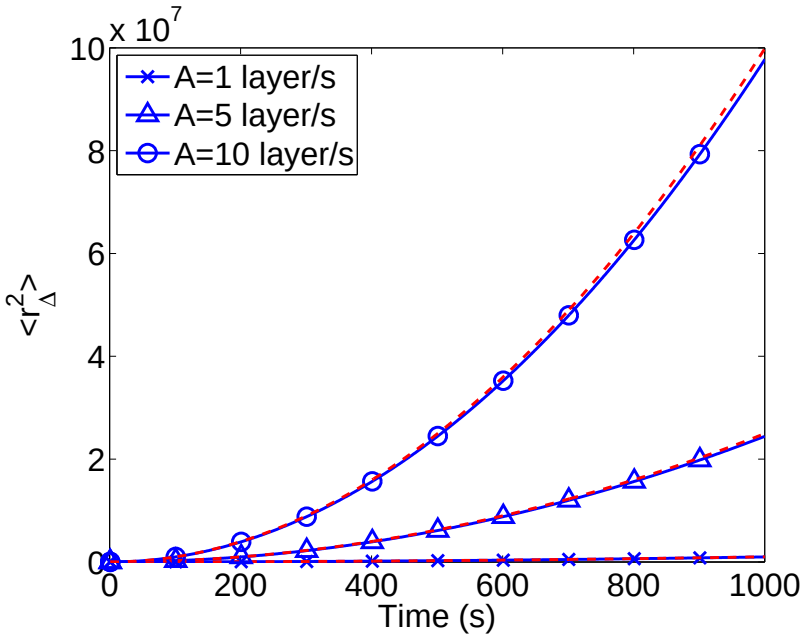

Figure 5.6: Evolution of expected aggregate surface roughness for different patterned deposition magnitudes from the kMC model (solid lines with symbols) and expected aggregate surface roughness solutions from the corresponding EW equations (dashed lines, $A_1 = A_2 = A$). The c_2 and σ^2 values of the EW equations were estimated from open-loop aggregate surface roughness kMC model data with spatially-uniform deposition rates.

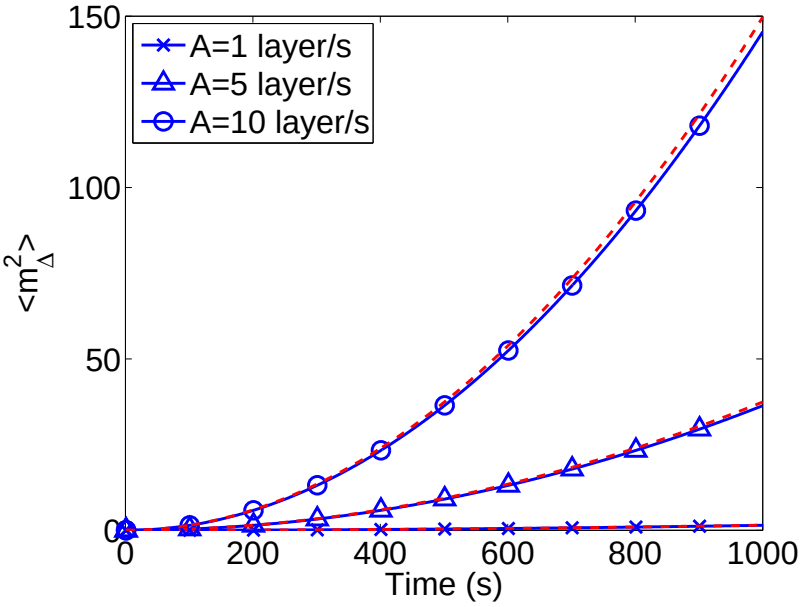

Figure 5.7: Evolution of expected aggregate surface slope for different patterned deposition magnitudes from the kMC model (solid lines with symbols) and expected aggregate surface slope solutions from the corresponding EW equations (dashed lines, $A_1 = A_2 = A$). The c_2 and σ^2 values of the EW equations were estimated from open-loop aggregate surface roughness kMC model data with spatially-uniform deposition rates.

5.3 Model predictive control

In this section, a model predictive controller is developed on the basis of the constructed closed-form dynamic model. The control objective is to regulate the expected aggregate rms slope square and the expected aggregate rms roughness square of the thin film to desired levels.

5.3.1 MPC formulation

Specifically, we consider the problem of simultaneous regulation of aggregate rms slope and aggregate rms roughness of the thin film to desired levels within a model predictive control framework. The expected values of aggregate rms slope square and of aggregate rms surface roughness square, $\langle m_\Delta^2 \rangle$ and $\langle r_\Delta^2 \rangle$, are chosen as the control objectives. Since the first stage of the deposition process mainly deals with the thickness of the thin film and the second stage of the process mainly shapes the morphology of the thin film, in this work the control problem focuses mainly on the second stage of the deposition process. The average deposition rate, w_0, and the amplitude of sine wave, A, are used as the manipulated input with a fixed substrate temperature, $T = 480$ K. The control action at time t is obtained by solving a finite-horizon optimal control problem. The cost function in the optimal control problem includes penalty on the deviation of $\langle m_\Delta^2 \rangle$ and of $\langle r_\Delta^2 \rangle$ from their set-point values, which are computed to optimize light reflectance of the thin film at desired values. The optimization problem is subject to the dynamics of the aggregate surface height. The

manipulated variable profiles are calculated by solving a finite-dimensional optimization problem in a receding horizon fashion. Specifically, the MPC problem is formulated as follows:

$$\begin{aligned}
\min_{(w_0(t_i),A_1(t_i),A_2(t_i))} J = \quad & \sum_{i=1}^{p} \Big\{ q_m[(m^2_{\Delta,set} - \langle m^2_\Delta(t_i)\rangle)/m^2_{\Delta,set}]^2 \\
& + q_r[(r^2_{\Delta,set} - \langle r^2_\Delta(t_i)\rangle)/r^2_{\Delta,set}]^2 \Big\}
\end{aligned}$$

$$\begin{gathered}
\text{subject} \quad \text{to} \\
\frac{\partial h_\Delta}{\partial t} = w(x,t) + c_2 \frac{\partial^2 h_\Delta}{\partial x^2} + \xi(x,t) \\
r_\Delta = \left[\frac{1}{L/\Delta} \sum_{i=1}^{L/\Delta} (h_{\Delta,i} - \bar{h}_\Delta)^2 \right]^{1/2} \\
m_\Delta = \left[\frac{1}{L/\Delta} \sum_{i=1}^{L/\Delta} \left(\frac{h_{\Delta,i} - h_{\Delta,i+1}}{\Delta} \right)^2 \right]^{1/2} \\
w_{min} < w_0(t_i) < w_{max}, \quad |w_0(t_i) - w_0(t_i - dt)| \le \delta w_{max} \\
w(x,t_i) = w_0(t_i) + A_1(t_i) \sin\left(\frac{2\pi k_1 x}{L} \right) + A_2(t_i) \sin\left(\frac{2\pi k_2 x}{L} \right) \\
0 \le A_1(t_i) + A_2(t_i) \le w_0 \\
i = 1, 2, \ldots, p
\end{gathered} \tag{5.22}$$

where t_i is the current time, dt is the length of the sampling interval, p is the number of prediction steps, pdt is the specified prediction horizon, $w_0(t_i)$, $i = 1, 2, \ldots, p$, is the average deposition rate at the ith step, q_r and q_m are the weighting penalty factors for the deviations of $\langle m^2_\Delta \rangle$ and $\langle r^2_\Delta \rangle$ from their respective set-points, $r^2_{\Delta,set}$ and $m^2_{\Delta,set}$, at the ith prediction step, w_{min} and w_{max} are the lower and upper bounds on the average deposition rate, respectively,

and δw_{max} is the limit on the rate of change of the average deposition rate. It is necessary to note that several constraints are added to the controller to account for a number of practical considerations. First, there is a constraint on the range of variation of the average deposition rate. Another constraint is imposed on the rate of change of the average deposition rate to account for actuator limitations. The optimal manipulated variable profile, $(w_0(t_i), A(t_i))$, is obtained from the solution of the optimization problem of Eqs. 5.22, which minimizes the deviation of the expected aggregate rms slope square and of the expected aggregate rms roughness square from their respective set-point values within the prediction horizon.

The surface aggregate rms roughness square and slope square can be calculated in terms of the state variance, as is shown in Eq. 5.16 and 5.17, then the MPC formulation can be

modified as follows:

$$\min_{(w_0(t_i),A_1(t_i),A_2(t_i))} J = \sum_{i=1}^{p} \Big\{ q_m[(m^2_{\Delta,set} - \langle m^2_\Delta(t_i)\rangle)/m^2_{\Delta,set}]^2 + q_r[(r^2_{\Delta,set} - \langle r^2_\Delta(t_i)\rangle)/r^2_{\Delta,set}]^2 \Big\}$$

$$\begin{gathered} \text{subject} \quad \text{to} \\ \langle r^2_\Delta(t)\rangle = \frac{1}{L}\sum_{n=1}^{L/(2\Delta)} \left(\langle z^2_{1,n}\rangle + \langle z^2_{1,n}\rangle\right) \\ \langle m^2_\Delta(t)\rangle = \sum_{p=1}^{2}\sum_{n=0}^{L/(2\Delta)} K_{p,n}\langle z^2_{p,n}\rangle \end{gathered} \tag{5.23}$$

$$w_{min} < w_0(t_i) < w_{max}, \quad |w_0(t_i) - w_0(t_i - dt)| \le \delta w_{max}$$

$$w(x,t_i) = w_0(t_i) + A_1(t_i)\sin\left(\frac{2\pi k_1 x}{L}\right) + A_2(t_i)\sin\left(\frac{2\pi k_2 x}{L}\right)$$

$$0 \le A_1(t_i) + A_2(t_i) \le w_0$$

$$i = 1, 2, \ldots, p$$

5.4 Regulation of surface slope and roughness for light trapping efficiency

In this section, we apply the predictive controller of Eqs. 5.23 to the kMC model of the thin film deposition process to regulate the surface aggregate slope and roughness at desired levels. The average deposition rate and amplitude of sine waves are chosen as manipulated variables. The substrate temperature is kept constant during all deposition runs. The controlled variables are the expected values of the aggregate rms slope square and of the

aggregate rms roughness square at the end of the deposition process.

In the closed-loop simulations, the aggregate surface height profile of the thin film is obtained from the kMC simulations and is transferred to the controller (state feedback control) at each sampling time. A finite number of modes, $L/(2\Delta)$, are reconstructed from the aggregate surface height profile and are used to calculate the predictions of the aggregate rms slope square and of the aggregate rms roughness square. The constrained optimization problem formulated in the MPC of Eqs. 5.23 is solved and the optimal input profile is obtained and is applied to the closed-loop system during the sampling time. The optimization problem is solved via a local constrained minimization algorithm with a broad set of initial guesses.

5.4.1 Surface regulation of two-stage deposition process with $k_1 = 5$, $k_2 = 0$ and $A_1 = A_2 = A$

In this subsection, several groups of set-points are picked to generate thin-film surfaces corresponding to different light reflectance values, $R/R_0 = 0.2$, $R/R_0 = 0.5$ and $R/R_0 = 0.9$. In the first stage of the simulation, open-loop simulations are carried out with $w_{fix} = 10$ layer/s and simulation time is $t_{fix} = 5000$ s. In the second stage of the simulation, close-loop simulations are carried out at different set-points with fixed weighing factors on roughness and slope of $q_r = q_m = 1$ and $A_1 = A_2 = A$. The obtained aggregate roughness and slope are used to calculate the corresponding reflectance value. Specifically, in the first group of simulations, $m^2_{\Delta,set} = 0.16$ and $r^2_{\Delta,set} = 160000\ layer^2/s$, and results are shown

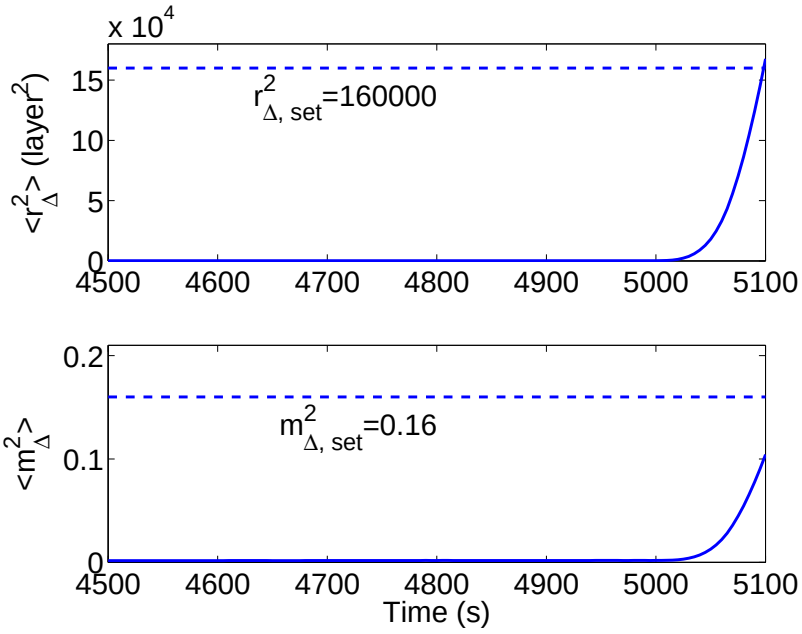

Figure 5.8: $\langle r_\Delta^2 \rangle$ and $\langle m_\Delta^2 \rangle$ at the end of the closed-loop thin film deposition with $k_1 = 5$ and $k_2 = 0$ corresponding to light reflectance value $R/R_0 = 0.2$ with $q_r = q_m = 1$, $r_{\Delta,set}^2 = 160000\ layer^2$, $m_{\Delta,set}^2 = 0.16$ and $A_1 = A_2 = A$.

in Fig. 5.8. It is clear in the plot that during the first stage of simulation ($t_{fix} = 5000$ s), aggregate surface roughness and slope increase very slowly and both variables increase fast and approach set-points during the second stage of the deposition. This is as expected because the amplitude value,A, is the key factor to shape the morphology of the thin film surface. Larger deviation from set-point is observed for aggregate slope than for aggregate roughness. This is determined by the ratio between the weighting factors and more details can be found in [27]. Light reflectance value with the obtained aggregate roughness and slope is $R/R_0 = 0.24$, which is close to the desired value. The surface snapshot in this case is shown in Fig. 5.9 and a clear pattern can be observed on the thin film surface.

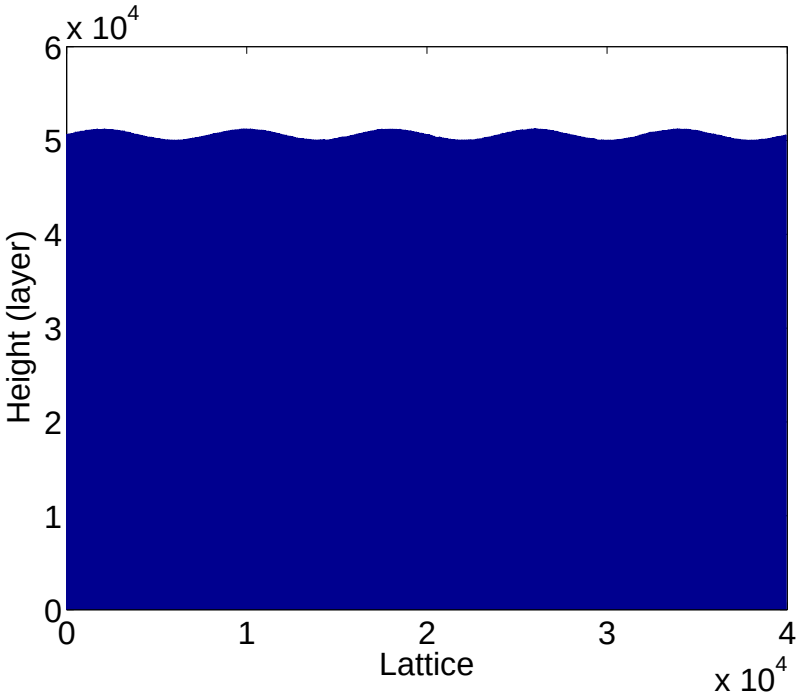

Figure 5.9: Surface snapshot for closed-loop thin film deposition using actuation with $k_1 = 5$ and $k_2 = 0$ corresponding to light reflectance value $R/R_0 = 0.2$ and $A_1 = A_2 = A$.

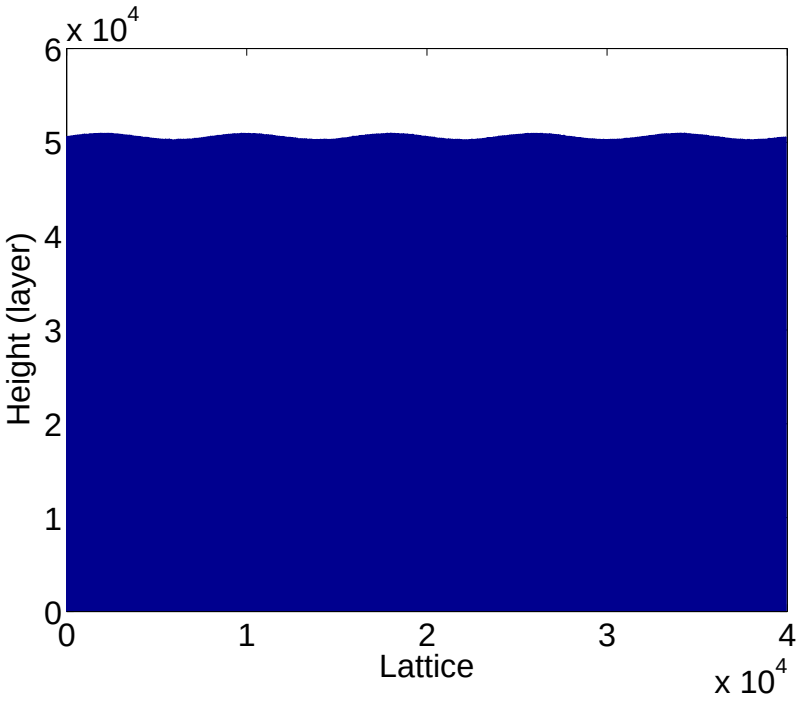

Figure 5.10: Surface snapshot for closed-loop thin film deposition using actuation with $k_1 = 5$ and $k_2 = 0$ corresponding to light reflectance value $R/R_0 = 0.5$ and $A_1 = A_2 = A$.

Similarly, simulations are carried out to generate surfaces with $R/R_0 = 0.5$ and $R/R_0 = 0.9$ and the resulting surface snapshots are shown in Fig. 5.10 and Fig. 5.11. The obtained light reflectance values in these two cases are $R/R_0 = 0.54$ and $R/R_0 = 0.89$ respectively, both of which are close to the desired values. As the surface becomes smoother, the light reflectance value approaches the reflectance for perfectly smooth surface, where $R = R_0$.

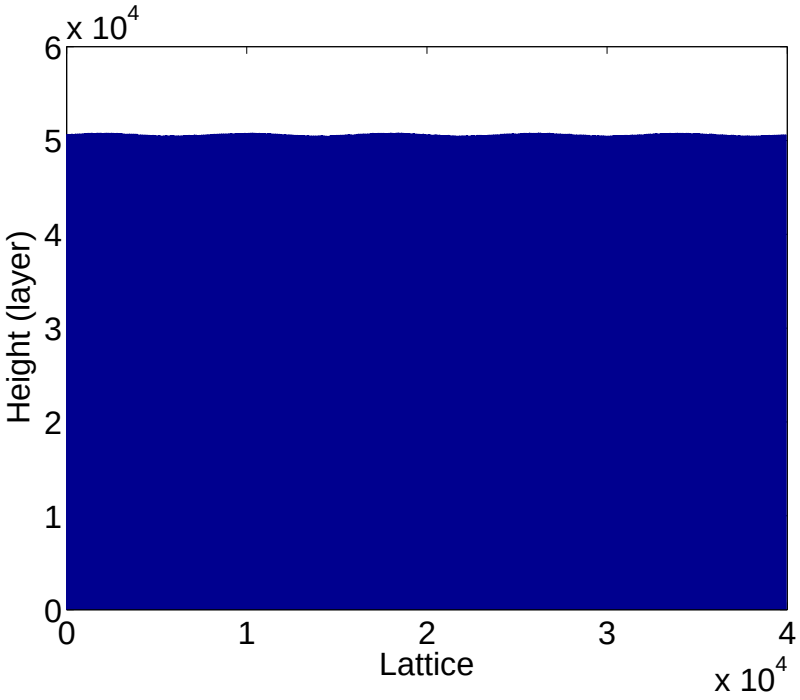

Figure 5.11: Surface snapshot for closed-loop thin film deposition using actuation with $k_1 = 5$ and $k_2 = 0$ corresponding to light reflectance value $R/R_0 = 0.9$ and $A_1 = A_2 = A$.

5.4.2 Separate control of aggregate surface roughness and slope for two-stage deposition process with $k_1 = 5, k_2 = 10$ and $A_1 = A_2 = A$

In this subsection, the two-stage kMC simulation model is replaced with the one which utilizes a spatially distributed deposition rate profile with multiple sine waves. To focus on the regulation of aggregate surface roughness and slope in the second stage of simulations, in this subsection the simulation time for the first stage of simulation is set to be short, $t_{fix} = 10$ s. In the second stage of simulations, multiple frequencies $k_1 = 5$ and $k_2 = 10$ are used. First, the problem of regulating aggregate surface roughness is considered. In this problem, the cost function has only penalty on the deviation of the expected aggregate surface roughness square from its set-point, i.e., $q_r = 1$, $q_m = 0$ and $A_1 = A_2 = A$. The set-point, $r^2_{\Delta,set}$ is 10000 $layer^2$. Fig. 5.12 shows the evolution profile of $\langle r^2_\Delta \rangle$ under the model predictive controller of Eq. 5.23. It is clear that the controller drives the expected aggregate surface roughness to its set-point at the end of the simulation. Fig. 5.13 shows the input profiles of w_0 and A for these simulations.

Next, the aggregate surface slope is regulated. The cost function includes only penalty on the deviation of the expected value of aggregate surface slope square from its set-point ($q_m = 1$, $q_r = 0$). The set-point, $m^2_{\Delta,set}$ is 0.25. Fig. 5.14 shows the evolution profile of the expected aggregate slope square. The aggregate slope reaches its set-point at $t = 110$ s. Fig. 5.15 displays the input profile in this scenario. It is necessary to point out that during the first half of the simulation time, the optimal solutions of w_0 are constrained by the rate of change constraint and the optimal solutions of A are bounded by the values of w_0.

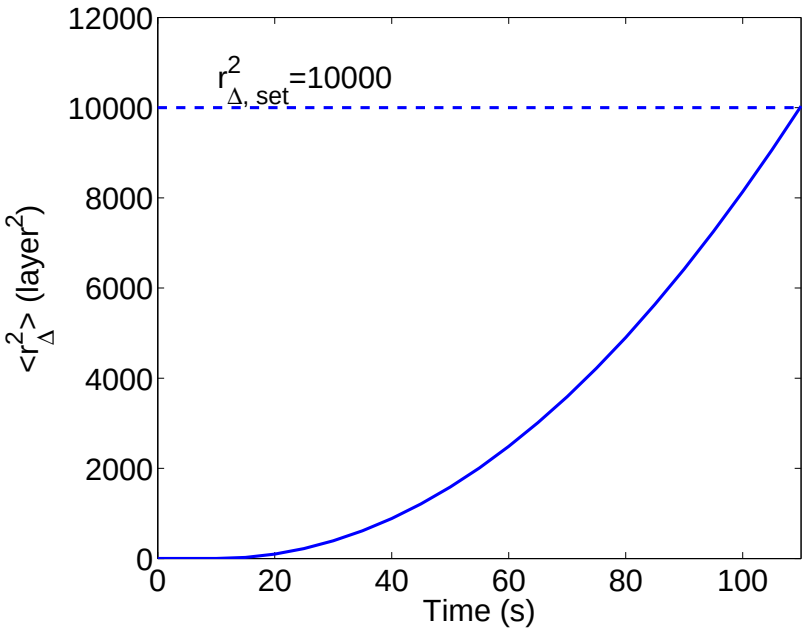

Figure 5.12: Profile of expected aggregate surface roughness square with $k_1 = 5$ and $k_2 = 10$. $q_r = 1$, $q_m = 0$, $r^2_{\Delta,set} = 10000\ layer^2$ and $A_1 = A_2 = A$.

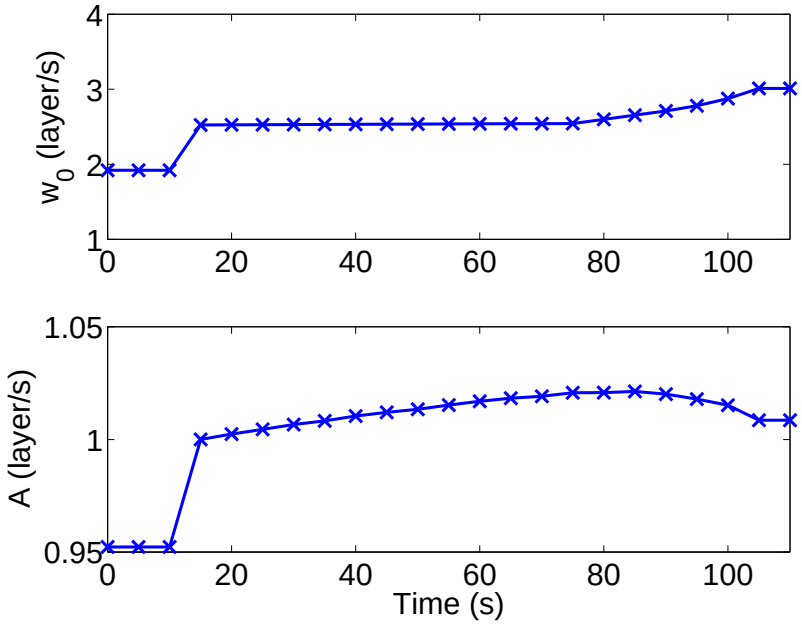

Figure 5.13: Manipulated input profiles with $k_1 = 5$ and $k_2 = 10$. $q_r = 1$, $q_m = 0$, $r^2_{\Delta,set} = 10000\ layer^2$ and $A_1 = A_2 = A$.

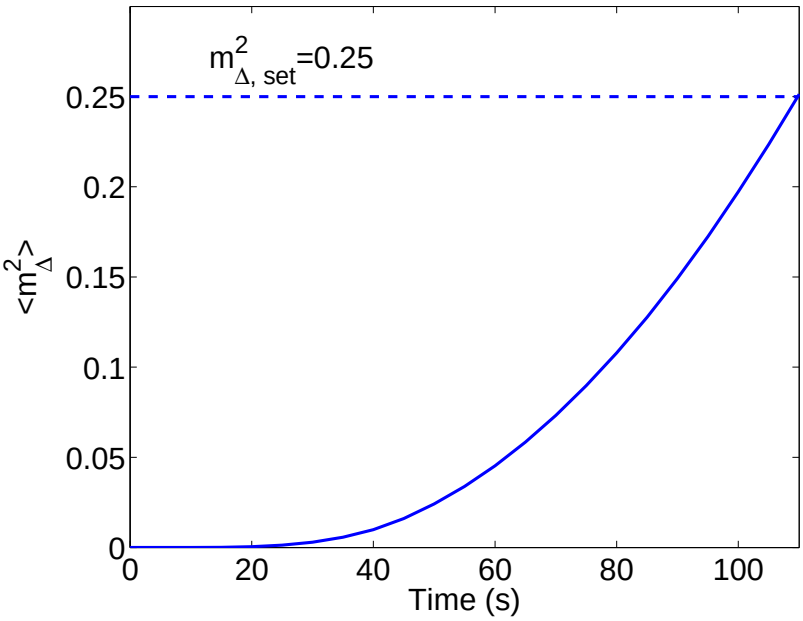

Figure 5.14: Profile of expected aggregate surface slope square with $k_1 = 5$ and $k_2 = 10$. $q_r = 0$, $q_m = 1$, $m^2_{\Delta,set} = 0.25$ and $A_1 = A_2 = A$.

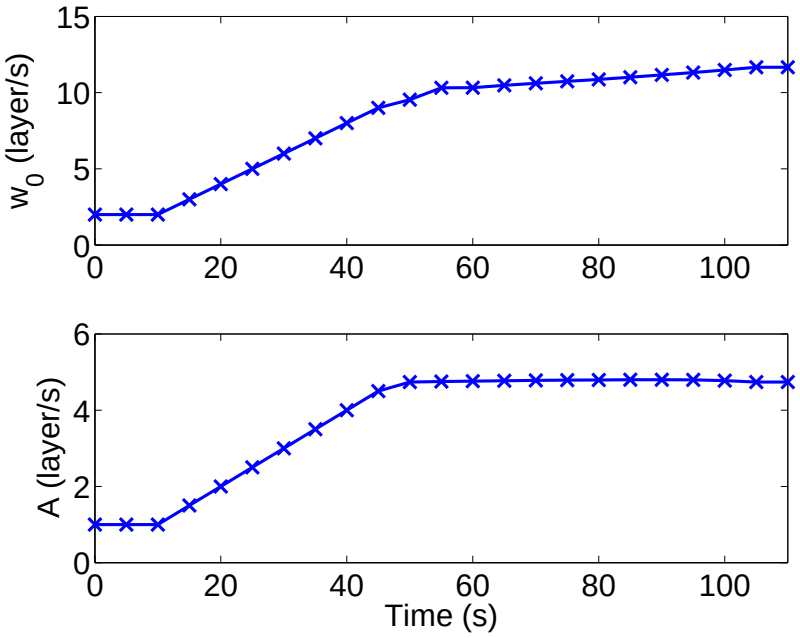

Figure 5.15: Manipulated input profiles with $k_1 = 5$ and $k_2 = 10$. $q_r = 0$, $q_m = 1$, $m^2_{\Delta,set} = 0.25$ and $A_1 = A_2 = A$.

5.4.3 Surface regulation of two-stage deposition process with $k_1 = 5$, $k_2 = 10$ and $A_1 = A_2 = A$

In this subsection, the kMC simulation model with a spatially distributed deposition rate profile with multiple sine waves is still utilized to carry out the simulation, but different from the previous part, the cost function in this subsection has penalties on both aggregate roughness and aggregate slope. The set-points $m^2_{\Delta,set} = 0.25$ and $r^2_{\Delta,set} = 160000\ layer^2/s$ are used. The closed-loop simulation results are shown in Fig. 5.16 and the obtained aggregate roughness and slope generates a surface with light reflectance value $R/R_0 = 0.21$, which is very close to the desired value. The resulting snapshot is shown in Fig. 5.17. It is important to point out that in the closed-loop simulations in this work, all the set-points are reached with $0 \leq A \leq 10$ layer/s, which means that the fitting used in this work is valid for all the set-points.

5.4.4 Surface regulation of two-stage deposition process with $k_1 = 5$, $k_2 = 10$ and $A_1 \neq A_2$

Similar to the previous subsection, the kMC model with $k_1 = 5$ and $k_2 = 10$ is utilized, but A_1 and A_2 are allowed to be adjusted independently by the controller. Specifically, the MPC has three manipulated variables, w_0, A_1 and A_2, all of which can change independently. The set-points $m^2_{\Delta,set} = 0.25$ and $r^2_{\Delta,set} = 160000\ layer^2/s$ are used. The closed-loop simulation results are shown in Fig. 5.16. It is clear that both $\langle r^2_\Delta \rangle$ and $\langle m^2_\Delta \rangle$ reach their set-points

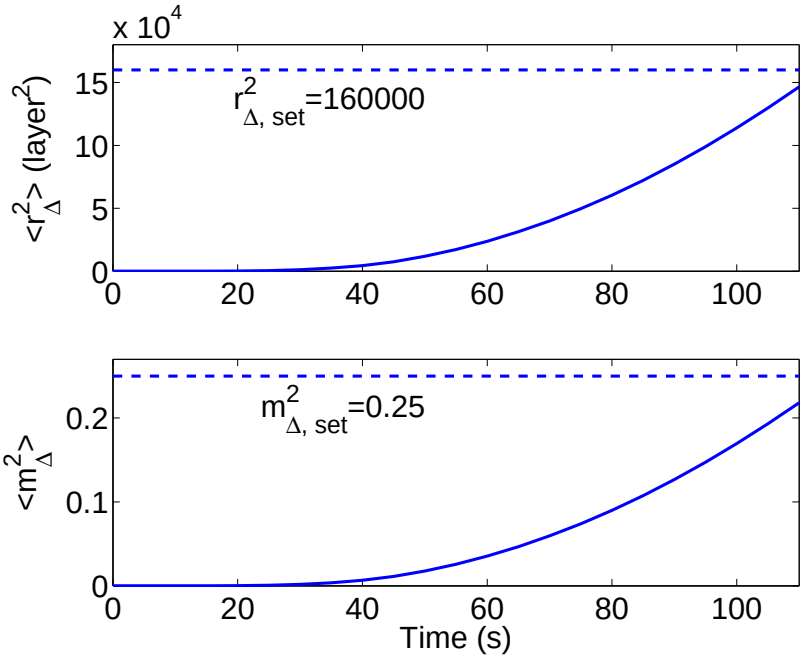

Figure 5.16: $\langle r_\Delta^2 \rangle$ and $\langle m_\Delta^2 \rangle$ at the end of the closed-loop thin film deposition with $k_1 = 5$ and $k_2 = 10$ corresponding to light reflectance value $R/R_0 = 0.2$ with $q_r = q_m = 1$, $r_{\Delta,set}^2 = 160000\ layer^2$, $m_{\Delta,set}^2 = 0.25$ and $A_1 = A_2 = A$.

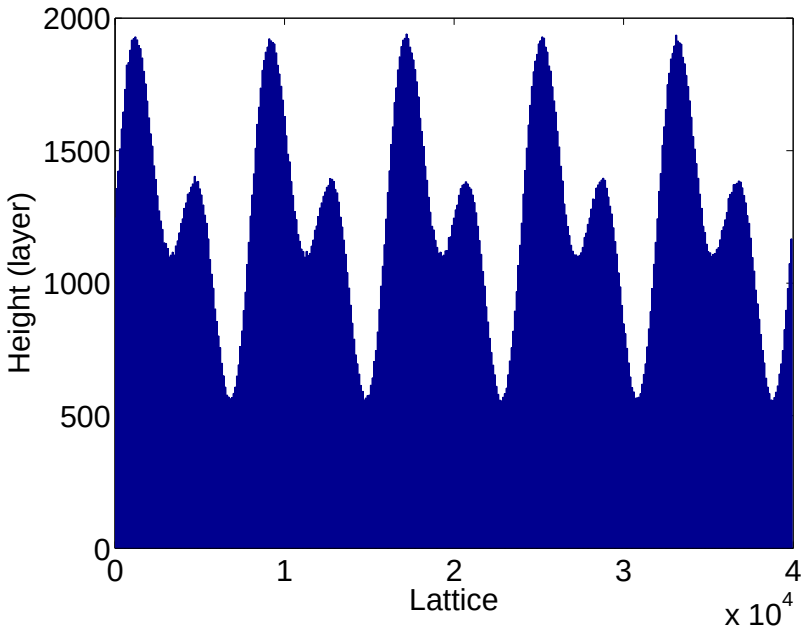

Figure 5.17: Surface snapshot for closed-loop thin film deposition using actuation with $k_1 = 5$ and $k_2 = 10$ corresponding to light reflectance value $R/R_0 = 0.2$ and $A_1 = A_2 = A$.

at the end of the closed-loop simulation. The ability to independently vary w_0, A_1 and A_2 makes it possible to reach the set-points for both aggregate roughness and slope at the same time and substantially improve the performance of the MPC. Fig. 5.19 shows the input profiles of w_0, A_1 and A_2 for the simulation and the corresponding thin film surface snapshot is shown in Fig. 5.20.

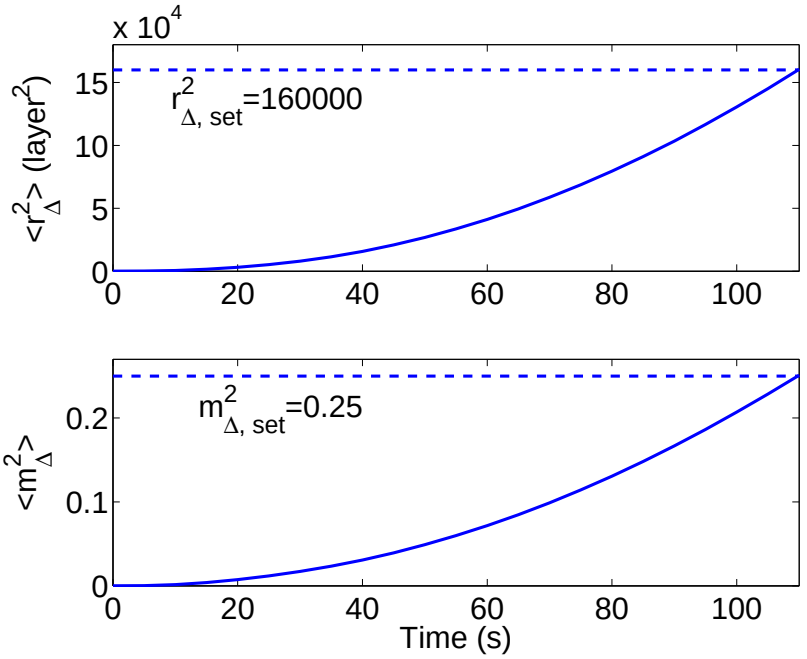

Figure 5.18: $\langle r_\Delta^2 \rangle$ and $\langle m_\Delta^2 \rangle$ at the end of the closed-loop thin film deposition with $k_1 = 5$ and $k_2 = 10$ corresponding to light reflectance value $R/R_0 = 0.2$ with $q_r = q_m = 1$, $r_{\Delta,set}^2 = 160000\ layer^2$ and $m_{\Delta,set}^2 = 0.25$.

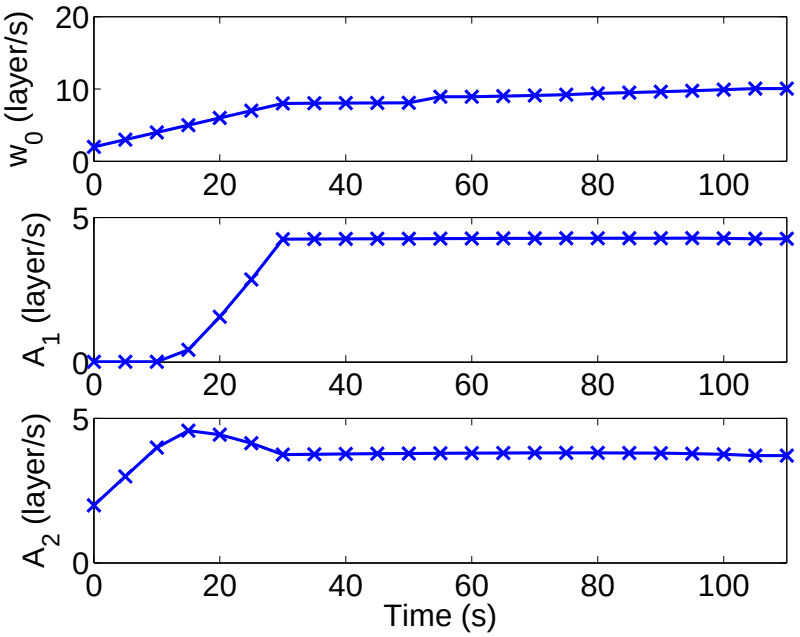

Figure 5.19: Manipulated input profiles with $k_1 = 5$ and $k_2 = 10$. $q_r = q_m = 1$, $r^2_{\Delta,set} = 160000\ layer^2$ and $m^2_{\Delta,set} = 0.25$.

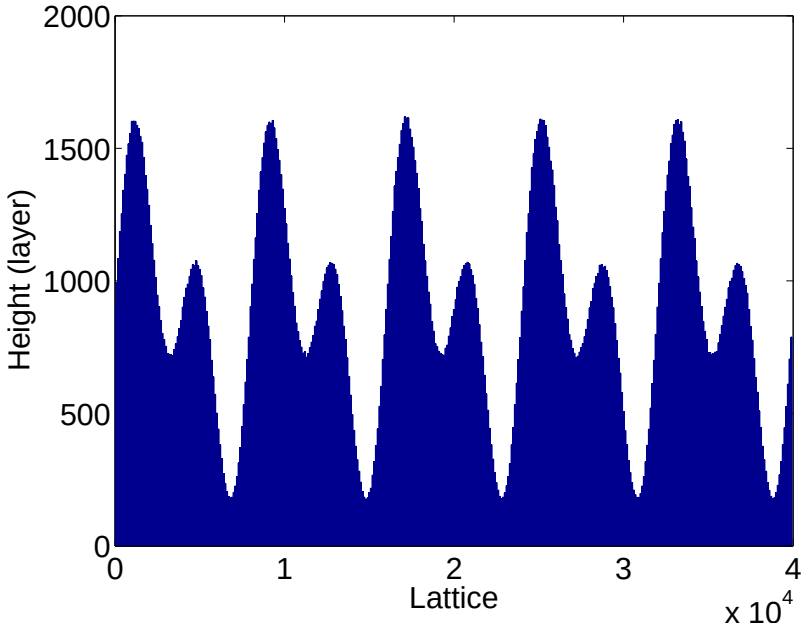

Figure 5.20: Surface snapshot for closed-loop thin film deposition using actuation with $k_1 = 5$ and $k_2 = 10$.

Chapter 6

Modeling and Control of Transparent Conducting Oxide Layer Surface Morphology for Improved Light Trapping

6.1 Introduction

This chapter focuses on the application of microscopic modeling and control to the process of TCO thin film deposition, which consists of ZnO and Al. Specifically, this work introduces a two species simulation for TCO layer deposition process and presents an integrated control actuator and control algorithm design framework for the regulation of deposition of

TCO thin films such that the final thin film surface morphology is controlled to a desired level. To demonstrate the approach, we focus on a two species thin film deposition process using a large-lattice (lattice size=40,000) kinetic Monte-Carlo simulation. Different deposition mechanisms are utilized for each component, ZnO and Al. Specifically, random deposition with surface relaxation (RDSR) mechanism is used for Al and deposition/migration mechanism is used for ZnO [23]. Subsequently, surface roughness and slope at different length-scales ranging from atomic scale to visible light wavelength scale are both calculated based on the generated thin film surface. It is found that a patterned actuator design is needed to induce thin film surface roughness and slope at visible light wavelength spatial scales to desired levels. Since a large-lattice kinetic Monte-Carlo model cannot be used as the basis for controller design and real-time controller calculations, an Edwards-Wilkinson-type equation is used to model the surface evolution at the visible light wavelength spatial scale and to form the basis for feedback controller design within a model predictive control framework. The cost function of the predicted controller involves penalties on both surface roughness and slope from set-point values as well as constraints on the magnitude and rate of change of the control action. The Edwards-Wilkinson equation model parameters are estimated from kinetic Monte-Carlo simulations and their dependence on the manipulated input (deposition rate) is used to predict the influence of the control action on the surface roughness and slope during the growth process. The controller formulation takes advantage of analytical solutions of the expected surface roughness and surface slope at the visible light wavelength spatial scale and the controller is applied to the large-lattice ki-

netic Monte-Carlo simulation. Extensive simulation studies demonstrate that the proposed controller and patterned actuator design successfully regulate surface roughness and slope at visible light wavelength spatial scales to set-point values at the end of the deposition.

6.2 Two species thin film deposition process description and modeling

In this section, a one-dimensional solid-on-solid (SOS) on-lattice kinetic Monte Carlo (kMC) model is used to simulate the two species thin film deposition process, which includes three microscopic processes: an adsorption process, in which particles are incorporated onto the film from the gas phase, a migration process and a surface relaxation process, in which surface particles move to adjacent sites [35, 34, 52, 53]. The model is valid for temperatures $T < 0.5T_m$, where T_m is the melting point of the deposited material [35]. At high temperatures ($0.5T_m \lesssim T \lesssim T_m$), the particles cannot be assumed to be constrained on the lattice sites and the on-lattice model may not be valid. In this work, a square lattice is selected to represent the structure of the film, as shown in Fig. 6.1. All particles are modeled as identical hard spheres and the centers of the particles deposited on the film are located on the lattice sites. The diameter of the particles equals the distance between two neighboring sites. The width of the lattice is fixed so that the lattice contains a fixed number of sites in the lateral direction. The new particles are always deposited from the top side of the lattice with vertical incidence; see Fig. 6.1. Particle deposition results in film growth

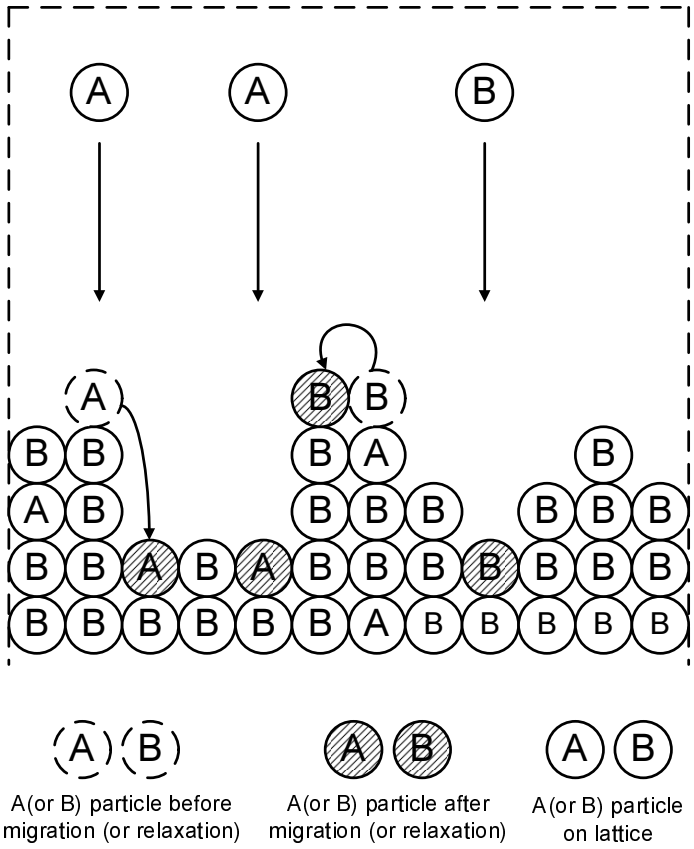

Figure 6.1: Two species thin film growth process on a solid-on-solid one-dimensional square lattice.

in the direction normal to the lateral direction. The direction normal to the lateral direction is thus designated as the growth direction. The number of sites in the lateral direction is defined as the lattice size and is denoted by L. Periodic boundary conditions (PBCs) are applied at the edges of the lattice in the lateral direction.

The top particles of each column are defined as the surface particles and the positions of the centers of all surface particles form the surface height profile. The number of nearest neighbors of a surface particle ranges from zero to two. A surface particle with zero nearest

neighbors is possible to move to one of its adjacent columns with equal probability. A surface particle with one nearest neighbor is possible to move to its adjacent column with lower height. A surface particle with two nearest neighbors can not move. Particles that are not on the film surface can not move.

The overall deposition rate, w, is expressed in the unit of layer per second and is a combination of two components, ZnO deposition rate w_1 and Al deposition rate w_2 ($w = w_1 + w_2$). The deposition ratio between ZnO and Al is 24 : 1 [8]. Different deposition mechanisms are used for each component. Random deposition with surface relaxation (RDSR) mechanism is used for Al. Specifically, in the RDSR process a site is randomly selected with uniform probability among all lattice sites and a particle is deposited on the top of this site. If the just deposited particle has less than two nearest neighbors, it will move according to the rules described above. A deposition/migration mechanism is used for ZnO. In this model, the deposition and migration events are separate and independent microscopic events. The deposition event is a random process, i.e., the same random deposition (without surface relaxation) as in the RDSR model. However, the migration event does not follow immediately the deposition of the particle. Instead, each surface particle, i.e., the top particle of a lattice site, is subject to its own migration event with a probability that depends on its local environment and the substrate temperature. The migration rate (probability) follows an Arrhenius-type law with a pre-calculated activation energy barrier that depends on the local environment of the particle, i.e., the number of the nearest neighbors of the particle chosen for a migration event. The migration rate of the ith surface

particle is calculated as follows:

$$r_m = \nu_0 \exp\left(-\frac{E_s + n_i E_n}{k_B T}\right) \tag{6.1}$$

where ν_0 denotes the pre-exponential factor, n_i is the number of the nearest neighbors of the ith particle and can take the values of 0 and 1, (r_m is zero when $n_i = 2$ since in the one-dimensional lattice this surface particle is fully surrounded by other particles and cannot migrate), k_B is the Boltzmann's constant, E_s is the contribution to the activation energy barrier from the site itself, and E_n is the contribution to the activation energy barrier from each nearest neighbor. In this work, $E_s = 3.4eV$ and E_n is assumed to be zero [39]. T is the substrate temperature of the thin film and in this work $T = 800$ K [38]. Since the film is thin, the temperature is assumed to be uniform throughout the film. For the detailed description and investigation of these models, please refer to [23].

6.2.1 Surface morphology at atomic level

Thin film surface morphology, which can be expressed in terms of surface roughness and slope, is a very important surface property influencing the light properties of TCO thin films. Surface roughness is defined as the root-mean-square (rms) of the surface height profile. Specifically, the definition of surface roughness is given as follows:

$$r = \left[\frac{1}{L}\sum_{i=1}^{L}(h_i - \bar{h})^2\right]^{1/2} \tag{6.2}$$

where r denotes surface roughness, h_i, $i = 1, 2, \ldots, L$, is the surface height at the i-th position in the unit of layer, L denotes the lattice size, and the surface mean height is given

by $\bar{h} = \frac{1}{L}\sum_{i=1}^{L} h_i$.

In addition to surface roughness, another quantity that also determines the surface morphology is the surface mean slope. In this work, the surface mean slope is defined as the rms of the surface gradient profile as follows:

$$m = \left[\frac{1}{L}\sum_{i=1}^{L} h_{s,i}^2\right]^{1/2} \tag{6.3}$$

where m denotes the rms slope and $h_{s,i}$ is the surface slope at the i-th lattice site, which is a dimensionless variable. The surface slope, $h_{s,i}$ is computed as follows:

$$h_{s,i} = \frac{h_{i+1} - h_i}{1} \tag{6.4}$$

Since the unit of height is layer and the distance between two adjacent particles (the diameter of particles) always equals to one layer, the denominator of $h_{s,i}$ is always one. Due to the use of PBCs, the slope at the boundary lattice site ($i = L$) is computed as the slope between the last lattice site (h_L) and the first lattice site (h_1).

To investigate the open-loop properties of surface morphology, a set of kMC simulations is carried out at different w with $T = 800$ K and $L = 40000$. In particular, the continuous-time Monte Carlo (CTMC) method is used in the kMC simulations. In this method, a list of events is constructed and an event is selected randomly with its respective probability. After the execution of the selected event, the list is updated based on the new lattice configuration. The following values are used for the parameters of the migration rate of Eq. 6.1, $\nu_0 = 10^{13}\text{s}^{-1}$, $E_s = 3.4$ eV and $E_n = 0$ eV. Fig. 6.2 and Fig. 6.3 show that both atomic roughness and slope increase with time and will reach steady-state values at

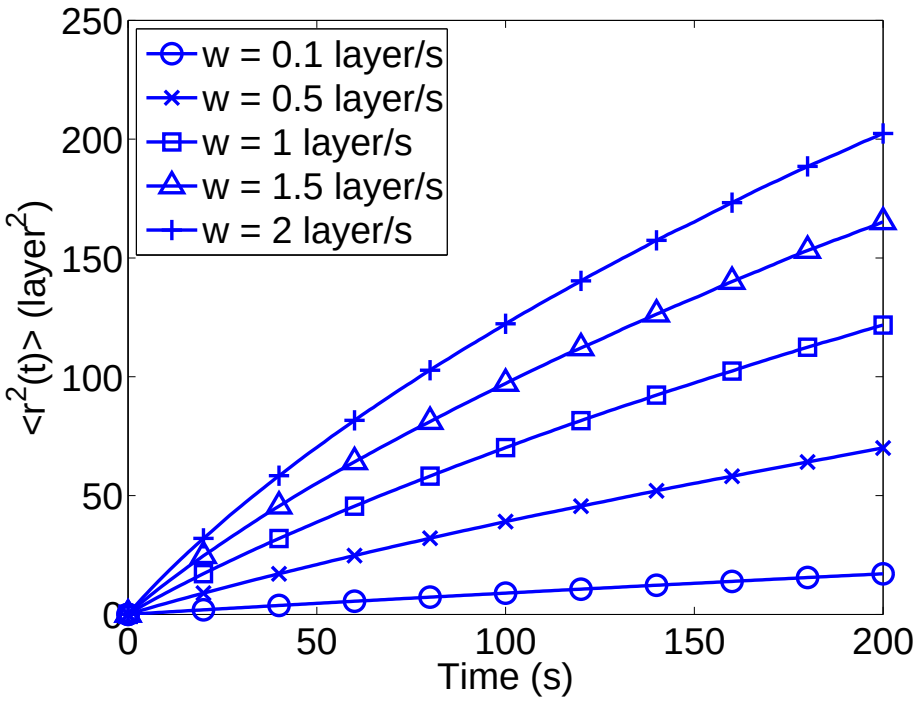

Figure 6.2: Evolution of expected atomic surface roughness with respect to time for different deposition rates (unit of w is layer/s) obtained from kMC simulations.

different time scales. Furthermore, both surface roughness and slope increase with total deposition rate w.

To further investigate the open-loop properties of this two species simulation model, simulations are carried out with different deposition rate ratio between the two components. As shown in Fig. 6.4 and 6.5, as $w_1\%(w_1\% = w_1/w))$ increases, the values of both the roughness and the slope increase since at this temperature ($T = 800$ K), the effect of the migration (which has the ability to smooth the surface compared to the RDSR process) is weak. Thus, as ZnO ($w_1\%$) dominates the deposition process, the surface becomes more

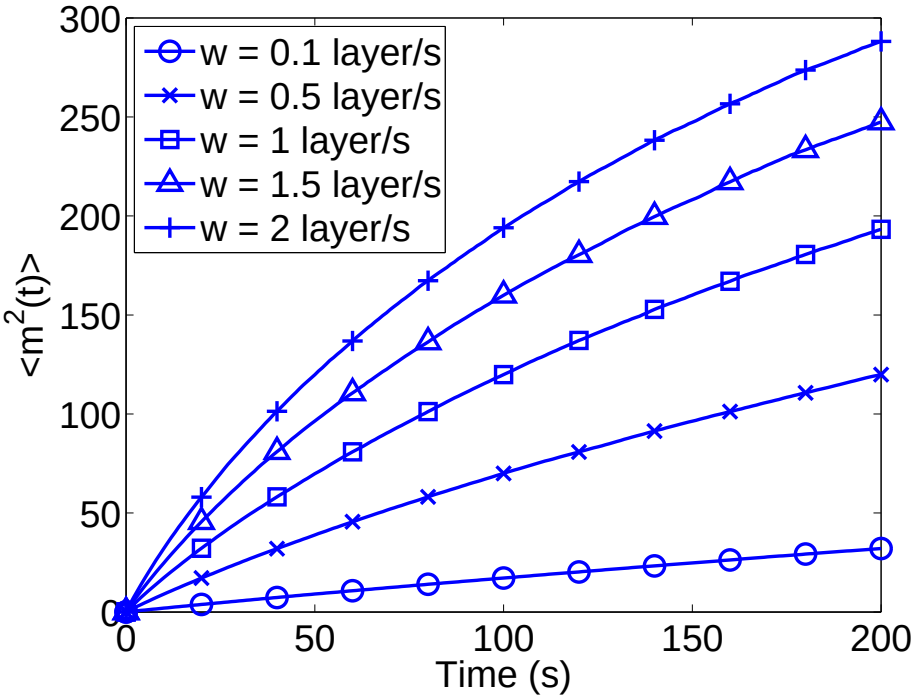

Figure 6.3: Evolution of expected atomic surface slope with respect to time for different deposition rates (unit of w is layer/s) obtained from kMC simulations.

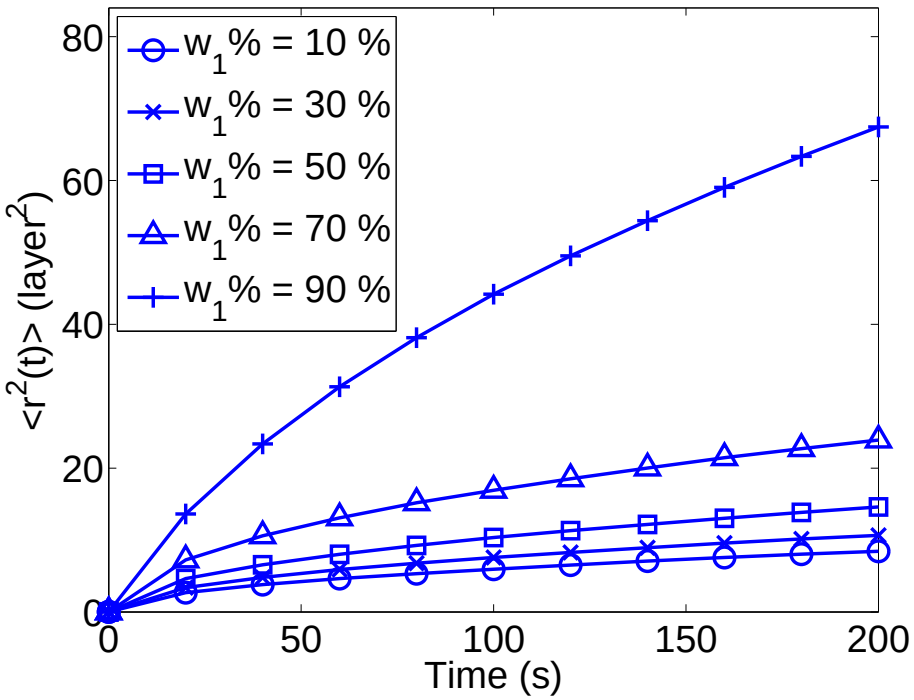

Figure 6.4: Evolution of expected atomic surface roughness with respect to time for different compositions from two species kMC simulations.

rough.

6.2.2 Aggregate surface morphology and spatial deposition rate profile

One of the most important applications of our work is to simulate and control the deposition process of thin film solar cells in order to improve solar cell efficiency. However, the wavelength of visible light (400nm – 700nm) is much larger than the diameter of ZnO particles (~ 0.3 nm) and thus, it is necessary to define an aggregate surface morphology at

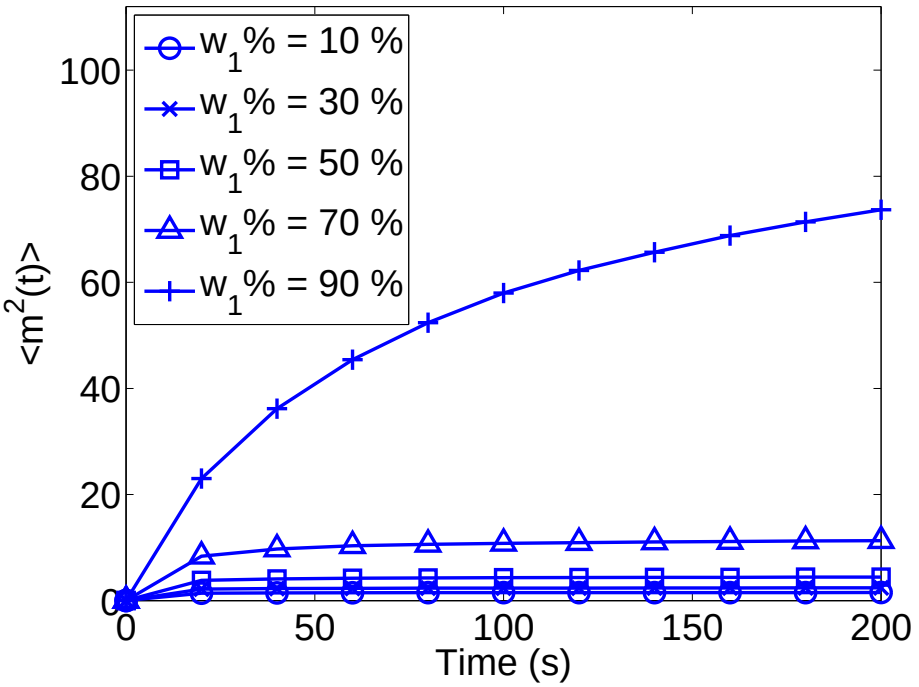

Figure 6.5: Evolution of expected atomic surface slope with respect to time for different compositions from two species kMC simulations.

length scales comparable to visible light wavelength [27].

Specifically, the aggregate surface morphology is computed similarly to the atomic surface morphology, but on the basis of the aggregate surface height profile, $h_{\Delta,i}$, which is defined as follows:

$$\begin{gathered} h_{\Delta,i} = (h_{i\Delta+1} + h_{i\Delta+2} + \cdots + h_{(i+1)\Delta})/\Delta, \\ i = 0, 1, \ldots, L/\Delta - 1 \end{gathered} \tag{6.5}$$

where $h_{\Delta,i}$ denotes the averaged surface height over the length scale of Δ sites, Δ denotes the aggregation size, i.e., the number of lattice sites used to calculate the aggregate surface height, and L/Δ denotes the number of aggregate sites of size Δ included in the spatial domain of the process. For the wavelength of visible light and silicon thin-film solar cells, the corresponding Δ is around 400; this follows from the fact that $0.3nm \cdot 400 = 120nm$, which is a length scale comparable to visible light wavelength [27]; the same aggregation level is used for the TCO layer in this work. The definition of aggregate surface roughness and slope is given as follows:

$$\begin{aligned} r_\Delta &= \left[\frac{1}{L/\Delta} \sum_{i=1}^{L/\Delta} \left(h_{\Delta,i} - \bar{h}_\Delta \right)^2 \right]^{1/2}, \\ m_\Delta &= \left[\frac{1}{L/\Delta} \sum_{i=1}^{L/\Delta} \left(\frac{h_{\Delta,i} - h_{\Delta,i+1}}{\Delta} \right)^2 \right]^{1/2}. \end{aligned} \tag{6.6}$$

The dynamics of aggregate roughness and slope are shown in Fig. 6.6 and Fig. 6.7. The simulation duration is $t_f = 200$ s and 100 independent simulations were carried out to calculate the expected values of aggregate surface roughness and slope. It is clear that at the aggregation length $\Delta = 400$, both $\left\langle r_\Delta^2(t_f) \right\rangle$ and $\left\langle m_\Delta^2(t_f) \right\rangle$ are much smaller compared to their corresponding value at atomic length scale. It is reported that the desired $\left\langle r_\Delta^2(t_f) \right\rangle$ for

optimum optical performance of TCO thin film ranges from 500 to 10000 nm^2 [31], which is much larger than available aggregate roughness value with practically viable simulation time and deposition rate magnitude. This small aggregate roughness at large characteristic length scales is partly because the operating conditions are spatially uniform throughout the entire deposition process, i.e., the same deposition rate and substrate temperature are applied throughout the spatial domain. Thus, a spatially non-uniform deposition rate profile is necessary for the purpose of optimizing thin film light trapping properties by manipulation of film aggregate surface roughness and slope at length scales comparable to visible light wavelength [27]. To this end, we introduce a patterned in space deposition rate profile, which is defined as follows:

$$\begin{aligned} w_1(x) &= w_{1,0} + A_1 \sin\left(\frac{2k\pi}{L}x\right), \quad A_1 \leq w_{1,0} \\ w_2(x) &= w_{2,0} + A_2 \sin\left(\frac{2k\pi}{L}x\right), \quad A_2 \leq w_{2,0} \\ w(x) &= w_1(x) + w_2(x) \\ w_0(x) &= w_{1,0}(x) + w_{2,0}(x), \quad A = A_1 + A_2 \end{aligned} \tag{6.7}$$

where x is a position along the lattice, $w_{1,0}$ and $w_{2,0}$ are the mean deposition rates, A_1 and A_2 are the magnitude of the patterned deposition profile, k is the number of sine waves along the entire lattice, and L is the lattice size. It is assumed that $w_1 : w_2 = w_{1,0} : w_{2,0} = A_1 : A_2 = 24 : 1$.

The dynamics of aggregate surface morphology with patterned deposition rate profile is studied by carrying out a series of simulations at different mean deposition rates w_0 with $L = 40000$, $\Delta = 400$, $T = 800$ K, $k = 5$ and $A = 0.1w_0$. The evolution profiles for aggregate roughness and slope are shown in Fig. 6.8 and Fig. 6.9. The introduction of patterned

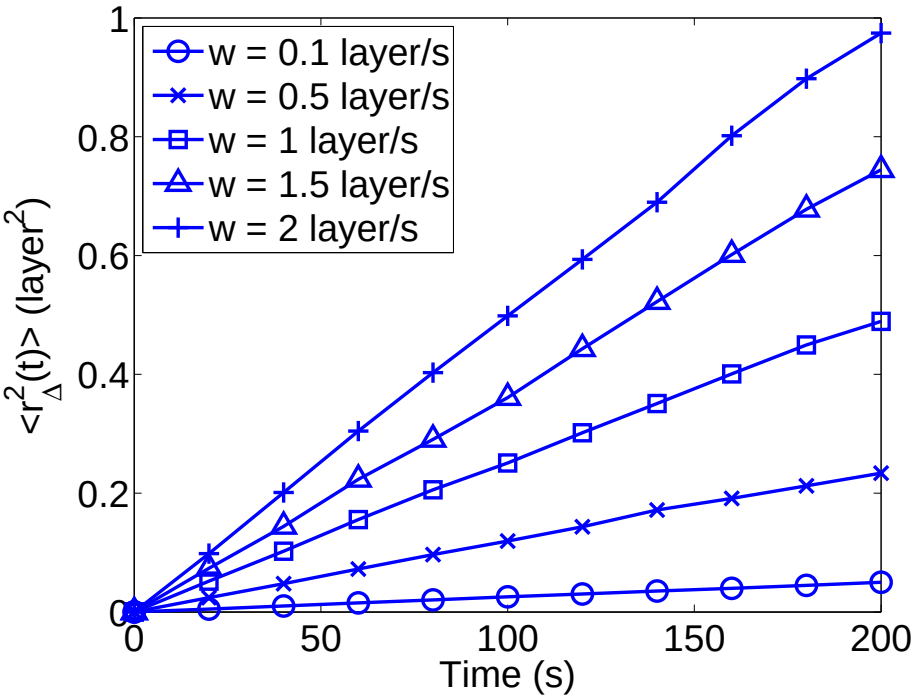

Figure 6.6: Evolution of expected aggregate surface roughness with respect to time for different deposition rates (unit of w is layer/s) obtained from kMC simulations.

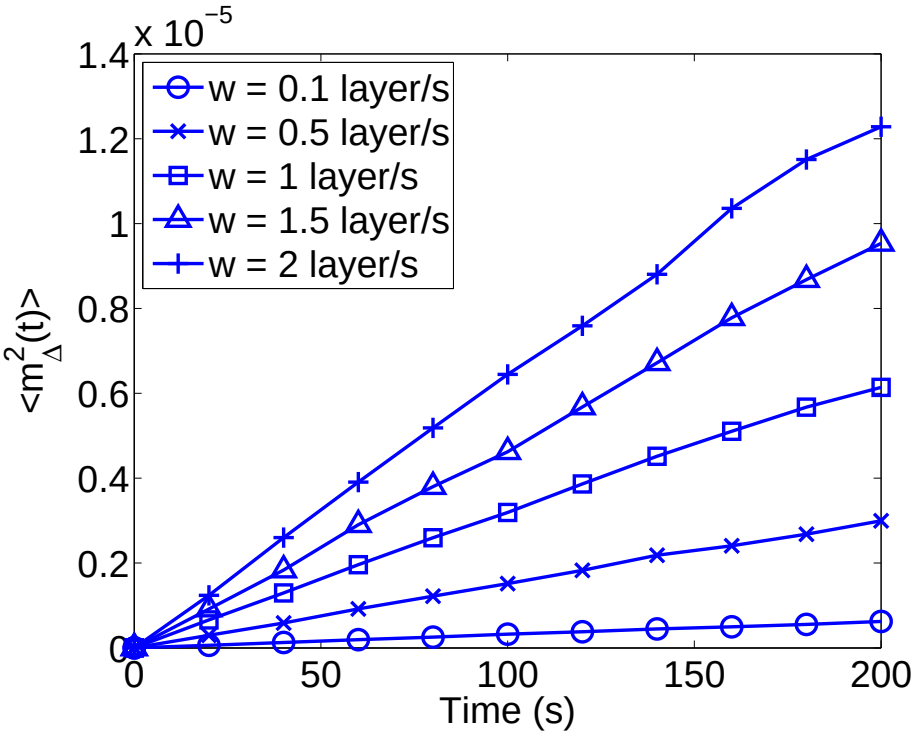

Figure 6.7: Evolution of expected aggregate surface slope with respect to time for different deposition rates (unit of *w* is layer/s) obtained from kMC simulations.

deposition rate profiles significantly changes the dynamic profiles of aggregate surface morphology. However, some properties obtained under uniform deposition rate evolution profiles remain valid, for example, the expected values of aggregate surface roughness and slope still increase with mean deposition rate w_0. Furthermore, simulations are carried out at $w_0 = 2$ layer/s with different magnitude, A, values to investigate the influence of the strength of patterned deposition on the evolution profiles of aggregate surface morphology. As shown in Fig. 6.10 and Fig. 6.11, the magnitude, A, has substantial influence on the dynamics of aggregate surface morphology. Both aggregate roughness and aggregate slope can be increased substantially by manipulating A compared to the aggregate surface morphology achieved with a uniform deposition rate profile. Thus, the introduction of a patterned deposition rate profile expands the range of surface morphology values that can be obtained and makes surface morphology control at length scales comparable to visible light wavelength possible.

6.3 Closed-form modeling and parameter estimation

6.3.1 Edward-Wilkinson-type equation of aggregate surface height

Given the complexity of the two species deposition process and the need to control surface roughness and slope at spatial scales comparable to the wavelength of visible light, the direct computation of a closed-form model, describing the surface height evolution and is suitable for controller design, from the microscopic deposition mechanisms is a very dif-

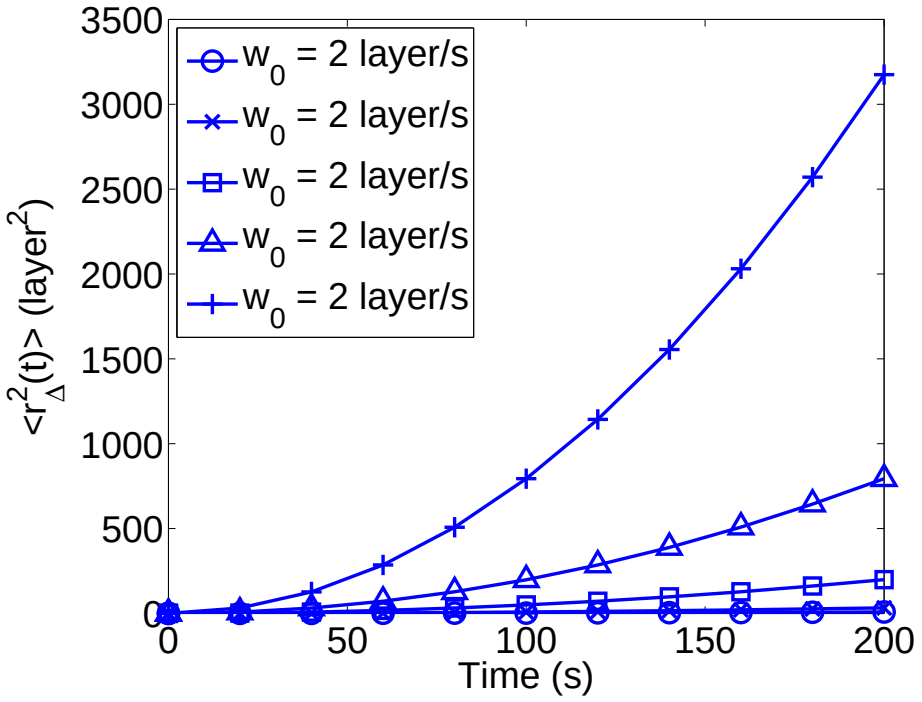

Figure 6.8: Evolution of expected aggregate surface roughness with respect to time for different mean deposition rates (unit of w_0 is layer/s) obtained from kMC simulations. Patterned deposition with $k = 5$ and $A = 0.1w_0$.

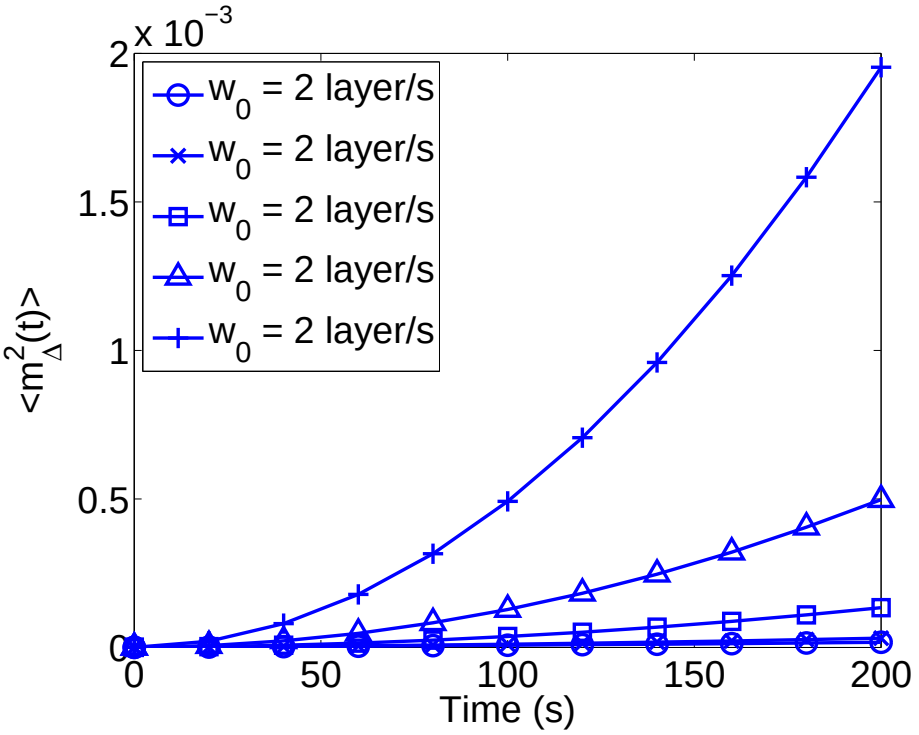

Figure 6.9: Evolution of expected aggregate surface slope with respect to time for different mean deposition rates (unit of w_0 is layer/s) obtained from kMC simulations. Patterned deposition with $k = 5$ and $A = 0.1w_0$.

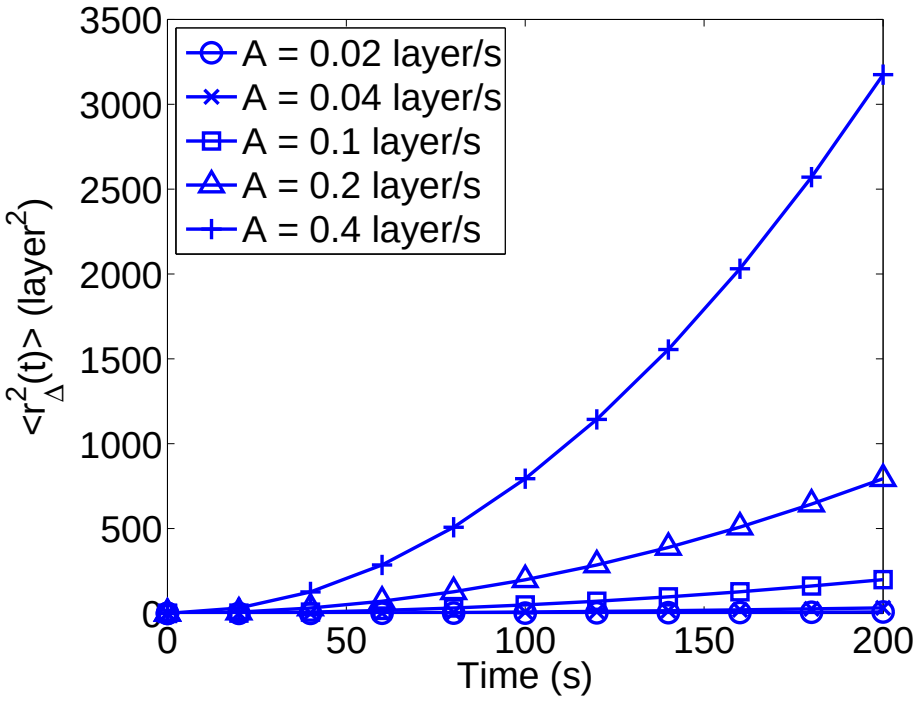

Figure 6.10: Evolution of expected aggregate surface roughness with respect to time for different patterned deposition rate magnitudes obtained from kMC simulations. Patterned deposition with $k = 5$ and $w_0 = 2$ layer/s.

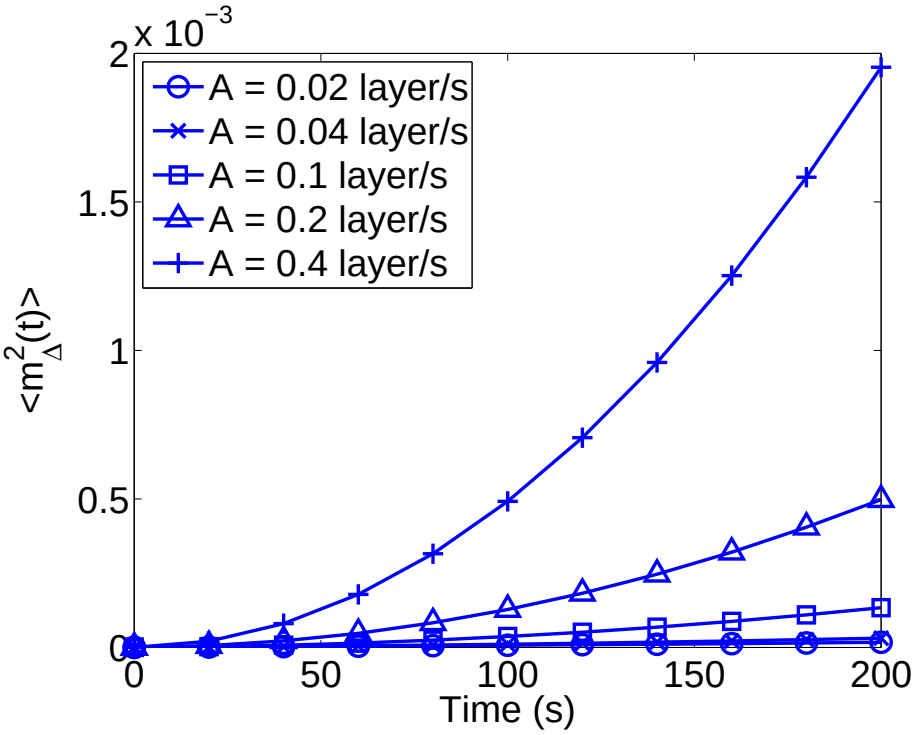

Figure 6.11: Evolution of expected aggregate surface slope with respect to time for different patterned deposition rate magnitudes obtained from kMC simulations. Patterned deposition with $k = 5$ and $w_0 = 2$ layer/s.

ficult (if not impossible) task. Therefore, a hybrid modeling approach should be used in which a basic closed-form modeling structure is used and the model parameters are computed such that the predictions of key variables from the closed-form model are close to the one of the kinetic Monte-Carlo model for a broad set of operating conditions. To this end, we use an Edward-Wilkinson(EW)-type equation, which is a second-order stochastic PDE, to describe the aggregate surface height evolution and compute its parameters from kMC data. The choice of the EW-equation is motivated by the fact that it has been used in many deposition processes that involve a thermal balance between adsorption and relaxation/migration [3]. Specifically, a one-dimensional EW-type equation is used to describe the evolution of aggregate surface height profile:

$$\frac{\partial h_\Delta}{\partial t} = w(x,t) + c_2 \frac{\partial^2 h_\Delta}{\partial x^2} + \xi(x,t) \tag{6.8}$$

subject to the following periodic boundary conditions

$$h_\Delta(0,t) = h_\Delta(L,t) \tag{6.9}$$

$$\frac{\partial h_\Delta}{\partial x}(0,t) = \frac{\partial h_\Delta}{\partial x}(L,t) \tag{6.10}$$

and the initial condition

$$h_\Delta(x,0) = h_\Delta^0(x) \tag{6.11}$$

where $x \in [0,L]$ is the spatial coordinate, t is the time, $h_\Delta(x,t)$ is the aggregate surface height and $\xi(x,t)$ is a Gaussian white noise with zero mean and the following covariance:

$$\left\langle \xi(x,t)\xi(x',t') \right\rangle = \sigma^2 \delta(x-x')\delta(t-t') \tag{6.12}$$

where $\delta(\cdot)$ denotes the Dirac delta function. In Eq. 6.8, the parameters c_2 and σ^2, corresponding to diffusion effects and stochastic noise respectively, depend on the deposition rate $w(x,t)$. In the case of a patterned deposition rate profile (control actuation), the term $w(x,t)$ is of the form:

$$w(x,t) = w_0(t) + A(t)\sin\left(\frac{2k\pi}{L}x\right) \tag{6.13}$$

where $w_0(t)$ is the total mean deposition rate and $A(t)$ is the total magnitude of patterned deposition rate. In the context of two species simulations, $w(x,t)$, $w_0(t)$ and $A(t)$ can be seen as the sum of corresponding values from each component (i.e., $w(x,t) = w_1(x,t) + w_2(x,t)$, $w_0(t) = w_{1,0}(t) + w_{2,0}(t)$, $A(t) = A_1(t) + A_2(t)$) and k is the number of sine waves between 0 and L.

To analyze the dynamics and obtain a solution of the EW equation suitable for real-time controller calculations, we first consider the eigenvalue problem of the linear operator of Eq. 6.8 subject to the periodic boundary conditions of Eqs. 6.9–6.10:

$$\mathscr{A}\bar{\phi}_n(x) = c_2\frac{d^2\bar{\phi}_n(x)}{dx^2} = \lambda_n\bar{\phi}_n(x), \tag{6.14}$$

$$\nabla^j\bar{\phi}_n(0) = \nabla^j\bar{\phi}_n(L), \quad j = 0,1 \tag{6.15}$$

where λ_n denotes an eigenvalue, $\bar{\phi}_n$ denotes an eigenfunction, and ∇^j, $j = 0$, 1, denotes the gradient of a given function. The solution of the eigenvalue problem of Eqs. 6.14–6.15 is

as follows:

$$\lambda_n = -\frac{4c_2\pi^2 n^2}{L^2} \tag{6.16}$$

$$\phi_{1,n}(x) = \phi_n = \sqrt{\frac{2}{L}}\sin(\frac{2n\pi}{L}x) \tag{6.17}$$

$$\phi_{2,n}(x) = \psi_n = \begin{cases} \sqrt{\frac{1}{L}} & n = 0 \\ \\ \sqrt{\frac{2}{L}}\cos(\frac{2n\pi}{L}x) & n \neq 0 \end{cases} \tag{6.18}$$

The solution of the EW equation of Eq. 6.8 can be expanded in an infinite series in terms of the eigenfunctions of the spatial differential operator of Eq. 6.14 as follows:

$$h_\Delta(x,t) = \sum_{n=0}^{L/(2\Delta)} \left(\phi_{1,n}(x)z_{1,n}(t) + \phi_{2,n}(x)z_{2,n}(t)\right), \tag{6.19}$$

where $z_{1,n}(t)$, $z_{2,n}(t)$ are time-varying coefficients.

Substituting the above expansion for the solution, $h_\Delta(x,t)$, into Eq. 6.8 and taking the inner product with the adjoint eigenfunctions, the following system of infinite stochastic linear ordinary differential equations (ODEs) for the temporal evolution of the time-varying coefficients in Eq. 6.19 is obtained:

$$\frac{dz_{2,0}(t)}{dt} = w_{2,0} + \xi_{2,0}(t), \tag{6.20}$$

$$\frac{dz_{p,n}(t)}{dt} = w_{p,n} + \lambda_n z_{p,n} + \xi_{p,n}(t) \tag{6.21}$$

$$p = 1,2, \quad n = 1,\cdots,\frac{L}{2\Delta},$$

where $\xi_{p,n}(t) = \int_0^L \xi(x,t)\phi_{p,n}(x)dx$ is the projection of the noise $\xi(x,t)$ on the ODE for $z_{p,n}$. The noise term, $\xi_{p,n}$, has zero mean and covariance

$$\left\langle \xi_{p,n}(t)\xi_{p,n}(t')\right\rangle = \sigma^2\delta(t-t'). \tag{6.22}$$

Similarly, $w_{p,n}$ is the projection of w on the ODE for $z_{p,n}(t)$, $w_{p,n} = \int_0^L \phi_{p,n}(x)w(x)dx$

- If $p = 1$,

$$w_{1,n} = \begin{cases} 0, & n \neq k \\ \\ A\sqrt{\dfrac{L}{2}}, & n = k \end{cases} \tag{6.23}$$

- If $p = 2$,

$$w_{2,n} = \begin{cases} 0, & n \neq 0 \\ \\ A\sqrt{L}, & n = 0 \end{cases} \tag{6.24}$$

The temporal evolution of the variance of mode $z_{p,n}$ can be obtained from the solution of the linear ODEs of Eqs. 6.20 and 6.21 as follows:

$$\left\langle z_{2,0}(t) \right\rangle = w_{2,0}(t - t_0) \tag{6.25}$$

$$\text{var}(z_{2,0}(t)) = \sigma^2(t - t_0) \tag{6.26}$$

$$\langle z(t) \rangle = e^{\lambda(t-t_0)} \langle z(t_0) \rangle + \frac{w_p}{\lambda}(e^{\lambda(t-t_0)} - 1) \tag{6.27}$$

$$\text{var}(z(t)) = e^{2\lambda(t-t_0)} \,\text{var}(z(t_0)) + \sigma^2 \frac{e^{2\lambda(t-t_0)} - 1}{2\lambda} \tag{6.28}$$

where $z(t) = z_{p,n}(t)$, $\lambda = \lambda_n$ and $w_p = w_{p,n}$ for $n \neq 0$.

Finally, it is necessary to point out that, when aggregate (discrete) surface height profile is used, the highest number of modes that can be accurately estimated from $h_\Delta(x,t)$ is limited by the spatial sampling points, $n \leq \dfrac{L}{2\Delta}$; the reader may refer to [57] for a detailed discussion of the issue.

6.3.2 Aggregate surface root–mean–square roughness

Aggregate surface roughness of the thin film is defined as the standard deviation of the aggregate surface height profile from its average height

$$r_\Delta(t) = \sqrt{\frac{1}{L}\int_0^L \left[h_\Delta(x,t) - \bar{h}_\Delta(t)\right]^2 dx} \tag{6.29}$$

where $\bar{h}_\Delta(t) = \dfrac{1}{L}\displaystyle\int_0^L h_\Delta(x,t)dx$ is the average aggregate surface height. According to Eq. 6.19, we have

$$\bar{h}_\Delta(t) = \frac{1}{L}\int_0^L \phi_{2,0} z_{2,0} dx = \sqrt{\frac{1}{L}} z_{2,0} \tag{6.30}$$

Using that

$$h_\Delta(x,t) - \bar{h}_\Delta(t) = \sum_{n=1}^{L/(2\Delta)} \sum_{p=1}^{2} \phi_{p,n}(x) z_{p,n}(t) \tag{6.31}$$

the expected aggregate surface roughness, $\left\langle r_\Delta^2(t)\right\rangle$, of Eq. 6.29 can be re-written as

$$\begin{aligned}
\left\langle r_\Delta^2(t)\right\rangle &= \left\langle \frac{1}{L}\int_0^L \left[\sum_{p=1}^{2}\sum_{n=1}^{L/(2\Delta)} z_{p,n}(t)\phi_{p,n}(x)\right]^2 dx \right\rangle \\
&= \left\langle \frac{1}{L}\int_0^L \sum_{n=1}^{L/(2\Delta)} \left(\phi_{1,n}^2(x) z_{1,n}^2(t) + \phi_{2,n}^2(x) z_{2,n}^2(t)\right) dx \right\rangle \\
&= \frac{1}{L}\sum_{n=1}^{L/(2\Delta)} \left(\left\langle z_{1,n}^2\right\rangle + \left\langle z_{2,n}^2\right\rangle\right)
\end{aligned} \tag{6.32}$$

where

$$\left\langle z_{p,n}^2\right\rangle = \mathrm{var}(z_{p,n}) + \left\langle z_{p,n}\right\rangle^2. \tag{6.33}$$

The expression of Eqs. 6.32–6.33 will be used in the MPC formulation; see Eq. 6.42 below.

6.3.3 Aggregate surface root–mean–square slope

The aggregate rms slope is defined as the root–mean–square of the aggregate surface slope in the x–direction as follows:

$$\begin{aligned} m_{\Delta}(t) &= \sqrt{\frac{1}{L}\int_0^L \left(\frac{\partial h_{\Delta}}{\partial x}\right)^2 dx} \\ &= \sqrt{\frac{1}{L}\sum_{i=0}^{L/\Delta}\left(\frac{h_{\Delta}(i+1,t)-h_{\Delta}(i,t)}{\Delta}\right)^2 \Delta} \end{aligned} \tag{6.34}$$

Using the expansion of Eq. 6.19, Eq. 6.34 can be written as:

$$\begin{aligned} \left\langle m_{\Delta}^2(t)\right\rangle &= \left\langle \frac{1}{L}\sum_{i=0}^{L/\Delta}\left(\frac{h_{\Delta}(i+1,t)-h_{\Delta}(i,t)}{\Delta}\right)^2 \Delta \right\rangle \\ &= \left\langle \frac{1}{L\Delta}\sum_{i=0}^{L/\Delta}\left\{\sum_{p=1}^{2}\sum_{n=0}^{L/(2\Delta)} z_{p,n}\left[\phi_{p,n}(i+1)-\phi_{p,n}(i)\right]\right\}^2 \right\rangle \\ &= \left\langle \frac{1}{L\Delta}\sum_{i=0}^{L/\Delta}\sum_{p_1=1}^{2}\sum_{n_1=0}^{L/(2\Delta)}\sum_{p_2=1}^{2}\sum_{n_2=0}^{L/(2\Delta)} z_{p_1,n_1}z_{p_2,n_2}d\phi_{p_1,n_1}(i)d\phi_{p_2,n_2}(i) \right\rangle \\ &= \frac{1}{L\Delta}\sum_{p_1=1}^{2}\sum_{n_1=0}^{L/(2\Delta)}\sum_{p_2=1}^{2}\sum_{n_2=0}^{L/(2\Delta)} \left\langle z_{p_1,n_1}z_{p_2,n_2}\right\rangle \left(\sum_{i=0}^{L/\Delta} d\phi_{p_1,n_1}(i)d\phi_{p_2,n_2}(i)\right) \end{aligned} \tag{6.35}$$

where

$$\begin{aligned} &\sum_{i=0}^{L/\Delta} d\phi_{p_1,n_1}(i)d\phi_{p_2,n_2}(i) \\ =&\sum_{i=0}^{L/\Delta}\left(\phi_{p_1,n_1}(i+1)-\phi_{p_1,n_1}(i)\right)\left(\phi_{p_2,n_2}(i+1)-\phi_{p_2,n_2}(i)\right) \\ =&\frac{2}{L}\left(\sum_{i=0}^{L/\Delta}\left(\sin(\frac{2n_1\pi}{L/\Delta}(i+1))-\sin(\frac{2n_1\pi}{L/\Delta}i)\right)\left(\sin(\frac{2n_2\pi}{L/\Delta}(i+1))-\sin(\frac{2n_2\pi}{L/\Delta}i)\right)\right) \\ =&\frac{8}{L}\sin(\frac{n_1\pi}{L/\Delta})\sin(\frac{n_2\pi}{L/\Delta})\sum_{i=0}^{L/\Delta}\left(\cos(\frac{n_1\pi}{L/\Delta}(2i+1))\cos(\frac{n_2\pi}{L/\Delta}(2i+1))\right) \end{aligned} \tag{6.36}$$

or more compactly:

$$\begin{aligned}\left\langle m_{\Delta}^{2}(t)\right\rangle &= \frac{1}{L\Delta}\sum_{p_1=1}^{2}\sum_{n_1=0}^{L/(2\Delta)}\sum_{p_2=1}^{2}\sum_{n_2=0}^{L/(2\Delta)}\left\langle z_{p_1,n_1}z_{p_2,n_2}\right\rangle\left(\sum_{i=0}^{L/\Delta}d\phi_{p_1,n_1}(i)d\phi_{p_2,n_2}(i)\right)\\ &= \frac{1}{L\Delta}\sum_{p=1}^{2}\sum_{n=0}^{L/(2\Delta)}\left\langle z_{p,n}\right\rangle^{2}\left(\frac{8}{L}\sin^{2}(\frac{n\pi}{L/\Delta})\sum_{i=0}^{L/\Delta}\left(\cos^{2}(\frac{n\pi}{L/\Delta}(2i+1))\right)\right) \qquad (6.37)\\ &= \sum_{p=1}^{2}\sum_{n=0}^{L/(2\Delta)}K_{p,n}\left\langle z_{p,n}^{2}\right\rangle\end{aligned}$$

where

$$\begin{aligned}K_{p,n} &= \frac{8}{L^{2}\Delta}\sin^{2}\left(\frac{\pi n}{L/\Delta}\right)\sum_{i=0}^{L/(2\Delta)}\left(\cos^{2}\left(\frac{n\pi}{L/\Delta}(2i+1)\right)\right)\\ &= \begin{cases}\dfrac{8}{L\Delta^{2}}\sin^{2}\left(\dfrac{\pi n}{L/\Delta}\right) & n=0\\ \dfrac{4}{L\Delta^{2}}\sin^{2}\left(\dfrac{\pi n}{L/\Delta}\right) & n\neq 0\end{cases}\end{aligned} \qquad (6.38)$$

Finally, using that

$$\begin{aligned}&\sum_{i=0}^{L/(2\Delta)}\left(\cos^{2}\left(\frac{n\pi}{L/\Delta}(2i+1)\right)\right)\\ &\quad= \sum_{i=0}^{L/(2\Delta)}\left(\frac{\cos\left(2n\pi(2i+1)/(L/\Delta)\right)+1}{2}\right)\\ &\quad= \begin{cases}\dfrac{L}{\Delta} & \text{if } n=0\\ \\ \dfrac{L}{2\Delta} & \text{if } n\neq 0\end{cases}\end{aligned} \qquad (6.39)$$

$\left\langle m_{\Delta}^{2}(t)\right\rangle$ can be expressed as:

$$\left\langle m^{2}(t)\right\rangle = \sum_{m=1}^{L/(2\Delta)}\left(K_{1,m}\left\langle z_{1,m}^{2}\right\rangle + K_{2,m}\left\langle z_{2,m}^{2}\right\rangle\right) \qquad (6.40)$$

The expression of Eq. 6.40 will be used in the MPC formulation; please see Eq. 6.42 below.

6.3.4 Parameter estimation

Referring to the EW equation of Eq. 6.8, there are two model parameters, c_2 and σ^2, that must be determined as functions of the total mean deposition rate w_0 and of the total patterned deposition rate magnitude A. These parameters affect the dynamics of aggregate surface roughness and slope and can be estimated by fitting the predicted evolution profiles for aggregate surface roughness and slope from the EW equation to profiles of aggregate surface roughness and slope from kMC simulations. Least-square methods are used to estimate the model parameters so that the EW-model predictions are close in a least-square sense to the kMC simulation data. Comparison of the predictions of both models are shown in Fig. 6.12. Based on c_2 and σ^2 values obtained from these fitting results, different functions are chosen to estimate c_2 and σ^2 values at different w with the least-square method. Specifically, a linear function with respect to $\log(w)$ is chosen to estimate $\log(c_2)$ and a linear function with respect to w is chosen to estimate σ^2, and the expressions are given as follows:

$$c_2(w) = w_{c_2}^{a} \cdot e_{c_2}^{b} \tag{6.41}$$

$$\sigma^2 = a_{\sigma^2} w + b_{\sigma^2}$$

where a_{c_2}, b_{c_2}, a_{σ^2} and b_{σ^2} are time-invariant fitting model parameters. The fitting results are shown in Fig. 6.13 and Fig. 6.14. To verify the fitting function, two more groups of simulations are carried out with larger deposition rates ($w = 5$ and 10 layer/s) and fitted to EW equation, and the obtained values for c_2 and σ^2 are used to extend the fitting curve

to show the validity of the chosen fitting functions. It is necessary to clarify that these fitting results are based on kMC simulations with uniform deposition rate profiles ($A = 0$). For simulations with patterned deposition rate profiles ($A \neq 0$), it is assumed that c_2 and σ^2 models obtained from uniform deposition rate simulations ($A = 0$) can be used to estimate c_2 and σ^2 values. To verify this assumption, the solutions of EW equations for aggregate surface evolution with patterned deposition rate profile are obtained based on c_2 and σ^2 models from open-loop kMC data with uniform deposition rate, and these dynamic evolution profiles are compared with open-loop kMC dynamic evolution profiles with patterned deposition rate profiles. As shown in Fig. 6.15 and Fig. 6.16, c_2 and σ^2 models from open-loop kMC data with uniform deposition rate can be used in the EW equation to predict aggregate surface roughness and slope of the kMC model with patterned deposition rate. We note that the approach presented for the computation of the parameters of the closed-form PDE model of Eq. 6.8 is not limited to the specific PDE system and can be used in the context of other dissipative PDE systems that model the evolution of surface height of deposition processes. Finally, referring to the dependence of surface roughness and slope on lattice size, we note that both atomic and aggregate surface roughness and slope increase with increasing lattice size (this issue has been extensively studied in another work [24]); however, the proposed approach to closed-form modeling and MPC design is scalable and can be used in the context of different lattice size kMC models as long as the parameters of the stochastic PDE model of Eq. 6.8 and their dependence on deposition rate are computed on the basis of data obtained from the lattice size considered.

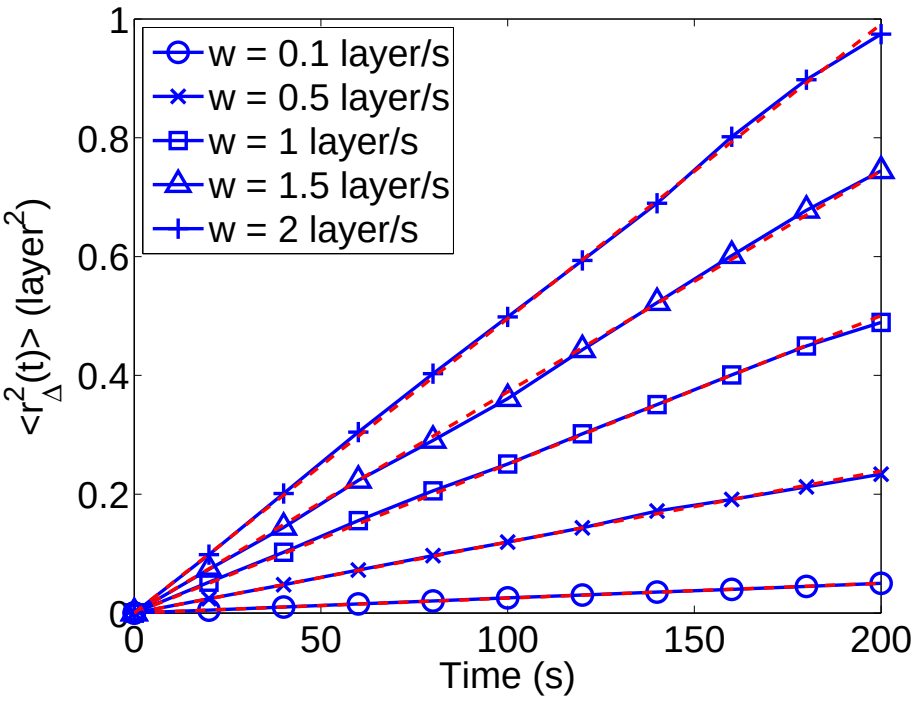

Figure 6.12: Evolution of expected aggregate surface roughness with respect to time for different spatially-uniform deposition rates obtained from kMC simulations (solid lines with symbols).The analytical solutions for the aggregate surface roughness obtained from the corresponding EW equations with the fitted values for c_2 and σ^2 are also shown (dashed lines).

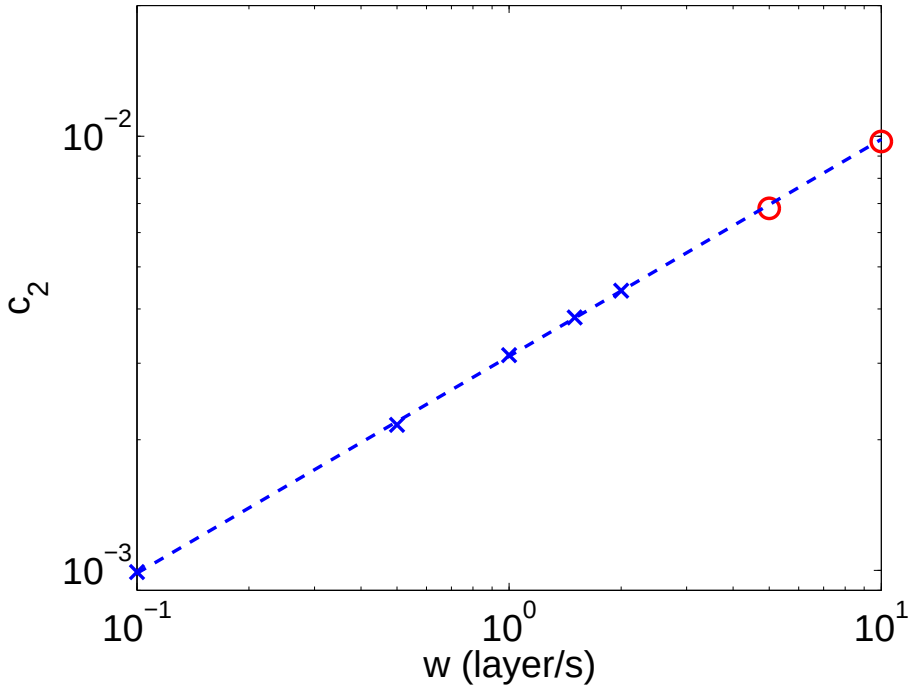

Figure 6.13: c_2 values for different spatially-uniform deposition rates w. The solid line is the result of a linear fitting function and it is the $log(c_2)$ versus $log(w)$ relationship used by the predictive controller. The first 5 blue cross markers are used to generate the fitting function, and the last 2 red circle markers are used to test the validity of the fitting function.

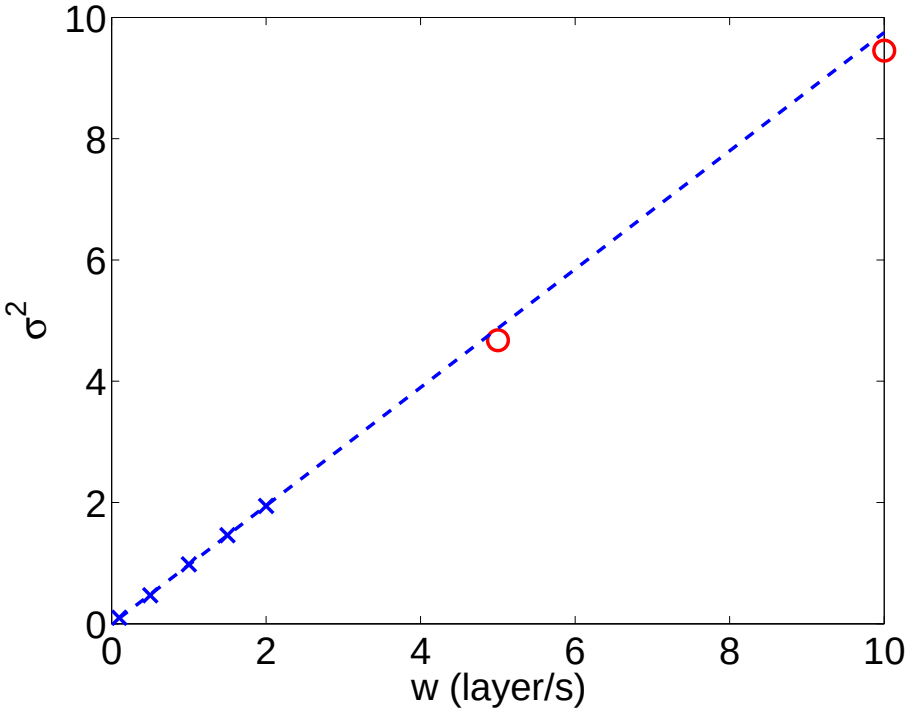

Figure 6.14: σ^2 values for different spatially-uniform deposition rates w. The solid line is the result of a linear fitting function.The first 5 blue cross markers are used to generate the fitting function, and the last 2 red circle markers are used to test the validity of the fitting function.

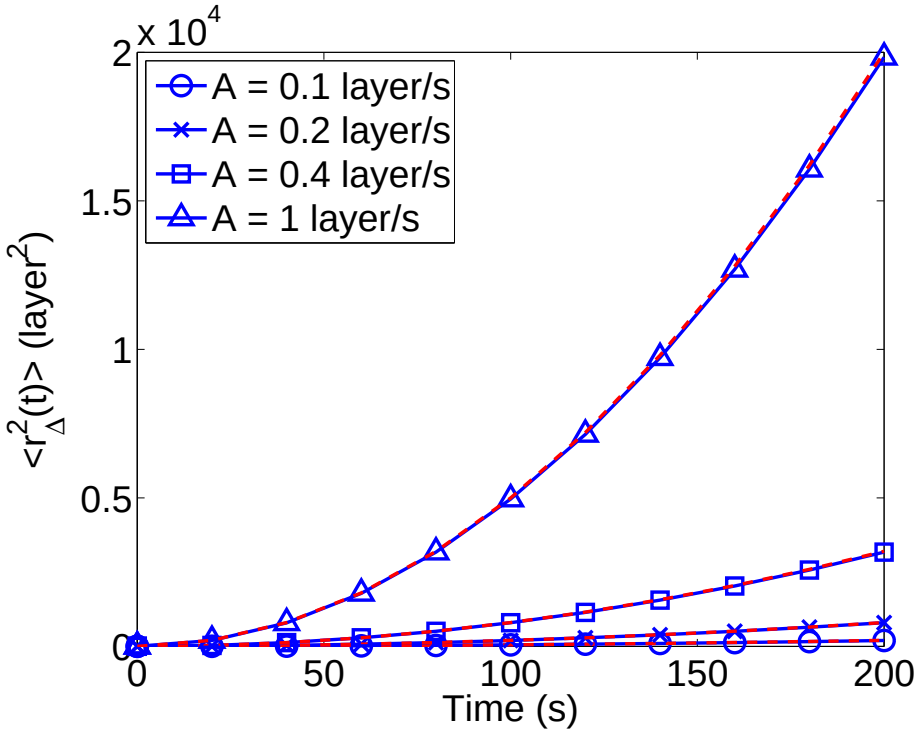

Figure 6.15: Evolution of expected aggregate surface roughness for different patterned deposition magnitudes from the kMC model (solid lines with symbols) and expected aggregate roughness solutions from the corresponding EW equations (dashed lines). The c_2 and σ^2 values of the EW equations were estimated from open-loop aggregate surface roughness kMC model data with spatially-uniform deposition rates.

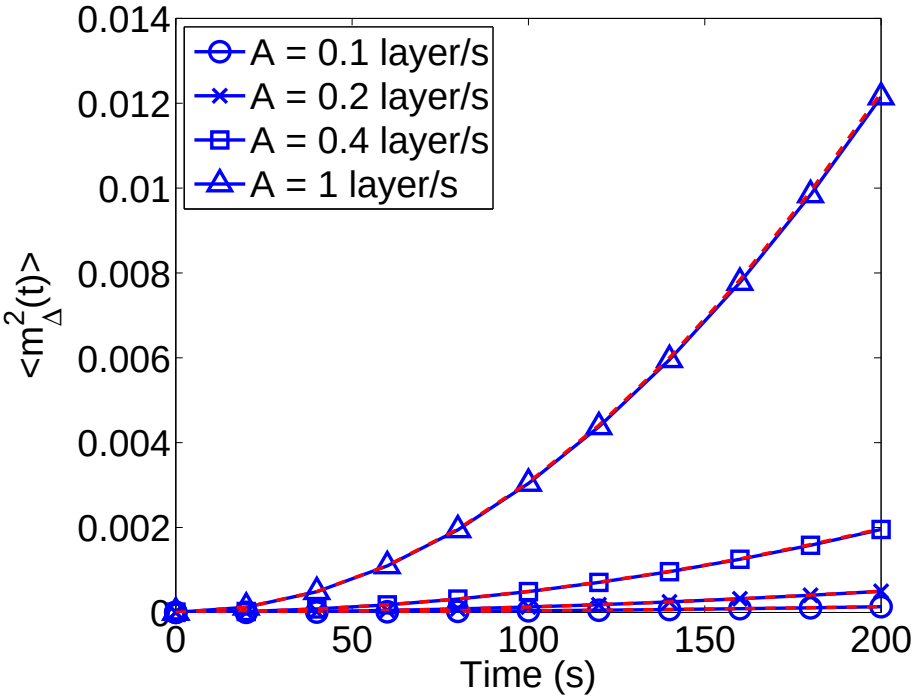

Figure 6.16: Evolution of expected aggregate surface slope for different patterned deposition magnitudes from the kMC model (solid lines with symbols) and expected aggregate slope solutions from the corresponding EW equations (dashed lines). The c_2 and σ^2 values of the EW equations were estimated from open-loop aggregate surface roughness kMC model data with spatially-uniform deposition rates.

6.4 Model predictive control

In this section, we design a model predictive controller based on the dynamic models of aggregate surface roughness and slope to simultaneously control the expected values of aggregate surface roughness and slope square to desired levels. The dynamics of aggregate surface roughness and slope of the TCO thin film are described by the EW equation of aggregate surface height of Eq. 6.8 with the computed parameters of subsection 6.3.4. State feedback control is considered in this work, i.e., $h_\Delta(x,t)$ is assumed to be available for feedback. In practice, real-time surface height measurements can be obtained via atomic force microscopy (AFM) systems.

6.4.1 MPC formulation for regulation of aggregate roughness and slope

We consider the problem of regulation of aggregate surface roughness and slope to desired levels within a model predictive control framework. Due to the stochastic nature of the variables, the expected values of aggregate surface roughness and slope, $\left\langle r_\Delta^2(t)\right\rangle$ and $\left\langle m_\Delta^2(t)\right\rangle$, are chosen as the control objectives. The total mean deposition rate, w_0 ($w_0 = w_{1,0} + w_{2,0}$), and magnitude of patterned deposition rate, A ($A = A_1 + A_2$), are chosen as the manipulated inputs; the substrate temperature is fixed at $T = 800K$ during all closed-loop simulations. To account for a number of practical considerations, several constraints are added to the control problem. In particular, since $w(x) \geq 0$, the constraint $0 \leq A_1 \leq w_{1,0}$ and $0 \leq A_2 \leq w_{2,0}$ are imposed to ensure $w(x,t) > 0$, $\forall (x,t)$. To ensure the validity of the

closed-form process model, there is a constraint on the range of variation of the mean deposition rate. Another constraint is imposed on the rate of change of the mean deposition rate to account for actuator limitations. The control action at time t is obtained by solving a finite-horizon optimal control problem. The cost function in the optimal control problem includes penalty on the deviation of $\left\langle r_{\Delta}^2 \right\rangle$ and $\left\langle m_{\Delta}^2 \right\rangle$ from their respective set-point values. Different weighting factors are assigned to the aggregate surface roughness and slope. Aggregate surface roughness and slope have very different magnitudes, therefore, relative deviations are used in the formulation of the cost function to make the magnitude of the two terms comparable in the cost function. The optimization problem is subject to the dynamics of the aggregate surface height of Eq. 6.8. The optimal w_0 and A values are calculated at each sampling time by solving a finite-dimensional optimization problem in a receding horizon fashion. Specifically, the MPC problem at time t is formulated as follows:

$$\min_{w_0,A} f(w_0,A) = q_{r^2}\left[\frac{r_{set}^2 - \left\langle r_{\Delta}^2(t_f)\right\rangle}{r_{set}^2}\right]^2 + q_{m^2}\left[\frac{m_{set}^2 - \left\langle m_{\Delta}^2(t_f)\right\rangle}{m_{set}^2}\right]^2 \tag{6.42}$$

where

$$\left\langle r_{\Delta}^2(t_f)\right\rangle = \frac{1}{L}\sum_{n=1}^{L/(2\Delta)}\sum_{p=1}^{2}\left\langle z_{p,n}^2(t_f)\right\rangle, \quad \left\langle m_{\Delta}^2(t_f)\right\rangle = \sum_{n=1}^{L/(2\Delta)}\sum_{p=1}^{2}\left(K_{p,n}\left\langle z_{p,n}^2(t_f)\right\rangle\right) \tag{6.43}$$

$$\left\langle z_{p,n}^2(t_f)\right\rangle = \mathrm{var}(z_{p,n}(t_f)) + \left\langle z_{p,n}(t_f)\right\rangle^2 \tag{6.44}$$

$$\left\langle z_{p,n}(t_f)\right\rangle = e^{\lambda_n(t_f-t)}\left\langle z_{p,n}(t)\right\rangle + \frac{w_p}{\lambda_n}(e^{\lambda_n(t_f-t)}-1) \tag{6.45}$$

$$\mathrm{var}(z_{p,n}(t_f)) = e^{2\lambda_n(t_f-t)}\,\mathrm{var}(z_{p,n}(t)) + \sigma^2(w)\frac{e^{2\lambda_n(t_f-t)}-1}{2\lambda_n} \tag{6.46}$$

$$\lambda_n = -\frac{4c_2(w)\pi^2}{L^2}n^2 \tag{6.47}$$

and

$$c_2(w_0) = w_0^{a_{c_2}} \cdot e_{c_2}^{b} \tag{6.48}$$

$$\sigma^2(w_0) = a_{\sigma^2} w_0 + b_{\sigma^2} \tag{6.49}$$

subject to:

$$w_{min} \leq w_0 \leq w_{max}, \quad |w_0(t) - w_0(t-dt)| \leq \delta w_{max}, \tag{6.50}$$

$$w_1 = w_{1,0} + A_1 \sin\left(\frac{k\pi x}{L}\right), \quad 0 \leq A_1 \leq w_{1,0} \tag{6.51}$$

$$w_2 = w_{2,0} + A_2 \sin\left(\frac{k\pi x}{L}\right), \quad 0 \leq A_2 \leq w_{2,0} \tag{6.52}$$

where t is the current time, dt is the sampling time, q_{r^2} and q_{m^2} are the weighting penalty factors for the deviations of $\langle r_\Delta^2 \rangle$ and $\langle m_\Delta^2 \rangle$ from their respective set-points at the ith prediction step, w_{min} and w_{max} are the lower and upper bounds on the mean deposition rate, respectively, and δw_{max} is the limit on the rate of change of the mean deposition rate. Given the batch nature of the deposition process, the MPC of Eq. 6.42 includes penalty on the discrepancy of the expected surface roughness and slope at the end of the deposition from the set-points values of surface roughness and slope that lead to desired film reflectance levels.

The optimal control actions are obtained from the solution of the multivariable optimization problem of Eq. 6.42 and are applied to the deposition process model over dt (i.e., either the EW equation model or the kMC model) during the time interval $(t, t+dt)$. At time $t+dt$, a new measurement of aggregate surface roughness and slope is received by the controller and the MPC problem of Eq. 6.42 is solved for the next set of control actions. An interior point method optimizer, IPOPT [51], is used to solve the optimization

problem in the MPC formulation. With respect to the stability of the closed-loop system, we note the following: the deposition process considered including atom adsorption and atom migration is an inherently stable process; this is evident by the negative values of all the eigenvalues of the spatial differential operator of the Edwards-Wilkinson-type equation (Eq. 6.8) used to model the evolution of surface height for all values of the deposition rare. Given this stability property of the open-loop process and the specific MPC design, the stability of the closed-loop system is ensured.

6.5 Simulation results

In this section, the model predictive controller of Eq. 6.42 is applied to both the one-dimensional EW equation type model of Eq. 6.8 and the one-dimensional kMC model of the thin film growth process. The mean deposition rate ranges from 0.1 to 2 layer/s, the substrate temperature is fixed at 800K, the lattice size of the kMC model is fixed at 40,000 sites, the aggregation size is fixed at 400 to make the results relevant to thin film solar cell applications and five sine waves are used in the patterned deposition rate profile. The sampling time is 10 s; this sampling time is enough for the MPC to carry out the calculations needed to compute the control action. In addition to the deposition rate, the temperature may be used as a manipulated input but it should vary in space to induce substantial aggregate surface roughness and slope values at spatial scales corresponding to the visible light wavelength. Each closed-loop simulation lasts for 200 s. Expected values are calculated from 10 independent closed-loop system simulation runs. In all the simulations, the aggre-

gate surface roughness and slope set-points remain the same, specifically, $r^2_{set} = 1000$ and $m^2_{set} = 0.005$.

6.5.1 MPC application to EW equation model

In this subsection, the EW equation model is utilized in the closed-loop control problem as the plant model. First, the problem of regulating aggregate surface roughness is considered. In this problem, the cost function includes only penalty on the deviation of the expected aggregate surface roughness square from its set-point, *i.e.*, $q_{r^2} = 1$ and $q_{m^2} = 0$. Fig. 6.17 shows the evolution profile of $\left\langle r^2_\Delta(t) \right\rangle$ under the model predictive controller of Eq. 6.42. It is clear that the controller drives the expected aggregate surface roughness to its set-point at the end of the simulation. Fig. 6.18 shows the input profiles of w_0 and A for these simulations. It is necessary to point out that during the first 40 seconds of the simulation time, the optimal solutions of w_0 are constrained by the rate of change constraint and the optimal solutions of A are bounded by the values of w_0.

Next, the aggregate surface slope is regulated. The cost function includes only penalty on the deviation of the expected value of aggregate surface slope square from its set-point ($q_{m^2} = 1$, $q_{r^2} = 0$). Fig. 6.19 shows the evolution profile of the expected aggregate slope square. The aggregate slope reaches its set-point at $t = 200s$. Fig. 6.20 displays the input profile in this scenario.

The next step is the simultaneous regulation of aggregate surface roughness and slope. The weighting factor of aggregate slope square, q_{r^2}, is kept at 1, while the weighting factor

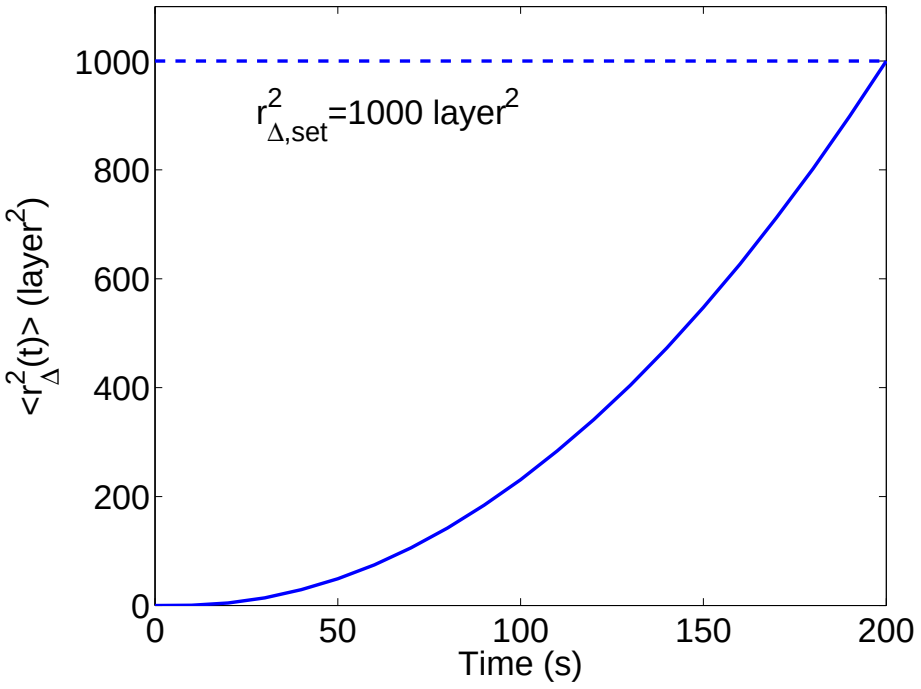

Figure 6.17: Profile of expected aggregate surface roughness square with EW equation as the plant model. $q_{r^2} = 1$, $q_{m^2} = 0$ and $r^2_{set} = 1000$.

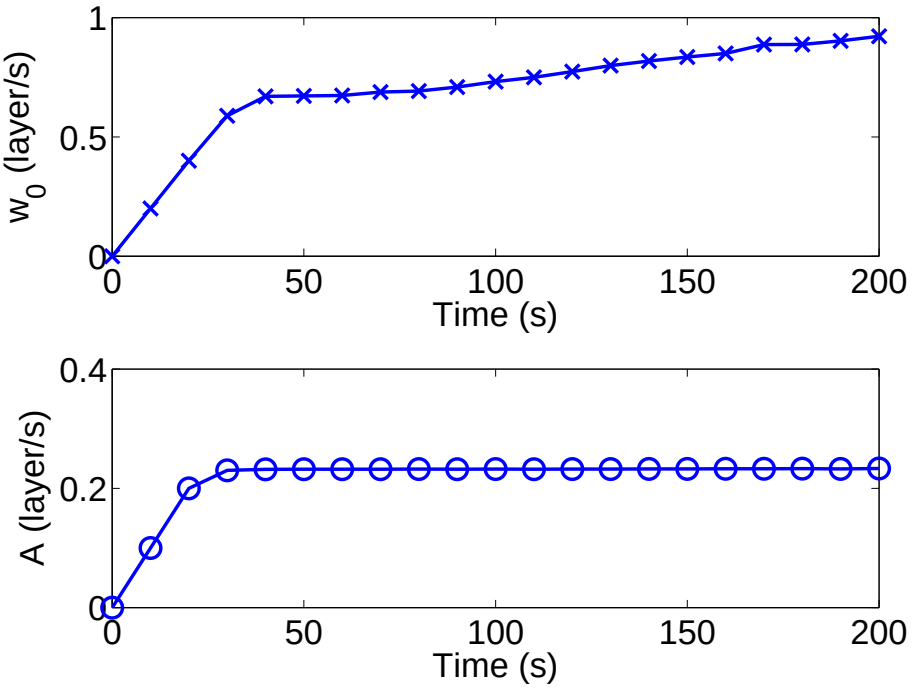

Figure 6.18: Input profiles for aggregate roughness-only control problem with EW equation as the plant model. $q_{r^2} = 1$, $q_{m^2} = 0$ and $r^2_{set} = 1000$.

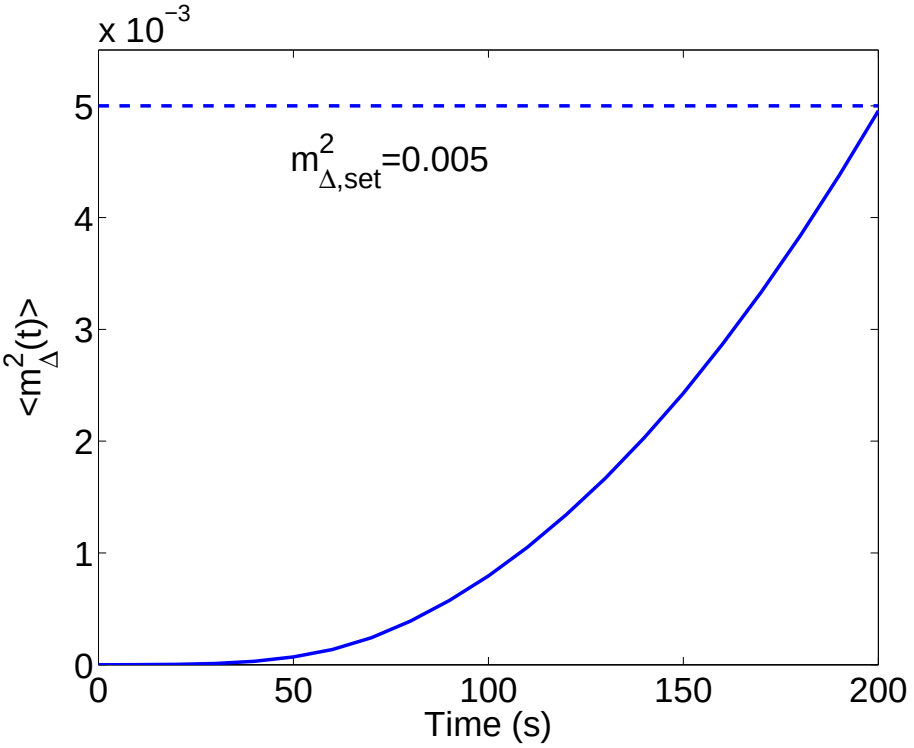

Figure 6.19: Profile of expected aggregate surface slope square with EW equation as the plant model. $q_{r^2} = 0$, $q_{m^2} = 1$ and $m^2_{set} = 0.005$.

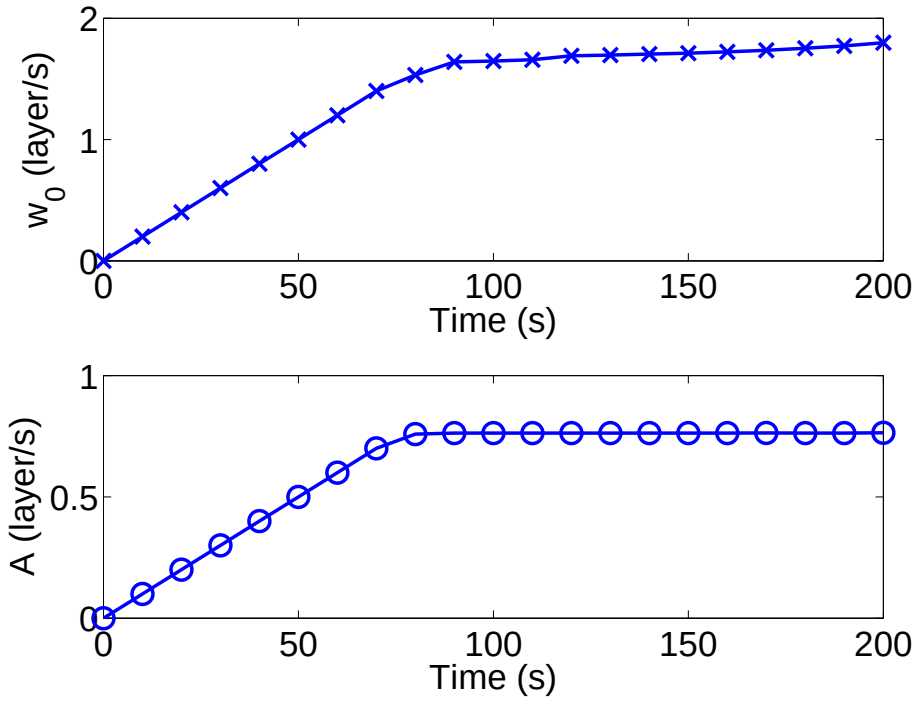

Figure 6.20: Input profiles for aggregate slope-only control problem with EW equation as the plant model. $q_{r^2} = 0$, $q_{m^2} = 1$ and $m^2_{set} = 0.005$.

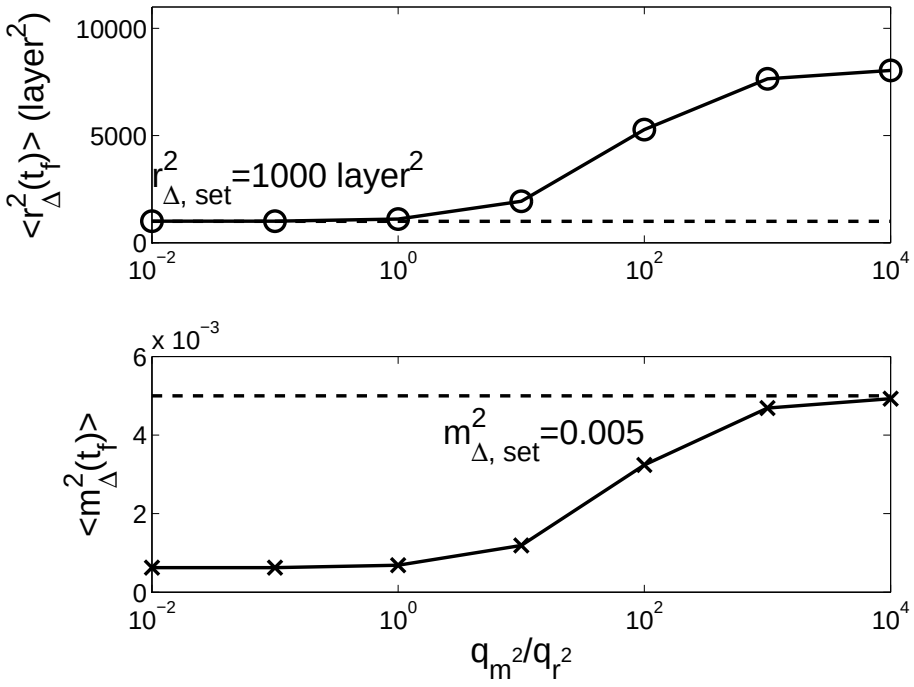

Figure 6.21: $\left\langle r^2_\Delta(t_f)\right\rangle$ and $\left\langle m^2_\Delta(t_f)\right\rangle$ at the end of closed-loop simulations ($t = 200s$) for different penalty weighting factors in the predictive controller with EW equation as the plant model. $10^{-2} \leq q_{m^2} \leq 10^4$, $q_{r^2} = 1$, $r^2_{set} = 1000$ and $m^2_{set} = 0.005$.

of aggregate roughness square, q_{m^2}, increases from 10^{-2} to 10^4. Fig. 6.21 shows the values of expected aggregate surface roughness and slope at the end of closed-loop simulations ($t_f = 200$s) as a function of q_{m^2}/q_{r^2}. It can be seen that as the weighting on aggregate roughness increases, the expected value of aggregate roughness approaches its set-point at the cost of larger deviation of the aggregate slope from its set-point.

6.5.2 MPC application to kMC model

In this subsection, the kMC model is used in the closed-loop control problem as the plant model, while all the other settings remain the same. Fig. 6.22 shows the aggregate surface roughness in the case of roughness-only control while Fig. 6.23 shows the aggregate surface slope in the case of slope-only control. From both plots, we see that both aggregate roughness and slope successfully reach their set-points at the end of the simulations ($t_f = 200$ s). Furthermore, the closed-loop evolution profiles with kMC as the plant model are very similar to the closed-loop profiles that use the EW equation as the plant model, which implies that the EW equation model used in this work can accurately predict the kMC simulation results.

Simultaneous regulation of aggregate surface roughness and slope has also been investigated. Similar to the case where the EW equation is used as the plant model, the weighting factor of aggregate slope square, q_{r^2}, is kept at 1, and the weighting factor of aggregate roughness square, q_{m^2}, ranges from 10^{-2} to 10^4. Fig. 6.24 shows the values of expected aggregate roughness and slope at the end of simulations as a function of q_{m^2}/q_{r^2}. It can be seen that the expected value of aggregate roughness approaches its set-point as q_{m^2} increases at the cost of larger deviation of the aggregate slope from its set-point.

Though with the current actuator design it is difficult to reach the set-points of aggregate roughness and slope at the same time, the actuator design can be easily improved to reach this goal. For example, one way to do this is to introduce a spatially distributed deposition rate profile with multiple sine waves that have independently controlled magnitude values,

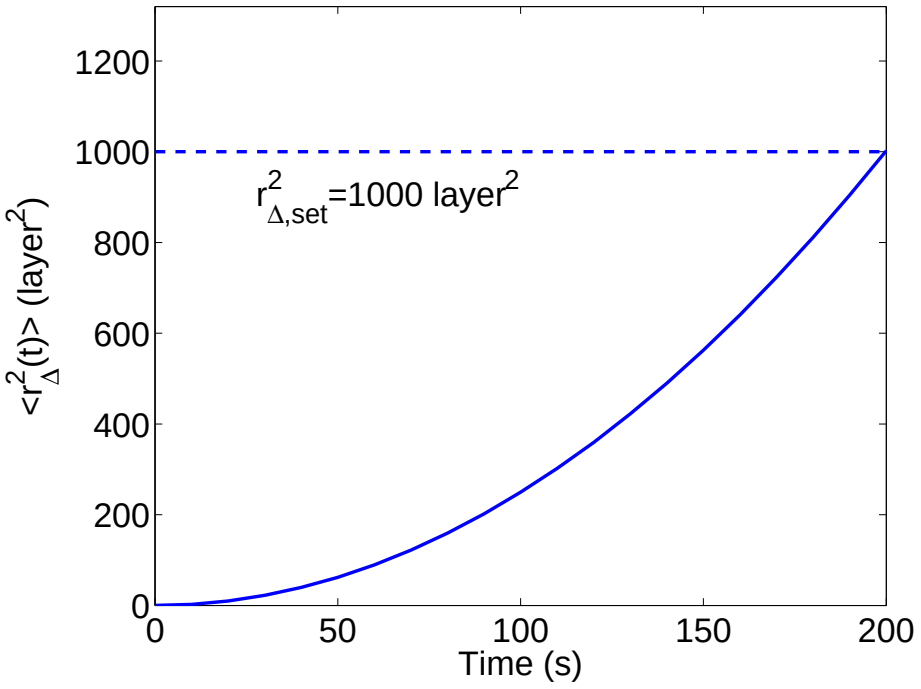

Figure 6.22: Profile of expected aggregate surface roughness square with kMC model as the plant model. $q_{r^2} = 1$, $q_{m^2} = 0$ and $r^2_{set} = 1000$.

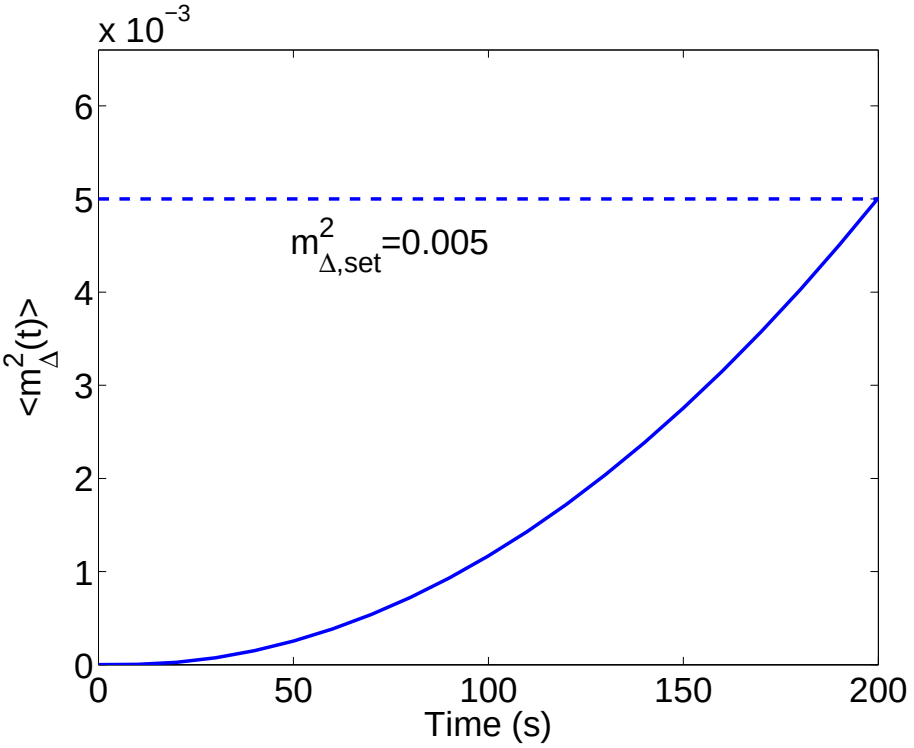

Figure 6.23: Profile of expected aggregate surface slope square with kMC model as the plant model. $q_{r^2} = 0$, $q_{m^2} = 1$ and $m^2_{set} = 0.005$.

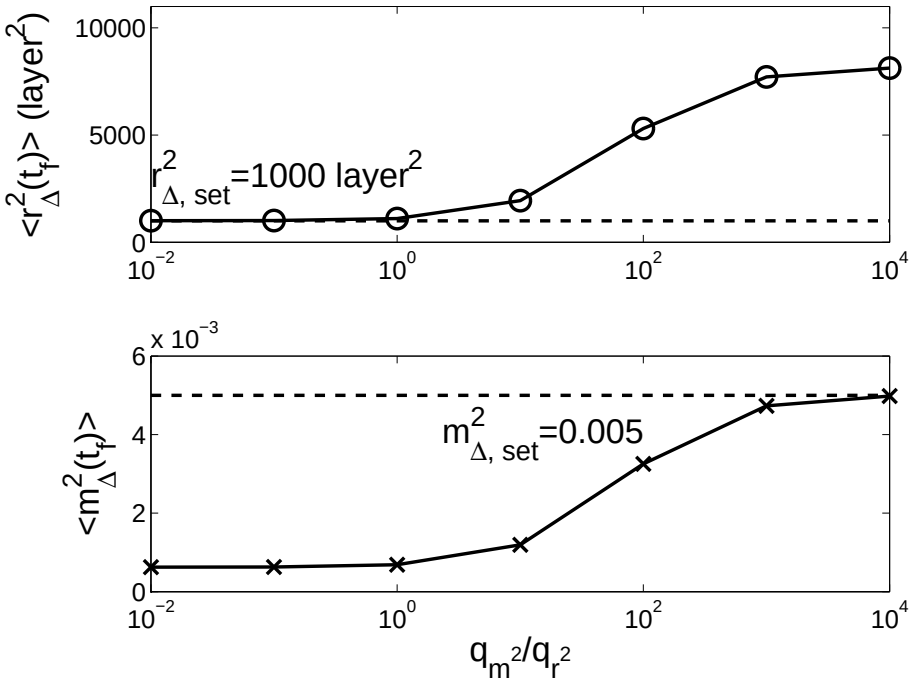

Figure 6.24: $\left\langle r^2_\Delta(t_f)\right\rangle$ and $\left\langle m^2_\Delta(t_f)\right\rangle$ at the end of closed-loop simulations ($t = 200s$) for different penalty weighting factors in the predictive controller with kMC model as the plant model. $10^{-2} \leq q_{m^2} \leq 10^4$, $q_{r^2} = 1$, $r^2_{set} = 1000$ and $m^2_{set} = 0.005$.

and the mean deposition rate and the magnitude value of each sine wave are used as the manipulated variables in the control problem. In this way, set-points of both aggregate roughness and slope can be achieved simultaneously; for details on this approach, please see [26].

Chapter 7

Surface Morphology Control of Transparent Conducting Oxide Layers for Improved Light Trapping Using Wafer Grating and Feedback Control

7.1 Introduction

This chapter focuses on the application of microscopic modeling and analysis of a TCO thin film deposition process on a sinusoidal grated wafer, and model predictive control is utilized to control the surface morphology to desired values. To demonstrate the approach, we focus on a two species thin film deposition process using a grated initial lattice, which

is modeled via kinetic Monte-Carlo simulation. The initial lattice is defined based on a sinusoidal function with proper magnitude ($M = 100$ layers) and 5 sine waves are placed across the lattice. Since a square lattice is used in the model, the initial heights of all the sites are rounded to the nearest lattice site. Different deposition mechanisms are utilized for each component, ZnO and Al. Specifically, a random deposition with surface relaxation (RDSR) mechanism is used for Al and a deposition/migration mechanism is used for ZnO [23]. Since a large-lattice kinetic Monte-Carlo model cannot be used as the basis for controller design and real-time controller calculations, an Edwards-Wilkinson-type equation is used to model the surface evolution and to form the basis for feedback controller design within a model predictive control framework. The cost function of the predicted controller involves penalties on both surface roughness and slope, following [26]. Extensive simulation studies demonstrate that the proposed controller and patterned actuator design successfully regulate surface roughness and slope at visible light wavelength spatial scales to desired set-point values at the end of the deposition.

7.2 Two species thin film deposition process description and modeling

In this section, a one-dimensional solid-on-solid (SOS) on-lattice model is used to simulate the two species thin film deposition process via a kinetic Monte Carlo method, which includes three microscopic processes: an adsorption process, in which particles are in-

corporated onto the film from the gas phase, a migration process and a surface relaxation process, in which surface particles move to adjacent sites [35, 34, 52, 53]. In this work, a square lattice is selected to represent the structure of the film and a sinusoidal grated wafer is used to initialize the deposition lattice, as shown in Fig. 7.1. The initial heights of all the particle sites are calculated as follows:

$$h_0(x) \approx M \cdot \sin(\frac{2\pi x}{p}) + M, \quad x \in [0, L] \tag{7.1}$$

All particles are modeled as identical hard spheres and the centers of the particles deposited on the film are located on the lattice sites. If the initial heights of the particles, $h_0(x)$, are not integers, they are approximated with the closest integers to satisfy the assumptions of on-lattice models. The diameter of the particles equals the distance between two neighboring sites. The width of the lattice is fixed so that the lattice contains a fixed number of sites in the lateral direction. The new particles are always deposited from the top side of the lattice with vertical incidence; see Fig. 7.1. Particle deposition results in film growth in the direction normal to the lateral direction. The direction normal to the lateral direction is thus designated as the growth direction. The number of sites in the lateral direction is defined as the lattice size and is denoted by L. Periodic boundary conditions (PBCs) are applied at the edges of the lattice in the lateral direction.

The top particles of each column are defined as the surface particles and the positions of the centers of all surface particles form the surface height profile. The number of nearest neighbors of a surface particle ranges from zero to two. A surface particle with zero nearest neighbors is possible to move to one of its adjacent columns with equal probability. A

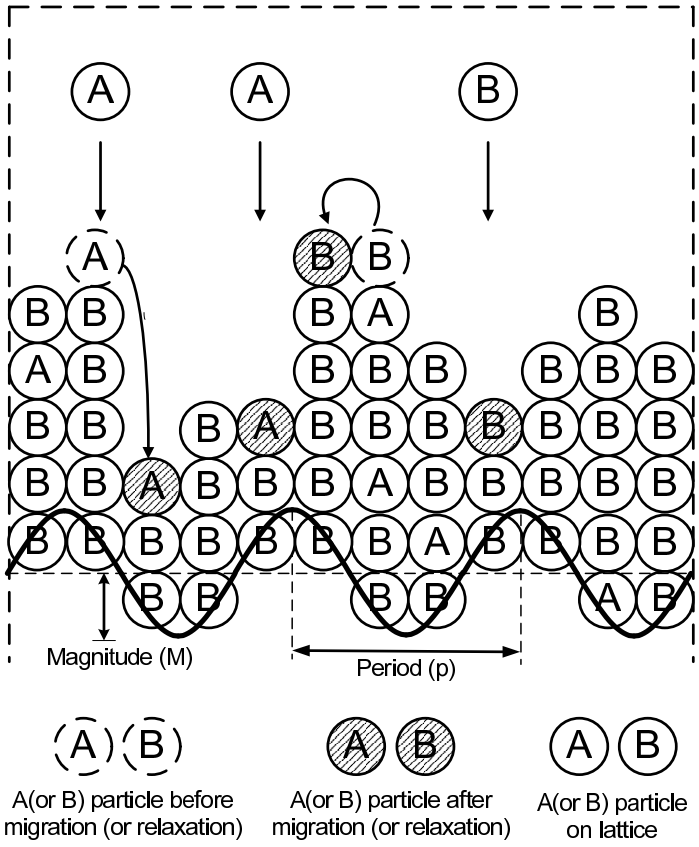

Figure 7.1: Two species thin film growth process on a solid-on-solid one-dimensional square lattice with sinusoidal grated wafer.

surface particle with one nearest neighbor is possible to move to its adjacent column with lower height. A surface particle with two nearest neighbors cannot move. Particles that are not on the film surface cannot move.

The overall deposition rate, w, is expressed in the units of layers per second and is a superposition of two components, ZnO deposition rate w_1 and Al deposition rate w_2 ($w = w_1 + w_2$). The deposition ratio between ZnO and Al is 24 : 1 [8]. Different deposition mechanisms are used for each component. Random deposition with surface relaxation (RDSR) mechanism is used for Al and deposition/migration mechanism is used for ZnO. For a description and comparison between these two mechanisms, please refer to [25]. The migration rate (probability) follows an Arrhenius-type law with a pre-calculated activation energy barrier that depends on the local environment of the particle, i.e., the number of the nearest neighbors of the particle chosen for a migration event. The migration rate of the ith surface particle is calculated as follows:

$$r_m = \nu_0 \exp\left(-\frac{E_s + n_i E_n}{k_B T}\right) \tag{7.2}$$

where ν_0 denotes the pre-exponential factor, n_i is the number of the nearest neighbors of the ith particle and can take the values of 0 and 1, (r_m is zero when $n_i = 2$ since in the one-dimensional lattice this surface particle is fully surrounded by other particles and cannot migrate), k_B is the Boltzmann's constant, E_s is the contribution to the activation energy barrier from the site itself, and E_n is the contribution to the activation energy barrier from each nearest neighbor. In this work, $E_s = 3.4$ eV and E_n is assumed to be zero [39]. T is the substrate temperature of the thin film and in this work $T = 800$ K [38]. Since the

film is thin, the temperature is assumed to be uniform throughout the film. For a detailed description and study of these models, please refer to [23].

7.2.1 Surface morphology at atomic level

Thin film surface morphology, which includes surface roughness and slope, is a very important surface property influencing the light properties of TCO thin films. Surface roughness is defined as the root-mean-square (rms) of the surface height profile as follows [24]:

$$r = \left[\frac{1}{L} \sum_{i=1}^{L} (h_i - \bar{h})^2 \right]^{1/2} \tag{7.3}$$

where r denotes surface roughness, h_i, ($i = 1, 2, \ldots, L$), is the surface height at the i-th position in the unit of layer, L denotes the lattice size, and the surface mean height is given by $\bar{h} = \frac{1}{L} \sum_{i=1}^{L} h_i$.

In addition to surface roughness, the surface mean slope is defined as the rms of the surface gradient profile as follows [24]:

$$m = \left[\frac{1}{L} \sum_{i=1}^{L} h_{s,i}^2 \right]^{1/2} \tag{7.4}$$

where m denotes the rms slope and $h_{s,i}$ is the surface slope at the i-th lattice site, which is a dimensionless variable. The surface slope, $h_{s,i}$ is computed as follows:

$$h_{s,i} = \frac{h_{i+1} - h_i}{1}. \tag{7.5}$$

7.2.2 Aggregate surface morphology and spatial deposition rate profile

In the context of TCO manufacturing for improved solar cell performance, the roughness and slope should be calculated at a length scale that is comparable to the wave length of visible light. Thus, aggregate surface morphology should be used in this work and the aggregation length, Δ, is 400. [24, 27]. Specifically, the aggregate surface morphology is computed similarly to the atomic surface morphology, but on the basis of the aggregate surface height profile, $h_{\Delta,i}$, which is defined as follows:

$$\begin{gathered} h_{\Delta,i} = (h_{i\Delta+1} + h_{i\Delta+2} + \cdots + h_{(i+1)\Delta})/\Delta, \\ i = 0, 1, \ldots, L/\Delta - 1 \end{gathered} \tag{7.6}$$

where $h_{\Delta,i}$ denotes the averaged surface height over the length scale of Δ sites, Δ denotes the aggregation size, i.e., the number of lattice sites used to calculate the aggregate surface height, and L/Δ denotes the number of aggregate sites of size Δ included in the spatial domain of the process. For the wavelength of visible light and silicon thin-film solar cells, the corresponding Δ is around 400; this follows from the fact that $0.3 \cdot 400 = 120$ nm, which is a length scale comparable to visible light wavelength [27]; the same aggregation level is used for the TCO layer in this work. The definition of aggregate surface roughness and slope is given as follows:

$$\begin{aligned} r_\Delta &= \left[\frac{1}{L/\Delta} \sum_{i=1}^{L/\Delta} \left(h_{\Delta,i} - \bar{h}_\Delta \right)^2 \right]^{1/2}, \\ m_\Delta &= \left[\frac{1}{L/\Delta} \sum_{i=1}^{L/\Delta} \left(\frac{h_{\Delta,i} - h_{\Delta,i+1}}{\Delta} \right)^2 \right]^{1/2}. \end{aligned} \tag{7.7}$$

To investigate the properties of aggregate roughness and slope in this model, multiple sets of simulations were carried out with different parameter values. First, simulations were carried out to investigate the surface morphology dependence on wafer grating parameters, specifically, magnitude (M) and period (P) of grating. As shown in Fig. 7.2 and Fig. 7.3, $W = 5$ layer/s, $T = 800$ K, $M = 100$ layers and 1000 independent simulations were carried out to calculate the expected values of aggregate surface roughness and slope. It is clear that as the period, P, decreases from 40000 to 4000, aggregate slope increases by two orders of magnitude while aggregate roughness decreases slightly. As shown in Fig. 7.4 and Fig. 7.5, with same T and W as in the previous simulation set and $P = 8000$, as the grating magnitude increases, both aggregate roughness and slope increase dramatically. Subsequently, more simulations were carried out with the same wafer grating parameters, $P = 8000$ and $M = 100$ layers, but different T and W. From Fig. 7.6 to Fig. 7.9, we observe that both the temperature, T, and the uniform deposition rate, W, have very limited influence on aggregate roughness and slope. This is as expected since wafer grating influences the shape of the surface in a macroscopic way, while T and W influence the surface in a microscopic way via the deposition and migration rates and they are not strong enough to influence the shape of the surface within a practically meaningful deposition time. In order to induce large enough aggregate surface roughness and slope to precisely control the surface morphology on a sinusoidal grated wafer, a spatially non-uniform deposition rate profile is necessary for the purpose of optimizing thin film light trapping properties by manipulation of film aggregate surface roughness and slope at length scales comparable to

visible light wavelength [27]. To this end, a spatially patterned deposition rate profile is used in this work, which is defined as follows:

$$\begin{aligned} w_1(x) &= w_{1,0} + A_1 \sin\left(\frac{2k\pi}{L}x\right), \quad A_1 \leq w_{1,0} \\ w_2(x) &= w_{2,0} + A_2 \sin\left(\frac{2k\pi}{L}x\right), \quad A_2 \leq w_{2,0} \\ w(x) &= w_1(x) + w_2(x) \\ w_0(x) &= w_{1,0}(x) + w_{2,0}(x), \quad A = A_1 + A_2 \end{aligned} \tag{7.8}$$

where x is a position along the lattice, $w_{1,0}$ and $w_{2,0}$ are the mean deposition rates, A_1 and A_2 are the magnitude of the patterned deposition profile, k is the number of sine waves along the entire lattice. It is considered that $w_1 : w_2 = w_{1,0} : w_{2,0} = A_1 : A_2 = 24 : 1$.

The dynamics of aggregate surface morphology with patterned deposition rate profile is studied by carrying out a series of simulations at different mean deposition rates w_0 with $M = 100$ layers, $P = 8000$, $L = 40000$, $\Delta = 400$, $T = 800$ K, $k = 1$ and $A = 0.1w_0$. The evolution profiles for aggregate roughness and slope are shown in Fig. 7.10 and Fig. 7.11. The introduction of patterned deposition rate profiles significantly changes the dynamic profiles of aggregate surface morphology, and the values of both aggregate roughness and slope increase by several orders of magnitude. Furthermore, simulations are carried out at $w_0 = 2$ layer/s with different magnitude, A, values to investigate the influence of the strength of patterned deposition on the evolution profiles of aggregate surface morphology. As shown in Fig. 7.12 and Fig. 7.13, the magnitude, A, has a substantial influence on the dynamics of aggregate surface morphology. Both aggregate roughness and aggregate slope can be increased substantially by manipulating A compared to the aggregate surface

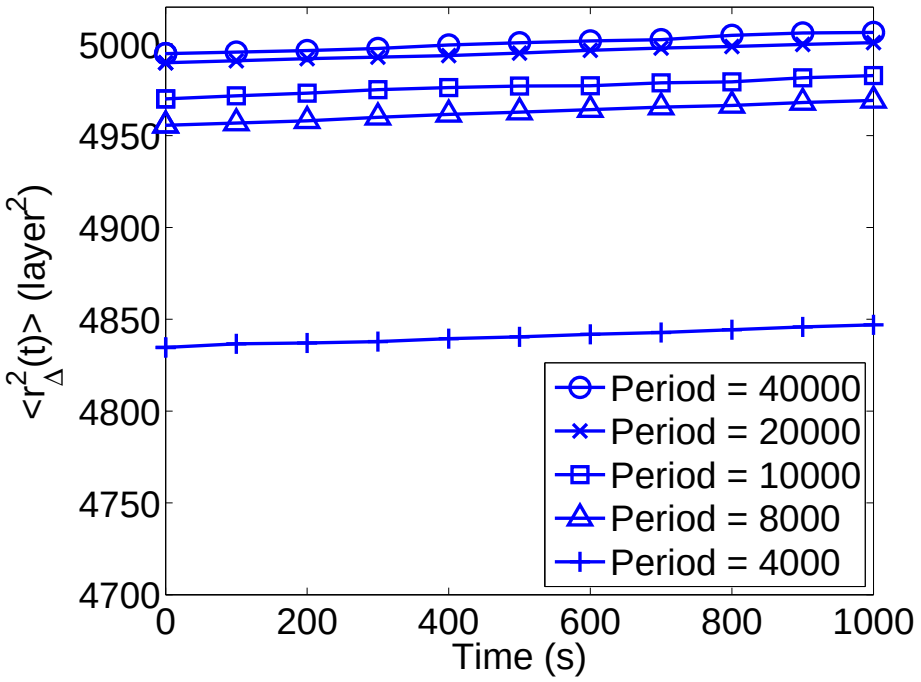

Figure 7.2: Evolution of expected aggregate surface roughness with respect to time for different grating period lengths obtained from kMC simulations.

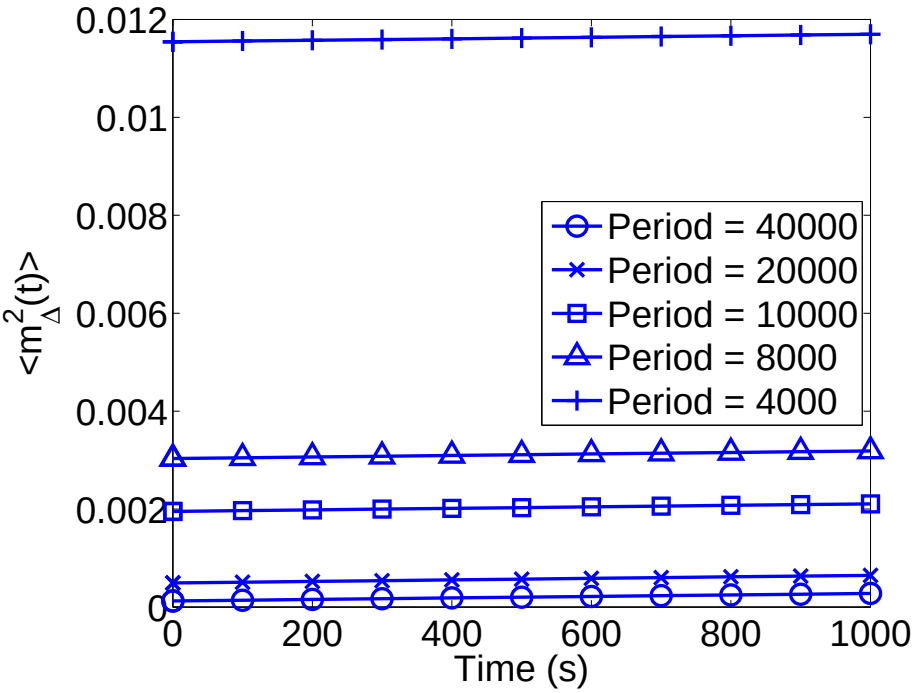

Figure 7.3: Evolution of expected aggregate surface slope with respect to time for different grating period lengths obtained from kMC simulations.

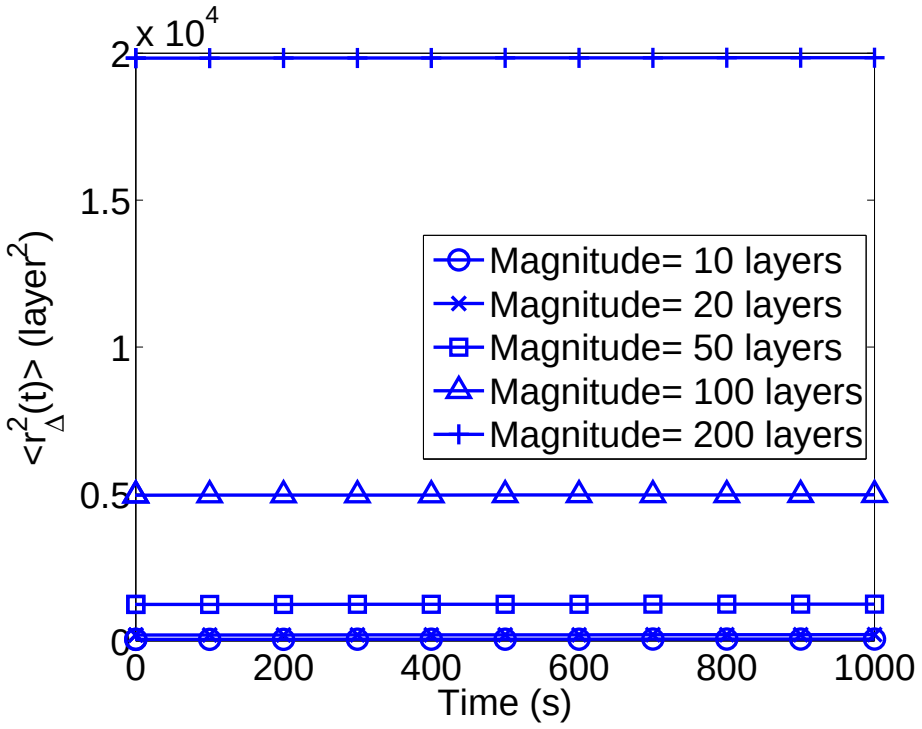

Figure 7.4: Evolution of expected aggregate surface roughness with respect to time for different grating magnitudes obtained from kMC simulations.

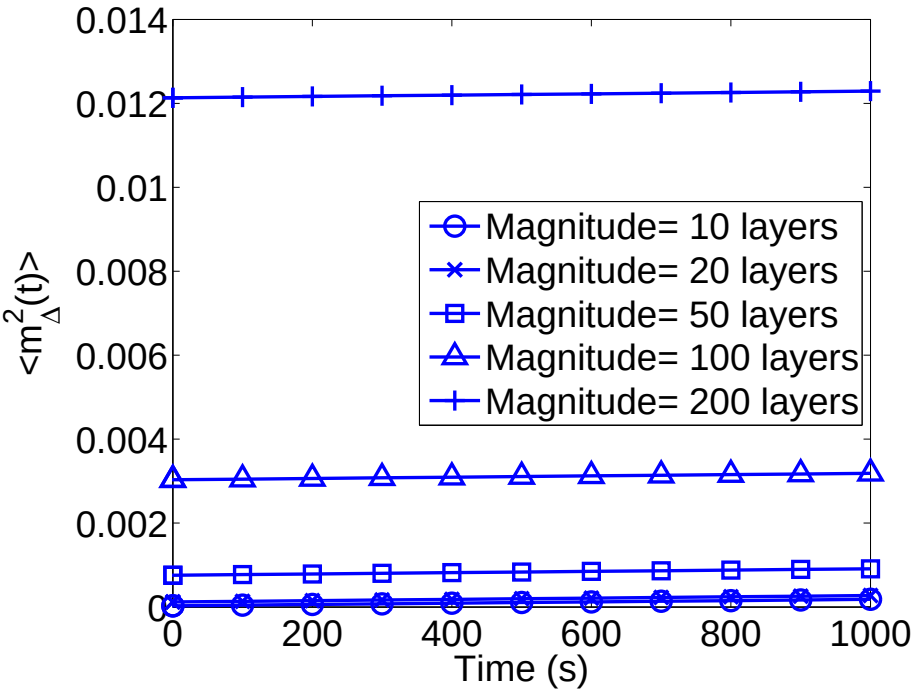

Figure 7.5: Evolution of expected aggregate surface slope with respect to time for different grating magnitudes obtained from kMC simulations.

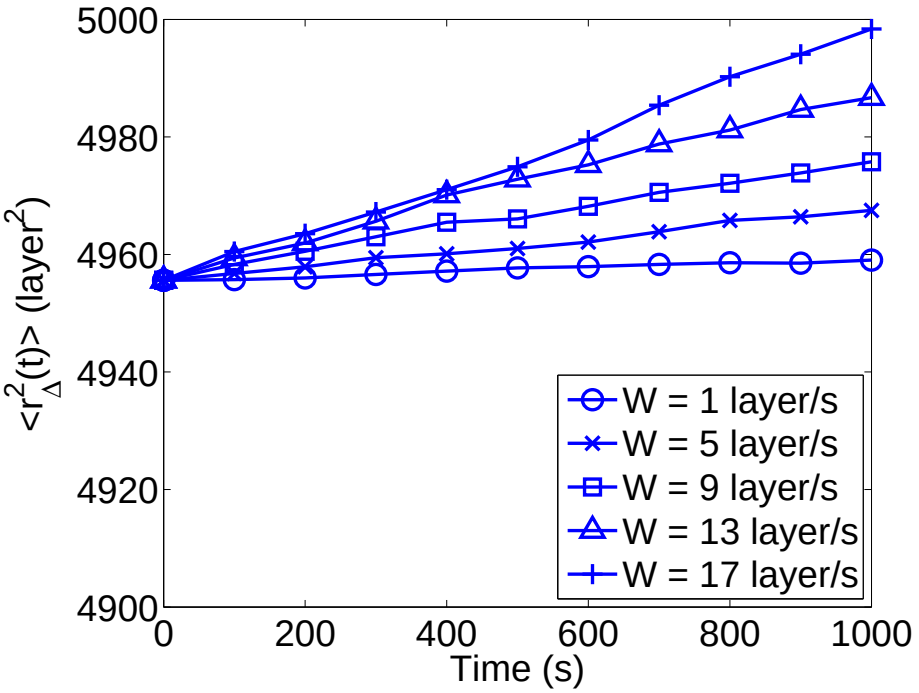

Figure 7.6: Evolution of expected aggregate surface roughness with respect to time for different uniform deposition rates obtained from kMC simulations.

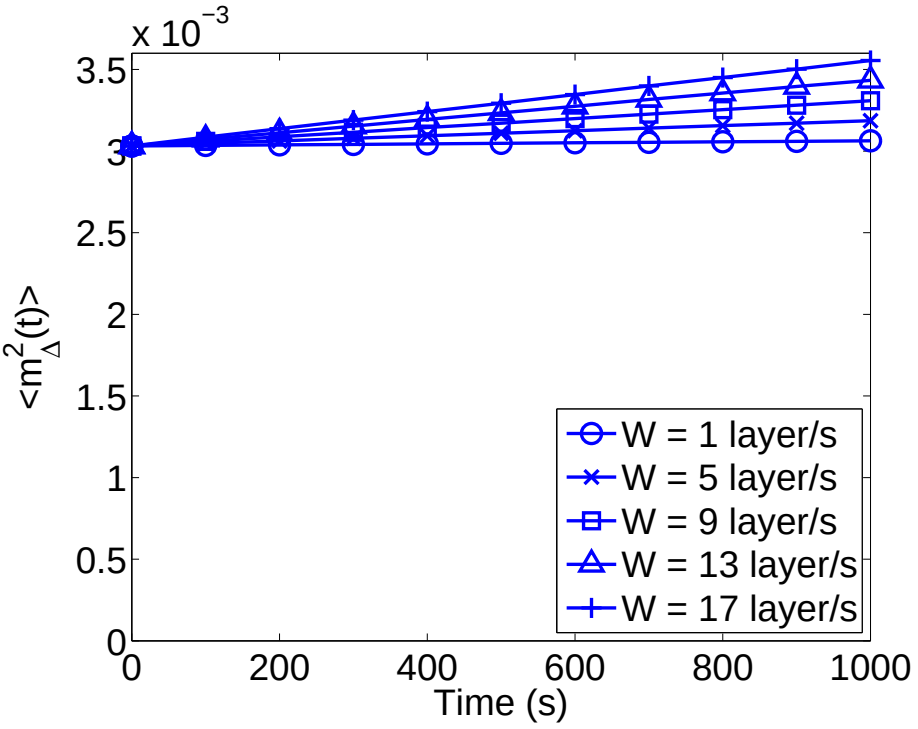

Figure 7.7: Evolution of expected aggregate surface slope with respect to time for different uniform deposition rates obtained from kMC simulations.

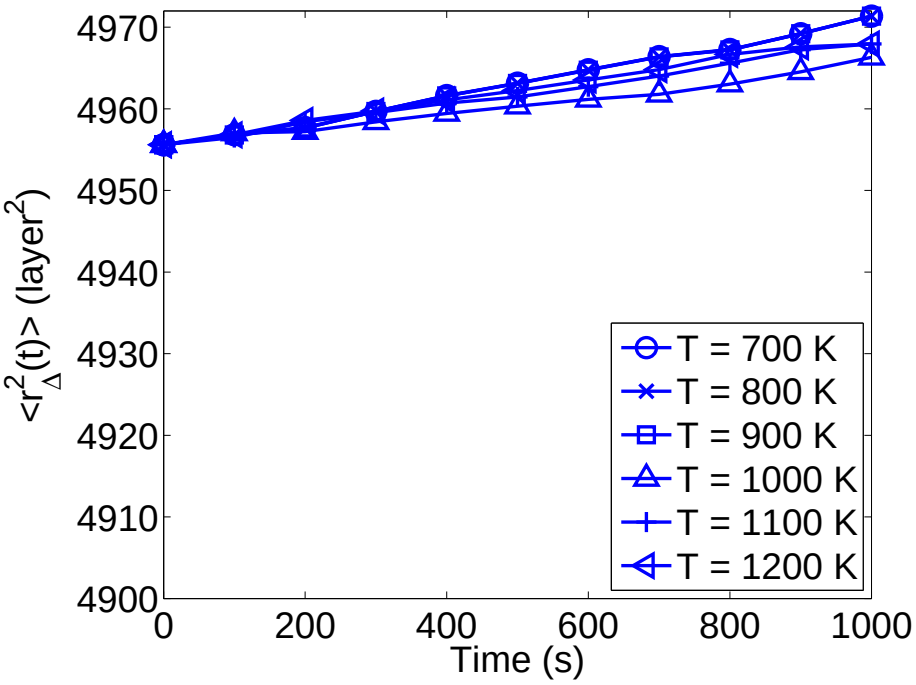

Figure 7.8: Evolution of expected aggregate surface roughness with respect to time for different temperatures obtained from kMC simulations.

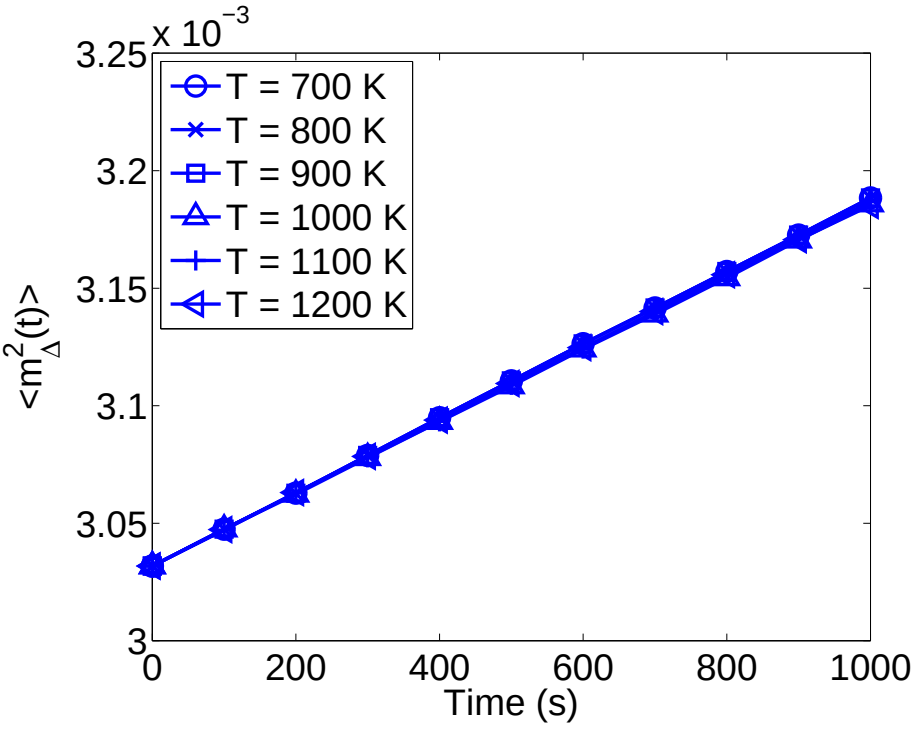

Figure 7.9: Evolution of expected aggregate surface slope with respect to time for different temperatures obtained from kMC simulations.

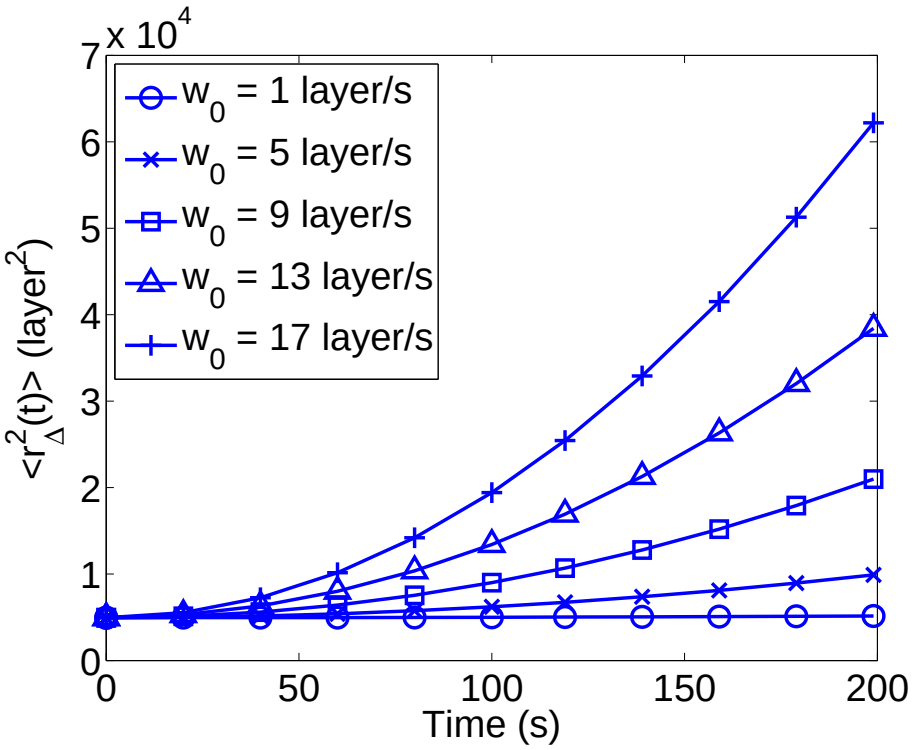

Figure 7.10: Evolution of expected aggregate surface roughness with respect to time for different mean deposition rates (unit of w_0 is layer/s) obtained from kMC simulations. Patterned deposition with $k = 1$, $P = 8000$, $M = 100$ layer/s and $A = 0.1w_0$.

morphology achieved with a uniform deposition rate profile. Thus, the introduction of a patterned deposition rate profile, in conjunction with wafer grating, expands the range of surface morphology values that can be obtained and makes surface morphology control at length scales comparable to visible light wavelength possible.

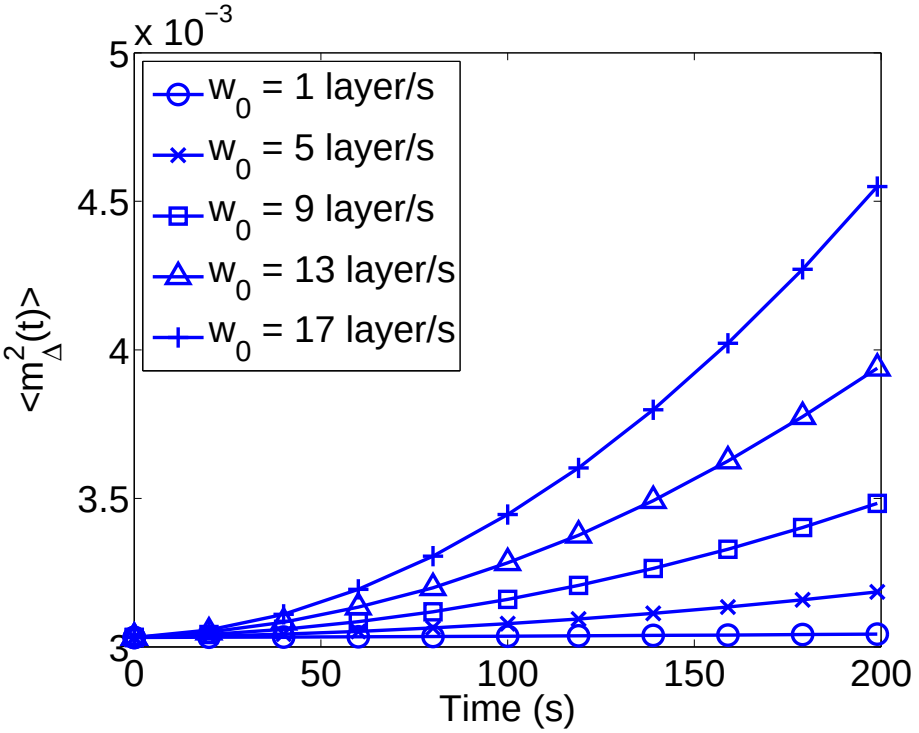

Figure 7.11: Evolution of expected aggregate surface slope with respect to time for different mean deposition rates (unit of w_0 is layer/s) obtained from kMC simulations. Patterned deposition with $k = 1$,P=8000,M=100$layer/s$, $P = 8000$, $M = 100$ layer/s and $A = 0.1w_0$.

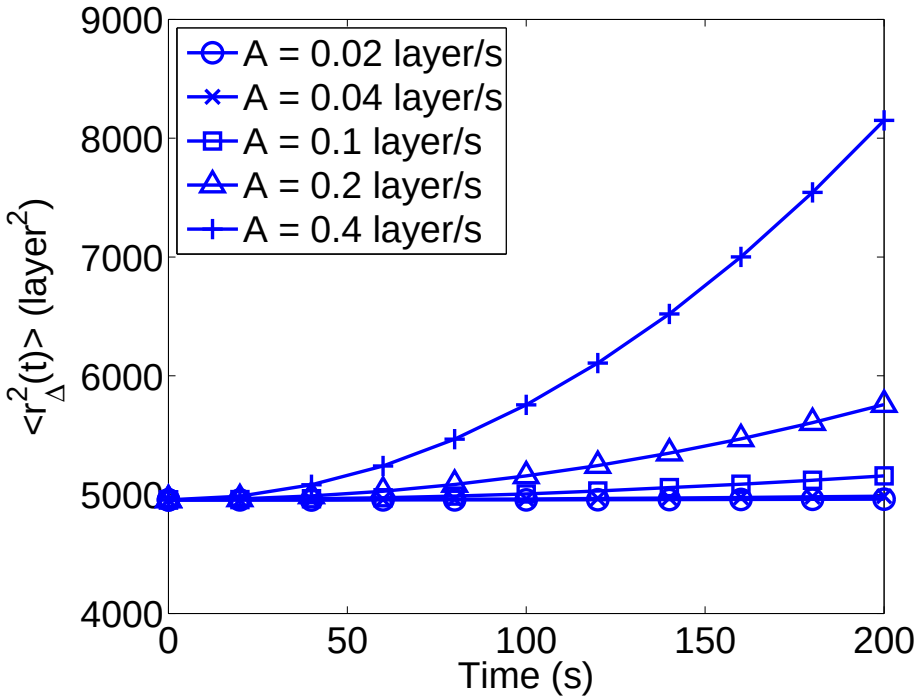

Figure 7.12: Evolution of expected aggregate surface roughness with respect to time for different patterned deposition rate magnitudes obtained from kMC simulations. Patterned deposition with $k = 1$, $P = 8000$, $M = 100$ layer/s and $w_0 = 2$ layer/s.

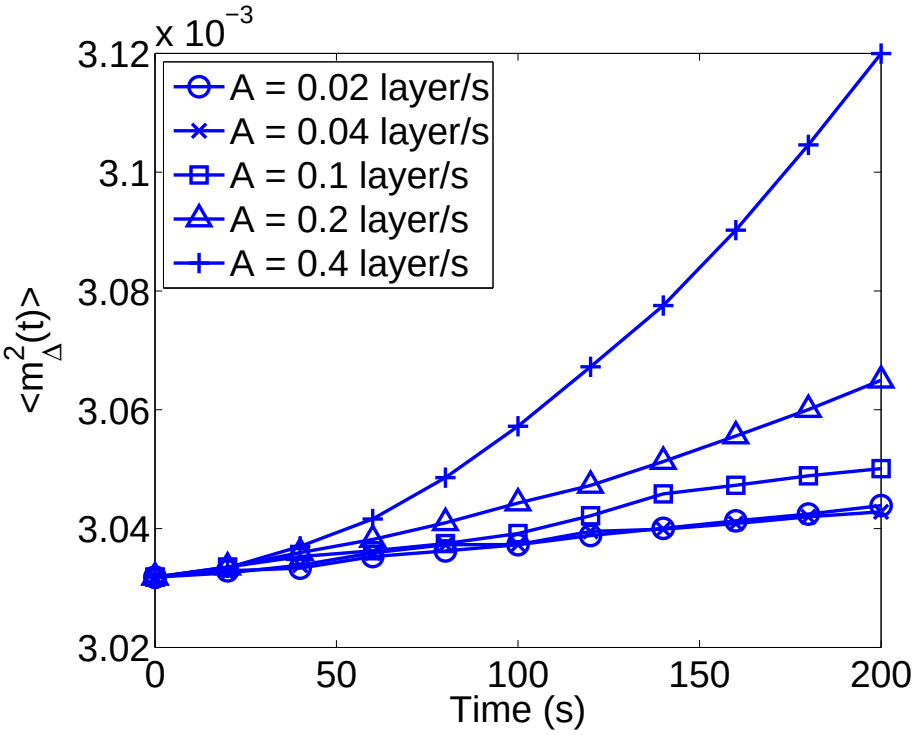

Figure 7.13: Evolution of expected aggregate surface slope with respect to time for different patterned deposition rate magnitudes obtained from kMC simulations. Patterned deposition with $k = 1$, $P = 8000$, $M = 100$ layer/s and $w_0 = 2$ layer/s.

7.3 Closed-form modeling and parameter estimation

7.3.1 Edward-Wilkinson-type equation of aggregate surface height

Given the complexity of the two species deposition process and the need to control surface roughness and slope at spatial scales comparable to the wavelength of visible light, the direct computation of a closed-form model describing the surface height evolution suitable for controller design, from the microscopic deposition mechanisms is a very difficult task. Therefore, a hybrid modeling approach should be used in which a basic closed-form modeling structure is first postulated and the model parameters are computed such that the predictions of key variables from the closed-form model are close to the one of the kinetic Monte-Carlo model for a broad set of operating conditions. It is well known that an Edward-Wilkinson(EW)-type equation, which is a second-order stochastic PDE, can be used in this case to describe and predict the aggregate surface height profile [27, 25] as follows:

$$\frac{\partial h_\Delta}{\partial t} = w(x,t) + c_2 \frac{\partial^2 h_\Delta}{\partial x^2} + \xi(x,t) \tag{7.9}$$

subject to the following periodic boundary conditions

$$h_\Delta(0,t) = h_\Delta(L,t) \tag{7.10}$$

$$\frac{\partial h_\Delta}{\partial x}(0,t) = \frac{\partial h_\Delta}{\partial x}(L,t) \tag{7.11}$$

In this work, the use of a sinusoidal grated wafer introduces a non-zero initial condition, as follows:

$$h_\Delta(x,0) = h_\Delta^0(x) = M_\Delta \cdot \sin(\frac{2\pi x}{L}) + M_\Delta \tag{7.12}$$

where $h_\Delta(x,t)$ is the aggregate surface height, $x \in [0, L/\Delta]$ is the spatial coordinate and M_Δ is the magnitude of wafer grating at the aggregate length scale. $\xi(x,t)$ is a Gaussian white noise with zero mean and the following covariance:

$$\left\langle \xi(x,t)\xi(x',t') \right\rangle = \sigma^2 \delta(x-x')\delta(t-t') \tag{7.13}$$

where $\delta(\cdot)$ denotes the Dirac delta function. In Eq. 7.9, the parameters c_2 and σ^2 depend on the deposition rate $w(x,t)$ [26]. A patterned deposition rate profile (control actuation), $w(x,t)$, is used of the form:

$$w(x,t) = w_0(t) + A(t)\sin\left(\frac{2k\pi}{L}x\right) \tag{7.14}$$

where $w_0(t)$ is the total mean deposition rate and $A(t)$ is the total magnitude of patterned deposition rate.

To analyze the dynamics and obtain a solution of the EW equation suitable for real-time controller calculations, we first consider the eigenvalue problem of the linear operator of Eq. 7.9 to obtain its eigenvalues and eigenfunctions. Then the aggregate surface height profile can be expanded in an infinite series in terms of the eigenfunctions times time-varing coefficients. Substituting this expansion into Eq. 7.9 and taking the inner product with the adjoint eigenfunctions, the stochastic PDE can be transformed into a system of

infinite stochastic linear ordinary differential equations (ODEs) of the form:

$$\frac{dz_{2,0}(t)}{dt} = w_{2,0} + \xi_{2,0}(t), \tag{7.15}$$

$$\frac{dz_{p,n}(t)}{dt} = w_{p,n} + \lambda_n z_{p,n} + \xi_{p,n}(t) \tag{7.16}$$

$$p = 1,2, \quad n = 1, \cdots, \frac{L}{2\Delta},$$

where $\xi_{p,n}(t) = \int_0^L \xi(x,t)\phi_{p,n}(x)dx$ is the projection of the noise $\xi(x,t)$ on the ODE for $z_{p,n}$. The noise term, $\xi_{p,n}$, has zero mean and covariance

$$\left\langle \xi_{p,n}(t)\xi_{p,n}(t') \right\rangle = \sigma^2 \delta(t-t'). \tag{7.17}$$

Similarly, $w_{p,n}$ is the projection of w on the ODE for $z_{p,n}(t)$, $w_{p,n} = \int_0^L \phi_{p,n}(x)w(x)dx$

- If $p = 1$,

$$w_{1,n} = \begin{cases} 0, & n \neq k \\ \\ A\sqrt{\dfrac{L}{2}}, & n = k \end{cases} \tag{7.18}$$

- If $p = 2$,

$$w_{2,n} = \begin{cases} 0, & n \neq 0 \\ \\ A\sqrt{L}, & n = 0 \end{cases} \tag{7.19}$$

The temporal evolution of the variance of mode $z_{p,n}$ can be obtained from the solution

of the linear ODEs of Eqs. 7.15 and 7.16 as follows:

$$\left\langle z_{2,0}(t)\right\rangle = w_{2,0}(t-t_0) \tag{7.20}$$

$$\mathrm{var}(z_{2,0}(t)) = \sigma^2(t-t_0) \tag{7.21}$$

$$\langle z(t)\rangle = e^{\lambda(t-t_0)}\langle z(t_0)\rangle + \frac{w_p}{\lambda}(e^{\lambda(t-t_0)}-1) \tag{7.22}$$

$$\mathrm{var}(z(t)) = e^{2\lambda(t-t_0)}\,\mathrm{var}(z(t_0)) + \sigma^2\frac{e^{2\lambda(t-t_0)}-1}{2\lambda} \tag{7.23}$$

where $z(t) = z_{p,n}(t)$, $\lambda = \lambda_n$, $w_p = w_{p,n}$ for $n \neq 0$ and $z(t_0) = z_{p,n}(t_0)$ can be calculated as follows:

- If $p = 1$,

$$z_{1,n}(t_0) = \begin{cases} 0, & n \neq P \\ \\ M_\Delta\sqrt{\dfrac{L}{2}}, & n = P \end{cases} \tag{7.24}$$

- If $p = 2$,

$$z_{2,n}(t_0) = 0. \tag{7.25}$$

For the details on how to solve Eq. 7.9, please refer to [25].

7.3.2 Aggregate surface root–mean–square roughness and slope

Aggregate surface roughness of the thin film is defined as the standard deviation of the aggregate surface height profile from its average height

$$r_\Delta(t) = \sqrt{\frac{1}{L}\int_0^L \left[h_\Delta(x,t) - \bar{h}_\Delta(t)\right]^2 dx} \tag{7.26}$$

where $\bar{h}_\Delta(t) = \dfrac{1}{L}\displaystyle\int_0^L h_\Delta(x,t)dx$ is the average aggregate surface height. It can be shown that [25],

$$\left\langle r_\Delta^2(t)\right\rangle = \frac{1}{L}\sum_{n=1}^{L/(2\Delta)}\left(\left\langle z_{1,n}^2\right\rangle + \left\langle z_{2,n}^2\right\rangle\right) \tag{7.27}$$

where

$$\left\langle z_{p,n}^2\right\rangle = \mathrm{var}(z_{p,n}) + \left\langle z_{p,n}\right\rangle^2. \tag{7.28}$$

The expression of Eqs. 7.27–7.28 will be used in the MPC formulation; see Eq. 7.33 below.

Similarly, the aggregate rms slope is defined as the root–mean–square of the aggregate surface slope in the x–direction as follows:

$$\begin{aligned} m_\Delta(t) &= \sqrt{\frac{1}{L}\int_0^L \left(\frac{\partial h_\Delta}{\partial x}\right)^2 dx} \\ &= \sqrt{\frac{1}{L}\sum_{i=0}^{L/\Delta}\left(\frac{h_\Delta(i+1,t)-h_\Delta(i,t)}{\Delta}\right)^2 \Delta} \end{aligned} \tag{7.29}$$

It can be shown that [25],

$$\begin{aligned} \left\langle m_\Delta^2(t)\right\rangle &= \sum_{p=1}^{2}\sum_{n=0}^{L/(2\Delta)} K_{p,n}\left\langle z_{p,n}^2\right\rangle \\ &= \sum_{m=1}^{L/(2\Delta)}\left(K_{1,m}\left\langle z_{1,m}^2\right\rangle + K_{2,m}\left\langle z_{2,m}^2\right\rangle\right) \end{aligned} \tag{7.30}$$

where

$$\begin{aligned} K_{p,n} &= \frac{8}{L^2\Delta}\sin^2\left(\frac{\pi n}{L/\Delta}\right)\sum_{i=0}^{L/(2\Delta)}\left(\cos^2\left(\frac{n\pi}{L/\Delta}(2i+1)\right)\right) \\ &= \begin{cases} \dfrac{8}{L\Delta^2}\sin^2\left(\dfrac{\pi n}{L/\Delta}\right) & n=0 \\ \dfrac{4}{L\Delta^2}\sin^2\left(\dfrac{\pi n}{L/\Delta}\right) & n\neq 0 \end{cases} \end{aligned} \tag{7.31}$$

The expression of Eq. 7.30 will be used in the MPC formulation; please see Eq. 7.33 below.

7.3.3 Parameter estimation

The two model parameters, c_2 and σ^2, in the EW equation of Eq. 7.9, can be determined as functions of the total mean deposition rate w_0 and of the total patterned deposition rate magnitude A. These parameters affect the dynamics of aggregate surface roughness and slope and can be estimated by fitting the predicted evolution profiles for aggregate surface roughness and slope from the EW equation to profiles of aggregate surface roughness and slope from kMC simulations. Least-square methods are used to estimate the model parameters so that the EW-model predictions are close in a least-square sense to the kMC simulation data. Comparison of the predictions of both models are shown in Fig. 7.14. Based on c_2 and σ^2 values obtained from these fitting results, two linear functions are chosen to estimate c_2 and σ^2 values at different w with the least-square method:

$$c_2(w) = a_{c_2} \cdot w + b_{c_2} \tag{7.32}$$

$$\sigma^2 = a_{\sigma^2} \cdot w + b_{\sigma^2}$$

where a_{c_2}, b_{c_2}, a_{σ^2} and b_{σ^2} are time-invariant fitting model parameters. The fitting results are shown in Fig. 7.15 and Fig. 7.16. To verify the fitting functions, two more groups of simulations were carried out with larger deposition rates ($w = 17$ and 21 layer/s) and fitted to EW equation, and the obtained values for c_2 and σ^2 are used to extend the fitting curve to show the validity of the chosen fitting functions. It has been verified that fitting results based

on kMC simulation with uniform deposition rate profiles ($A = 0$) can be used to estimate c_2 and σ^2 values for simulations with spatially distributed deposition rate profiles [27], and this assumption is still used in this work.

7.4 Model predictive control

In this section, a model predictive controller is designed based on the dynamic models of aggregate surface roughness and slope to simultaneously control the expected values of aggregate surface roughness and slope square to desired levels. The dynamics of aggregate surface roughness and slope of the TCO layers are described by both the kMC model and the EW equation. State feedback control is considered in this work, and $h_\Delta(x,t)$ is assumed to be available for feedback. In practice, real-time surface height measurements can be obtained via atomic force microscopy (AFM) systems.

7.4.1 MPC formulation for regulation of aggregate roughness and slope

The control objective in this work is to regulate aggregate surface roughness and slope to desired levels within a model predictive control framework. Due to the stochastic nature of the variables, the expected values of aggregate surface roughness and slope, $\left\langle r_\Delta^2(t)\right\rangle$ and $\left\langle m_\Delta^2(t)\right\rangle$, are chosen as the control objectives. The total mean deposition rate, w_0 ($w_0 = w_{1,0} + w_{2,0}$), and magnitude of patterned deposition rate, A ($A = A_1 + A_2$), are chosen as the manipulated inputs; the substrate temperature is fixed at $T = 800$ K during all

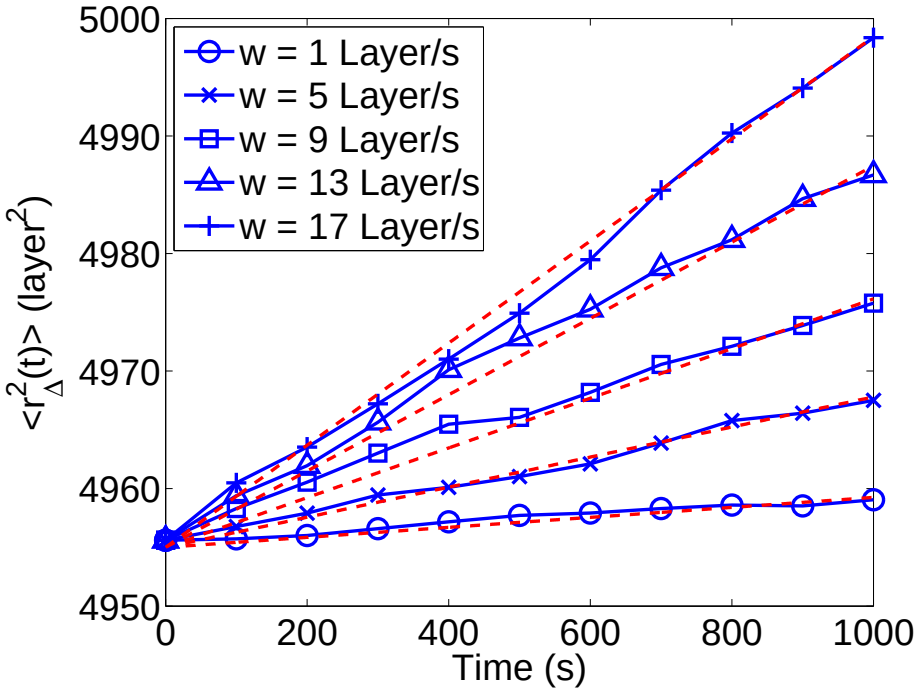

Figure 7.14: Evolution of expected aggregate surface roughness with respect to time for different spatially-uniform deposition rates obtained from kMC simulations (solid lines with symbols).The analytical solutions for the aggregate surface roughness obtained from the corresponding EW equations with the fitted values for c_2 and σ^2 are also shown (dashed lines).

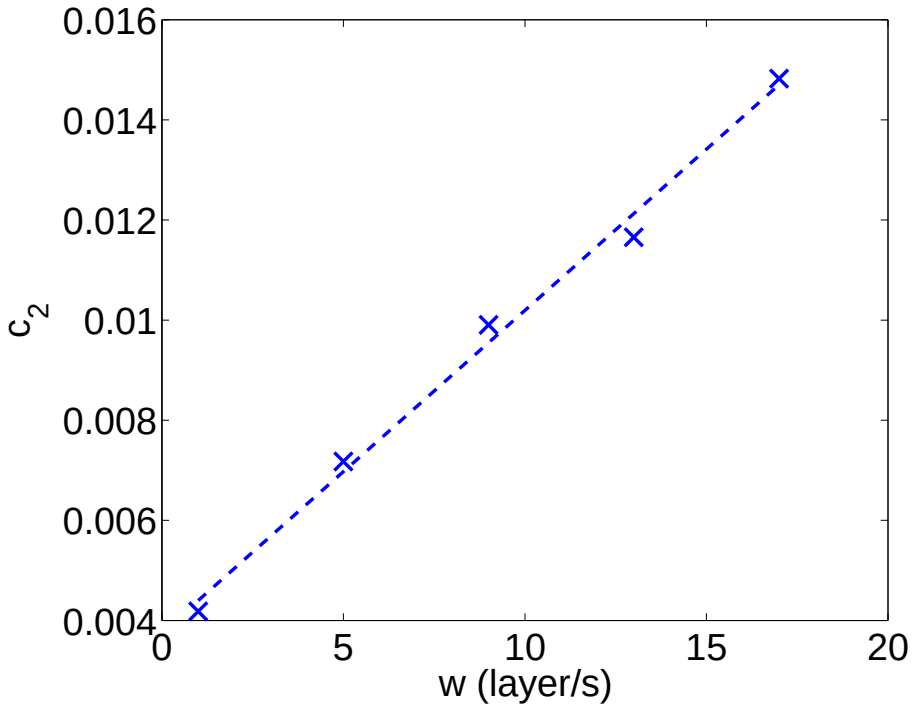

Figure 7.15: c_2 values for different spatially-uniform deposition rates w. The solid line is the result of a linear fitting function and it is the c_2 versus w relationship used by the predictive controller.

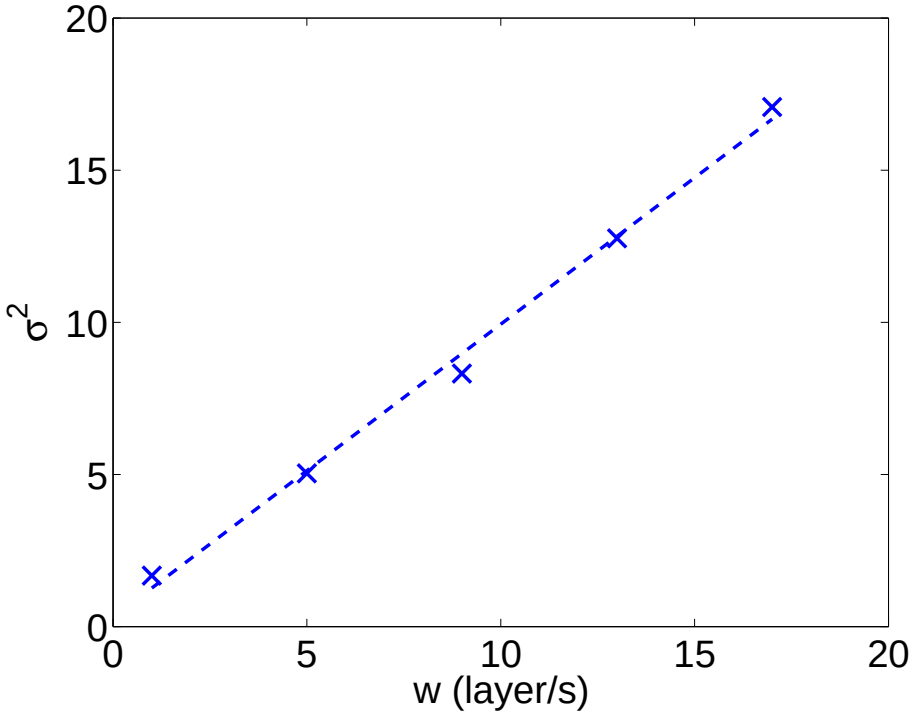

Figure 7.16: σ^2 values for different spatially-uniform deposition rates w. The solid line is the result of a linear fitting function.

closed-loop simulations. To account for a number of practical considerations, several constraints are added to the control problem. In particular, since $w(x) \geq 0$, the constraints $0 \leq A_1 \leq w_{1,0}$ and $0 \leq A_2 \leq w_{2,0}$ are imposed to ensure $w(x,t) > 0$, $\forall (x,t)$. To ensure the validity of the closed-form process model, there is a constraint on the range of variation of the mean deposition rate. Another constraint is imposed on the rate of change of the mean deposition rate to account for actuator limitations. The control action at time t is obtained by solving a finite-horizon optimal control problem. The cost function in the optimal control problem includes penalty on both aggregate roughness and slope with independent weighting factors. Since the dynamics of aggregate surface roughness and slope are different by several orders of magnitudes, relative deviations are used in the formulation of the cost function to make the magnitude of these two terms comparable in the cost function. The optimization problem is subject to the dynamics of the aggregate surface height of Eq. 7.9, which account for wafer grating. Specifically, the MPC problem at time t is formulated as follows:

$$\min_{w_0,A} f(w_0,A) = q_{r^2} \left[\frac{r_{set}^2 - \left\langle r_\Delta^2(t_f) \right\rangle}{r_{set}^2} \right]^2 + q_{m^2} \left[\frac{m_{set}^2 - \left\langle m_\Delta^2(t_f) \right\rangle}{m_{set}^2} \right]^2 \tag{7.33}$$

where

$$\left\langle r_\Delta^2(t_f) \right\rangle = \frac{1}{L} \sum_{n=1}^{L/(2\Delta)} \sum_{p=1}^{2} \left\langle z_{p,n}^2(t_f) \right\rangle, \quad \left\langle m_\Delta^2(t_f) \right\rangle = \sum_{n=1}^{L/(2\Delta)} \sum_{p=1}^{2} \left(K_{p,n} \left\langle z_{p,n}^2(t_f) \right\rangle \right) \tag{7.34}$$

$$\left\langle z_{p,n}^2(t_f)\right\rangle = \mathrm{var}(z_{p,n}(t_f)) + \left\langle z_{p,n}(t_f)\right\rangle^2 \tag{7.35}$$

$$\left\langle z_{p,n}(t_f)\right\rangle = e^{\lambda_n(t_f-t)}\left\langle z_{p,n}(t)\right\rangle + \frac{w_p}{\lambda_n}(e^{\lambda_n(t_f-t)}-1) \tag{7.36}$$

$$\mathrm{var}(z_{p,n}(t_f)) = e^{2\lambda_n(t_f-t)}\,\mathrm{var}(z_{p,n}(t)) + \sigma^2(w)\frac{e^{2\lambda_n(t_f-t)}-1}{2\lambda_n} \tag{7.37}$$

$$\lambda_n = -\frac{4c_2(w)\pi^2}{L^2}n^2 \tag{7.38}$$

and

$$c_2(w_0) = a_{c_2}\cdot w_0 + b_{c_2} \tag{7.39}$$

$$\sigma^2(w_0) = a_{\sigma^2}\cdot w_0 + b_{\sigma^2} \tag{7.40}$$

subject to:

$$w_{min} \le w_0 \le w_{max}, \quad |w_0(t) - w_0(t-dt)| \le \delta w_{max}, \tag{7.41}$$

where t is the current time, dt is the sampling time, q_{r^2} and q_{m^2} are the weighting penalty factors for the deviations of $\left\langle r_\Delta^2\right\rangle$ and $\left\langle m_\Delta^2\right\rangle$ from their respective set-points at the ith prediction step, w_{min} and w_{max} are the lower and upper bounds on the mean deposition rate, respectively, and δw_{max} is the limit on the rate of change of the mean deposition rate. Due to the influence of wafer grating, $z_{p,n}(t_0)$ follows Eqs. 7.24 and 7.25.

The optimal control actions are obtained from the solution of the multivariable optimization problem of Eq. 7.33 and are applied to the deposition process model over dt (i.e., either the EW equation model or the kMC model) during the time interval $(t, t+dt)$. At time $t+dt$, a new measurement of aggregate surface roughness and slope is received by the controller and the MPC problem of Eq. 7.33 is solved for the next set of control actions.

An interior point method optimizer, IPOPT [51], is used to solve the optimization problem in the MPC formulation. The stability of the closed-loop system is inherently guaranteed by the negative values of all the eigenvalues of the spatial differential operator of Eq. 7.9 used to describe the dynamics of surface height profiles.

7.5 Simulation results

In this section, the model predictive controller of Eq. 7.33 is applied to both the one-dimensional EW equation type model of Eq. 7.9 and the one-dimensional kMC model of the thin film growth process. The sinusoidal grated wafer period is 8000, the grating magnitude is 100 layers, the mean deposition rate ranges from 0.1 to 10 layer/s, the substrate temperature is fixed at 800K, the lattice size of the kMC model is fixed at 40,000 sites, the aggregation size is fixed at 400 to make the results relevant to thin film solar cell applications and five sine waves are used in the patterned deposition rate profile. The sampling time is 10 s; this sampling time is enough for the MPC to carry out the calculations needed to compute the control action. In addition to the deposition rate, the temperature may be used as a manipulated input but it should vary in space to induce substantial aggregate surface roughness and slope values at spatial scales comparable to the visible light wavelength. Each closed-loop simulation lasts for 200 s. Expected values are calculated from 10 independent closed-loop system simulation runs; further increase of the number of independent simulations did not appreciably change the computed expected values. In all the simulations, the aggregate surface roughness and slope set-points remain the same,

specifically, $r^2_{set} = 5500$ and $m^2_{set} = 0.005$.

7.5.1 MPC application to EW equation model

In this subsection, the EW equation model is utilized in the closed-loop control problem as the plant model. First, the problem of regulating aggregate surface roughness is considered. In this problem, the cost function includes only penalty on the deviation of the expected aggregate surface roughness square from its set-point, *i.e.*, $q_{r^2} = 1$ and $q_{m^2} = 0$. Fig. 7.17 shows the evolution profile of $\left\langle r^2_\Delta(t) \right\rangle$ under the model predictive controller of Eq. 7.33. It is clear that the controller drives the expected aggregate surface roughness to its set-point at the end of the simulation. Fig. 7.18 shows the input profiles of w_0 and A for these simulations.

Next, the aggregate surface slope is regulated. In this case, the cost function includes only penalty on the deviation of the expected value of aggregate surface slope square from its set-point ($q_{m^2} = 1,\ q_{r^2} = 0$). Fig. 7.19 shows the evolution profile of the expected aggregate slope square. The aggregate slope reaches its set-point at $t_f = 200$ s. Fig. 7.20 displays the input profile in this scenario.

7.5.2 MPC application to kMC model

In this subsection, the kMC model is used in the closed-loop control problem as the plant model, while all the other settings remain the same. Fig. 7.21 shows the aggregate surface roughness in the case of roughness-only control and its corresponding manipulated input

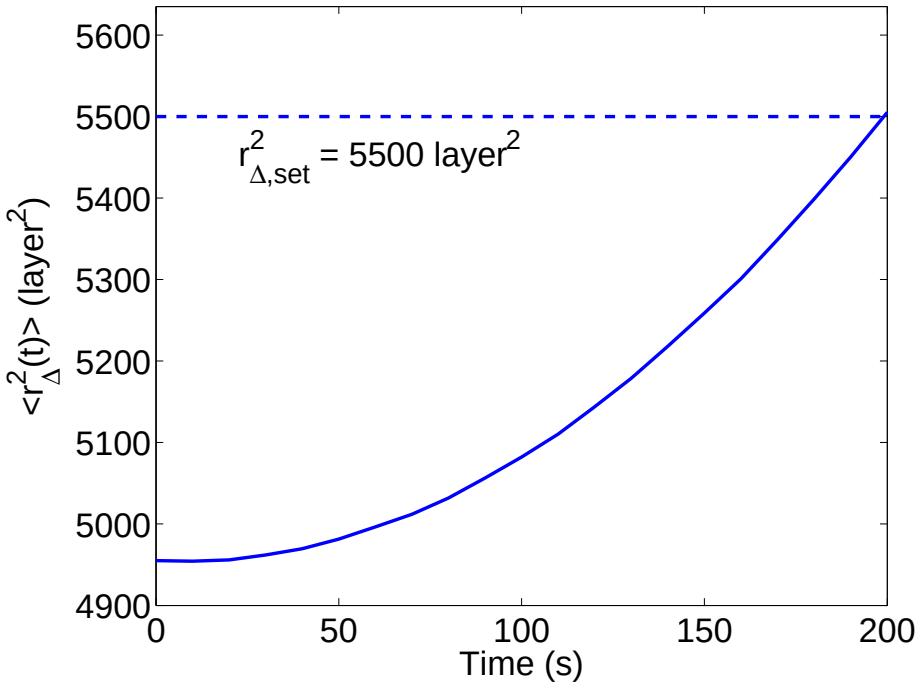

Figure 7.17: Profile of expected aggregate surface roughness square with EW equation as the plant model. $q_{r^2} = 1$, $q_{m^2} = 0$ and $r^2_{set} = 5500$.

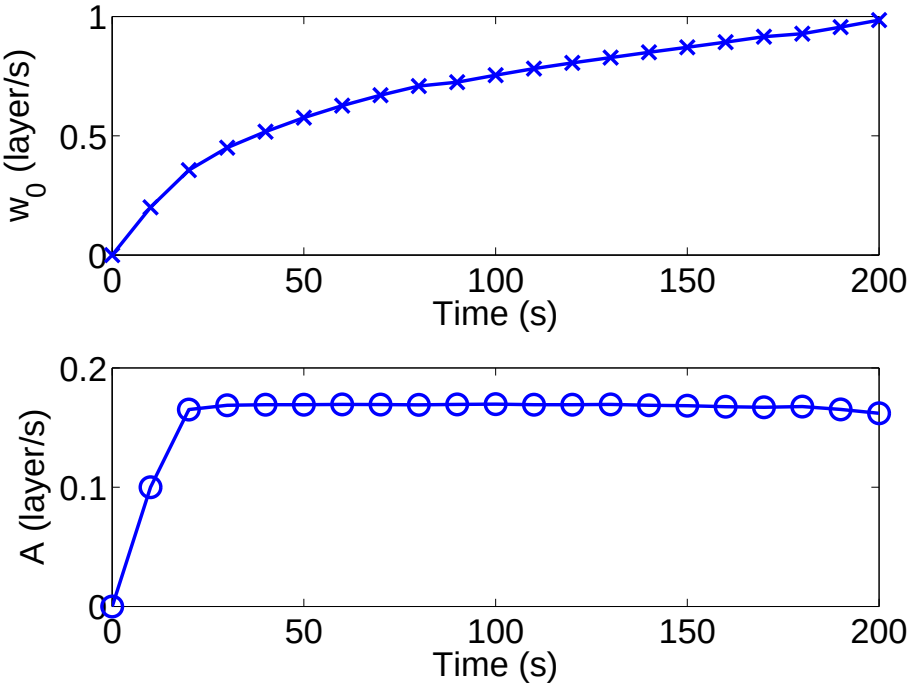

Figure 7.18: Input profiles for aggregate roughness-only control problem with EW equation as the plant model. $q_{r^2} = 1$, $q_{m^2} = 0$ and $r^2_{set} = 5500$.

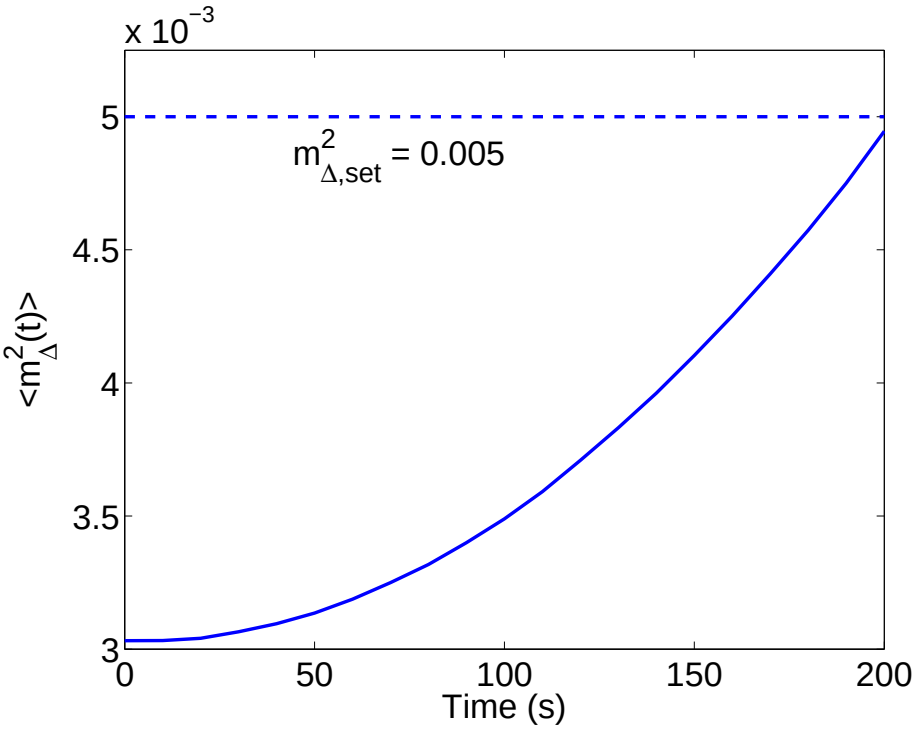

Figure 7.19: Profile of expected aggregate surface slope square with EW equation as the plant model. $q_{r^2} = 0$, $q_{m^2} = 1$ and $m^2_{set} = 0.005$.

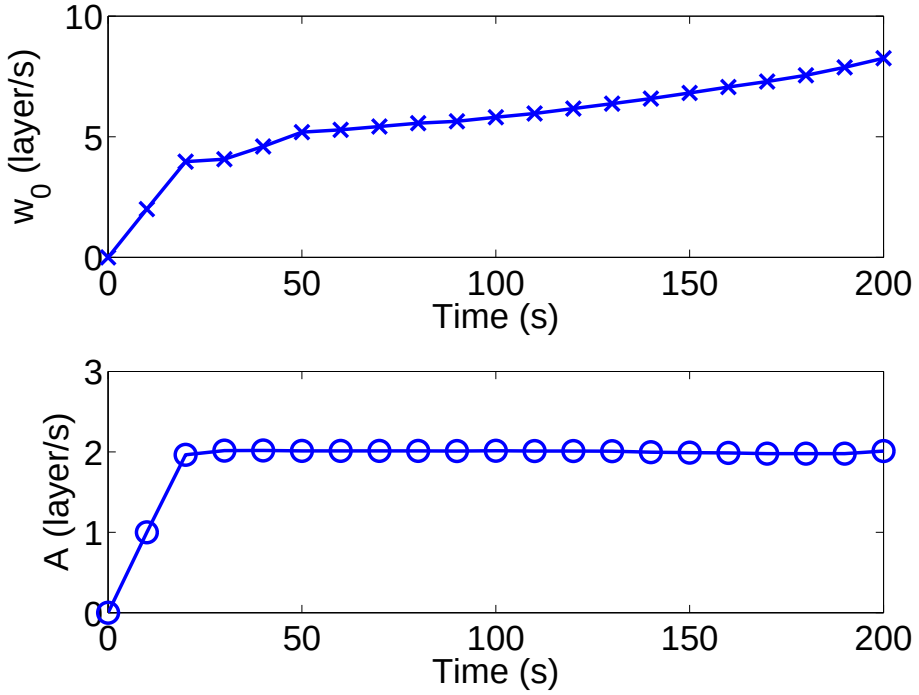

Figure 7.20: Input profiles for aggregate slope-only control problem with EW equation as the plant model. $q_{r^2} = 0$, $q_{m^2} = 1$ and $m^2_{set} = 0.005$.

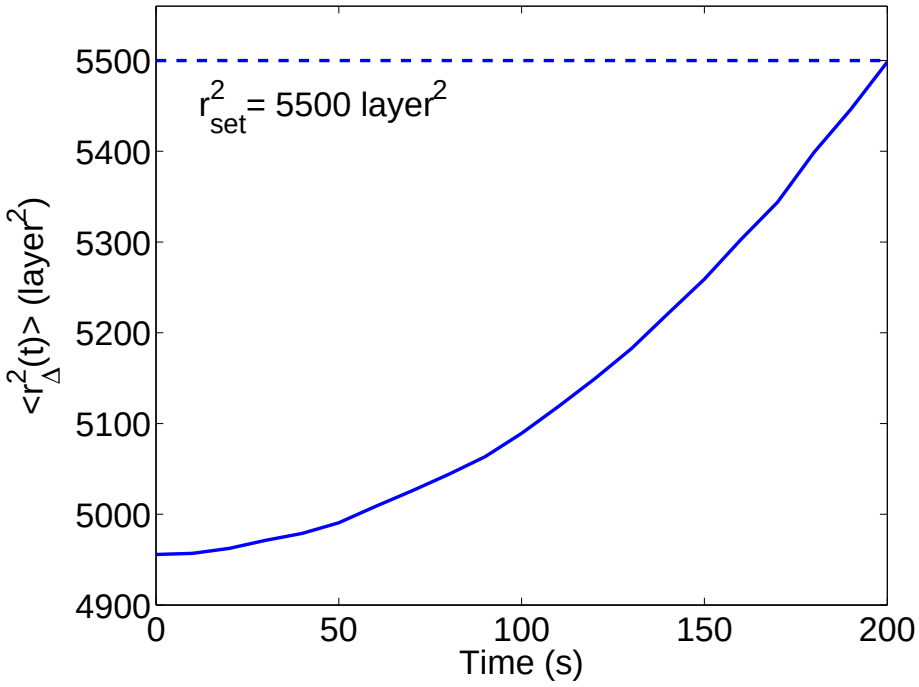

Figure 7.21: Profile of expected aggregate surface roughness square with kMC model as the plant model. $q_{r^2} = 1$, $q_{m^2} = 0$ and $r^2_{set} = 5500$.

profiles are shown in Fig. 7.22, while Fig. 7.23 shows the aggregate surface slope in the case of slope-only control and its corresponding manipulated input profiles are shown in Fig. 7.24. In both conditions, we see that both aggregate roughness and slope successfully reach their set-points at the end of the simulations ($t_f = 200$ s). Furthermore, the closed-loop evolution profiles with kMC as the plant model are very similar to the closed-loop profiles that use the EW equation as the plant model, which implies that the EW equation model used in this work can accurately predict the kMC simulation results.

Simultaneous regulation of aggregate surface roughness and slope has also been investigated. Similar to the case where the EW equation is used as the plant model, the

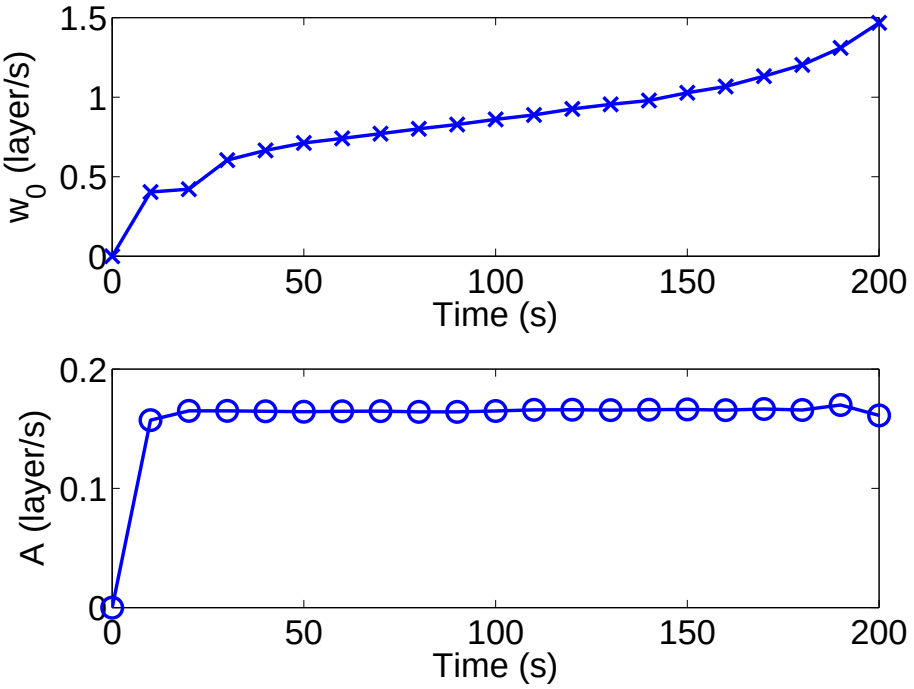

Figure 7.22: Input profiles for aggregate roughness-only control problem with kMC model as the plant model. $q_{r^2} = 1$, $q_{m^2} = 0$ and $r^2_{set} = 5500$.

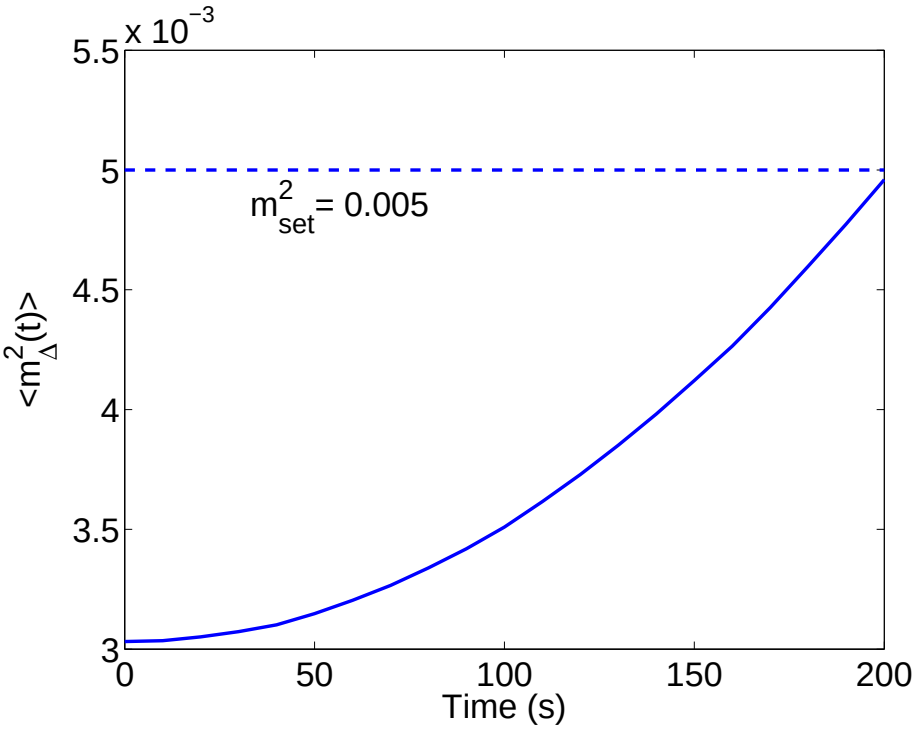

Figure 7.23: Profile of expected aggregate surface slope square with kMC model as the plant model. $q_{r^2} = 0$, $q_{m^2} = 1$ and $m^2_{set} = 0.005$.

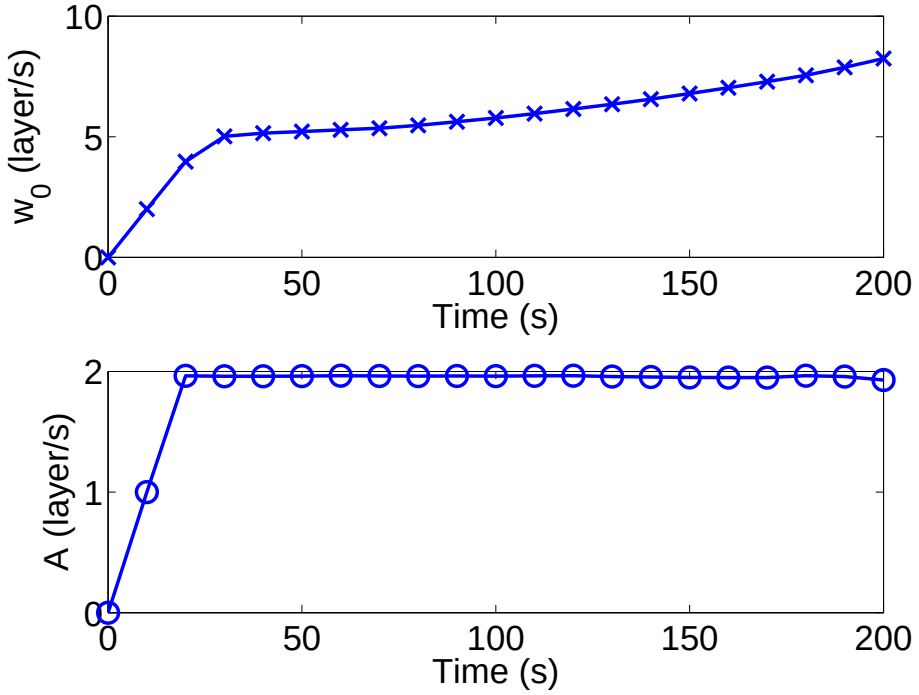

Figure 7.24: Input profiles for aggregate slope-only control problem with kMC model as the plant model. $q_{r^2} = 0$, $q_{m^2} = 1$ and $r^2_{set} = 0.005$.

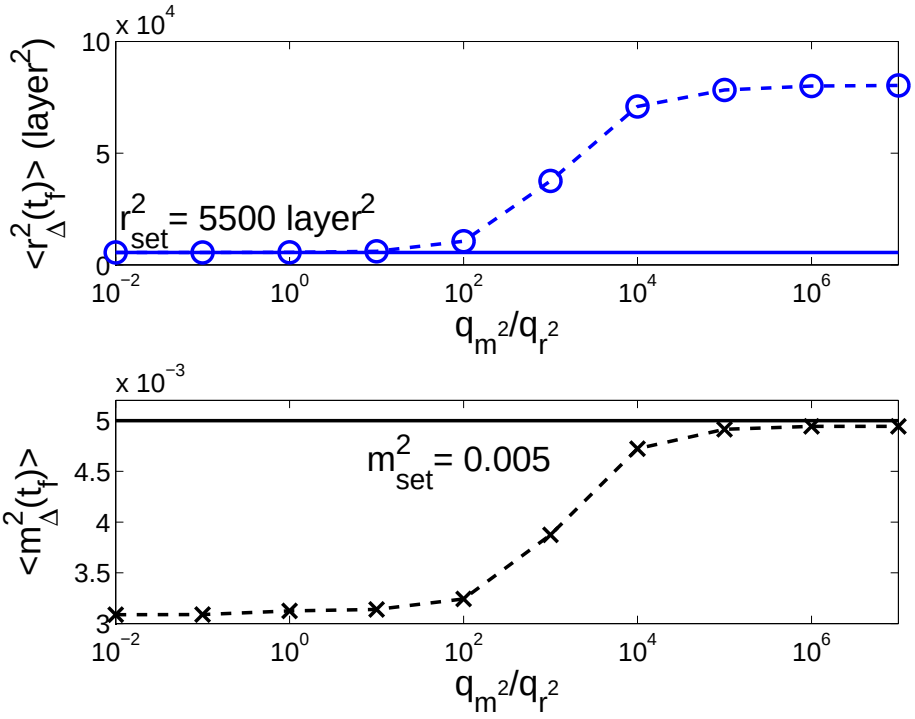

Figure 7.25: $\langle r_\Delta^2(t_f)\rangle$ and $\langle m_\Delta^2(t_f)\rangle$ at the end of closed-loop simulations ($t_f = 200$ s) for different penalty weighting factors in the predictive controller with kMC model as the plant model. $10^{-2} \leq q_{m^2} \leq 10^7$, $q_{r^2} = 1$, $r_{set}^2 = 5500$ and $m_{set}^2 = 0.005$.

weighting factor of aggregate slope square, q_{r^2}, is kept at 1, and the weighting factor of aggregate roughness square, q_{m^2}, ranges from 10^{-2} to 10^7. Fig. 7.25 shows the values of expected aggregate roughness and slope at the end of simulations as a function of q_{m^2}/q_{r^2}. It can be seen that the expected value of aggregate roughness approaches its set-point as q_{m^2} increases at the cost of larger deviation of the aggregate slope from its set-point.

Chapter 8

Conclusions

Motivated by the increasing importance of thin film solar cells, this dissertation developed a systematic methodology for modeling and control of thin film solar cell surface roughness and slope on both silicon layers and TCO layers. Kinetic Monte Carlo (kMC) methods and stochastic differential equation models were constructed to account for the stochastic nature of the thin film growth processes and were used as the basis for controller design.

Specifically, in Chapters 2 and 3, the lattice-size dependence and dynamic behavior of thin film surface roughness and slope under different characteristic length scales were studied in two thin film deposition process models and using different lattice dimensions. The simulation results indicate that the expected mean slope square reaches quickly a steady-state value and exhibits a very weak dependence with respect to lattice size variation. The simulation findings were corroborated by an analysis of appropriate finite-difference discretizations of surface height profiles computed by an EW-type partial differential equation

that can be used to describe the dynamics of surface height profile in the deposition processes under consideration. Aggregate surface roughness and slope were also introduced to apply these results in the context of solar cell performance improvement.

Subsequently, in Chapter 4, a thin film deposition process was simulated via a kinetic Monte Carlo method in a large lattice ($L = 40000$) and a patterned deposition rate profile was introduced to generate significant aggregate surface roughness and slope at a length scale comparable to the wavelength of visible light. An Edwards-Wilkinson-type equation for the aggregate surface profile was used to predict the surface temporal evolution of aggregate surface roughness and slope. A model predictive controller was designed to regulate aggregate surface roughness and slope to desired levels, and the controller was applied to the EW equation and the kMC model of the deposition process with $L = 40000$. Simulation results demonstrated the applicability and effectiveness of the controller and of the spatially-patterned deposition rate profile by demonstrating that different thin-film reflectance values can be generated by successfully controlling aggregate roughness and slope to desired values.

Chapter 5 developed a model predictive control algorithm to regulate the aggregate surface slope and roughness of a two-stage thin film growth process simulated via kMC method. A spatially uniform deposition rate profile was used in the first stage to control the film thickness and a spatially distributed deposition rate profile was utilized in the second stage to control the surface morphology. Similar to Chapter 4, aggregate surface roughness and aggregate surface slope were used to characterize the surface morphology and an EW-

type equation was used to predict process dynamics and form the basis of feedback control design. Closed-loop simulation results were presented to demonstrate the effectiveness of the proposed model predictive control algorithm in successfully regulating the aggregate rms slope and the aggregate rms roughness at desired levels that generate desired thin film light reflectance and transmittance.

Finally, in Chapters 6 and 7, we extended the method of Chapter 5 to simulate and control the TCO layer manufacturing process via kMC method. The deposition process was a two species thin film deposition process and different growth mechanisms were used for each species (ZnO and Al) and a patterned deposition rate profile was introduced to generate significant aggregate surface roughness and slope at a length scale comparable to the wavelength of visible light. To make the process more practical, wafer grating was combined with spatially distributed deposition rate profile to precisely control the surface morphology of TCO layers. An Edwards-Wilkinson-type equation for the aggregate surface profile was used to predict the surface temporal evolution of aggregate surface roughness and slope. A model predictive controller was designed to regulate aggregate surface roughness and slope to desired levels, and the controller was applied to the EW equation and the kMC model of the deposition process with $L = 40000$. Simulation results demonstrated the applicability and effectiveness of the controller and of the spatially-patterned deposition rate profile and wafer grating. The results of this work pave the way for the manufacturing of TCO layers with desired light trapping properties.

Bibliography

[1] A.-L. Barabási and H. E. Stanley. *Fractal Concepts in Surface Growth*. Cambridge University Press, New York, 1995.

[2] H. E. Bennett and J. O. Porteus. Relation between surface roughness and specular reflectance at normal incidence. *Journal of the optical society of America*, 51:123–129, 1961.

[3] C. Buzea and K. Robbie. State of the art in thin film thickness and deposition rate monitoring sensors. *Reports on Progress in Physics*, 68:385–409, 2005.

[4] A. Campa, O. Isabella, R. Van Erven, P. Peeters, H. Borg, J. Krč, M. Topic, and M. Zeman. Optimal design of periodic surface texture for thin-film a-si:h solar cells. *Progress in Photovoltaics*, 18:160–167, 2010.

[5] J. Chen, Q. Wang, and H. Li. Microstructured design of metallic diffraction gratings for light trapping in thin-film silicon solar cells. *Optics Communications*, 283:5236–5244, 2010.

[6] P. D. Christofides. *Nonlinear and Robust Control of PDE Systems: Methods and Applications to Transport-Reaction Processes*. Birkhäuser, Boston, 2001.

[7] P. D. Christofides, A. Armaou, Y. Lou, and A. Varshney. *Control and Optimization of Multiscale Process Systems*. Birkhäuser, Boston, 2008.

[8] R. Das, T. Jana, and S. Ray. Degradation studies of transparent conducting oxide: a substrate for microcrystalline silicon thin film solar cells. *Solar Energy Materials and Solar Cells*, 86:207–216, 2005.

[9] H. Davies. The reflection of electromagnetic waves from a rough surface. *Proc. Inst. Elec. Engrs.*, 101:209, 1954.

[10] S. F. Edwards and D. R. Wilkinson. The surface statistics of a granular aggregate. *Proceedings of the Royal Society of London Series A - Mathematical Physical and Engineering Sciences*, 381:17–31, 1982.

[11] F. Family. Scaling of rough surfaces: effects of surface diffusion. *Journal of Physics A: Mathematical and General*, 19:L441–L446, 1986.

[12] V. Ferry, A. Polman, and H. Atwater. Modeling light trapping in nanostructured solar cells. *ACS Nano*, 5:10055–10064, 2011.

[13] J. Gospodyn and J. C. Sit. Characterization of dielectric columnar thin films by variable angle mueller matrix and spectroscopic ellipsometry. *Optical Materials*, 29:318–325, 2006.

[14] M. A. Green. Thin-film solar cells: Review of materials, technologies and commercial status. *Journal of Materials Science: Materials in Electronics*, 18:15–19, 2007.

[15] C. A. Haselwandter and D. D. Vvedensky. Stochastic equation for the morphological evolution of heteroepitaxial thin films. *Physical Review B*, 74:121408, 2006.

[16] C. A. Haselwandter and D. D. Vvedensky. Renormalization of stochastic lattice models: Basic formulation. *Physical Review E*, 76:041115, 2007.

[17] C. A. Haselwandter and D. D. Vvedensky. Renormalization of stochastic lattice models: Epitaxial surfaces. *Physical Review E*, 77:061129, 2008.

[18] G. Hu, J. Huang, G. Orkoulas, and P. D. Christofides. Investigation of film surface roughness and porosity dependence on lattice size in a porous thin film deposition process. *Physical Review E*, 80:041122, 2009.

[19] G. Hu, Y. Lou, and P. D. Christofides. Dynamic output feedback covariance control of stochastic dissipative partial differential equations. *Chemical Engineering Science*, 63:4531–4542, 2008.

[20] G. Hu, G. Orkoulas, and P. D. Christofides. Modeling and control of film porosity in thin film deposition. *Chemical Engineering Science*, 64:3668–3682, 2009.

[21] G. Hu, G. Orkoulas, and P. D. Christofides. Regulation of film thickness, surface roughness and porosity in thin film growth using deposition rate. *Chemical Engineering Science*, 48:3903–3913, 2009.

[22] G. Hu, G. Orkoulas, and P. D. Christofides. Stochastic modeling and simultaneous regulation of surface roughness and porosity in thin film deposition. *Industrial & Engineering Chemistry Research*, 48:6690–6700, 2009.

[23] J. Huang, G. Hu, G. Orkoulas, and P. Christofides. Dependence of film surface roughness and slope on surface migration and lattice size in thin film deposition processes. *Chemical Engineering Science*, 65:6101–6111, 2010.

[24] J. Huang, G. Hu, G. Orkoulas, and P. D. Christofides. Dynamics and lattice-size dependence of surface mean slope in thin-film deposition. *Industrial & Engineering Chemistry Research*, 50:1219–1230, 2011.

[25] J. Huang, G. Orkoulas, and P. D. Christofides. Modeling and control of transparent conducting oxide layer surface morphology for improved light trapping. *Chemical Engineering Science*, 74:135–147, 2012.

[26] J. Huang, G. Orkoulas, and P. D. Christofides. Simulation and control of aggregate surface morphology in a two-stage thin film deposition process for improved light trapping. *Chemical Engineering Science*, 71:520–530, 2012.

[27] J. Huang, X. Zhang, G. Orkoulas, and P. D. Christofides. Dynamics and control of aggregate thin film surface morphology for improved light trapping: Implementation on a large-lattice kinetic monte carlo model. *Chemical Engineering Science*, 66:5955–5967, 2011.

[28] O. Isabella, J. Krč, and M. Zeman. Modulated surface textures for enhanced light trapping in thin-film silicon solar cells. *Applied Physics Letters*, 97:101–106, 2010.

[29] M. Kardar. Roughness and ordering of growing films. *Physica A*, 281:295–310, 2000.

[30] J. Krč and M. Zeman. Experimental investigation and modelling of light scattering in α-Si:H solar cells deposited on glass/ZnO:Al substrates. *Material Research Society Proceedings*, 715, 2002.

[31] J. Krč and M. Zeman. Effect of surface roughness of zno:al films on light scattering in hydrogenated amorphous silicon solar cells. *Thin Solid Films*, 426:296–304, 2003.

[32] J. Krč and M. Zeman. Optical modeling of thin-film silicon solar cells deposited on textured substrates. *Thin Solid Films*, 451:298–302, 2004.

[33] F. Leblanc and J. Perrin. Numerical modeling of the optical properties of hydrogenated amorphous-silicon-based P-I-N solar cells deposited on rough transparent conducting oxide substrates. *J. Appl. Phys*, 75:1074, 1994.

[34] S. W. Levine and P. Clancy. A simple model for the growth of polycrystalline Si using the kinetic Monte Carlo simulation. *Modelling and Simulation in Materials Science and Engineering*, 8:751–762, 2000.

[35] S. W. Levine, J. R. Engstrom, and P. Clancy. A kinetic Monte Carlo study of the growth of Si on Si(100) at varying angles of incident deposition. *Surface Science*, 401:112–123, 1998.

[36] H. Li, Q. Wang, J. Chen, J. Krč, and W. Soppe. Light trapping in amorphous silicon solar cells with periodic grating structures. *Optics Communications*, 285:808–815, 2012.

[37] Y. Lou and P. D. Christofides. Feedback control of surface roughness using stochastic PDEs. *AIChE Journal*, 51:345–352, 2005.

[38] E. Mirica, G. Kowach, P. Evans, and H. Du. Morphological evolution of zno thin films deposited by reactive sputtering. *Crystal Growth & Design*, 4:147–156, 2004.

[39] S. Moller and R. Palumbo. Solar thermal decomposition kinetics of zno in the temperature range 1950-2400 k. *Chemical Engineering Science*, 56:4505–4515, 2001.

[40] J. Muller and B. Rech. TCO and light trapping in silicon thin film solar cells. *Solar Energy*, 77:917–930, 2004.

[41] D. Ni and P. D. Christofides. Multivariable predictive control of thin film deposition using a stochastic PDE model. *Industrial & Engineering Chemistry Research*, 44:2416–2427, 2005.

[42] A. Poruba, A. Fejfar, Z. Remeš, J. Špringer, M. Vaněček, and J. Kočka. Optical absorption and light scattering in microcrystalline silicon thin films and solar cells. *Journal of Applied Physics*, 88:148–160, 2000.

[43] S. F. Rowlands, J. Livingstone, and C.P. Lund. Optical modelling of thin film solar cells with textured interface using the effective medium approximation. *Solar Energy*, 76:301–307, 2004.

[44] J. Springer and A. Poruba. Improved optical model for thin film silicon solar cells. *17th European Photovoltaic Solar Energy Conference*, 0:11, 2001.

[45] G. Tao and M. Zeman. Optical modeling of α-Si:H based solar cells on textured substrates. *1994 IEEE First World Conference on Photovoltaic Energy Conversion. Conference Record of the Twenty Fourth IEEE Photovoltaic Specialists Conference-1994 (Cat.No.94CH3365-4)*, 1:666, 1994.

[46] W. van Sark, G. W. Brandsen, M. Fleuster, and M. P. Hekkert. Analysis of the silicon market: Will thin films profit? *Energy Policy*, 35:3221–3125, 2007.

[47] A. Varshney and A. Armaou. Multiscale optimization using hybrid PDE/kMC process systems with application to thin film growth. *Chemical Engineering Science*, 60:6780–6794, 2005.

[48] A. Varshney and A. Armaou. Optimal operation of GaN thin-film epitaxy employing control vector parametrization. *AIChE Journal*, 52:1378–1391, 2006.

[49] D. G. Vlachos, L. D. Schmidt, and R. Aris. Kinetics of faceting of crystals in growth, etching, and equilibrium. *Physical Review B*, 47:4896–4909, 1993.

[50] T.V. Vorburger, E. Marx, and T.R. Lettieri. Regimes of surface-roughness measurable with light-scattering. *Applied Optics*, 32:3401–3408, 1993.

[51] A. Wächter and L.T. Biegler. On the implementation of an interior-point filter line-search algorithm for large-scale nonlinear programming. *Mathematical Programming*, 106:25–57, 2006.

[52] L. Wang and P. Clancy. Kinetic Monte Carlo simulation of the growth of polycrystalline Cu films. *Surface Science*, 473:25–38, 2001.

[53] Y. G. Yang, R. A. Johnson, and H. N. Wadley. A Monte Carlo simulation of the physical vapor deposition of nickel. *Acta Materialia*, 45:1455–1468, 1997.

[54] M. Zeman and R. Vanswaaij. Optical modeling of α-Si : H solar cells with rough interfaces: Effect of back contact and interface roughness. *Journal of Applied Physics*, 88:6436–6443, 2000.

[55] P. Zhang, X. Zheng, S. Wu, J. Liu, and D. He. Kinetic Monte Carlo simulation of Cu thin film growth. *Vacuum*, 72:405–410, 2004.

[56] X. Zhang, G. Hu, G. Orkoulas, and P.D. Christofides. Predictive control of surface mean slope and roughness in a thin film deposition process. *Chemical Engineering Science*, 65:4720–31, 2010.

[57] X. Zhang, J. Huang, G. Orkoulas, and P.D. Christofides. Controlling aggregate thin film surface morphology for improved light trapping using a patterned deposition rate profile. *Chemical Engineering Science*, 67:101–110, 2012.